Understanding and Enhancing the Photostability of Nanoporous Metal Oxide Thin Films for Solar Hydrogen Generation

A Dissertation

Presented in Partial Fulfillment of the Requirements for the

Degree of Doctorate of Philosophy

with a

Major in Materials Science & Engineering

in the

College of Graduate Studies

University of Idaho

by

Kalyan Chakravarthi Chitrada

Major Professor: Krishnan Raja, Ph.D.

Committee Members: Indrajit Charit, Ph.D.; Batric Pesic, Ph.D.; Thomas Bitterwolf, Ph.D.

Department Administrator: Eric Aston, Ph.D.

May 2016

Authorization to Submit Dissertation

This dissertation of Kalyan Chakravarthi Chitrada, submitted for the degree of Doctorate of Philosophy with a Major in Materials Science & Engineering and titled **"Understanding and Enhancing the Photostability of Nanoporous Metal Oxide Thin Films for Solar Hydrogen Generation**," has been reviewed in final form. Permission, as indicated by the signatures and dates below, is now granted to submit final copies to the College of Graduate Studies for approval.

Major Professor: _____ Date: _____
Krishnan Raja, Ph.D.

Committee Member: _____ Date: _____
Batric Pesic, Ph.D.

_____ Date: _____
Indrajit Charit, Ph.D.

_____ Date: _____
Thomas Bitterwolf, Ph.D.

Department Administrator: _____ Date: _____
Eric Aston, Ph.D.

Abstract

Solar water splitting is an environmentally benign process which has received wide attention in the recent years as an alternate method for a clean and safe production of hydrogen. This process employs a semiconductor based photocatalyst, water, and sunlight to produce hydrogen. Metal oxide based semiconductors are considered to be ideal photocatalytic materials because of their stability against photo corrosion combined with relatively narrow energy band gap, appropriately placed band edge positions with reference to oxygen and hydrogen energy levels, less scattering of charges due to wider valence band, high dielectric constant, natural abundance, and non-toxicity. In this dissertation, two metal oxide based semiconductors viz., iron (III) oxide and bismuth (III) oxide were investigated to understand and enhance their photo activity as photoanodes for solar water splitting application.

Iron (III) oxide has a well suited band gap to capture solar spectrum but it suffers from inappropriately positioned band edges, recombination losses due to low electron mobility, and a small minority carrier diffusion length. However, it was hypothesized that the Iron (III) oxide might show interesting photoelectrochemical properties by alloying with *4f* elements and shifting the conduction band minimum of the iron oxide favorably to more negative potentials. In the present study, a nanoporous iron oxide layer incorporated with Nd^{3+} and B^{3+} was synthesized by electrochemical anodization of a FeNdB alloy. The photoelectrochemical behavior of this oxide was compared with thermally oxidized FeNdB alloy and the iron oxides obtained by anodization and thermal oxidation of pure iron foil. Incorporation of Nd^{3+} and B^{3+} in the iron oxide showed a direct bandgap of 2.05 eV, an indirect bandgap of 1.9 eV and shifted the flatband potentials to –0.8 $V_{Ag/AgCl}$ in 1 M KOH solution. The FeNdB oxide showed marginally better catalytic activity for the oxygen evolution reaction than pure iron oxide under dark conditions.

The binary bismuth (III) oxide, in spite being a good photocatalytic material, did not receive as much attention as other bismuth based ternary oxides for photoelectrochemical water splitting application. In this present study, large surface area nanoporous bismuth

oxide thin films were synthesized by the electrochemical anodization. These anodic oxides exhibited a dual layered structure having a planar inner oxide and nanoporous outer oxide. Effect of the nanoscale dimensions of the oxides on the photoelectrochemical behavior was studied to understand the charge transport, charge recombination behavior, and long term stability of the material. A maximum photo current density of 0.97 mA/cm^2 was observed for the sample anodized at 10 V at 1.53 V_{RHE}. The nanoporous anodic oxides showed a charge carrier density in the range of 1.2 x 10^{17} – 4.8 x 10^{18} cm^{-3} without illumination and about 60% increase in the charge carrier density upon illumination. However a decay in photo current was observed for the bismuth oxide samples was due to accumulation of holes on the electrode surface. This hole-accumulation was mitigated by the addition of hole scavengers. Addition of hydrogen peroxide as hole scavenger increased the photo current density by about 4 times in 0.5 M Na_2SO_4 (pH: 5.8) electrolyte. Addition of H_2O_2 in 1 M KOH (pH: 13.7) showed an increase-decrease behavior and high photo current density of ~10 mA/cm^2 at a bias potential of 0.65 V_{RHE}. The high photo activity observed in this electrolyte was attributed to the in-situ formation of Bi_2O_{4-x} phase by the photo-conversion of the β-Bi_2O_3 at the surface. The photo-converted Bi_2O_{4-x} has a smaller band gap (1.4 eV) and therefore harvested more light in the visible region. This in-situ formation of low band gap phases in the presence of H_2O_2 during solar water splitting is an interesting observation which has been reported for the first time and this will help design material with very high photo-activity.

Acknowledgements

It is my great pleasure to express my deep sense of gratitude to my academic advisor, Dr. Krishnan S Raja, for giving me an opportunity and especially for being patient with me for past three years. I am thankful for his keen attention, constant encouragement and inspiring guidance without which this work would not have come to fruition. I am grateful to my committee members, Dr. Indrajit Charit, Dr. Batric Pesic and Dr. Thomas Bitterwolf, for their insight, constructive criticism and support.

I would like to thank Dr. Dev Chidambaram and his students Ruchi Gakhar, David Rodriguez and Zachary Karmiol at University of Nevada, Reno for their help and suggestions. I would also like to acknowledge the support of Dr. Eric Aston (Chair, ChMSE), Margaret Baker and Gail Bergman (Administrative Assistants, ChMSE) for extending their support during my course of study. A special note of thanks to Dr. Tom Williams (Director of electron microscopy facility), Dr. David N. McIlroy and Dr. Jo Ellen Force (Department of Physics) for providing support, when needed. Likewise, a special thanks to my lab mates, Stuart Whitman, Steven Sitler, Colin Lunstrum and Melissa Fernandes for providing a friendly work environment with their positive discussions.

Finally, thanks and acknowledgments go to everyone without whom I could not have reached where I am right now and I extend my thanks to everyone with whom I was associated during my stay here, whose influence significantly helped me grow professionally and otherwise. I would like to express my heartfelt gratitude to my friends who extended unwavering support and love that helped me through this journey successfully. I am grateful to my family members for their understanding, optimism and constant backing throughout my education, as I am where I am-- because of their love and support.

Dedication

This work is dedicated to my family and friends

Table of Contents

Authorization to Submit Dissertation ii

Abstract iii

Acknowledgements v

Dedication vi

Table of Contents vii

List of Figures x

List of Tables xx

1. Introduction 1

1.1. The Energy Challenge 1

1.2. Solar-Hydrogen: Towards A Renewable Energy Future 2

1.3. Principle of Photoelectrochemical Water Splitting 5

1.3.1. Semiconductors 6

1.3.2. Semiconductor-electrolyte interface 8

1.3.3. Photoelectrochemical water splitting mechanism 10

1.3.4. Solar-to-hydrogen efficiency 11

1.4. Materials Challenge for Photoelectrochemical Water Splitting 12

1.5. Iron (III) Oxide 16

1.6. Bismuth (III) Oxide 19

1.6.1. Crystal structure 20

1.6.2. Electronic structure 23

1.6.3. Issues with bismuth oxide based photoelectrodes 25

1.7. Objectives and Scope of this Dissertation 27

1.8. References 29

2. Photoelectrochemical Behavior of Iron Oxide alloyed with Nd and B Nanoporous Oxide of FeNdB Alloy 34

2.1. Abstract 34

2.2. Introduction 34

2.3. Experimental Methods 38

2.3.1. Materials and methods 38

2.3.2. Characterization 39

2.3.3. Photoelectrochemical studies 39

2.4. Results and Discussions 40
2.4.1. Morphology 40
2.4.2. XRD analysis 44
2.4.3. Raman analysis 45
2.4.4. Band gap calculation 46
2.4.5. Photoelectrochemical behavior 48
2.4.6. Mott-Schottky behavior 50
2.5. Conclusions 55
2.6. References 56
3. Enhanced Photoelectrochemical Performance of Anodic Nanoporous β-Bi_2O_3 62
3.1. Abstract 62
3.2. Introduction 62
3.3. Experimental Methods 65
3.3.1. Materials and methods 65
3.3.2. Characterization 65
3.3.3. Photoelectrochemical studies 66
3.4. Results and Discussion 66
3.4.1. Potentiodynamic polarization 66
3.4.2. Potentiostatic anodization 68
3.4.3. Material characterization 72
3.4.4. Photoelectrochemical behavior 82
3.4.5. Electrochemical impedance spectroscopy 88
3.4.6. Mott-Schottky analysis 91
3.5. Conclusions 97
3.6. References 97
4. Enhanced Performance of β-Bi_2O_3 by in-situ Photo-conversion to Bi_2O_3-BiO_{2-x} Composite Photoanode for Solar Water Splitting 104
4.1. Abstract 104
4.2. Introduction 104
4.3. Experimental Methods 107
4.3.1. Fabrication of nanoporous oxide films 107
4.3.2. Material characterization 107
4.3.3. Photoelectrochemical testing 108

4.4. Results and Discussion 110
4.4.1. Morphology and structural characterization 110
4.4.2. Photoelectrochemical Behavior 111
4.4.3. Material testing after photoelectrochemical testing 129
4.4.4. Electrochemical impedance spectroscopy 134
4.4.5. Mott-Schottky analysis 135
4.5. Conclusions 137
4.6. References 138
5. Stability of the Nanoporous Bismuth Oxide Photoanodes for Solar Water Splitting . 143
5.1. Abstract 143
5.2. Introduction 143
5.3. Synthesis and characterization of Bi_2O_3 polymorphs for photo-catalytic applications: 145
5.4. Experimental 151
5.4.1. Materials and methods 151
5.4.2. Photoelectrochemical studies 152
5.5. Results and Discussion 153
5.5.1. Morphology and structural characterization 153
5.5.2. Optical characteristics 157
5.5.3. Photoelectrochemical behavior 159
5.5.4. Impedance spectroscopy 165
5.5.5. Significance of the flat band potential 168
5.5.6. Photodecomposition 174
5.6. Summary 175
5.7. References 176
Appendix A. Supplementary Information for Chapter 2 179
Appendix B. Supplementary Information for Chapter 3 191
Appendix C. Supplementary Information for Chapter 4 198

List of Figures

Figure 1.1. Projected world energy consumption (Source: OECD/IEA World Energy Outlook 2004) 1

Figure 1.2. Schematic design of an industrial scale photoelectrochemical cell for hydrogen generation by solar water splitting. Source: Photoelectrochemistry competence center, EPFL, Lausanne, Switzerland 5

Figure 1.3. Energy band diagram of metal, insulator and semiconductor. 6

Figure 1.4. Energy band diagram of n-type and p-type semiconductors. E_F is Fermi energy.. 8

Figure 1.5. Energy Diagram of the n-type semiconductor-electrolyte interface, a) before equilibrium, b) after equilibrium. 9

Figure 1.6. Schematic of a photoelectrochemical water splitting cell. 10

Figure 1.7. Band edge positioning in an ideal n-type photoelectrode. 13

Figure 1.8. Diagram of bandgaps and band edges (CB bottom and VB top) of some wide bandgap semiconductors (pH = 0, vs. NHE at room temperature). Adapted from Ref [8]. ... 15

Figure 1.9. Crystal structures of Fe_2O_3: a) α-Fe_2O_3, b) β-Fe_2O_3, c) ϒ- Fe_2O_3 & d) ε-Fe_2O_3. Adapted from Ref [11]. 17

Figure 1.10. Temperature dependent phase transformations of Bi_2O_3 polymorphs. Adapted from ref [18] 20

Figure 1.11. Lattice structure of a) α-Bi_2O_3, b) β-Bi_2O_3 and c) the β-Bi_2O_3 tunnel looking top down from the c axis. Adapted from a) http://payneresearch.org/research/lone-pair-materials/ and b) Ref [38] 22

Figure 1.12. a) Molecular orbital diagram of Bi_2O_3. Only the bonding e_g states are illustrated and the nonbonding t_{2g} states are omitted. B and AB denote bonding and antibonding, respectively. b) Arrangement of Lone-Pairs in α and β Bi_2O_3. Adapted from Ref [34] and [42] respectively. 23

Figure 1.13. Electronic structures of (a) α-Bi_2O_3 and (b) β-Bi_2O_3. Adapted from Ref [37]. 25

Figure 1.14. Schematic of Electrochemical Anodization set-up. 28

Figure 2.1. FESEM images of (a-b) pure iron foil, (c-d) FeNdB samples thermally oxidized in air at 450 °C for 2 h. These samples are referred as thermal iron oxide and oxidized FeNdB respectively in the text. FESEM images of the anodized surfaces of the (e-f) FeNdB and (g-h) iron foil samples electrochemically anodized in ethylene glycol solution containing 0.1 M NH4F and 5 vol% water at 40 V for 15 minutes and thermally annealed at 450 °C for 2h. These samples are referred as anodized iron oxide and anodized FeNdB respectively in the text. 41

Figure 2.2. TEM image of the anodized FeNdB sample electrochemically anodized in ethylene glycol solution containing 0.1 M NH_4F and 5 vol% water at 40 V for 15 minutes. 42

Figure 2.3. Energy dispersive X-ray Spectrometry (EDS) of the anodized FeNdB sample and X-ray elemental mapping analyses. (a) Image of the oxide layer analyzed, (b) EDS spectrum indicating presence of Fe, Nd, and O, (c) overall mapping, mappings of: (d) iron, (e) oxygen, and (f) neodymium. 43

Figure 2.4. Glancing angle X-ray diffraction pattern of the anodized FeNdB sample that was annealed at 450 °C for 2 h. 45

Figure 2.5. Raman spectra of the oxide layers of $Fe_{14}Nd_2B$ alloy. (a) Thermally oxidized at 450 ^oC for 2 h; (b) Anodized at 40 V for 15 minutes and annealed at 450 ^oC for 2 h. 46

Figure 2.6. (a) Optical absorbance Vs wavelength plots of thermally oxidized and anodized FeNdB samples based on the diffuse reflectance measurements. (b) Tauc plots of thermally oxidized and anodized iron and FeNdB samples. Photo currents were measured by illuminating the samples by different wavelengths of light using band pass filters in the range of 450 – 700 nm at 50 nm intervals. The sample was polarized at 0.5 $V_{Ag/AgCl}$ in 1 M KOH solution. 48

Figure 2.7. Photocurrent density vs. time plots of iron oxide and FeNdB samples in 1M KOH solution illuminated at 1-sun intensity using AM 1.5 filter. The samples were biased by an external potential of 0.5 $V_{Ag/AgCl}$. 51

Figure 2.8. Mott-Schottky results of the thermally oxidized samples with and without illumination in 1 M KOH electrolyte: (a) thermal iron oxide; and (b) oxidized FeNdB..... 54

Figure 2.9. Mott-Schottky results of the anodized and annealed samples with and without illumination in 1 M KOH electrolyte: (a) anodic iron oxide; and (b) anodized FeNdB. 55

Figure 3.1. Anodic polarization of bismuth in 0.3 M citric acid solution with and without illumination of simulated solar light. The inset shows the polarization at lower potentials . 67

Figure 3.2. Transients of anodization current densities recorded at different anodization potentials during potentiostatic anodization 69

Figure 3.3. FESEM images of the nanoporous morphology of the bismuth oxide synthesized by anodization of bismuth at 60 V for a) 3s, b) 30s, c) 300s, d) 600s, e) & f) 1800s 73

Figure 3.4 FESEM images of the bismuth oxide nanoporous oxide layer prepared at various anodization potentials, a) 3 V, b) 5 V, c) 10 V, d) 20 V, e) 40 V and f) 60 V for 30mins 75

Figure 3.5. X-ray diffraction pattern of the nanoporous bismuth oxide synthesized by anodization of bismuth at 10 V for 30 minutes and annealed at 200 ^{o}C for 2h..... 77

Figure 3.6. XPS spectra of (a) as anodized bismuth oxide surface- Bi 4f; (b) anodized and annealed bismuth oxide surface- Bi 4f. where B and E: bismuth carbonate, C and F: bismuth oxide, (c) as anodized bismuth oxide surface- O 1s ; and (d) anodized and annealed bismuth oxide surface- O 1s. Where A: carbonate, B: Oxide, C; Water 79

Figure 3.7. Raman spectra of the bismuth oxide nanoporous oxide layer prepared at anodization potentials, 10-60 V for 30 mins and annealed at 200 ^{o}C for 2h 80

Figure 3.8. Energy band gap of the bismuth oxide nanoporous oxide layer prepared at various anodization potentials based on: (a) the UV-VIS diffuse reflectance measurements; (b) Tauc plots of the annealed Bi_2O_3 samples corresponding to a direct transition; and (c) Tauc plot of indirect transition 81

Figure 3.9. Potential vs current density plots of the anodic Bi_2O_3 prepared at different anodization potentials: (a) 3-10 V; and (b) 20-60 V. Thermal oxidation was carried out at 200 ºC for 2 h. The potentials were scanned at a rate of 2.5 mV/s in 1 M KOH solution and

illuminated with a 1-sun intensity simulated solar light. The light was interrupted at regular intervals to record the dark current. 84

Figure 3.10. Photo current and dark current densities of the anodic Bi_2O_3 prepared at different anodization potentials: (a) 3-10 V; and (b) 20-60 V. Thermal oxidation was carried out at 200 ºC for 2 h. in 1 M KOH solution and illuminated with a 1-sun intensity simulated solar light. The light was interrupted at regular intervals to record the dark current..... 85

Figure 3.11. Electrochemical impedance spectroscopy (Bode plots) of the anodic nanoporous Bi_2O_3 samples anodized at 10 V for 30 min and 20 V 30min and annealed at 200 ^oC for 2 h in 1 M KOH with applied potential of 0.5 V without (a) and with (b) illumination. Z (filled markers) - refers to impedance modulus and ω (unfilled markers) refer to phase angle..... 89

Figure 3.12. Equivalent circuit for the EIS data in Table 3.3..... 90

Figure 3.13. Mott-Schottky of the anodic nanoporous Bi_2O_3 anodized at 20 V for 30 min and annealed at 200 ºC for 2 h in 1 M KOH with and without illumination..... 94

Figure 3.14. Schematics of the potential levels of anodic (anodized at 10 V) nanoporous Bi_2O_3 in pH:14 solution with reference to absolute vacuum scale and saturated Ag/AgCl electrode (Not to scale). All energy scales were converted to potential scale (1 eV corresponds to 1 V). 95

Figure 4.1. (a) & (b) SEM image of the surface morphology of the nanoporous β-Bi_2O_3, c) XRD pattern and d) Raman spectrum of the nanoporous β-Bi_2O_3..... 111

Figure 4.2. (a) I-V characteristics and (b) Potentiostatic current transients of nanoporous Bi_2O_3 in 1 M KOH and 0.5 M Na_2SO_4 under chopped illumination 113

Figure 4.3. (a) Potentiostatic current transients of nanoporous Bi_2O_3 at 1.5 V_{RHE} in 1 M KOH under continuous illumination with and without stirring. Potentiostatic current transients with the addition of 10 vol % methanol as hole-scavenger for the nanoporous Bi_2O_3 at 1.5 V_{RHE} in (b) 1 M KOH solution; and (c) 0.5 M Na_2SO_4 solution. 115

Figure 4.4. I-V characteristics of nanoporous Bi_2O_3 in (a) 1 M KOH (b) 1 M KOH with H_2O_2, (c) 0.5 M Na_2SO_4 and (d) 0.5 M Na_2SO_4 with H_2O_2 under continuous illumination. 120

Figure 4.5. (a) Potentiostatic current transients with the addition of H_2O_2 as hole-scavenger for the nanoporous Bi_2O_3 at 0.65 V_{RHE} in 1 M KOH solution; (b) Cumulative hydrogen evolution as a function of time measured by water displacement using a pipette in comparison with the charge accumulation. (c) Potentiostatic current transients with the addition of H_2O_2 as hole-scavenger for the nanoporous Bi_2O_3 at 0.8 V_{RHE} in 0.5 M Na_2SO_4 solution; (d) Cumulative hydrogen evolution as a function of time measured by water displacement using a pipette in comparison with the charge accumulation. 127

Figure 4.6. (a) Potentiostatic current transients with the addition of H_2O_2 as hole-scavenger for the nanoporous Bi_2O_3 at 0.80 V_{RHE} in 0.5 M Na_2SO_4 and pH 7 Phosphate buffer solution. (b) Current transients at different bias potentials with chopped illumination conditions in presence of H_2O_2 as hole-scavenger for the nanoporous Bi_2O_3 in 1 M KOH solution..... 128

Figure 4.7. Characterization results of the β-Bi_2O_3 photoanode after initial illumination in 1 M KOH + 0.3 M H_2O_2 at 0.65 V_{RHE}. (a) surface morphology after 200 s testing; (b) surface morphology after 300 s testing; (c) UV-Vis diffuse reflectance spectra before and after testing for 300 s in 1 M KOH + 0.3 M H_2O_2 at 0.65 V_{RHE}, (d) XRD pattern of the sample after photo electrochemical testing in the 1 M KOH + 0.3 M H_2O_2 solution at 0.65 V_{RHE} for 300 s; (e) X-ray photoelectron spectroscopy of samples tested in 1 M KOH + 0.3 M H_2O_2 solution at 0.65 V_{RHE} with and without illumination: Bi 4f spectra; and (f) O-1s spectra 131

Figure 4.8. Surface morphology of the nanoporous Bi_2O_3 after 1 hour PEC testing in 1 M KOH at 1.5 V_{RHE}, (a) No H_2O_2 addition, (b) 0.15 M H_2O_2 addition, and (c) 0.3 M H_2O_2 addition. . 132

Figure 4.9. Surface morphology of the nanoporous Bi_2O_3 after 1 hour PEC testing in 0.5 M Na_2SO_4 at 1.5 V_{RHE}, (a) No H_2O_2 addition, (b) 0.15 M H_2O_2 addition, and (c) 0.3 M H_2O_2 addition. 133

Figure 4.10. Mott-Schottky plots of of nanoporous bismuth oxide in 1 M KOH + 0.3 M H_2O_2 with and without illumination 136

Figure 5.1. FESEM images of the nanoporous morphology of the bismuth oxide synthesized by anodization of bismuth at 60 V for 30 minutes: (a) as-anodized condition; and (b) annealed at 240 ^oC for 2 h 154

Figure 5.2. FESEM images of the nanoporous morphology of the bismuth oxide synthesized by anodization of bismuth at 60 V for 30 minutes: (a) annealed at 240 ^{o}C for 4 h; and (b) annealed at 240 ^{o}C for 2 h 155

Figure 5.3. X-ray diffraction patterns of the nanoporous bismuth oxide synthesized by anodization of bismuth at 60 V for 30 minutes and annealed at 240 ^{o}C for 2, 4, and 6 h. Increasing the annealing time increased the volume fraction of monoclinic α-Bi_2O_3. 156

Figure 5.4. Optical absorbance spectra (obtained from the UV-VIS diffuse reflectance spectroscopy)of the nanoporous bismuth oxide synthesized by anodization of bismuth at 60 V for 30 minutes and annealed at 240 ^{o}C for 4, and 6 h. Inflections of optical absorbance were observed at three different energy levels indicating optical transitions occurred due to multiple phases. Baseline corrections were applied by comparing the spectrum obtained using barium sulfate. 158

Figure 5.5. Raman spectra of the anodic nanoporous Bi_2O_3 annealed at 240 ^{o}C for 6 h before and after the photo electrochemical tests. The change in intensity implies decrease in the thickness of the oxide layer and modification of the surface morphology/roughness. 158

Figure 5.6.(a) Photo current density of the nanoporous anodic Bi_2O_3 annealed at 240 ^{o}C for different times. The samples were polarized at 0.2 V Ag/AgCl in 1 M KOH solution and illuminated with a 1-sun intensity simulated solar light. (b) Photo current and dark current densities of the nanoporous anodic Bi_2O_3 annealed at 240 ^{o}C for 6 h. The light was interrupted at regular intervals to record the dark current. (c) Photocurrent and dark current densities of the thermally oxidized Bi_2O_3. Thermal oxidation was carried out at 240 ^{o}C for 2, 4, and 6 h. 160

Figure 5.7. FESEM images of the nanoporous morphology of the bismuth oxide synthesized by anodization of bismuth at 60 V for 30 minutes and annealed at 240 ^{o}C for 2 h: (a) before the PEC testing, and (b) after the PEC testing at 0.2 $V_{Ag/AgCl}$ in 1 M KOH for ~ 3 h of illumination. 163

Figure 5.8. Tauc plots of the nanoporous anodic Bi_2O_3 annealed at 240 ^oC for 2 and 4 h after long term photo electrochemical experiments. The band gap values increased from 2.5 to > 2.7 eV after > 2 h of photo illumination. 164

Figure 5.9. XRD patterns of the nanoporous anodic Bi_2O_3 annealed at 240 ^oC for 2, 4, and 6 h after long term photo electrochemical experiments. 165

Figure 5.10. Electrochemical impedance spectroscopy (Bode plots) of the anodic nanoporous Bi_2O_3 annealed at 240 ^oC for 4 h in 1 M KOH without (a) and with (b) illumination. 166

Figure 5.11. Mott-Schottky of the anodic nanoporous Bi_2O_3 annealed at 240 ^oC for 4 h in 1 M KOH without (a) and (b) with illumination 167

Figure 5.12. Electrochemical impedance spectroscopy (Bode plots) of the anodic nanoporous Bi_2O_3 annealed at 240 ^oC for 6 h in 1 M KOH without (a) and with (b) illumination. 171

Figure 5.13. Mott-Schottky of the anodic nanoporous Bi_2O_3 annealed at 240 C for 6 h in 1 M KOH without (a) and (b) with illumination. 172

Figure 5.14. Schematics of the potential levels of anodic nanoporous Bi_2O_3 in pH:14 solution with reference to absolute vacuum scale and saturated Ag/AgCl electrode. All energy scales were converted to potential scale (1 eV corresponds to 1 V). 174

Figure A1. Cross-sectional FESEM images of (a) pure iron foil and (b) FeNdB samples thermally oxidized in air at 450 °C for 2 h. These samples are referred as thermal iron oxide and oxidized FeNdB respectively in the text. Cross-sectional FESEM images of the anodized surfaces of the (c) FeNdB and (d) iron foil samples electrochemically anodized in ethylene glycol solution containing 0.1 M NH_4F and 5 vol% water at 40 V for 15 minutes and thermally annealed at 450 °C for 2h. These samples are referred as anodized iron oxide and anodized FeNdB respectively in the text. 179

Figure A2. High resolution X-ray photo electron spectra of the FeNdB samples in three different surface conditions: air oxidized, as-anodized, and anodized + annealed. (a) Fe 2p spectra, (b) Nd 3d spectra, and (c) O 1s spectra 180

Figure A3. Valence band structure of the oxide layers of pure iron and $Fe_{14}Nd_2B$ alloy. 182

Figure A4. Galvanodynamic polarization results of the oxides of iron and FeNdB alloy in 1 M KOH solution with and without illumination: (a) Samples thermally oxidized in air; and (b) Samples anodized and annealed. The scan rate was 5 $\mu Acm^{-2}s^{-}$ 184

Figure A5. (a) Electrochemical impedance spectroscopy results (Bode plots) of thermally oxidized iron and FeNdB samples in 1 M KOH solution with and without illumination. The samples were biased by an external potential of 0.5 $V_{Ag/AgCl}$. (b) Electrochemical impedance spectroscopy results (Bode plots) of anodized iron and FeNdB samples in 1 M KOH solution with and without illumination. The samples were biased by an external potential of 0.5 $V_{Ag/AgCl}$. 187

Figure A6. Equivalent circuit for the EIS data in Table A2. 188

Figure B1. Pore size distribution of anodic bismuth oxide prepared by anodization at 60 V for 30 min. similar frequencies of distribution were observed for other anodization conditions as well. 191

Figure B2. Cross-sectional FESEM images of the bismuth oxide nanoporous oxide layer prepared at various anodization potentials, a) 3 V, b) 5 V, c) 10 V, d) 20 V, e) 40 V and f) 60 V for 30mins 192

Figure B3. Result of a long term potentiostatic photoelectrochemical test carried out on the nanoporous Bi_2O_3 sample anodized at 20 V 30 min. in 1 M KOH at 0.5 $V_{Ag/AgCl}$. 193

Figure B4. Hydrogen evolution measurement during potentiostatic (0.5 $V_{Ag/AgCl}$) polarization of the nanoporous anodic bismuth oxide sample (anodized at 20 V, 30 min.) in 1 M KOH. The top curve is constructed based on the charge accumulation due to photocurrent. The bottom curve is the actual hydrogen volume measured by water displacement. The difference in the values is attributed to the dissolved hydrogen in the KOH and other experimental limitations. 193

Figure B5. SEM image of the surface morphology of the nanoporous bismuth oxide sample (anodized at 20 V, 30 min.) after potentiostatic photoelectrochemical test at 0.5 $V_{Ag/AgCl}$ for 1 h. The nanoporous morphology was not significantly altered after 1 h exposure to simulated sunlight and applied potential. 194

Figure B6. XRD of the nanoporous bismuth oxide sample (anodized at 20 V, 30 min.) after potentiostatic photoelectrochemical test at 0.5 $V_{Ag/AgCl}$ for 1 h..... 194

Figure B7. Electrochemical impedance spectroscopy (Nyquist plots) of the anodic nanoporous Bi_2O_3 samples anodized at a) 3 V, b) 5 V, c) 10 V, d) 20 V, e) 40 V and f) 60 V for 30mins with and without illumination. 195

Figure B8. Electrochemical impedance spectroscopy (Bode plots) of the anodic nanoporous Bi_2O_3 samples anodized at a) 3 V & 5 V without illumination., b) 3 V & 5 V with illumination, c) 40 V & 60 V without illumination and d) c) 40 V & 60 V with illumination 196

Figure B9. Mott-Schottky analysis of the anodic nanoporous Bi_2O_3 samples anodized at a) 3 V, b) 5 V, c) 10 V, d) 40 V and e) 60 V for 30mins with and without illumination. 197

Figure C1. Tauc plots of nanoporous anodic Bi_2O_3 based on the photo current measurements in 1 M KOH at a bias potential of 1.5 V_{RHE}. 198

Figure C2. (a) Potentiostatic current transients with the addition of H_2O_2 as hole-scavenger for the nanoporous Bi_2O_3 at 1.5 V_{RHE} in 1 M KOH solution; (b) Cumulative hydrogen evolution as a function of time measured by water displacement using a pipette in comparison with the charge accumulation with and without H_2O_2. (c) Potentiostatic current transients with the addition of H_2O_2 as hole-scavenger for the nanoporous Bi_2O_3 at 1.5 V_{RHE} in 0.5 M Na_2SO_4 solution; (d) Cumulative hydrogen evolution as a function of time measured by water displacement using a pipette in comparison with the charge accumulation with and without H_2O_2 199

Figure C3. Tauc plot constructed using the β-Bi_2O_3/BiO_{2-x} composite sample. 200

Figure C4. Equivalent circuit diagram of the ‘‘2 RC-in-series’ model used for fitting the experimental values and derived the values of circuit parameters listed in Tables S1-S2. . 200

Figure C5. Summary of the values of equivalent circuit components fitted using the ‘2RC-in series model’ with the EIS data of nanoporous bismuth oxide in 1 M KOH with and without addition of hole scavengers. 201

Figure C6. Summary of the values of equivalent circuit components fitted using the ‘2CPE-Warburg model’ with the EIS data of nanoporous bismuth oxide in 0.5 M Na_2SO_4 with and without addition of 0.15 M and 0.3 M of hydrogen peroxide. 201

Figure C7. Nyquist plots of β-Bi_2O_3 tested in 1 M KOH + 0.3 M H_2O_2 with illumination (labeled as light) and without illumination (labeled as dark). 204

Figure C8. Equivalent circuit for fitting the electrochemical impedance spectroscopic data. 204

List of Tables

Table 1.1. Overview of global power generating capacities of sustainable energy sources. Adapted from Ref. [2]. 3

Table 1.2. Summary of structure parameters of bismuth oxides. 22

Table 1.3. The energies of fermi level, valence and conduction bands of α-Bi_2O_3 and β-Bi_2O_3. Adapted from Ref[42] 24

Table 2.1. Summary of the Mott-Schottky analyses 53

Table 3.1. Summary of the current transient exponents at different stages of the anodization 70

Table 3.2. Average thicknesses of anodic oxides prepared at different potentials for 30 minutes of anodization 76

Table 3.3. Summary of the values of the equivalent circuit elements describing electrochemical impedance of anodized Bi_2O_3 oxide samples in 1 M KOH solution with and without illumination at 0.5 $V_{Ag/AgCl}$. 91

Table 3.4. Summary of the Mott-Schottky analyses 96

Table 4.1. Hydrogen collected at the Pt counter electrode compartment by water displacement method using nanoporous bismuth oxide as photo electrode at an applied bias of 1.53 V_{RHE}..... 124

Table 4.2. Cathodic charge accumulation due to surface states on the nanoporous Bi_2O_3 at different potentiostatic conditions with chopped illumination. 124

Table 4.3. Summary of the Mott-Schottky results of nanoporous bismuth oxide in 1 M KOH + 0.3 M H_2O_2 with and without illumination (Figure 10)..... 137

Table 5.1. Summary of Mott-Schottky results of the anodic nanoporous Bi_2O_3 sample annealed at 240 °C for 4 h after different illumination cycles. Each cycle represents illumination of the sample using 1-sun intensity simulated solar light for 20 minutes under an applied potential of 0.2 $V_{Ag/AgCl}$ in 1 M KOH. 168

Table 5.2. Summary of Mott-Schottky results of the anodic nanoporous Bi_2O_3 sample annealed at 240 °C 6 h after different illumination cycles. Each cycle represents illumination of the sample using 1-sun intensity simulated solar light for 20 minutes under an applied potential of 0.2 $V_{Ag/AgCl}$ in 1 M KOH. 173

Table 5.3. Summary of Mott-Schottky results of the anodic nanoporous Bi_2O_3 sample annealed at 240 °C for 2 h after different illumination cycles. Each cycle represents illumination of the sample using 1-sun intensity simulated solar light for 20 minutes under an applied potential of 0.2 $V_{Ag/AgCl}$ in 1 M KOH. 173

Table A1. Exchange current densities and Tafel slopes of OER of the oxides of pure iron and FeNdB alloy 186

Table A2. Model parameters for electrochemical impedance spectroscopic results of the oxide layers of pure iron and FeNdB alloy under an applied potential of 0.5 $V_{Ag/AgCl}$ in 1 M KOH 189

Table B1 Estimated surface area of the anodic Bi_2O_3 samples per 1 cm^2 projected area based on geometric relation 191

Table C1. Summary of the values of equivalent circuit components fitted using the '2RC-in series model' with the EIS data of nanoporous bismuth oxide in 1M KOH with and without addition of hole scavengers. 202

Table C2. Summary of the values of equivalent circuit components fitted using the 'Rc in series model' with the EIS data of nanoporous bismuth oxide in 0.5 M Na_2SO_4 with and without addition of hole scavengers. 202

Table C3. Flat band potentials and charge carrier densities as a function of frequency based on the Mott-Schottky analyses of nanoporous Bi_2O_3 in 1 M KOH without hole scavengers. 202

Table C4. Flat band potentials and charge carrier densities as a function of frequency based on the Mott-Schottky analyses of nanoporous Bi_2O_3 in 1 M KOH with the addition of 0.15 M H_2O_2. 203

Table C5. Flat band potentials and charge carrier densities based on the Mott-Schottky analyses of nanoporous Bi_2O_3 in different solutions at 1000 Hz. 203

Table C6. Summary of the values of equivalent circuit components fitted using the model in Figure S7 with the EIS data (Figure S5 and S6) of nanoporous bismuth oxide in 1 M KOH and 1 M KOH + 0.3 M H_2O_2 with and without illumination. 204

1. Introduction

1.1. The Energy Challenge

A steady and clean supply of energy is one of the biggest challenges we are facing in this century. Since the days of industrial revolution, there has been an exponential increase in world energy demands. At present, with a population exceeding over 7 billion, the annual energy consumption is about 15 TW (Terawatts). By 2050, the population is projected to increase by 38% bringing the total population close to 9.5 billion. To meet these growing energy demands, experts predict that the world will need 30 TW of energy to maintain the economic growth and accommodate the increasing energy requirements of rapidly growing economies. Therefore, it is a significant challenge to meet these energy demands using existing resources. Currently, about 85% of the energy is supplied by fossil fuels consisting of oil, coal, and natural gas and another 5% by nuclear resources. The rest of the energy is supplied through renewable sources viz., solar, wind power, hydroelectric, biomass and geothermal power.[1]

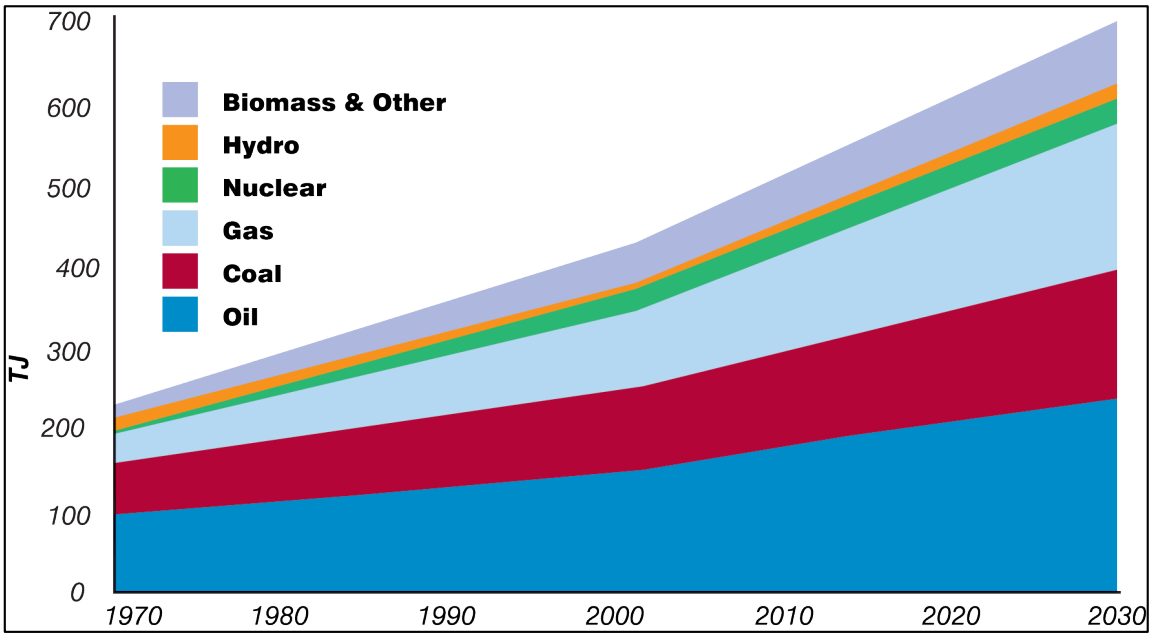

Figure 1.1. Projected world energy consumption (Source: OECD/IEA World Energy Outlook 2004)

From figure 1.1, it is quite evident that we rely mainly on fossil fuels, whose consumption rate is expected to almost double by the year 2050. Although, at this moment, consumption of the fossil fuels seems quite attractive and efficient, the availability of these fuels in the long run is highly debatable due to rapid depletion of these fuel reserves. According to the International Energy Agency, our fossil fuel reserves will be exhausted in another 100 years leading to an energy crisis. An even more compelling reason for an urgent switch from fossil fuels is climate change due to the emission of greenhouse gases, particularly carbon dioxide (CO_2), which is the main cause of the global warming. The limited reserves combined with the environmental consequences of greenhouse gas emissions make fossil fuels a meagre long term energy resource.

1.2. Solar-Hydrogen: Towards A Renewable Energy Future

At present, there is a need for an energy source that is almost infinite and yet does not emit greenhouse gas emissions. This energy source should be based on renewable sources which are naturally abundant, sustainable and easily harvestable. Table 1.1 shows the global power generating capacities of various renewable energy sources. Each form of these sustainable energies has its own advantages and drawbacks depending on its availability and geographical locations where these can be harvested and utilized efficiently.

If these energies, solar energy offers the greatest potential to meet all our energy demands. It is well known that the earth receives an abundant amount of solar energy. If we could capture and convert all the solar energy that earth receives into usable forms, then we could meet the annual global energy demand in one hour.[2] That is why efficient conversion of solar energy is considered the holy-grail. Earth's surface receives about 120,000 TW of solar energy and out of this only 30% is received by the land. This energy is so enormous that if a solar energy conversion system, with a trivial efficiency of about 10%, covering an area of about 0.8% of earth surface would easily harvest at least 30 TW of power.[3] Unfortunately, one of the greatest challenges in adopting solar energy is that it is not as viable as fossil fuels. Times of high energy demand are not always times of high availability due to the diurnal cycle, various weather seasons, geographic locations, etc. Because of these limitations, energy

needs to be stored between times of high energy harvesting and times of high demand. Many methods for energy storage have been developed which include flywheels, electrochemical storage (battery banks), and energy storage molecules (fuels). Usually, fuels offer an energy density at least 2-3 orders of magnitude higher when compared to electrochemical capacitors or batteries. Therefore, the most effective way of storing this energy is in the form of chemical fuels. Typical fuels with high energy density are methanol, methane, hydrogen, etc. At present, production of these fuels predominantly rely on fossil fuels, which produce undesired greenhouse gases as a byproduct. By harvesting solar light and using abundant molecules such as carbon dioxide and water, solar energy can be successfully stored as chemical fuels. However, solar production of methanol and methane require complex electrochemical conversion reactions to convert CO_2 into these fuels. On the other hand, hydrogen can be produced through a simple water splitting reaction using solar energy. Water is an abundant source of hydrogen and it splits into oxygen and hydrogen with a minimum energy of 237 kJ/mol. This energy can be provided by solar energy, making the entire process clean, renewable and carbon-free.

Table 1.1. Overview of global power generating capacities of sustainable energy sources. Adapted from Ref. [2].

Energy Source	Power (TW)	Remarks
Wind	4	Represents 10–15% of global technical potential for on- and off-shore installations
Hydroelectric	1-2	Remaining untapped potential is 0.5 TW
Tidal and ocean currents	<2	
Geothermal	12	Only a small fraction of this can be exploited
Biomass	10	Requires 10% of earth's land surface to be covered with switchgrass
Nuclear	10	Requires construction of a 1-GWpeak power plant every 35 h for the next 40 years. Finite uranium supplies imply need for fast breeder or thorium reactors
Solar	>20	Requires 0.16% of the earth's surface to be covered with 10% efficient solar cells. Total solar power reaching the earth's surface is 120,000 TW

Hydrogen is a highly versatile chemical that may become one of the key pillars to support our future energy infrastructure. It is an attractive fuel with a very high energy density that can be efficiently converted into electricity using a fuel cell, or it can directly drive an internal combustion engine and it is used in producing ammonia based fertilizers. Using hydrogen is clean; the only reaction product upon oxidation is pure water, with little or no exhaust of greenhouse gases, and that is why hydrogen is refereed as the fuel of the future. It can be stored in gaseous, liquid or metal hydride form. At present, there are still many challenges in implementing hydrogen as a common fuel. The biggest challenge is that it needs to be generated inexpensively and most importantly in an environmentally clean manner.

There are various pathways for generating hydrogen using solar energy and water like photoelectrochemical water splitting, coupled photovoltaic – electrolysis systems, photocatalytic water splitting and photobiological methods. We are interested in photoelectrochemical water splitting since it offers the following advantages over the other methods:[3] a) both hydrogen and oxygen are produced at separate electrodes which allows for easy collection of gases b) the whole process can be totally carried out at room temperature, c) it is constructed as a single monolithic device which is more durable and chemically inert. Photoelectrochemical water splitting uses a photoelectrochemical cell containing water and two electrodes (of which at least one is a photoelectrode that is capable of harvesting the solar light). Electrolysis of water could be achieved provided that the photoelectrode generates sufficient potential and sustainable current. Figure 1.2 shows the schematic design of an industrial scale photoelectrochemical cell for hydrogen generation by solar water splitting as proposed by the EPFL, Lausanne, Switzerland. The U.S. Department of Energy specifies 100 $Js^{-1}m^{-2}$ of hydrogen production as a performance goal of energy conversion using AM 1.5 solar spectrum. The AM 1.5 solar energy could be approximated as 1 kW/m^2. Therefore, the target will be to develop materials that have more than 10% solar-to-hydrogen conversion efficiencies.

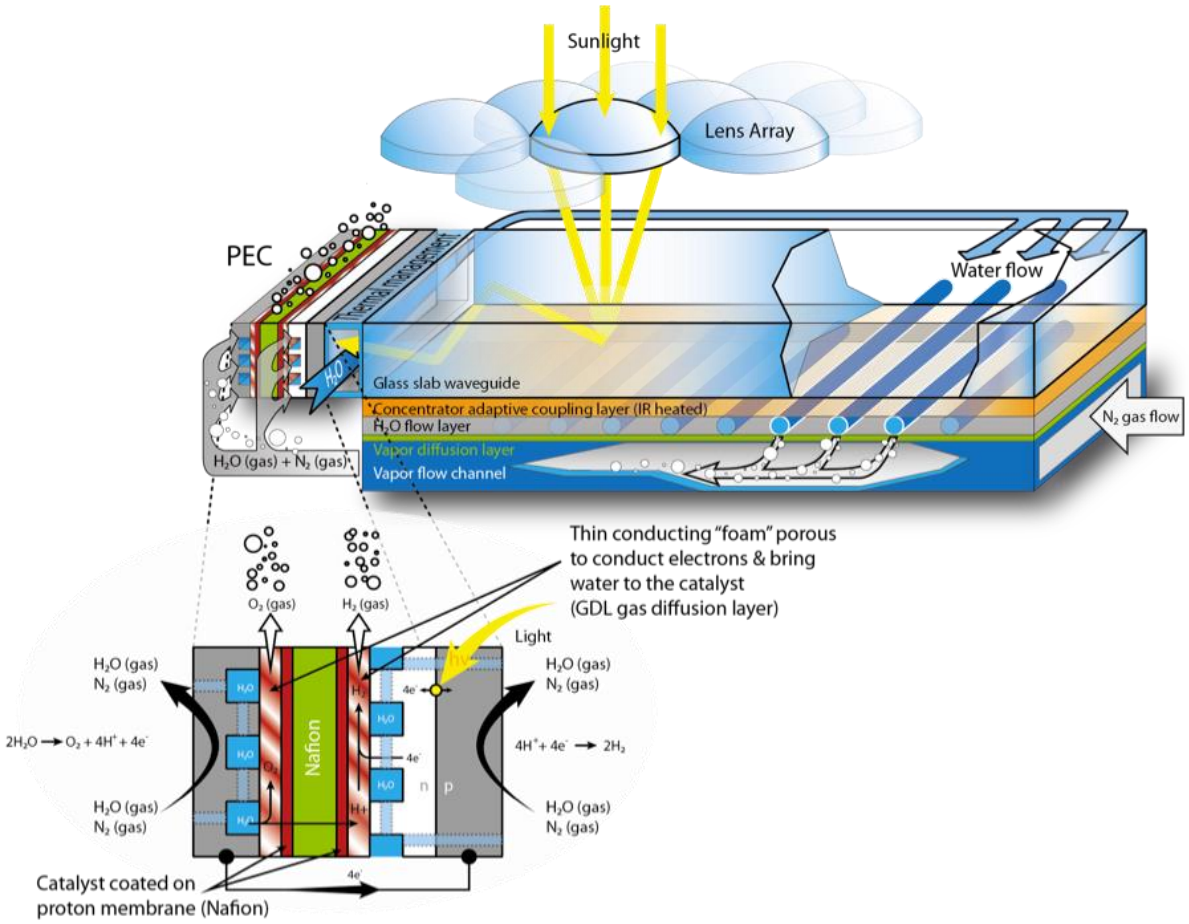

Figure 1.2. Schematic design of an industrial scale photoelectrochemical cell for hydrogen generation by solar water splitting. Source: Photoelectrochemistry competence center, EPFL, Lausanne, Switzerland

1.3. Principle of Photoelectrochemical Water Splitting

In photoelectrochemical water splitting, the photoelectrode is the most important component where conversion of the incident photons to electron-hole pair takes place. Usually different types of semiconductors are employed, taking advantage of the fact that photons with energy equal to their optical bandgap can create the required electron–hole pair to initiate the water splitting reaction. This section presents a review on semiconductors, semiconductor-electrolyte interface mechanism involved in photoelectrochemical water splitting and solar-to-hydrogen efficiency.

1.3.1. Semiconductors

The electronic structure of solids is often discussed in terms of energy bands, which are made up of discrete atoms and atomic orbitals. These energy bands are so closely spaced and have such low energy differences that they are considered a continuum of energy. The highest energy band filled with electrons is called valence band (VB) and the lowest unoccupied band is called conduction band (CB). The energy difference between top of the valence band (E_V) and bottom of the conduction band (E_C) is defined as the bandgap (Eg). Conductivity in solids can be distinguished by their bandgap. Figure 1.3 shows the band diagrams for three classes of materials, viz., metals, semiconductors and insulators. In metals, the conduction and valence bands overlap. Therefore, with no bandgap, there is a free flow of electrons making them good conductors. In insulators, the flow of electrons from the valence band to the conduction band is restricted due to the wide bandgap (Eg >> 4 eV) making them poor conductors. The intermediate of metal and insulator is a semiconductor with a moderate bandgap (Eg =1- 4 eV). In semiconductors, the electrons can be moved from the valence band to the conduction band, leaving a positively charged vacancy in the valence band called a hole. Usually, these electrons cannot be excited at room temperature, however, they can be excited thermally or by optical excitation.

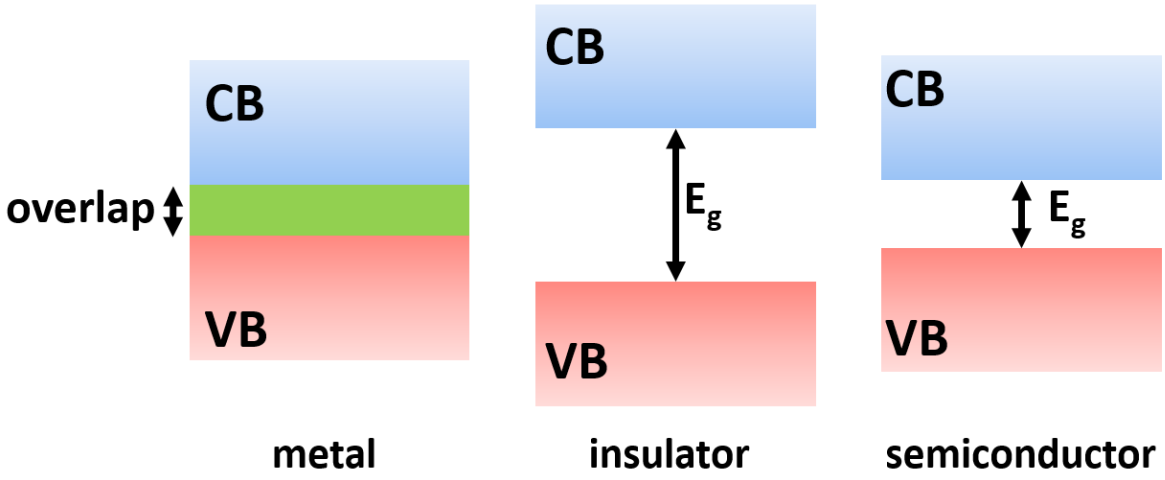

Figure 1.3. Energy band diagram of metal, insulator and semiconductor.

The Fermi-Dirac distribution and Fermi energy level describe the distribution of electrons available over all energy levels in solids. The distribution describes the probability of an energy level E occupied by an electron at a temperature *T*, which is given by:

$$f(E) = \frac{1}{exp\left(\frac{E - E_F}{kT}\right) + 1} \qquad [1.1]$$

Where E_F is the Fermi energy level, which is defined as the energy level at which the probability of finding an electron is half, *k* is the Boltzmann constant and *T* is the temperature in kelvin. This distribution is valid only at thermodynamic equilibrium. The Fermi energy level can be used to distinguish the different class of materials. In metals, E_F is located in the valence band for metals and in the forbidden gap for semiconductors and insulators. Fermi energy can be considered as the electrochemical potential of the electrons in the semiconductor. If a semiconductor has an equal number of electrons in the conduction band and holes in the valence band as charge carriers, it is called an intrinsic semiconductor. For this type of semiconductor, the Fermi energy level lies exactly between the conduction and valence bands. These intrinsic semiconductors have poor conductivity and by doping with elements like phosphorous, boron etc., energy carriers can be generated. These doped semiconductors are referred to as extrinsic semiconductors. There are two types of dopants depending on the effect they have on the intrinsic semiconductor: a) donor and b) acceptor forming n-type and p-type semiconductors respectively. In n-type, high valence elements like phosphorous, arsenic, antimony and bismuth are doped in silicon leading to a surplus of electrons. Similarly, in p-type lower valence elements like boron, aluminum, indium, and gallium are doped in silicon leading to a surplus of holes. Figure 1.4 shows the energy band diagram of an n-type and a p-type semiconductor. In n-type semiconductors, where electrons are the majority carriers and holes are the minority carriers, the Fermi energy level shifts closer to the conduction band and while with p-type material, where holes are the majority carriers and electrons are the minority carriers, the Fermi level is just above the valence band.

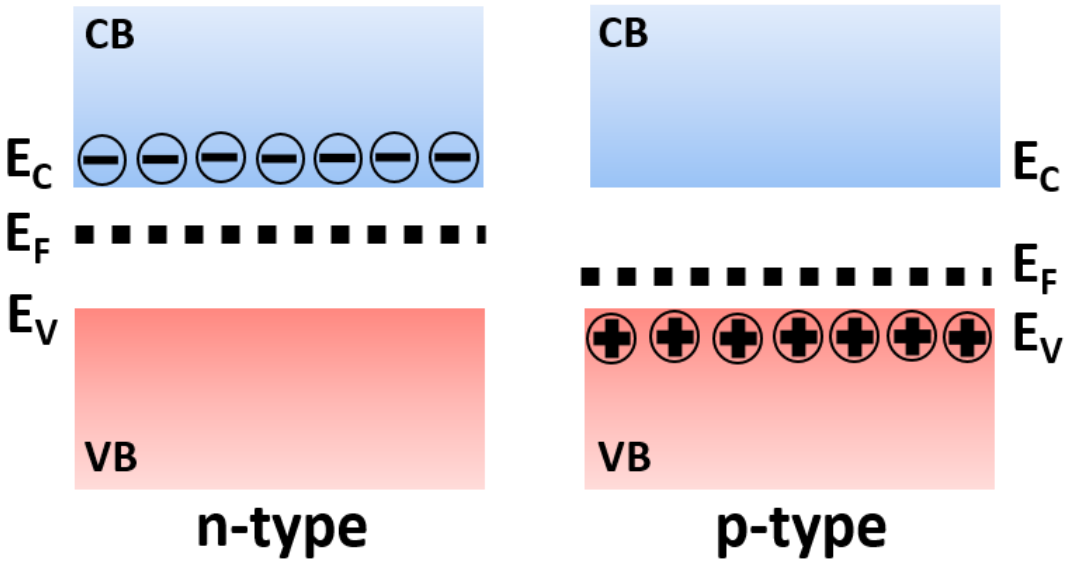

Figure 1.4. Energy band diagram of n-type and p-type semiconductors. E_F is Fermi energy.

1.3.2. Semiconductor-electrolyte interface

In semiconductor electrochemistry, it is very important to understand interactions occurring at the semiconductor-electrolyte interface. In this dissertation, the semiconductor-electrolyte will be discussed as an n-type photoelectrode in contact with an electrolyte in a photoelectrochemical cell. An ideal semiconductor-electrolyte interface is considered a Schottky barrier. Usually, the redox potential of the electrolyte and Fermi level of the semiconductor do not lie at the same energy, but when the semiconductor is brought into contact with the electrolyte, there is a movement of charge between the semiconductor and the electrolyte until an electrochemical equilibrium condition is achieved. Figure 1.5 (a) shows the energy level of an n-type semiconductor before coming in contact with electrolyte. In this type of semiconductor, electrons are the majority carriers and the Fermi energy level lies below the conduction band edge. Therefore, the Fermi energy level of the semiconductor (E_F) and redox couple ($E_{F,\,redox}$) will not be in equilibrium. When the semiconductor comes into contact with the electrolyte, there will be a flow of electrons from the surface to the electrolyte until the surface is positively charged. At this equilibrium, the Fermi level of the semiconductor is at the same level as the redox level of the electrolyte. As a result there is a region depleted of electrons near the semiconductor surface resulting in an upward band

bending. This region is called the depletion layer or the space charge layer. Similarly, on the electrolyte side, a thin Helmholtz layer is generated by the adsorption of ions on the semiconductor surface.

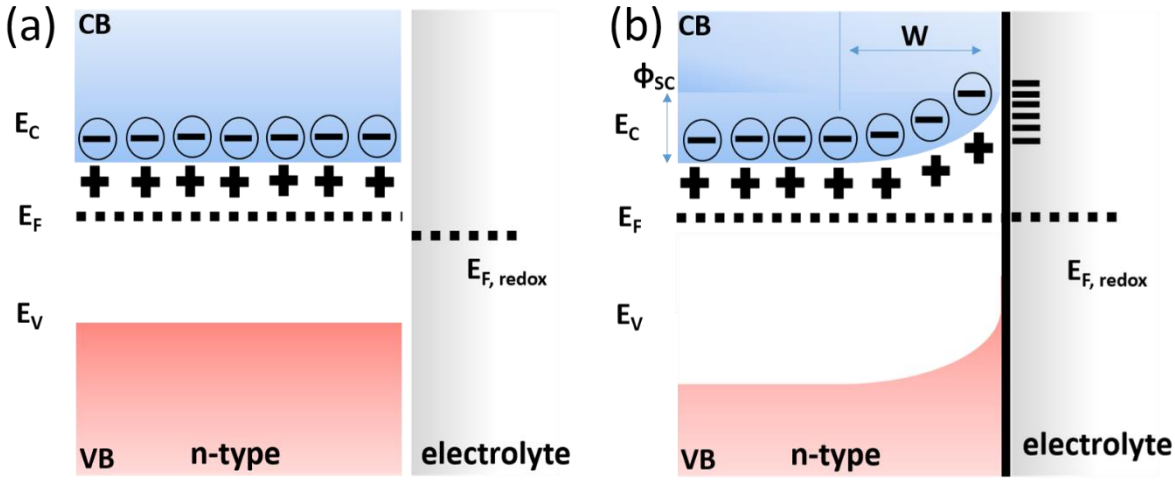

Figure 1.5. Energy Diagram of the n-type semiconductor-electrolyte interface, a) before equilibrium, b) after equilibrium.

The space charge layer plays an important role in photoelectrochemical water splitting. When the semiconductor is illuminated, the photogenerated electron and hole charge carriers are separated by the electric field in the space charge layer. The width of the space charge (*W*) is determined by the following equation:

$$W = \sqrt{\frac{2\varepsilon_o \varepsilon_r}{eN_D}\left(\phi_{sc} - \frac{kT}{e}\right)} \qquad [1.2]$$

Where, N_D is the concentration of ionized donors, ε_0 is the dielectric permittivity of vacuum and ε_r is the relative dielectric permittivity of the semiconductor. For an n-type semiconductor, the electrons move into the bulk and the holes migrate to the electrolyte interface. This movements generates a photovoltage moving the Fermi level upwards and as a result, the band bending is reduced.

1.3.3. Photoelectrochemical water splitting mechanism

Photoelectrochemical water splitting is truly a sustainable way to produce hydrogen. The Figure 1.6 shows a schematic of the photoelectrochemical cell composed of a semiconductor photoanode, a metal based counter electrode (usually inert electrode like platinum) and reference electrode immersed in an aqueous electrolyte. Upon illumination, semiconductor absorbs photons with energy greater than or equal to its bandgap then the electrons in the valence band are excited into the conduction band, creating electron-hole pairs. These electrons and holes are separated due to the presence of an electric field in the semiconductor. The photogenerated electrons are transported from conduction band through an external circuit connected to a metal counter electrode, where they reduce to form hydrogen gas. The holes are swept to the semiconductor-electrolyte interface of the photoanode, where they oxidize to form oxygen.

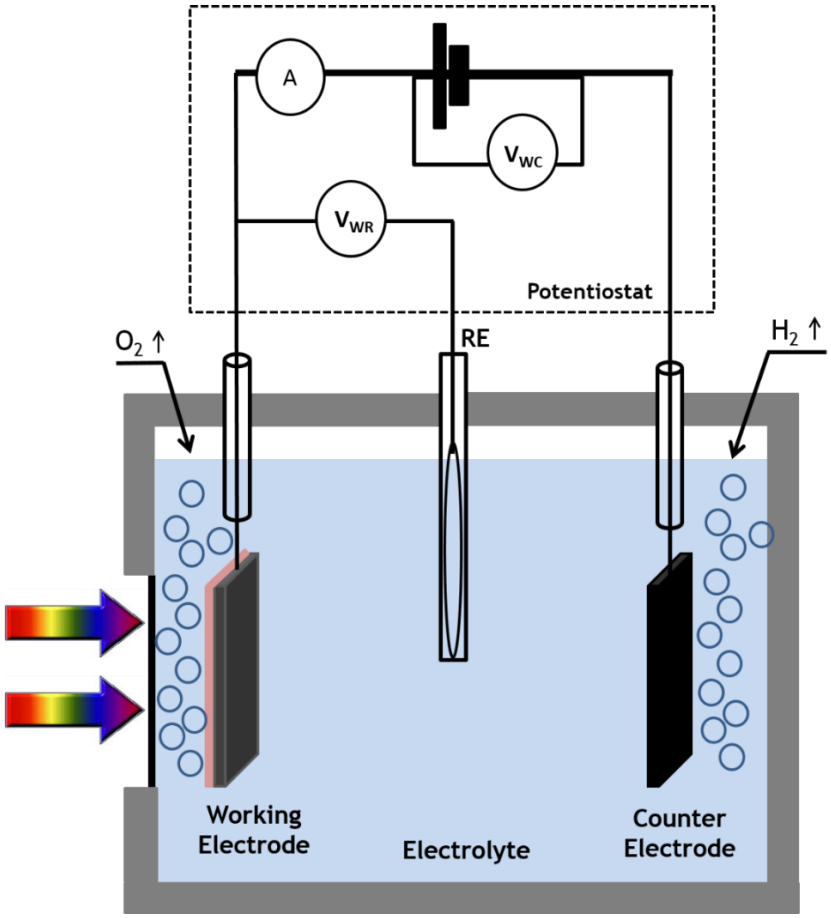

Figure 1.6. Schematic of a photoelectrochemical water splitting cell.

For an alkaline electrolyte, the reduction and oxidation reactions are:

$$4H_2O + 4e^- \rightarrow 2H_2 + 4OH^- \quad E^o_{red} = -0.828\ V\ vs.NHE \qquad [1.3]$$

$$4OH^- + 4h^+ \rightarrow 2H_2O + O_2 \quad E^o_{ox} = -0.401\ V\ vs.NHE \qquad [1.4]$$

For neutral and acidic electrolyte, the appropriate reactions are:

$$4H^+ + 4e^- \rightarrow 2H_2 \quad E^o_{red} = +0.000\ V\ vs.NHE \qquad [1.5]$$

$$2H_2O + 4h^+ \rightarrow 4H^+ + O_2 \quad E^o_{ox} = -1.229\ V\ vs.NHE \qquad [1.6]$$

The overall water splitting reaction involves four photons that generate four electron-hole pairs to produce two hydrogen molecules and one oxygen. The reaction is given by:

$$2H_2O \overset{hv}{\rightarrow} 2H_2 + O_2 \qquad \Delta G = 237\ kJ/mol \qquad [1.7]$$

1.3.4. Solar-to-hydrogen efficiency

Solar-to-hydrogen (STH) efficiency is one of important parameter to characterize a photoelectrochemical device. It is defined as chemical energy of the hydrogen produced divided by solar energy input from sunlight incident on the process.[4] This is given by:

$$\eta_{STH} = \frac{\Delta G\ \times R_{H_2}}{P\ \times\ A} \qquad [1.8]$$

Where ΔG is Gibbs free energy per mole of H_2, R_{H2} is the chemical energy of hydrogen produced, P is the incident power of the solar energy input (1000 W/m^2 is normally used for standard AM1.5G condition), and A is the area of the electrode. For a photoelectrochemical water splitting cell, where an external bias is applied and 100% Faradaic conversion efficiency is assumed, replacing the Gibbs free energy with the corresponding voltage (1.23 V) and the rate of hydrogen evolution with the photocurrent density (*j*), above equation can be modified to the following:

$$\eta_{STH} = \frac{1.23 - V_{RHE}\ \times\ J}{P\ \times\ A} \qquad [1.9]$$

Also, the total efficiency of the PEC water splitting process can be defined in terms of absorption, separation and catalytic efficiencies as shown below:[5]

$$\eta_{STH} = \eta_{abs} \times \eta_{sep} \times \eta_{cat} \qquad [1.10]$$

Where, the absorption efficiency (η_{abs}) is defined as the ratio of the electron-hole pairs created to the amount of incident photons. The ratio between the number of electrons and holes reaching the interfaces to the photogenerated electron-hole pairs is called the separation efficiency (η_{sep}). The number of holes that undergo the water oxidation reaction normalized to the ones reaching the semiconductor/electrolyte interface is the catalytic efficiency (η_{cat}).

1.4. Materials Challenge for Photoelectrochemical Water Splitting

The selection of an optimum semiconductor is a critical aspect to split water with solar irradiation. Since the first illustration of the photoelectrochemical generation of hydrogen using the semiconductor titanium dioxide by Fujishima and Honda, significant research efforts were devoted to develop low cost sustainable semiconductor photoelectrodes.[6] In order to be considered a good material for PEC water splitting, an ideal photoelectrode need to fulfill several requirements.[1] First, it needs to absorb most of the visible light spectrum to drive the water splitting reaction. Usually, the optimum band gap to thermodynamically split water into hydrogen and oxygen is 1.23 eV, but considering thermodynamic losses and overpotentials during the process there is an estimated loss of around 0.8eV. Therefore, the actual required bandgap is about 2 eV. However, to develop materials that have more than 10% solar-to-hydrogen conversion efficiencies optimum value of the bandgap should be around 2.4 eV. The second requirement is the band edge positioning, which is a necessary condition for spontaneous water splitting upon illumination. The band edges of the semiconductor should straddle the redox potential of water, i.e., the conduction band edge should lie more negative relative to the reduction potential of water and the valence band edge should be more positive compared to the oxidation potential (as shown in Figure 1.7). That way the photoexcited electrons and holes can have enough electrochemical potential to

drive water splitting without external bias. Third, the chemical stability of the semiconductor photoelectrode at different pH levels and in illuminated conditions is a critical issue.

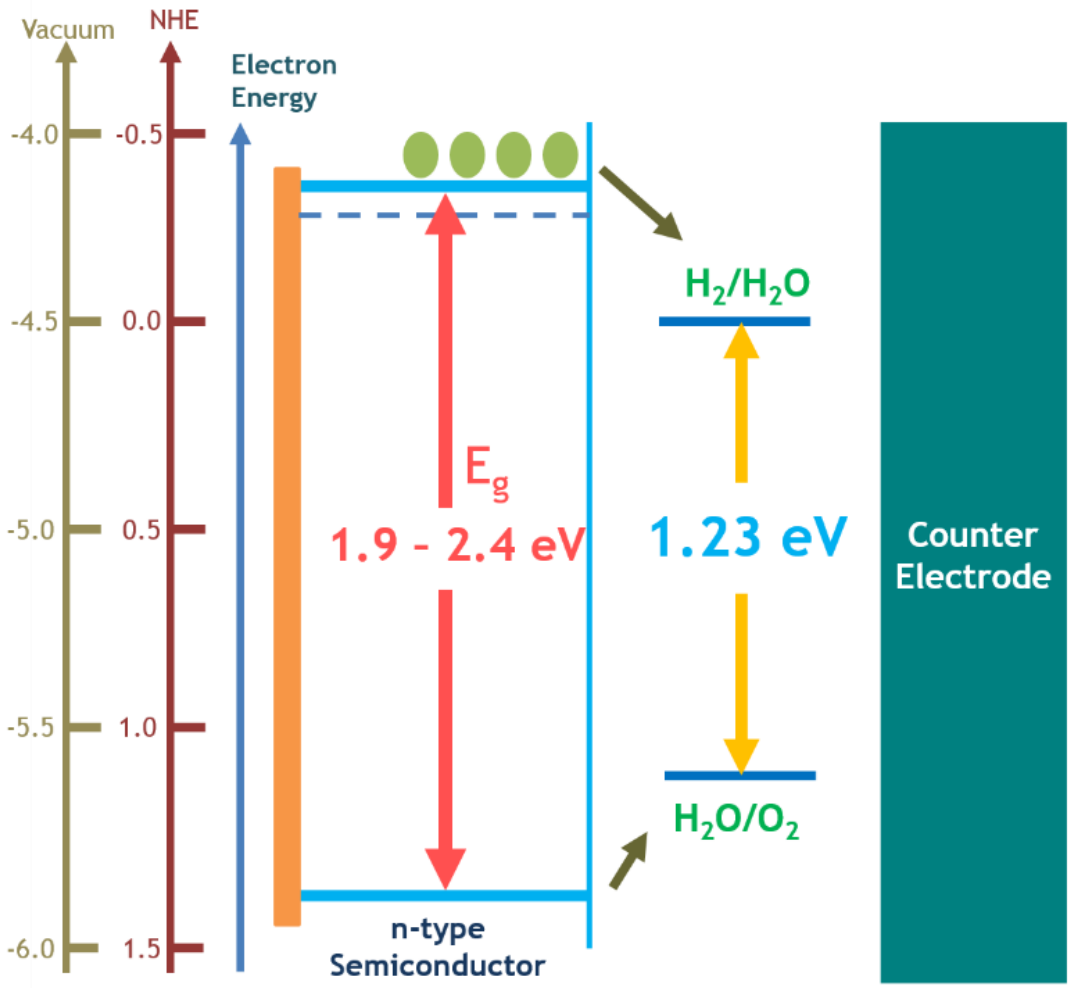

Figure 1.7. Band edge positioning in an ideal n-type photoelectrode.

Usually, if the energy level of the anodic or cathodic decomposition reaction of the semiconductor lies within the energy bandgap, then the material will be prone to photo corrosion.[7] Semiconductors that show n-type behavior have higher tendency for photo corrosion than their p-type counterparts. This phenomenon is attributed to the oxidation reaction of the holes at the surface of the n-type semiconductor that acts as a photo anode:

$$MX + Zh^+ \rightarrow M^{Z+} + X \qquad [1.11]$$

On the other hand, p-type semiconductor material acts as a photo cathode where the photochemical reaction is hydrogen ion reduction. Therefore, in general, the p-type material is cathodically protected during the solar water splitting. These requirements are of utmost importance when considering a material for an ideal photoelectrode. Additionally, the material should have good conductivity, high catalytic activity toward oxidation or reduction of water, high charge transport properties and low electron-hole recombination losses in order to exhibit high solar-to-hydrogen conversion efficiency. Also a nanostructured morphology increases the specific surface area. The related increase in the number of surface sites greatly enhances the overall charge transfer kinetics at the semiconductor-electrolyte interface. Finally, the semiconductor must be non-toxic, environmentally benign and economically viable.

In order to understand bandgap, band edge positioning and chemical stability of photoelectrodes, the bandgap energies and band edge positions of a few common semiconductor materials that have been recommended for solar water splitting are shown in Figure 1.8,[8] along with their standard reduction potentials for water reduction and oxidation vs NHE at pH 0. In general, metal chalcogenides such as CdS and CdSe have an apt bandgap to harvest the visible light with properly aligned band edges with respect to water electrolysis potentials. However, they are not stable and can be easily oxidized to metal oxides in aqueous system.[9] Similarly, metal nitrides or metal oxynitrides also suffer from photo corrosion and photo oxidation. Small bandgap semiconductors like silicon can absorb a large portion of solar light but their valence bands are not positive enough to oxidize water which requires an external bias. They can also be photoelectrochemically unstable due to the surface oxidation and large surface over-potential.[9] The wide bandgap metal oxides like TiO_2, $SrTiO_3$, and ZrO_2 can be chemically stable and also straddle the water reduction and oxidation potentials, but their large bandgaps limit their absorption of sunlight.[1, 3, 9] These wide bandgap semiconductors only absorb UV light which encompasses only 5% of the solar spectrum. For small bandgap metal oxides, such as Fe_2O_3, $BiVO_4$, and WO_3, their conduction band potentials are more positive than water reduction potential and they do not have sufficient energy to reduce water to hydrogen because of an electron transfer barrier.[10] For

these materials, spontaneous water splitting is impossible. An external electrical bias or internal chemical bias is needed to assist these semiconductors in water splitting. Metal oxides are well-studied photoelectrodes for solar water splitting due to their abundance, stability, ease of fabrication and low costs. They also exemplify most of the requirements for solar water splitting. Unlike non-oxide materials, many metal oxide semiconductors exhibit Nernstian behavior. The conduction and valence band edge potentials shift -59 mV/pH in the same direction as the water oxidation and reduction potentials, due to the interaction of H^+ or OH^- ions at the semiconductor surface. As a result, the thermodynamic over-potentials for water splitting are pH independent, allowing for versatile operating conditions.

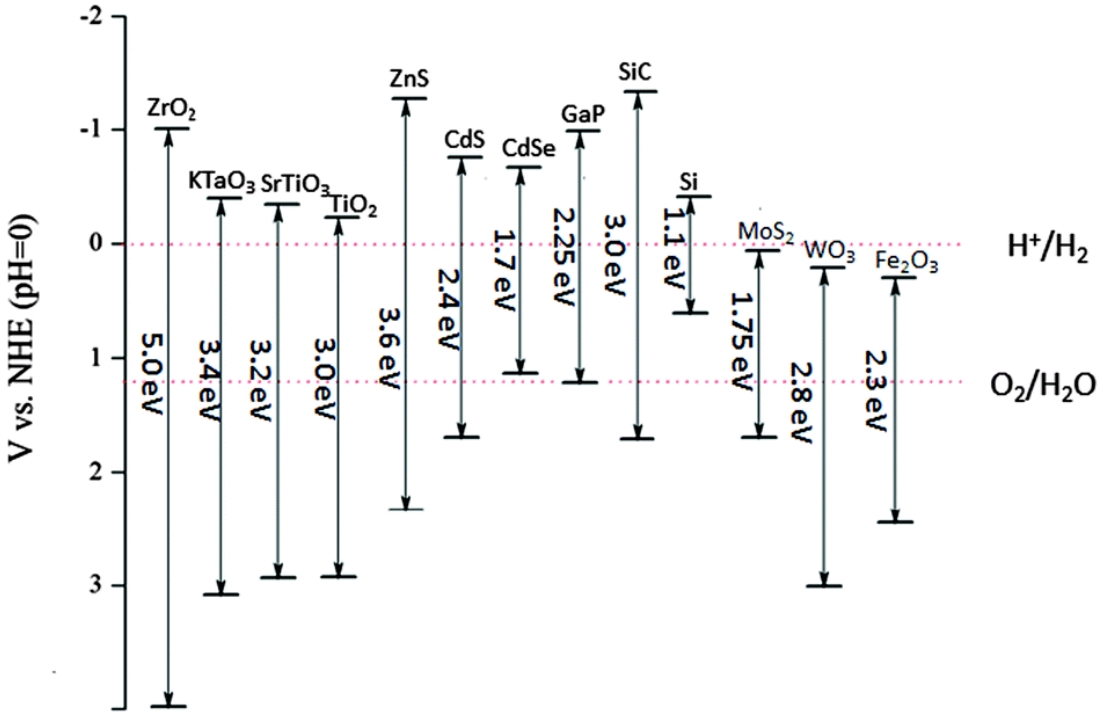

Figure 1.8. Diagram of bandgaps and band edges (CB bottom and VB top) of some wide bandgap semiconductors (pH = 0, vs. NHE at room temperature). Adapted from Ref [8].

Because no single material is found to possess all the required properties, it is very difficult to find an ideal, sustainable semiconductor material for solar water splitting. The challenge is therefore to develop materials with novel compositions, unique morphologies, and hybrid nanostructures to overcome these limitations while meeting the necessary requirements for water splitting. In this dissertation, two metal oxides, α-Fe_2O_3 (hematite)

and β-Bi_2O_3, are studied and following sections give detailed information of these metal oxides.

1.5. Iron (III) Oxide

Iron is one of the most abundant elements on the earth. Iron, Fe, with a chemical configuration of [Ar] $3d^6$ $4s^2$ has eight valence electrons and it readily oxidizes in air to the ferrous (+2) and ferric (+3) states. This transition metal oxide is found in a variety of forms in nature such as: FeO (wustite), α-Fe_2O_3 (hematite), ϒ- Fe_2O_3 (maghemite), and Fe_3O_4 (magnetite). Recently, Iron (III) oxides (Fe_2O_3) have attracted a lot of interest due to their applications in diverse fields like biomedicine, catalysis, energy storage devices and solar water splitting. In this section, an overview of crystal and electronic structure of Iron (III) oxide polymorphs is presented. Also, issues concerning the current challenges and future prospects of α-Fe_2O_3 (hematite) as an ideal photoelectrode is briefly discussed. There are four polymorphs of Fe_2O_3:[11] a) α-Fe_2O_3 (hematite), b) β-Fe_2O_3, c) ϒ- Fe_2O_3 (maghemite) and d) ε-Fe_2O_3. Out of these four, both α-Fe_2O_3 and ϒ-Fe_2O_3 occur naturally as hematite and maghemite minerals respectively. However, only a few research efforts reported the rare β-Fe_2O_3 and ε-Fe_2O_3 polymorphs presence and there is no evidence of these occurring naturally.[12, 13] Figure 1.9 shows the different crystal structures of these polymorphs.

The α-Fe_2O_3 is the most stable and common polymorph of Fe_2O_3. It has a corundum type rhombohedrally centered hexagonal structure with hexagonal close-packed O^{2-} anions along the [001] direction and two-thirds of the octahedral sites are occupied by Fe^{3+} ions (Figure 1.9.a). It crystallizes in the $R\bar{3}c$ space group, with lattice parameters a = 5.036 Å and c = 13.749 Å, and six formula units per unit cell. The rare polymorph β-Fe_2O_3 (Figure 1.9.a) exhibits a body-centered bixbyite cubic structure where the Fe^{3+} ions occupy two nonequivalent octahedral sites. This phase is thermodynamically unstable and it transforms to α-Fe_2O_3 or ϒ- Fe_2O_3 on heating.[12] The second most common and stable form, ϒ- Fe_2O_3 exhibits an inverse spinel type structure which crystallizes in the $P4_132$ space group with a = 8.351 Å. In this polymorph, cations occupy the tetrahedral and octahedral positions leaving behind vacant cation sites usually in the octahedral positions (Figure 1.9.c). Depending upon

the ordering of vacancies in the octahedral sites of ϒ- Fe_2O_3, at least three crystal symmetries have been reported. At an appropriate temperature, the thermodynamically unstable ϒ-Fe_2O_3 usually converts to the more stable α-Fe_2O_3. The second rare polymorph, ε-Fe_2O_3 has an orthorhombic crystal structure with the *Pna*2_1 space group and lattice parameters a = 5.095 Å, b = 8.789 Å, and c = 9.437 Å (Figure 1.9.d). It possess six crystallographically nonequivalent anion and four cation (Fe_1, Fe_2, Fe_3, and Fe_4) positions with no vacancies in the crystal structure. The three cation positions Fe_1, Fe_2, and Fe_3 are octahedrally coordinated and the fourth Fe_4 cation position is tetrahedrally coordinated. This rare metastable phase is usually regarded as an intermediate polymorph, due to similarities with both γ-Fe_2O_3 and α-Fe_2O_3 in reference to close packing of oxygen layers.[13, 14]

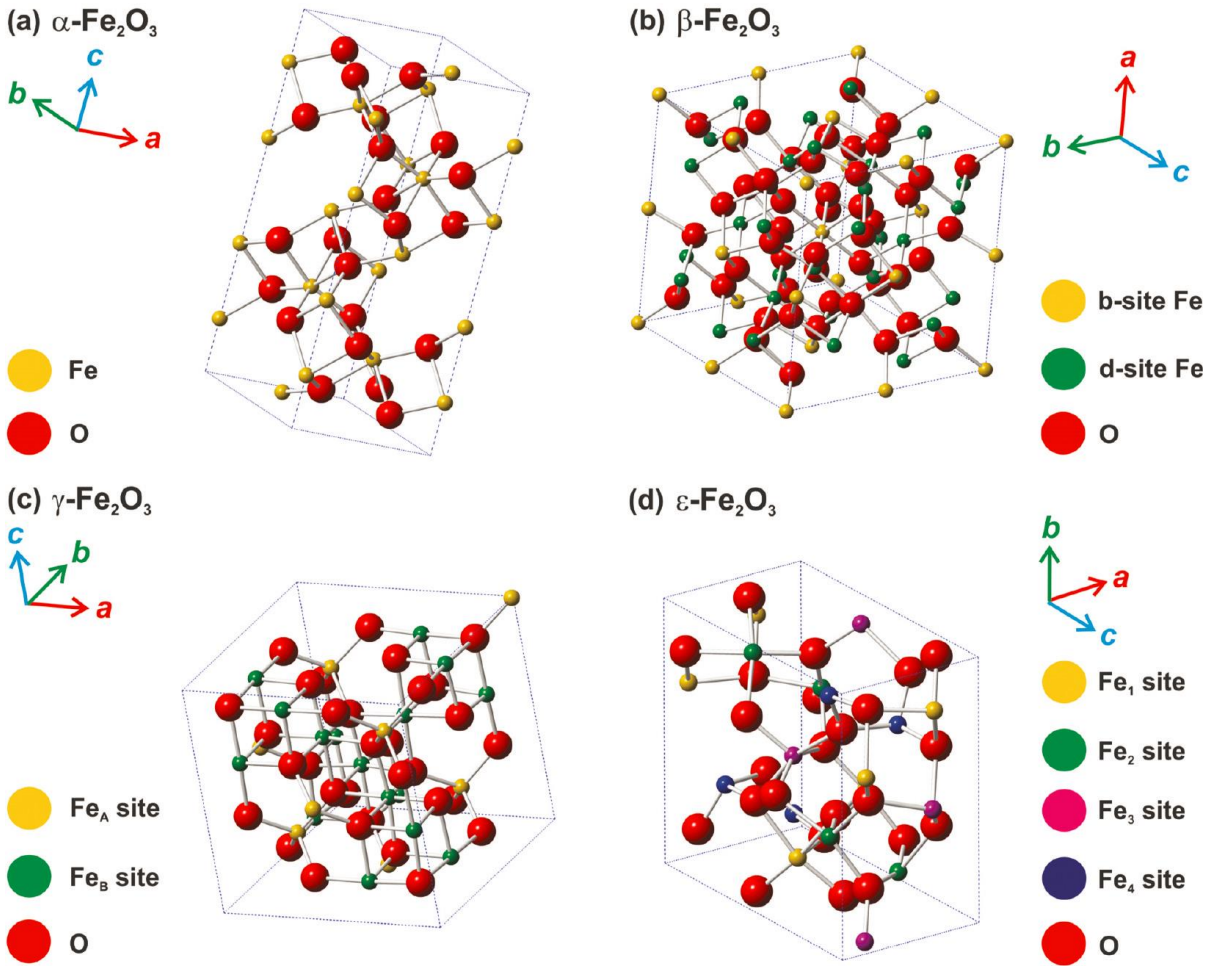

Figure 1.9. Crystal structures of Fe_2O_3: a) α-Fe_2O_3, b) β-Fe_2O_3, c) ϒ- Fe_2O_3 & d) ε-Fe_2O_3. Adapted from Ref [11].

Temperature induced phase transformations of Fe_2O_3 polymorphs depend on a range of internal factors, including the polymorph structure, particle size, particle morphology, surface coating, particle aggregation, and embedding of particles in a matrix as listed below: [11]

For γ-Fe_2O_3:

a) Nanoparticles in supporting medium,

$$\Upsilon - Fe_2O_3 \xrightarrow{>1000\,℃} \varepsilon - Fe_2O_3 \xrightarrow{>1300\,℃} \alpha - Fe_2O_3 \qquad [1.12]$$

b) Less agglomerated nanoparticles,

$$\Upsilon - Fe_2O_3 \xrightarrow{>400\,℃} \varepsilon - Fe_2O_3 \xrightarrow{>700\,℃} \alpha - Fe_2O_3 \qquad [1.13]$$

c) Highly agglomerated nanoparticles,

$$\Upsilon - Fe_2O_3 \xrightarrow{>300\,℃} \alpha - Fe_2O_3 \qquad [1.14]$$

d) Coated nanoparticles,

$$\Upsilon - Fe_2O_3 \xrightarrow{>600\,℃} \alpha - Fe_2O_3 \qquad [1.15]$$

e) Big crystals and/or bulk crystals

$$\Upsilon - Fe_2O_3 \xrightarrow{\sim 400\,℃} \alpha - Fe_2O_3 \qquad [1.16]$$

For β -Fe_2O_3:

a) Nano powder,

$$\beta - Fe_2O_3 \xrightarrow{>590\,℃} \alpha - Fe_2O_3 \qquad [1.17]$$

b) Hollow nanoparticles

$$\beta - Fe_2O_3 \xrightarrow{> 400\,^{\circ}C} \alpha - Fe_2O_3 \qquad [1.18]$$

In this dissertation, we are interested in only α-Fe_2O_3 (hematite), as it is considered a viable semiconducting photoelectrode for solar water splitting in hydrogen generation. The α-Fe_2O_3 is viewed as a promising photoanode due to its optimal bandgap 2.1 eV, which absorbs about 40 % of the solar spectrum. Also, α-Fe_2O_3 has a low valence band edge position coupled with good morphological and chemical stability over a wide of range of pH levels. Due to these attractive characteristics along with an estimated theoretical efficiency of 12.9%, α-Fe_2O_3 is indeed one of the most promising candidates that has been subjected to intensive research efforts.[15] However, just like every other potential photoanode, there are some challenges with hematite too.[10] First, the band edges are not optimally positioned for spontaneous water splitting requiring an external bias to drive the reaction. Second it has a very short diffusion length which leads to a shorter lifetime of photo excited electron-hole pairs and low mobility of holes. Also, a higher prospect of charge recombination coupled with low reactivity of holes and poor conductivity of materials limit the efficiency to 5% compared to theoretical efficiency of 12.9%. To overcome these limitations, various strategies have been proposed like nano-sizing, using localized surface plasmon resonance, doping, using an oxygen evolution catalyst layer, etc.[10, 16] A more detailed discussion on α-Fe_2O_3 as a potential photoanode, its challenges and progress towards a solution are discussed in detail in chapter 2.

1.6. Bismuth (III) Oxide

Bismuth (III) oxide is available naturally as bismite (monoclinic) and sphaerobismoite (tetragonal) minerals. In a pure binary oxide, the common oxidation state of Bi is (+3), however a (+5) state in mixed and ternary oxides along with subvalent bismuth oxide like BiO have been reported. Bismuth (III) oxide has received considerable attention due to its polymorphs and their remarkably useful solid state properties. In this section, an overview of the crystal and electronic structure of Bismuth (III) oxide polymorphs is presented. Also, issues concerning the challenges in using bismuth oxide (especially β-Bi_2O_3) as an ideal photoelectrode is discussed.

1.6.1. Crystal structure

There are six known polymorphs of Bi_2O_3:[17] a) α – monoclinic, b) β – tetragonal, c) γ – body centered cubic, d) δ – face centered cubic, e) ε – orthorhombic and f) ω – triclinic. Out of these, only α- Bi_2O_3 and δ- Bi_2O_3 phases are stable while the others are metastable phases. Figure 1.10 shows the schematic of the temperature dependent phase transformation of the Bi_2O_3 polymorphs.[18]

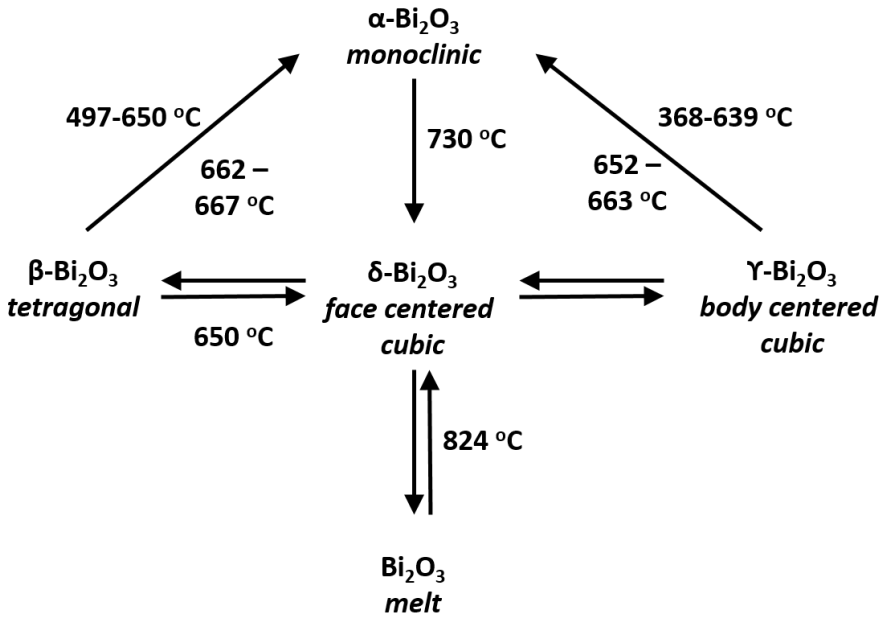

Figure 1.10. Temperature dependent phase transformations of Bi_2O_3 polymorphs. Adapted from ref [18]

The room temperature stable monoclinic α-Bi_2O_3 transforms to a cubic δ-Bi_2O_3 at 730 °C. The δ-Bi_2O_3 structure melts at a temperature of 824 °C and the boiling point is around 1184 °C in air. Two alternatively occurring metastable phases are reported during cooling of the δ-Bi_2O_3 structure leading to the formation of either tetragonal β-Bi_2O_3 or body centered cubic γ- Bi_2O_3. However, the transformation of δ-Bi_2O_3 to β-Bi_2O_3 or γ-Bi_2O_3 phases is challenging to control and strongly subjective to the presence of trace amounts of impurities and sample conditions. The environments under which these phases form depend on the synthesis route and thermal treatment. Further cooling of these metastable phases below 500 °C leads to the formation of the stable monoclinic α-Bi_2O_3. The metastable β-Bi_2O_3 and γ-Bi_2O_3 phases can be stabilized at room temperature by carefully controlling the thermal

conditions and impurities. Furthermore, the metastable β-Bi_2O_3 can be stabilized at room temperature by decomposition of $(BiO)_2CO_3$ in air or by adopting bismuth citrate or an oxalate preparation route followed by thermal decomposition.[19-21] Also, the β-Bi_2O_3 phase can stabilized by incorporating various oxides like Sb_2O_3, HfO, CeO_2, TiO_2, Y_2O_3, Ln_2O_3-TeO_2 (Ln = La, Sm, Gd, Er), PbO-PbF_2, PbF_2.[22-26] Similarly the body centered cubic (bcc) γ-Bi_2O_3 phase can be stabilized at room temperature by the addition of small amount of dopant M_2O_x-type oxide, such as M = Y, Mo, V, Co, Sb, W, Sr, Ca, La and Gd.[17, 27, 28] Stabilization of the δ- Bi_2O_3 phase to lower temperatures can be achieved by the addition of appropriate dopants, such as rare-earth oxides or transition metal oxides. This allows the δ-Bi_2O_3 phase to be stabilized and maintain its structure even at room temperature, but this doping leads to a considerable loss of oxide ion conductivity.[29-33] In addition to the above mentioned phases, a few research efforts reported the synthesis of the metastable orthorhombic ε-Bi_2O_3 and ω-Bi_2O_3.[34, 35]

The three extensively studied polymorphs of Bi_2O_3 are: α-Bi_2O_3, b) β-Bi_2O_3 and c) δ-Bi_2O_3. Figure 1.11 shows crystal structures of α-Bi_2O_3 and β-Bi_2O_3 polymorphs and a summary of the cell parameters of all the polymorphs is given Table 1.2. The α-Bi_2O_3 phase crystallizes in a monoclinic structure with a fivefold oxygen coordination of the Bi atoms. It exhibits a three-dimensional (3D) network of corner and edge-sharing distorted square-pyramidal BiO_5 units where the bismuth center is pseudooctahedral distorted. Due to the high distortions in the structure it has different bond lengths between Bi and O, ranging from 2.1–3.4 Å.[36] The β-Bi_2O_3 exhibits a tetragonal phase with different bonds lengths between bismuth and oxygen lattice causing the formation of an irregular BiO_4 tetrahedron. This tetrahedron shares oxygen at the corners to give a network with empty channels to form large-size straight tunnels throughout the entire crystal resulting in an excellent separation of the electron–hole pairs, hence demonstrating very good photocatalytic activity.[37, 38] The δ-Bi_2O_3 phase exhibits a defective fluorite-type structure with a six fold oxygen coordination. In this lattice, the oxygen atom defects are statistically distributed such that only six out of eight anion sites are occupied with oxygen. Usually the Bi ions occupy the 4*a* sites at (0, 0, 0), forming a face-centered-cubic sub lattice, and oxide ions occupy the 8*c* sites at (¼, ¼, ¼), forming a simple cubic sub lattice. Due to the vacant O sites this polymorph is the most effective oxide ion

conductor. [36, 39, 40] It is also interesting note to that α-Bi_2O_3 and β-Bi_2O_3 phases exhibit p and n-type semiconductivity respectively.

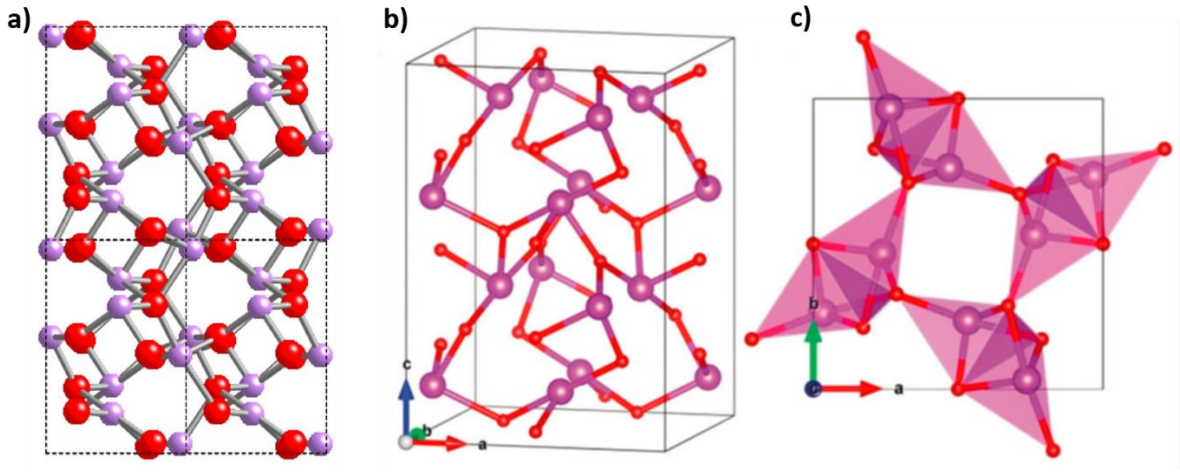

Figure 1.11. Lattice structure of a) α-Bi_2O_3, b) β-Bi_2O_3 and c) the β-Bi_2O_3 tunnel looking top down from the c axis. Adapted from a) http://payneresearch.org/research/lone-pair-materials/ and b) Ref [38]

Table 1.2. Summary of structure parameters of bismuth oxides.

Bi_2O_3 polymorph	Crystal structure	Space group	Lattice parameter	Bandgap (eV)
α	monoclinic	$P2_1/c$	a = 5.84 Å b = 8.15 Å c = 7.50 Å β = 112.97°	2.8
β	tetragonal	$P\bar{4}2_1c$	a = 7.74 Å c = 5.64 Å	2.5
ϒ	body centered cubic	I23	a = 10.25 Å	2.8
δ	face centered cubic	$Fm\bar{3}m$	a = 5.53 Å	3.1
ε	orthorhombic	Pbnb	a = 4.95 Å b = 5.58 Å c = 12.72 Å	-
ω	triclinic	$P\bar{1}$	a = 7.26 Å b = 8.63 Å c = 11.96 Å α = 87.71° β = 93.22° ϒ= 86.65°	-

1.6.2. Electronic structure

In general, the electronic structure of a photoelectrode has a strong relationship to photocatalytic behavior which influences the separation efficiency of the photoinduced carriers and the light absorption range. The electronic structure of the valence band maximum of Bi_2O_3 is dominated by the interaction of the O 2p states with the Bi 6s and 6p states. The Bi^{3+} oxidation state results in a filled 6*s* subshell and an electronic configuration of $5d^{10}6s^26p^0$. Usually the $6s^2$ electrons occupy the inert orbital resulting from the hybridization of Bi 6*s* and 6*p* states leading to a distorted crystal structure. This stereochemical distortion resembles a highly asymmetric charge distribution, often referred to as lone-pair effect. In bismuth based oxides, the occupied cation 6s/6p orbital interacts with the O 2p orbital forming a bonding state at the bottom of the valence band and an antibonding state at the top of the valence band as shown in the molecular orbital diagram (Figure 1.12). Due to the distorted crystal lattice, the interaction between the Bi 6s and the O 2p states leads to hybridization of the unoccupied cation 6p orbital with the antibonding state. Interaction of Bi 6p states with antibonding Bi 6s and O 2p states results in stabilization of the occupied antibonding states which is responsible for the asymmetric electron density and therefore formation of lone-pair orbital. The lone electron pairs of Bi(III) $6s^2$ induces intrinsic polarizabilities which facilitate the separation of photo generated electron-hole pairs and their transport, making Bi(III) an ideal photocatalytic material.[41]

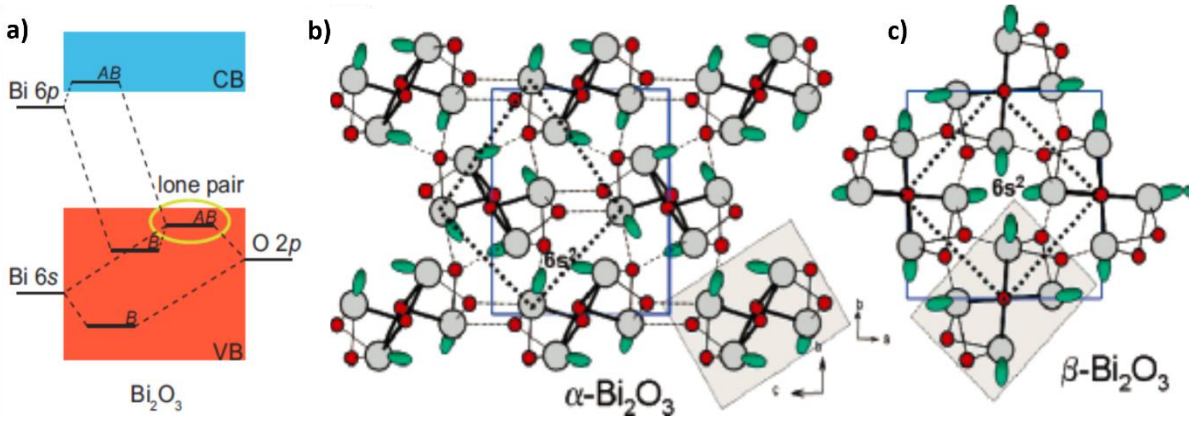

Figure 1.12. a) Molecular orbital diagram of Bi_2O_3. Only the bonding e_g states are illustrated and the nonbonding t_{2g} states are omitted. B and AB denote bonding and antibonding, respectively. b) Arrangement of Lone-Pairs in α and β Bi_2O_3. Adapted from Ref [34] and [42] respectively.

Crystal structure of a photoelectrode significantly influences the corresponding photocatalytic performances. Out of the three most studied Bi_2O_3 polymorphs, the α-Bi_2O_3 and β-Bi_2O_3 phases exhibit high crystallinity compared to the δ phase whose vacant O sites act as charge recombination centers.[37] Moreover, the bandgap of the δ-Bi_2O_3 phase is about 3.01 eV which will absorb only a small fraction of visible light subsequently reducing the photocatalytic activity. However, the higher photocatalytic efficiencies of the α-Bi_2O_3 and β-Bi_2O_3 phases are attributed to their crystal structures which are favorable to the presence of fewer recombination sites. The α-Bi_2O_3 phase has a highly distorted structure due to different Bi-O bond lengths, it exhibits a zigzag configuration which leads to an increase in charge recombination.[37] Nonetheless, for the β-Bi_2O_3 phase the tunnels provide channels for efficient transfer of the photogenerated charge carriers preventing excessive recombination. Therefore, it is widely believed that β -Bi_2O_3 shows a much higher photocatalytic performance than α-Bi_2O_3.[37, 38, 42]

Also, the position of the conduction band minimum and the valence band minimum, greatly influences the photocatalytic performance of the photoelectrode. As discussed earlier, for Bi based oxides, the valence band comprises of Bi 6s and O 2p orbitals which narrows the bandgap into the visible region making it sensitive to light irradiation and the bottom of conduction band is dominantly constructed by Bi 6p orbital. The energies of the Fermi level, valence and conduction bands of α-Bi_2O_3 and β-Bi_2O_3 is given in Table 1.3. The energy differences between the Fermi levels and the valence bands of α-Bi_2O_3 and β-Bi_2O_3 is +1.35 eV.

Table 1.3. The energies of fermi level, valence and conduction bands of α-Bi_2O_3 and β-Bi_2O_3. Adapted from Ref[42]

	Bandgap (eV)	**Valence band (eV vs. NHE)**	**Conduction band (eV vs. NHE)**	**Fermi level (eV vs. NHE)**
α -Bi_2O_3	2.8	+3.08	+0.26	+1.73
β -Bi_2O_3	2.5	+1.89	-0.66	+0.54

The band structures of α-Bi_2O_3 and β-Bi_2O_3 can be studied by combining the bandgap along with the values of the Fermi levels and the energy differences between the Fermi levels and the valence bands as shown in Figure 1.13. It is quite evident that the valence bands of α-Bi_2O_3 and β-Bi_2O_3 are similar, but β-Bi_2O_3 with more dispersive bands has its bottom portion of the conduction band shifting more to the negative potentials, resulting in a smaller bandgap than α-Bi_2O_3. In this dissertation we studied exclusively the β-Bi_2O_3 which has an optimum bandgap (2.5 eV) coupled with a tunnel structure that will be more suitable for photocatalytic application by absorbing more visible light and favoring transport of photo induced charge carriers.[37, 38, 42]

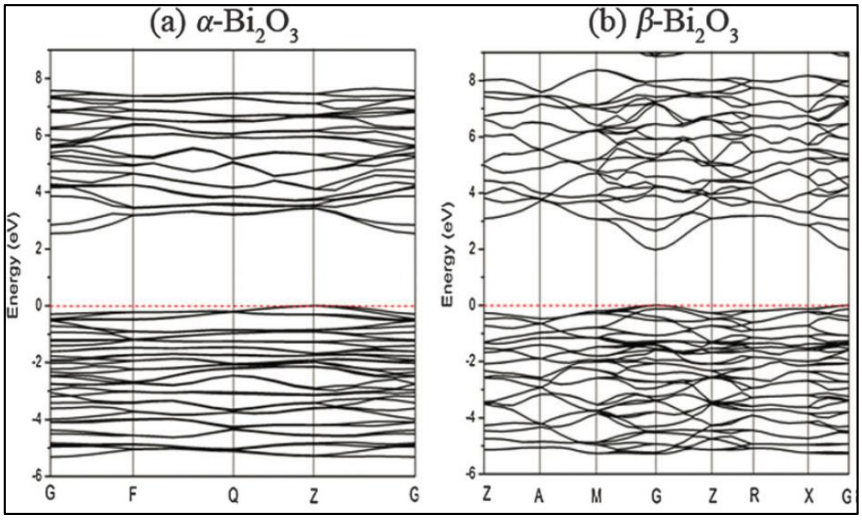

Figure 1.13. Electronic structures of (a) α-Bi_2O_3 and (b) β-Bi_2O_3. Adapted from Ref [37].

1.6.3. Issues with bismuth oxide based photoelectrodes

Recently, bismuth based ternary oxides such as $BiVO_4$, Bi_3NbO_7, and $BiFeO_3$ have attracted substantial attention as a promising high efficiency photocatalysts for solar water splitting applications.[43-45] Particularly, $BiVO_4$ has attracted more attention because of its optimal band edge positions for water splitting and potential to achieve a theoretical maximum photo current density of 7.5 mA/cm^2.[46] However, even after extensive research on the bismuth ternary oxide systems, the understanding of the photo electrochemical behavior

of bismuth binary oxide (Bi_2O_3), which is the building block of the ternary systems is not complete. In this thesis we address this knowledge gap.

There are few critical issues that need to be addressed in order to consider the binary bismuth oxides as a viable photoelectrodes. The stability of the Bi_2O_3 photocatalyst is considered to be affected by the oxidation reaction of Bi^{3+} to higher valence states such as Bi^{4+} and Bi^{5+} due to the reactions (1.19) – (1.22) in the solution during the UV light illumination:

$$Bi^{3+} + 2h^+ \rightarrow Bi^{5+} \quad [1.19]$$

$$2H_2O + 4h^+ \rightarrow 4H^+ + O_2 \quad [1.20]$$

$$Bi_2O_3 + H_2O + 2h^+ \rightarrow Bi_2O_{4-x} + 2H^+ \quad [1.21]$$

$$Bi_2O_3 + 2H_2O + 4h^+ \rightarrow Bi_2O_{5-x} + 4H^+ \quad [1.22]$$

The photo generated super-oxide radicals formed during illumination have the strongest oxidation ability and sufficiently long life time. These can oxidize Bi^{3+} to Bi^{4+} and Bi^{5+} and form Bi_2O_{4-x} and Bi_2O_{5-x} type phases on the surface based on the following reactions:

$$O_2 + e^- \rightarrow O_2^- \quad [1.23]$$

$$2O_2^- + 2H^+ \rightarrow H_2O_2 + O_2 \quad [1.24]$$

$$Bi_2O_3 + 4H^+ \rightarrow 2BiOH^+ + H_2O \quad [1.25]$$

$$Bi_2O_3 + 2H^+ \rightarrow 2BiO^+ + H_2O \quad [1.26]$$

$$2BiO^+ + OH^- \rightarrow BiOOH \quad [1.27]$$

$$BiOOH + OH^- \rightarrow BiO_2^- + H_2O \quad [1.28]$$

$$2BiO_2^- + 2OH^- \rightarrow Bi_2O_5 + H_2O + 4e^- \quad [1.29]$$

$$Bi_2O_3 + Bi_2O_5 \rightarrow 2Bi_2O_4 \quad [1.30]$$

These transformations may affect the photo activity of the Bi_2O_3, which is not fully understood. Second, the photocatalytic activity of the β-Bi_2O_3 is affected by its metastable nature. The β-Bi_2O_3 phase exhibits an n-type semiconductor behavior similar to the bismuth based ternary oxides. However, under extensive periods of light irradiation, the β-Bi_2O_3 phase may partially transformation into the more stable α-Bi_2O_3 phase which is a p-type semiconductor material. Mixed phases of α-Bi_2O_3 and β-Bi_2O_3 may be advantageous for photocatalytic reactions but not for photo electrochemical reactions where the anodic and cathodic reactions occur at specific electrode surfaces. Moreover, the long term stability of the bismuth oxides against photo corrosion/degradation is not well understood.

Likewise, it was observed that the bismuth based ternary oxides show low catalytic activity for oxygen evolution reaction (OER) and slow charge transport properties.[47] The poor electron transport in bismuth based ternary oxides, particularly in $BiVO_4$, is performance limiting. The low electron conductivity is attributed to the lack of connectivity between the VO_4 tetrahedra within the scheelite crystal structure.[48] Doping with aliovalent elements like Si, W, Mo, Eu, Dy, and Pd is considered to address the conductivity issue of the $BiVO_4$.[49-54] Similarly, the low activity for OERs is overcome by providing a thin layer of OER catalysts such as cobalt phosphate, FeOOH, or NiOOH on the photoanode or by adding hole scavenging agents such as methanol, H_2O_2, etc. to the electrolyte to enhance the oxygen evolution reaction.[55-57] In this research, we address the issues pertaining to binary bismuth oxide and also adopt the solutions used to mitigate and improve the photoelectrochemical performance of bismuth based ternary oxides for binary bismuth oxide.

1.7. Objectives and Scope of this Dissertation

Two photoanodes, α-Fe_2O_3 (hematite) and β-Bi_2O_3 thin films are investigated in this thesis. These thin films were prepared using an electrochemical anodization technique, which is essentially a low cost process with no sophisticated equipment or high vacuum chambers. The photoelectrode preparation involves just two steps: a) anodization performed in a two-electrode system with the material to be anodized as the anode and platinum foil as the counter electrode in an appropriate electrolyte followed by b) thermal annealing. This

method is highly scalable, highly reproducible and has the capability of producing large geometric area nanoporous electrodes, where the size of the electrode is limited only by the size of the electrolyte tank (Schematic shown in figure 1.14). The most important aspect of using this technique is that the metal substrate will act as a current collector and the nanoporous oxide layer grown on the metal substrate will make an ohmic contact which significantly reduces electron loss at the metal/oxide interface. The primary objective of chapter 2 was studying the photoelectrochemical behavior of nanoporous α-Fe_2O_3 oxide layer incorporated with Nd^{3+} and B^{3+}, which was prepared by electrochemical anodization of permanent magnet $Fe_{14}Nd_2B$. The photoelectrochemical behavior of the this oxide layer was compared with thermally oxidized permanent magnet $Fe_{14}Nd_2B$ and the iron oxides obtained by anodization and thermal oxidation of pure iron foil.

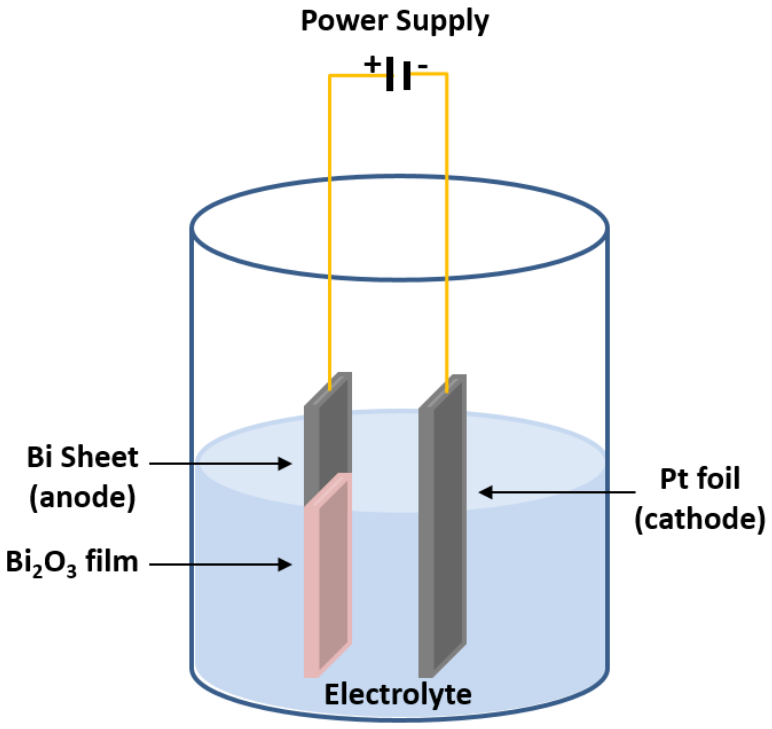

Figure 1.14. Schematic of Electrochemical Anodization set-up.

As stated above, β-Bi_2O_3 photoanode was chosen for its good photocatalytic properties and the n-type behavior like the bismuth based ternary oxides. The aim of the work relating to the β-Bi_2O_3 was five-fold: 1) to synthesize large surface area nanoporous bismuth oxide thin films by electrochemical anodization that have uniform dimensions and

ordered configurations resulting in 1-D or 2-D confinement for charge transport, 2) obtain β-Bi_2O_3 phase of the bismuth oxide without intentional doping so that the type of semiconductivity is similar to the ternary bismuth oxides such as $BiVO_4$, 3) investigate the effect of nanoscale dimensions of the β-Bi_2O_3 on the photo electrochemical performance, 4) investigate the long term stability of the β-Bi_2O_3 photo electrodes with and without hole scavengers, OER catalysts etc., and finally 5) recommend design strategies to improve the PEC performance of the bismuth based oxides for solar hydrogen generation applications. In chapter 3, the primary focus was to synthesize nanoporous β-Bi_2O_3 thin films and study the effect of varying pore size, wall and film thicknesses on the photoelectrochemical behavior of the material. However the performance of these thin films was limited due to accumulation of photo generated holes at the β-Bi_2O_3/electrolyte interface. In Chapter 4, various strategies were suggested to overcome the limitations and improve the performance of the photoanode and finally, stability of the materials was discussed in chapter 5.

1.8. References

1. Gratzel, M., Photoelectrochemical cells. *Nature* **2001,** *414* (6861), 338-344.

2. Smalley, R. E., Future Global Energy Prosperity: The Terawatt Challenge. *MRS Bulletin* **2005,** *30* (06), 412-417.

3. Van de Krol, R.; Grätzel, M., *Photoelectrochemical hydrogen production*. Springer New York: 2012.

4. Chen, Z.; Dinh, H.; Miller, E., *Photoelectrochemical Water Splitting: Standards, Experimental Methods, and Protocols*. Springer New York ; Imprint: Springer: 2013.

5. Abdi, F. F. Towards Highly Efficient Bias-Free Solar Water Splitting. TU Delft, Delft University of Technology, 2013.

6. Fujishima, A.; Honda, K., Electrochemical Photolysis of Water at a Semiconductor Electrode. *Nature* **1972,** *238* (5358), 37-38.

7. Gerischer, H., On the stability of semiconductor electrodes against photodecomposition. *Journal of Electroanalytical Chemistry and Interfacial Electrochemistry* **1977,** *82* (1–2), 133-143.

8. Liu, B.; Zhao, X.; Terashima, C.; Fujishima, A.; Nakata, K., Thermodynamic and kinetic analysis of heterogeneous photocatalysis for semiconductor systems. *Physical Chemistry Chemical Physics* **2014,** *16* (19), 8751-8760.

9. Grimes, C. A.; Varghese, O. K.; Ranjan, S., *Light, Water, Hydrogen: The Solar Generation of Hydrogen by Water Photoelectrolysis*. Springer US: 2007.

10. Li, Z.; Luo, W.; Zhang, M.; Feng, J.; Zou, Z., Photoelectrochemical cells for solar hydrogen production: current state of promising photoelectrodes, methods to improve their properties, and outlook. *Energy & Environmental Science* **2013,** *6* (2), 347-370.

11. Machala, L.; Tuček, J.; Zbořil, R., Polymorphous Transformations of Nanometric Iron(III) Oxide: A Review. *Chemistry of Materials* **2011,** *23* (14), 3255-3272.

12. Sakurai, S.; Namai, A.; Hashimoto, K.; Ohkoshi, S.-i., First Observation of Phase Transformation of All Four Fe2O3 Phases (γ → ε → β → α-Phase). *Journal of the American Chemical Society* **2009,** *131* (51), 18299-18303.

13. Tuček, J.; Zbořil, R.; Namai, A.; Ohkoshi, S.-i., ε-Fe2O3: An Advanced Nanomaterial Exhibiting Giant Coercive Field, Millimeter-Wave Ferromagnetic Resonance, and Magnetoelectric Coupling. *Chemistry of Materials* **2010,** *22* (24), 6483-6505.

14. Gich, M.; Frontera, C.; Roig, A.; Taboada, E.; Molins, E.; Rechenberg, H. R.; Ardisson, J. D.; Macedo, W. A. A.; Ritter, C.; Hardy, V.; Sort, J.; Skumryev, V.; Nogués, J., High- and Low-Temperature Crystal and Magnetic Structures of ε-Fe2O3 and Their Correlation to Its Magnetic Properties. *Chemistry of Materials* **2006,** *18* (16), 3889-3897.

15. Lin, Y.; Yuan, G.; Sheehan, S.; Zhou, S.; Wang, D., Hematite-based solar water splitting: challenges and opportunities. *Energy & Environmental Science* **2011,** *4* (12), 4862-4869.

16. Wheeler, D. A.; Wang, G.; Ling, Y.; Li, Y.; Zhang, J. Z., Nanostructured hematite: synthesis, characterization, charge carrier dynamics, and photoelectrochemical properties. *Energy & Environmental Science* **2012,** *5* (5), 6682-6702.

17. Drache, M.; Roussel, P.; Wignacourt, J.-P., Structures and Oxide Mobility in Bi–Ln–O Materials: Heritage of Bi2O3. *Chemical Reviews* **2007,** *107* (1), 80-96.

18. Eberl, J., *Visible Light Photo-oxidations in the Presence of Bismuth Oxides*. 2008.

19. Mansour, S. A. A., Thermal decomposition of anhydrous bismuth citrate. *Thermochimica Acta* **1994,** *233* (2), 257-268.

20. Greaves, C.; Blower, S. K., Structural relationships between Bi2O2CO3 and β-Bi2O3. *Materials Research Bulletin* **1988,** *23* (7), 1001-1008.

21. Monnereau, O.; Tortet, L.; Llewellyn, P.; Rouquerol, F.; Vacquier, G., Synthesis of Bi2O3 by controlled transformation rate thermal analysis: a new route for this oxide? *Solid State Ionics* **2003,** *157* (1–4), 163-169.

22. Chen, X. L.; Eysel, W., The Stabilization of β-Bi2O3by CeO2. *Journal of Solid State Chemistry* **1996,** *127* (1), 128-130.

23. Ayala, A.; López-Garcia, A.; Leyva, A. G.; de Benyacar, M. A. R., Stabilization of β-Bi2O3 by hafnia. *Solid State Communications* **1996,** *99* (6), 451-455.

24. Horiuchi, S.; Izumi, F.; Mitsuhashi, T.; Uchida, K.; Shimomura, T.; Ogasahara, K., Structural studies of β-Bi2O3 stabilized by the addition of PbF2. *Journal of Solid State Chemistry* **1988,** *74* (2), 247-255.

25. Mercurio, D.; El Farissi, M.; Frit, B.; Reau, J. M.; Senegas, J., Fast ionic conduction in new oxide materials of the Bi2O3 · Ln2O3 · TeO2 systems (Ln=La, Sm, Gd, Er). *Solid State Ionics* **1990,** *39* (3), 297-304.

26. Ducke, J.; Tromel, M.; Hohlwein, D.; Kizler, P., Yttrium and Titanium Bismuthates with Structures Related to [beta]-Bi2O3. *Acta Crystallographica Section C* **1996,** *52* (6), 1329-1331.

27. Sammes, N. M.; Tompsett, G. A.; Näfe, H.; Aldinger, F., Bismuth based oxide electrolytes— structure and ionic conductivity. *Journal of the European Ceramic Society* **1999,** *19* (10), 1801-1826.

28. Turkoglu, O.; Belenli, I., Electrical conductivity of g-Bi2O3-V2O5 solid solution. *Journal of Thermal Analysis and Calorimetry* **2003,** *73* (3), 1001-1012.

29. Wang, F.; Wang, J. B.; Zhong, X. L.; Li, B.; Zhou, Y. C., Synthesis and characterization of Bi3.15Nd0.85Ti3O12 nanotube arrays. *Journal of Crystal Growth* **2009,** *311* (20), 4495-4498.

30. Struzik, M.; Liu, X.; Abrahams, I.; Krok, F.; Malys, M.; Dygas, J. R., Defect structure and electrical conductivity in the pseudo-binary system Bi3TaO7–Bi3NbO7. *Solid State Ionics* **2012,** *218*, 25-30.

31. Durmuş, S.; Çorumlu, V.; Çifci, T.; Ermis, I.; Arı, M., Electrical, structural and thermal properties of nanoceramic (Bi2O3)1−x−y(Ho2O3)x(Tm2O3)y ternary system. *Ceramics International* **2013,** *39* (5), 5241-5246.

32. Katayama, H.; Tamura, S.; Imanaka, N., New bismuth ion conducting solid electrolyte. *Solid State Ionics* **2011,** *192* (1), 134-136.

33. Ling, C. D.; Withers, R. L.; Schmid, S.; Thompson, J. G., A Review of Bismuth-Rich Binary Oxides in the Systems Bi2O3–Nb2O5, Bi2O3–Ta2O5, Bi2O3–MoO3, and Bi2O3–WO3. *Journal of Solid State Chemistry* **1998,** *137* (1), 42-61.

34. Cornei, N.; Tancret, N.; Abraham, F.; Mentré, O., New ε-Bi2O3 Metastable Polymorph. *Inorganic Chemistry* **2006,** *45* (13), 4886-4888.

35. Gualtieri, A. F.; Immovilli, S.; Prudenziati, M., Powder X-ray diffraction data for the new polymorphic compound ω-Bi2O3. *Powder Diffraction* **1997,** *12* (02), 90-92.

36. Hull, S.; Norberg, S. T.; Tucker, M. G.; Eriksson, S. G.; Mohn, C. E.; Stolen, S., Neutron total scattering study of the [small delta] and [small beta] phases of Bi2O3. *Dalton Transactions* **2009,** (40), 8737-8745.

37. Cheng, H.; Huang, B.; Lu, J.; Wang, Z.; Xu, B.; Qin, X.; Zhang, X.; Dai, Y., Synergistic effect of crystal and electronic structures on the visible-light-driven photocatalytic performances of Bi2O3 polymorphs. *Physical Chemistry Chemical Physics* **2010,** *12* (47), 15468-15475.

38. Zhang, J.; Dang, W.; Yan, X.; Li, M.; Gao, H.; Ao, Z., Doping indium in [small beta]-Bi2O3 to tune the electronic structure and improve the photocatalytic activities: first-principles calculations and experimental investigation. *Physical Chemistry Chemical Physics* **2014,** *16* (42), 23476-23482.

39. Walsh, A.; Watson, G. W.; Payne, D. J.; Edgell, R. G.; Guo, J.; Glans, P.-A.; Learmonth, T.; Smith, K. E., Electronic structure of the alpha and delta phases of Bi2O3: A combined ab initio and x-ray spectroscopy study. *Physical Review B* **2006,** *73* (23), 235104.

40. Matsumoto, A.; Koyama, Y.; Tanaka, I., Structures and energetics of Bi2O3 polymorphs in a defective fluorite family derived by systematic first-principles lattice dynamics calculations. *Physical Review B* **2010,** *81* (9), 094117.

41. Lin, X.; Huang, F.; Wang, W.; Shi, J., Photocatalytic activity of Bi24Ga2O39 for degrading methylene blue. *Scripta Materialia* **2007,** *56* (3), 189-192.

42. Jiang, H.-Y.; Li, P.; liu, G.; Ye, J.; Lin, J., Synthesis and photocatalytic properties of metastable [small beta]-Bi2O3 stabilized by surface-coordination effects. *Journal of Materials Chemistry A* **2015,** *3* (9), 5119-5125.

43. Cao, D.; Wang, Z.; Nasori; Wen, L.; Mi, Y.; Lei, Y., Switchable Charge-Transfer in the Photoelectrochemical Energy-Conversion Process of Ferroelectric BiFeO3 Photoelectrodes. *Angewandte Chemie* **2014,** *53* (41), 11027-31.

44. Berglund, S. P.; Flaherty, D. W.; Hahn, N. T.; Bard, A. J.; Mullins, C. B., Photoelectrochemical Oxidation of Water Using Nanostructured BiVO4 Films. *The Journal of Physical Chemistry C* **2011,** *115* (9), 3794-3802.

45. Zhu, A.; Zhao, Q.; Li, X.; Shi, Y., BiFeO3/TiO2 Nanotube Arrays Composite Electrode: Construction, Characterization, and Enhanced Photoelectrochemical Properties. *ACS Applied Materials & Interfaces* **2013,** *6* (1), 671-679.

46. Abdi, F. F.; Han, L.; Smets, A. H. M.; Zeman, M.; Dam, B.; van de Krol, R., Efficient solar water splitting by enhanced charge separation in a bismuth vanadate-silicon tandem photoelectrode. *Nat Commun* **2013,** *4*.

47. Pilli, S. K.; Furtak, T. E.; Brown, L. D.; Deutsch, T. G.; Turner, J. A.; Herring, A. M., Cobalt-phosphate (Co-Pi) catalyst modified Mo-doped BiVO4 photoelectrodes for solar water oxidation. *Energy & Environmental Science* **2011,** *4* (12), 5028-5034.

48. Abdi, F. F.; van de Krol, R., Nature and Light Dependence of Bulk Recombination in Co-Pi-Catalyzed BiVO4 Photoanodes. *The Journal of Physical Chemistry C* **2012,** *116* (17), 9398-9404.

49. Zhang, X.; Quan, X.; Chen, S.; Zhang, Y., Effect of Si doping on photoelectrocatalytic decomposition of phenol of BiVO4 film under visible light. *Journal of Hazardous Materials* **2010,** *177* (1–3), 914-917.

50. Li, M.; Zhao, L.; Guo, L., Preparation and photoelectrochemical study of BiVO4 thin films deposited by ultrasonic spray pyrolysis. *International Journal of Hydrogen Energy* **2010,** *35* (13), 7127-7133.

51. Yao, W.; Iwai, H.; Ye, J., Effects of molybdenum substitution on the photocatalytic behavior of BiVO4. *Dalton Transactions* **2008,** (11), 1426-1430.

52. Wang, Q.; Liu, H.; Jiang, L.; Yuan, J.; Shangguan, W., Visible-light-responding Bi0.5Dy0.5VO4 Solid Solution for Photocatalytic Water Splitting. *Catal Lett* **2009,** *131* (1-2), 160-163.

53. Zhang, A.; Zhang, J., Effects of europium doping on the photocatalytic behavior of BiVO4. *Journal of Hazardous Materials* **2010,** *173* (1–3), 265-272.

54. Ge, L., Synthesis and characterization of novel visible-light-driven Pd/BiVO4 composite photocatalysts. *Materials Letters* **2008,** *62* (6–7), 926-928.

55. Kanan, M. W.; Nocera, D. G., In Situ Formation of an Oxygen-Evolving Catalyst in Neutral Water Containing Phosphate and Co2+. *Science* **2008,** *321* (5892), 1072-1075.

56. McDonald, K. J.; Choi, K.-S., A new electrochemical synthesis route for a BiOI electrode and its conversion to a highly efficient porous BiVO4 photoanode for solar water oxidation. *Energy & Environmental Science* **2012,** *5* (9), 8553-8557.

57. Kim, T. W.; Choi, K.-S., Nanoporous BiVO4 Photoanodes with Dual-Layer Oxygen Evolution Catalysts for Solar Water Splitting. *Science* **2014,** *343* (6174), 990-994.

2. Photoelectrochemical Behavior of Iron Oxide alloyed with Nd and B Nanoporous Oxide of FeNdB Alloy*

2.1. Abstract

Oxide nanoporous layer was synthesized by electrochemical anodization of commercially available sintered $Fe_{14}Nd_2B$ permanent magnets. The anodized oxide layer consisted of predominantly α-Fe_2O_3 alloyed with Nd and B ions. The photoelectrochemical behavior of the anodic oxide was compared with thermally oxidized counterpart and the iron oxides obtained by anodization and thermal oxidation of pure iron foil. The oxide of FeNdB showed higher electron density of states, charge carrier density, and lower bandgap than the un-alloyed iron oxide. The catalytic activity of FeNdB oxide for the oxygen evolution reaction was slightly higher than that of the un-alloyed iron oxide. However, the photocatalytic behavior of the FeNdB oxide was inferior to the iron oxide, which could be attributed to the increased charge recombination and hole accumulation occurring at the FeNdB oxide surface.

2.2. Introduction

Iron oxide, in the form of α-Fe_2O_3, has attracted revived interest as a material for alternate energy applications such as photoanode in solar water splitting and host for ionic intercalation in energy storage devices.[1] The advantages of using iron oxide as photoanode for solar energy conversion are its natural abundance, low cost and environmentally benign characteristics, stability in wide range of pH solutions, optimum energy bandgap (~2.1 eV) that not only provides sufficient over-potentials for oxygen and hydrogen evolution but also harvests a significant portion of light in the visible region, and appropriately positioned valence band that supplies energetic holes for water oxidation.[2] In spite of having all these positive characteristics to be a promising material for solar water splitting, its application in commercially viable device is still a far-fetched reality because of the following limitations:[3] 1) low dielectric constant[4-9] that results in high electrostatic attraction of the charge carriers and high probability of charge recombination, 2) short diffusion length for minority carriers

* This chapter has been published: Kalyan Chitrada, Krishnan S. Raja, David Rodriguez and Dev Chidambaram, Journal of The Electrochemical Society, 162 (4) H220-H228 (2015)

(holes) in the order of 2 – 10 nm depending on the preparation conditions, 3) low electron mobility (about 0.1 $cm^2V^{-1}s^{-1}$) and low conductivity, and 4) occurrence of conduction band minimum below the energy level for water reduction (hydrogen evolution) requiring high bias potential to split water.

The general strategy employed to overcome the limitation of low conductivity and high recombination losses was simultaneous doping and nano-sizing of the material that matches the hole diffusion length.[3-7, 10-15] Both isovalent and non-isovalent doping were found to increase the conductivity of the hematite either by increasing the defect (charge carrier) concentration or by polaron hopping mechanism.[8] Among various dopants, Si, Ti, and Sn have been widely investigated.[9, 16, 17] Recently, Liu et al reported a 3-fold increase in the photocurrent density of Fe_2O_3 when doped with 8% Ni.[18] Seki et al observed a red-shift in the bandgap of Rh-doped hematite and more than five-fold increase in the photocurrent density.[19]Doping of Fe_2O_3 not only increases the conductivity, but also modifies the band edge positions. For example, Meng et al.[20] showed that, based on the first principle calculations, that Ti-doping introduced shallow donor levels below the conduction band minimum (CBM) and shrunk the band gap of the hematite by 0.34 eV. On the other hand, the calculations showed that Cu doping would shift the CBM position above the H_2/H_2O energy level (conversely the CBM will be more negative to the hydrogen evolution potential). In order to have spontaneous solar water splitting without any external bias, it is important that the band edge positions straddle the water redox potential levels. In that context, doping with 4f elements may shift the CBM of Fe_2O_3 favorably to more negative potentials. Cerium doping of TiO_2 was observed to move the CBM to more negative potential.[21] However, in case of doping with Nd, the 4f electrons were considered to be located close to the lower edge of the conduction band of TiO_2 and that resulted in decreased band gap.[22] Nd doping was reported to increase the visible light absorption of the TiO_2 nanotubes and enhance the photocatalytic activity.[23] Increased magnetic anisotropy was reported for α-Fe_2O_3 doped with Nd.[24] The magnetic moment of Fe_2O_3 increased marginally with the Nd doping even though Nd was found to be non-magnetic at room temperature.

Doping of iron oxide with other rare earth elements have also resulted in several interesting results. Enhanced photoelectrochemical properties were reported for Ce doped hematite film.[25] Terbium doped iron oxide showed superparamagnetic behavior and exhibited photoluminescence at room temperature.[26] Bloemen et al[27] observed enhanced magneto-optical properties of holmium doped iron oxide nanoparticles. In addition to the electronic properties associated with photoactivity, effective catalysis for oxygen evolution by water oxidation is important for designing novel photoanodes. During electrolysis of water, substantial overpotential is required to drive the oxygen evolution reaction at the anode. In case of photoelectrolysis, the potential required for oxygen evolution reaction (OER) is considered to be supplied by the accumulation of holes generated by the light harvesting capability of the photoanode. Localization of holes on the oxygen lattice sites of the oxide photoanode is proposed to be a necessary condition for water oxidation which is facilitated by energetically favorable charge transfer excitation from oxygen ligand to metal.[28] The following reaction steps have been proposed for the water oxidation at the photoanode:[29, 30]

$$H_2O + (*) + h^+ \rightarrow HO^* + H^+ \qquad [2.1]$$

$$HO^* + h^+ \rightarrow O^* + H^+ \qquad [2.2]$$

$$O^* + H_2O + h^+ \rightarrow HOO^* + H^+ \qquad [2.3]$$

$$HOO^* + h^+ \rightarrow (*) + O_2(g) + H^+ \qquad [2.4]$$

The overall reaction is given as:

$$2H_2O + 4h^+ \rightarrow O_2(g) + 4H^+ \qquad [2.5]$$

Where, (*) represents an oxygen vacancy site; and HO*, O*, and HOO* are intermediate species chemisorbed at the oxygen vacancy sites.

The above reaction steps [2.1] to [2.4] indicate that the binding energies of the reaction intermediate species with the reaction sites are important in determining the OER

overpotential. Theoretical calculations of energetics of OER on various transition metal oxides have indicated that the free energy difference between HO*, and HOO* is almost constant and independent of the binding strength of the surface.[31] This result implies that HO* and HOO* prefer same type of binding site and therefore, the overpotential of OER is predominantly determined by the O* adsorption energy and reaction steps [2.2] and [2.3]. A volcano type plot has been proposed [29-31] to describe the OER overpotential as a function of the free energy difference between O* and HO* species ($\Delta G_{O*}^0 - \Delta G_{HO*}^0$). When the value of $\Delta G_{O*}^0 - \Delta G_{HO*}^0$ is around 1.48 eV, the calculated OER overpotential was on the lower side.[31] Liao et al. [28] observed that the $\Delta G_{O*}^0 - \Delta G_{HO*}^0$ value was smaller for doped iron oxides when the Bader charges of the dopant transition metal cations were larger. They attributed the better catalytic activity of the Ni doped hematite to its optimal $\Delta G_{O*}^0 - \Delta G_{HO*}^0$ value at 1.7 eV and moderate propensity for hole localization on the active O anions.[28]

It is well known that rare earth based perovskite oxides such as $LaFeO_3$, $LaCoO_3$, $LaNiO_3$, and $LaSr_xFe_{1-x}O_3$ have excellent OER catalytic activities.[32] Rare earth based oxides are being used as catalysts in several chemical processes, such as hydrocarbon reforming [33] and oxidation of hazardous waste,[34] that require oxygen activity. It is interesting to note that most of the literature on doped iron oxide for photoelectrolysis of water application pertains to transition metal doping. Not much of theoretical or experimental work on rare earth doped iron oxide has been reported to the best of our knowledge. In order to determine the effect of incorporation of rare earth in the iron oxide on the photoelectrochemical behavior, anodized oxide layers formed on commercial FeNdB (discs of permanent magnet) alloy were investigated. However, Iwamoto et al [35] synthesized spinel ferrite nanoparticles containing Nd and B, and illustrated much higher magnetic coercivity than their magnetite counterpart. Since magnetic dipoles play crucial roles in the charge transfer kinetics and catalytic behavior, it is hypothesized that the oxide layer of the FeNdB alloy might show interesting photoelectrochemical properties. Furthermore, the nanoporous oxide layer formed on the FeNdB is considered to be corrosion resistant and provides anchorage for additional corrosion protection coatings.[36]

2.3. Experimental Methods

2.3.1. Materials and methods

Two types of materials were investigated: 1) oxide layers formed on commercially available $Fe_{14}Nd_2B$ alloy and 2) oxide layers formed on pure iron as control for comparison.

Oxides on permanent magnets: The Nd and B incorporated iron oxide samples were prepared by modifying the bare surface of commercially available permanent magnet discs. Samples consisted of 16 mm diameter and 3 mm thick commercial permanent magnet discs ($Fe_{14}Nd_2B$ alloy, MAGCRAFT, Vienna, VA, USA) that were metallographically polished after removing the protective Ni-Cu-Ni layer down to 1500 grit finish. Samples then underwent ultrasonic cleaning in methanol, followed by acetone, and were dried using nitrogen. One set of samples was anodized and the other set was air oxidized. Anodization was performed in an electrolyte containing 0.1 M NH_4F in 5 vol% water and 95 vol% ethylene glycol at a potential of 40 V for 15 minutes. The oxide layer in as-anodized condition is expected to be amorphous and in order to obtain crystalline structure of the oxide phase, the anodized samples were annealed at 450 °C for 2 h.[36] A thick golden-brown oxide layer could be observed after anodization. Visual inspection of the anodized and annealed surface indicated that the formation of an anodized oxide prevented further oxidation of the sample as the color of the annealed surface did not change from its original golden-brown color. These samples are referred to as 'anodized FeNdB' in this report. The air oxidized samples were prepared by heating the samples in a tubular furnace at 450 °C for 2 h without purging any gas. The heating and cooling of the samples were carried out at a ramp rate of 5 °C/min to keep thermal stresses low. These samples are referred to as 'oxidized FeNdB' in this report.

Oxides on pure iron: Samples consisted of circular discs of 16 mm diameter that were punched out of a 0.25 mm thick iron foil (99.99% purity, Alfa Aeser). The anodization and the air oxidation procedure for the iron foil was similar to that of procedure described above for the FeNdB magnet. This air oxidized iron sample is referred to as 'thermal iron oxide' and the anodized oxide layer as 'anodized iron oxide' in this report. These samples represented the

un-doped iron oxide controls to which the oxides formed on permanent magnets are compared.

2.3.2. Characterization

Surface morphology of the samples were characterized using scanning electron microscopes LEO SUPRA 35VP and FEI Quanta 200F. Transmission electron microscopy studies and energy dispersive spectroscopy (EDS) analysis were carried out using JEOL 2100F. Structural characterization was performed by grazing angle XRD (GIXRD) on a PANalytical X'Pert Pro MRD diffractometer equipped with a Copper x-ray tube and parallel-beam optics. The incident angle was fixed at 0.9°. X-ray photoelectron spectroscopy (PHI Quantum 2000) was employed to evaluate the surface valence states and electron density of states at the surface of the samples. Mono-chromated Al-Kα (1488.6 eV) radiation was used as the source with an acceptance angle of ±23° and take-off angle of 45°. Charge correction was carried out by considering the C 1s peak at 284.8 eV. Absorbance spectra were recorded using a Shimadzu UV-2401PC spectrometer equipped with tungsten lamp. The scans were recorded over a range of 250-900 nm. Barium sulfate was used as standard reference. The step size and slit width used were 1 nm and 5 nm, respectively. Thermo Scientific DXR Raman microscope was used to characterize the Raman active components present in the surface films. The DXR system was fitted with a 532nm laser of 5mW power. Data was collected from a spot diameter of 0.7 µm utilizing 32 exposures at an exposure time of 5 seconds.

2.3.3. Photoelectrochemical studies

Photoelectrochemical characterization was carried out using a three-electrode configuration with a 7.5 cm^2 platinum flag counter electrode, Ag/AgCl solution reference electrode. A polyether ether ketone (PEEK) sample holder was used to electrically connect the sample to the potentiostat (Gamry Instruments, model: Reference 600) by exposing 1 cm^2 of the active surface. The samples were illuminated using a solar simulator (SOLAR Light, Glenside, PA, USA, Model: 16S-300) with a 300 W xenon lamp, and an air mass global 1.5 filter that gave 1-sun intensity (100 mW/cm^2) at appropriate settings. The samples were polarized at 0.5 V in 1 M KOH solution for constructing the Tauc plots. Band pass filters (Edmund Optics)

in the range of 400 -700 nm at 50 nm intervals were used to obtain the action spectra. The intensity of the light was measured using a pyranometer probe (SOLAR Light, USA, model: PMA 2144) and a radiometer (SOLAR Light, USA, model: PMA 2100). Galvanodynamic, potentiostatic, electrochemical impedance spectroscopy (EIS), and Mott-Schottky analysis studies were performed under dark and illuminated conditions. Potentiostatic measurements were carried out in 1 M KOH solution at 0.5 V. Potential Vs current plots were constructed by scanning the potential of the sample from the open circuit potential to 0.5 V at a scan rate of 5 mV/s or scanning the current from 0 µA to 2000 µA at a rate of 5 µA/s in 1 M KOH solution. Potentiostatic EIS was performed at 0.5 V with an amplitude of 10 mV in the frequency range of 100 KHz to 100 mHz. Mott-Schottky measurements were conducted at a frequency (*f*) of 1000 Hz by scanning the potential of the sample from 0.5 V to -0.6 V at 50 mV steps for every two seconds. The capacitance (*C*) of the space charge layer was calculated from the imaginary impedance (*Z"*) using the relation $C = -1/(2\pi fZ")$. All potentials are relative to the Ag/AgCl reference electrode.

2.4. Results and Discussions

2.4.1. Morphology

Figures 2.1a–1d show the FESEM images of the oxidized FeNdB and the thermal iron oxide samples. The thermal iron oxide samples showed a flaky or leaf like morphology as seen in Figure 2.1a & 2.1b. The flakes were less than 13 nm thick. The aspect ratio of the flakes varied from 1–8. The width of the flake ranged from 150–560 nm. The cross sectional SEM images of the oxide layers are given in Figure A1 of the Appendix A. The total thickness of the oxide film was about 2 µm, as seen in Figure A1(a). Figure 2.1c & 2.1d shows the morphology of oxidized FeNdB sample to be predominantly sintered granular structure (∼160 nm in diameter equiaxed grains) with discrete acicular and flaky structures. The thickness of the oxide layer was about 0.5 µm, as seen in Figure A1(b). Figure 2.1e & 2.1f show the FESEM images of the anodized FeNdB sample. The diameter of the pores varied from 30–60 nm with a wall thickness in the range of 10–14 nm. The thickness of the anodized layer was about 0.5 µm.

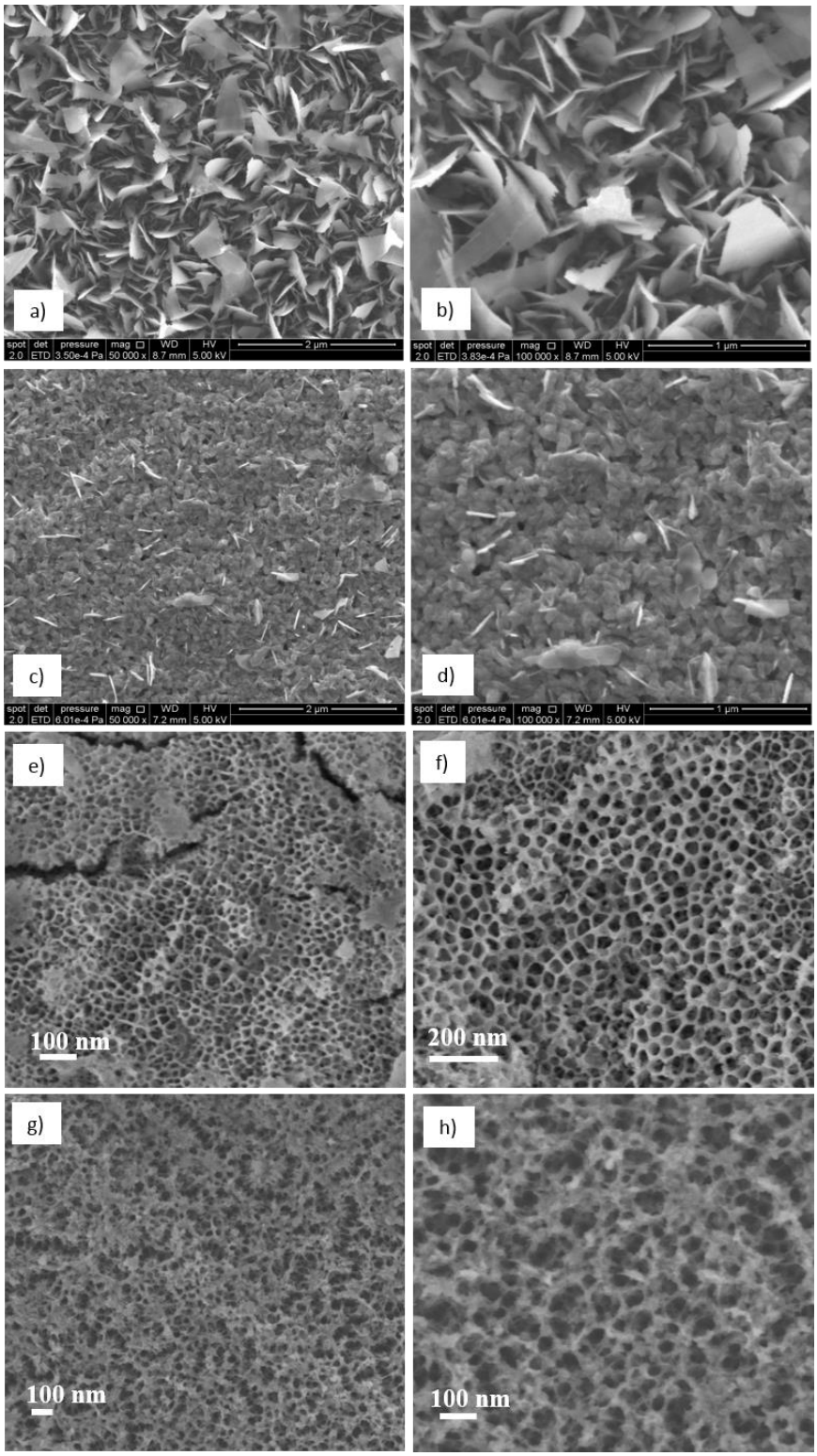

Figure 2.1. FESEM images of (a-b) pure iron foil, (c-d) FeNdB samples thermally oxidized in air at 450 °C for 2 h. These samples are referred as thermal iron oxide and oxidized FeNdB respectively in the text. FESEM images of the anodized surfaces of the (e-f) FeNdB and (g-h) iron foil samples electrochemically anodized in ethylene glycol solution containing 0.1 M NH4F and 5 vol% water at 40 V for 15 minutes and thermally annealed at 450 °C for 2h. These samples are referred as anodized iron oxide and anodized FeNdB respectively in the text.

The FESEM images of anodized iron oxide in Figures 2.1g & 2.1h also show a nanoporous structure similar to FeNdB samples, but the pores are very irregular and the diameters of the pores varied from 60–100 nm. The thickness of the layer was about 1 µm. The transmission electron microscopic image of the anodized FeNdB layer is shown in Figure 2.2. For observation under TEM, the anodized layer was scraped and loaded on to the copper grids.

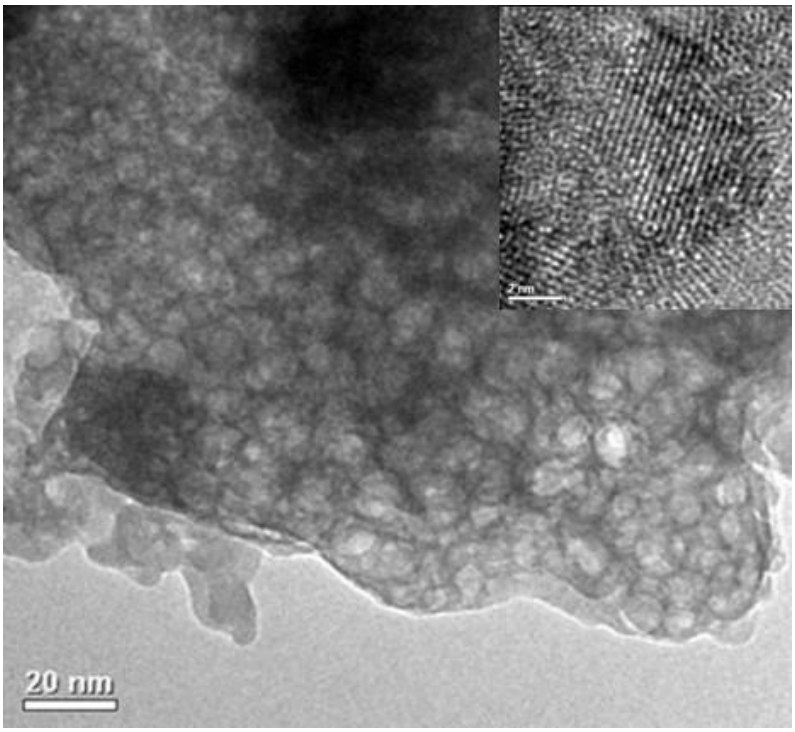

Figure 2.2. TEM image of the anodized FeNdB sample electrochemically anodized in ethylene glycol solution containing 0.1 M NH_4F and 5 vol% water at 40 V for 15 minutes.

The inset of Figure 2.2 shows typical image of the lattice fringes which indicates polycrystalline nature of the oxide with highly disordered crystallite boundaries. The disorder could be attributed to the incorporation of the larger Nd^{3+} cations in the Fe_2O_3 lattice structure. This type of disordered boundaries with highly ordered core nanostructure was uniformly observed in multiple samples. Similar observations were reported for the air oxidized FeNdB samples by Li et al.[37] These authors observed a mixture of nanocrystalline iron oxides surrounded by amorphous Nd-B-oxide. Figure 2.3a–f show typical results of energy dispersive X-ray spectra and elemental X-ray mapping of neodymium, iron and oxygen

present in the anodized oxide layer of anodized FeNdB. The results of the elemental mapping clearly indicated that the Nd was uniformly distributed in the oxide and no separation of Nd rich phase was observed. Energy dispersive X-ray analyses (EDAX) of the samples indicated that the anodized FeNdB oxide contained 8.3 ± 1.2 at% neodymium and 4.4 ± 1.8 at% of boron.

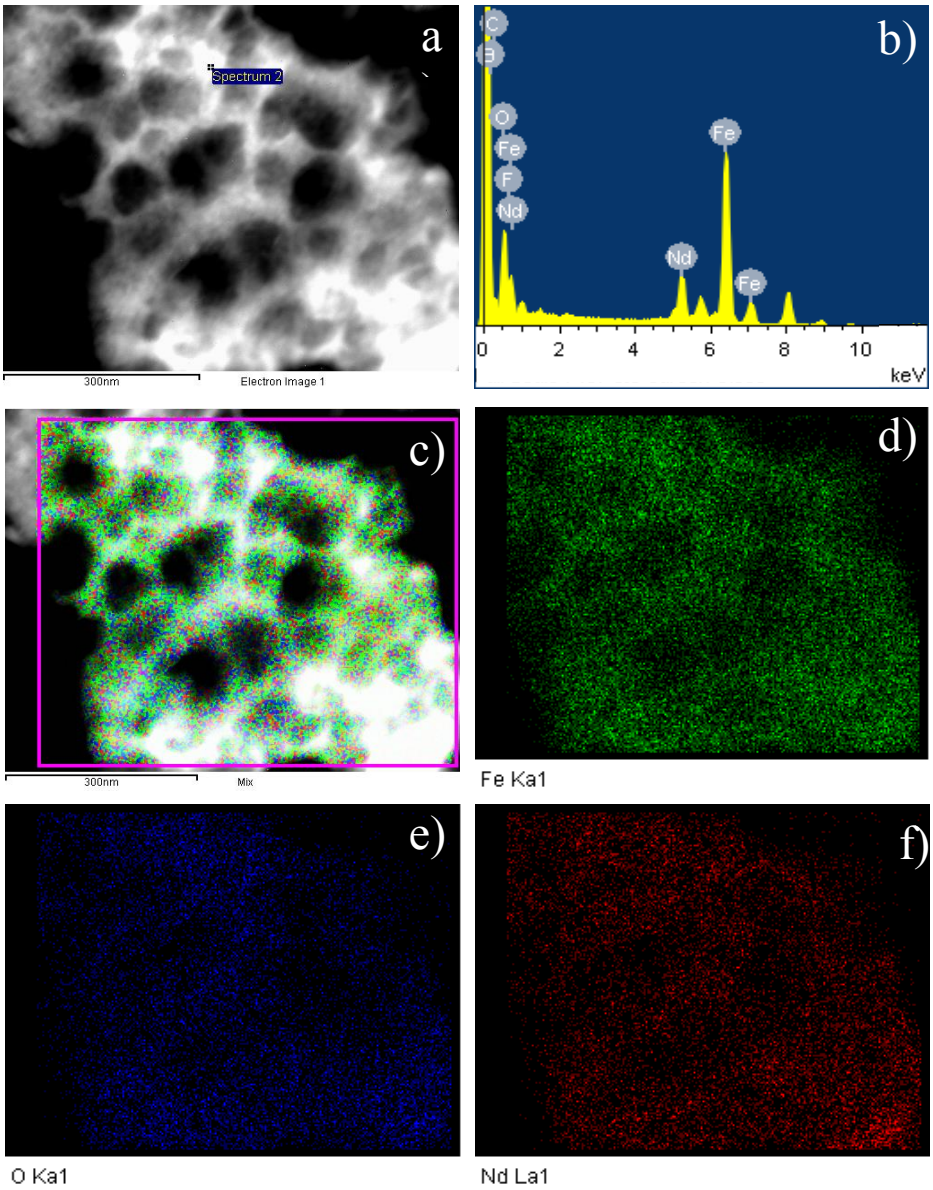

Figure 2.3. Energy dispersive X-ray Spectrometry (EDS) of the anodized FeNdB sample and X-ray elemental mapping analyses. (a) Image of the oxide layer analyzed, (b) EDS spectrum indicating presence of Fe, Nd, and O, (c) overall mapping, mappings of: (d) iron, (e) oxygen, and (f) neodymium.

2.4.2. XRD analysis

Figure 2.4 shows the XRD patterns of the anodized FeNdB sample which was annealed at 450 °C for 2 h. A complete crystalline oxide structure was observed after annealing the anodized film at 450 °C for 2 h. The oxide layer showed presence of predominantly rhombohedral α-Fe_2O_3, along with marginal γ-Fe_2O_3 and a minor peak of Nd_2O_3. The oxidized FeNdB sample also showed predominantly α-Fe_2O_3 (hematite) peaks and minor γ-Fe_2O_3 peaks (data not included), but no Nd_2O_3 peaks could be identified in this sample. The thermal iron oxide sample also showed predominantly α-Fe_2O_3 peaks. Presence of predominantly maghemite structure has been reported in the iron oxide nanotubes synthesized by anodization of pure iron foil.[38] The electrochemically passivated or anodized iron typically shows a bi-layered surface oxide consisting of magnetite (Fe_3O_4) inner layer and maghemite inner layer.[39] When thermally annealed, the maghemite to hematite transformation occurs at about 377 °C and the transformation temperature increases with decrease in the oxide particle size[40] and increase in the doping level.[41, 42] In this investigation, Nd^{3+} ions are considered to be incorporated in the Fe_2O_3 lattice structure. The XPS data of the samples also indicated significant incorporation of the Nd3+ as given in the Figure A2 (a)–(c) (Appendix A). Incorporation of Nd^{3+} in the hematite structure was reported with a formula of $Fe_{1.5}Nd_{0.5}O_3$ and a significant increase in the unit cell volume of hematite was observed (from 0.30156 nm^3 to 0.30323 nm^3, about 0.55% increase) with 10 mol% Nd substitution.[43] In this study, minor shifts in the peaks of the sample to slightly lower 2θ values than that of standard hematite peaks (JCPDS pattern: 033-0664) were observed which indicated increase in the lattice parameter due to the incorporation of Nd^{3+} and boron in the α-Fe_2O_3.

Based on the XRD results, the calculated lattice parameters of the anodized FeNdB sample were: a = 0.50563 nm, and c = 1.39172 nm. The calculated cell volume of this oxide was 0.30813 nm^3, about 2% volume increase. Comparing the results of Bhuiyan et al[43] who indicated 10 mol% of Nd^{3+} in the solid solution of α-Fe_2O_3 for a 0.55% increase in the lattice volume, it could be argued that the 2% lattice volume increase observed in the anodic oxide of $Fe_{14}Nd_2B$ alloy could be attributed to the incorporation of the 8.3 at% Nd and 4.4 at% B in the Fe_2O_3 based on the EDAX analyses. The resultant oxide could be expressed as

$Fe_{1.365}Nd_{0.415}B_{0.22}O_3$. The observed minor peak of Nd_2O_3 could be attributed to the reprecipitated layer of debris adhering to the nanoporous surface of the anodized oxide. Higher concentration of Nd was observed by X-ray elemental mapping at these debris as seen in the bottom right corner of Figure 2.3(a) and (d).

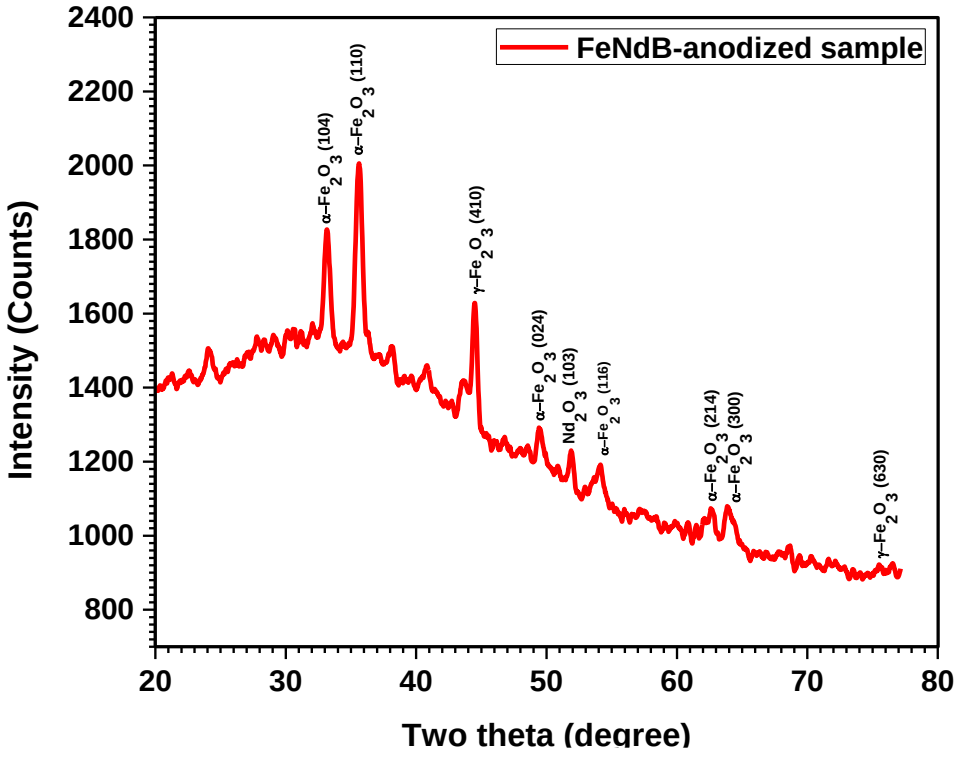

Figure 2.4. Glancing angle X-ray diffraction pattern of the anodized FeNdB sample that was annealed at 450 °C for 2 h.

2.4.3. Raman analysis

Figure 2.5 show the Raman spectra of the anodized FeNdB and oxidized FeNdB samples. The peaks at 225 and 500 cm^{-1} are associated with the A_{1g} modes of the pure synthetic hematite.[44] The peaks at 245, 291, 411, and 611 cm^{-1} are assigned to the E_g modes of the synthetic hematite[45]. The peaks at 1330 and 1600 cm^{-1} are attributed to burnt organic matter present in the hematite and maghemite.[45] Presence of carbonaceous species was also observed by the XPS analysis as given in the Figure A2(c) (supporting information). In this study, the peaks corresponding to the A_{1g} and E_g modes of hematite were observed in the oxidized FeNdB samples. The anodized sample showed a predominant peak at 1800 cm^{-1} corresponding to Nd_2O_3.[46] Broadening of phonon peaks were observed that could be

attributed to the nano-crystallite size of the oxides and of high concentration of oxygen vacancies.[46] The XRD results of the anodized FeNdB presence samples indicated increase in lattice parameters compared to that of pure hematite. Increase in the lattice parameter and subsequent increase in the bond length results in red shift of the wave number because of lowering of the force constant following a simple relation between the frequency (v), force constant (*k*), and mass of the ions forming a bond:

$$\vartheta = \frac{1}{2\pi}\sqrt{\frac{k(m_1+m_2)}{m_1 m_2}} \qquad [2.6]$$

Increase in the mass of cation also results in the red shift of the Raman peaks. Therefore, the observed red shifts in the Raman peaks of the FeNdB oxides could be attributed to the increased lattice parameters due to incorporation of Nd and B in the hematite lattice. The Raman spectroscopic results support the XRD, XPS and TEM results.

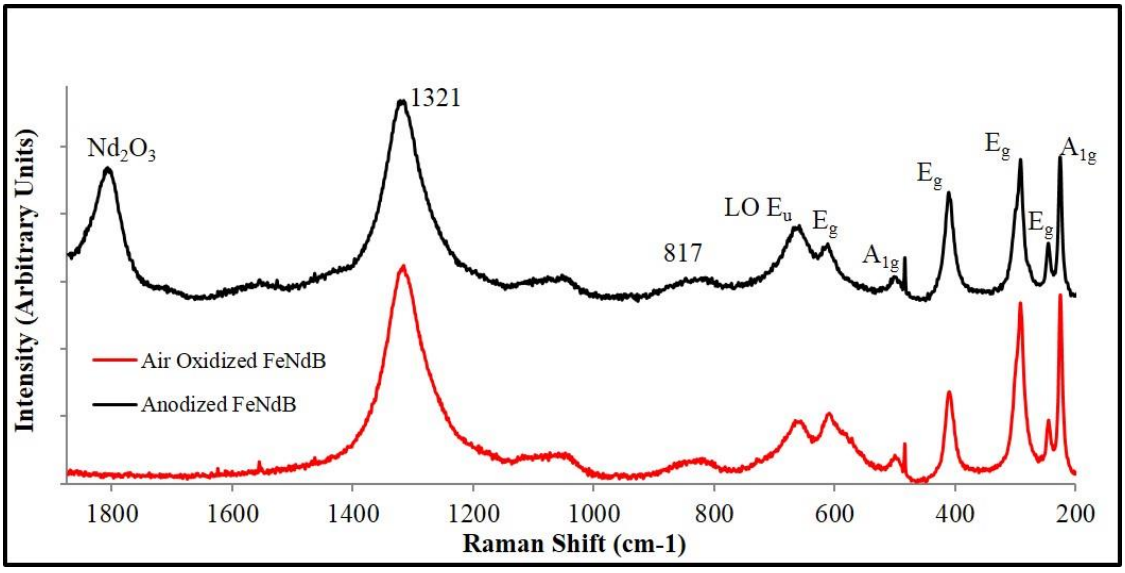

Figure 2.5. Raman spectra of the oxide layers of $Fe_{14}Nd_2B$ alloy. (a) Thermally oxidized at 450 °C for 2 h; (b) Anodized at 40 V for 15 minutes and annealed at 450 °C for 2 h.

2.4.4. Band gap calculation

Figure 2.6 (a) shows the optical absorbance of the oxides of oxidized FeNdB and anodized FeNdB as a function of wavelength of the light. The as-anodized FeNdB oxide layer showed a sharp increase in the absorbance at wavelengths shorter than 600 nm. The

annealed anodic oxide samples showed a red shift of about 40 nm for the take-off of the absorbance. The air oxidized samples showed several shoulders that made the analysis difficult. Figure 6 (b) shows the Tauc plots of oxides of both iron and FeNdB samples constructed by following the well-established relation: $(\alpha h\nu) = A(h\nu - E_g)^n$, where A = constant, $h\nu$ = photon energy, E_g = energy band gap of the semiconductor and the exponent, n = 0.5 or 2 for direct and indirect energy transition, respectively. In this investigation, the observed photocurrent density was assumed to be proportional to the optical absorption coefficient, α. Pure iron oxide prepared either by thermal oxidation or by anodization showed a direct band gap of 2.35 eV. On the other hand, oxidized FeNdB sample showed a direct band gap of 2.4 eV while the anodized FeNdB sample showed a direct band gap of 2.05 eV. It should be noted that when considering the indirect band gap of the samples *(*based on the *hv* vs $(I_{ph}h\nu)^{1/2}$ plots, data not shown here), the iron oxide (both thermally oxidized and anodized) showed a value of 2.05 eV. The oxidized FeNdB sample also showed a similar indirect band gap of 2.05 eV as that of the iron oxide. The indirect band gap of the anodized and annealed FeNdB alloy was 1.9 eV. Similar values were reported for the α-$(Cr_xFe_{1-x})_2O_3$ by Mashiko et al.[47] These authors attributed the lowest energy transition to charge transfer from Cr t_{2g} and O *2p* states to Fe t_{2g} state. Liu et al[10] reported an indirect band-gap of 1.96 – 2.04 eV for Ni doped Fe_2O_3 thin film prepared by electrodeposition.

The Tauc plots results indicated band-gap narrowing of the FeNdB oxide samples. The band gap narrowing could be attributed to the induced states of Nd *4f* located at the conduction band minimum, similar to the effect observed in the TiO_2 [48]. Furthermore, incorporation of boron in the Fe_2O_3 lattice also would shift the valence band closer to the conduction band and thus narrowing the band gap. Figure A3 (Appendix A) shows the valence band structure of the oxide layers of pure iron and FeNdB alloy. Pure iron oxide in the as anodized and anodized + annealed conditions showed almost similar valance band structure near the Fermi energy level. The valence band of the anodized FeNdB sample was observed to have shifted by 0.1 eV to lower binding energies. The lowering of the binding energy of the valence band should result in moving the Fermi level away from the conduction band and decrease in the conductivity.[49]

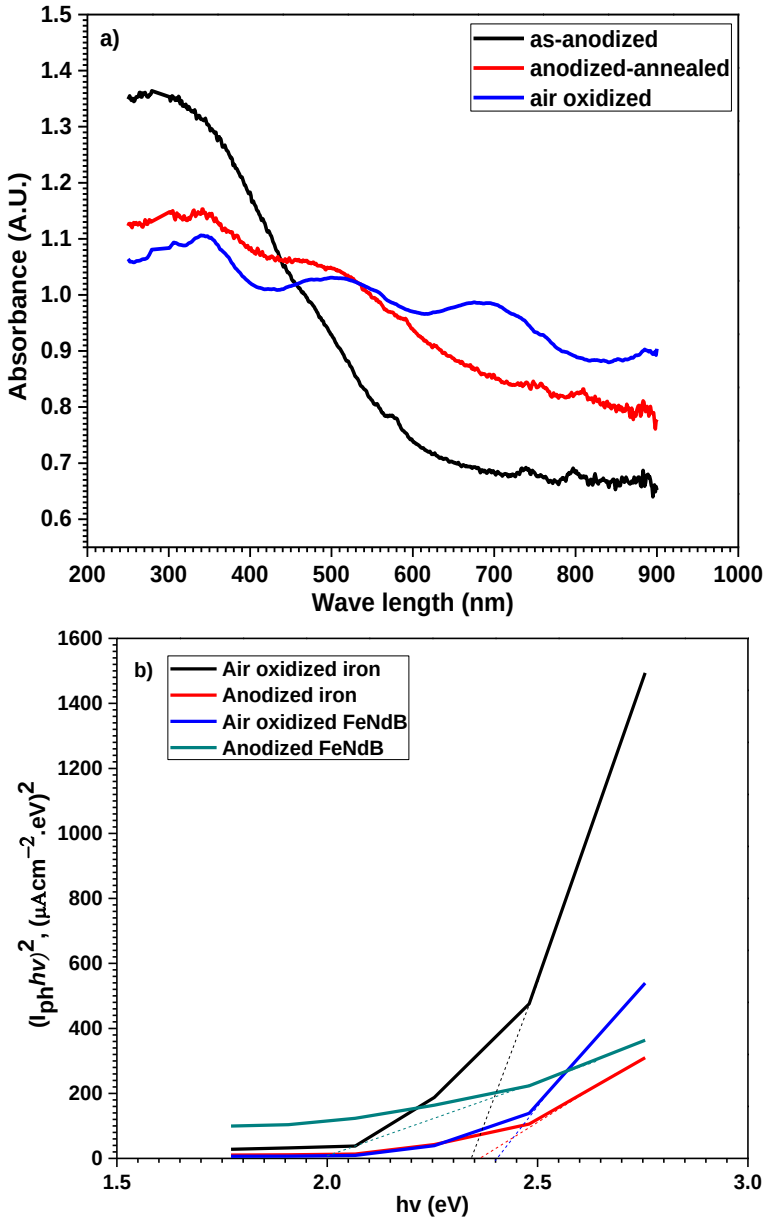

Figure 2.6. (a) Optical absorbance Vs wavelength plots of thermally oxidized and anodized FeNdB samples based on the diffuse reflectance measurements. (b) Tauc plots of thermally oxidized and anodized iron and FeNdB samples. Photo currents were measured by illuminating the samples by different wavelengths of light using band pass filters in the range of 450 – 700 nm at 50 nm intervals. The sample was polarized at 0.5 $V_{Ag/AgCl}$ in 1 M KOH solution.

2.4.5. Photoelectrochemical behavior

Figure 2.7 shows the current transients during the potentiostatic tests of different samples at 0.5 V Ag/AgCl (1.53 V_{RHE}). The recorded photocurrent densities of the thermal iron oxide, anodized iron oxide, oxidized FeNdB, and anodized FeNdB were 2.6, 1.1, 1.58, and 0.5 mA/cm^2, respectively. The recorded dips in the current densities were due to interruption of

the entire spectrum of simulated solar light (dark condition). The lowest magnitude of current density was associated with the dark current. The observed dark current density of thermal iron oxide, anodized iron oxide, oxidized FeNdB, and anodized FeNdB were 3.7, 7.2, 6.7, and 3.1 μA/cm^2, respectively The maximum photocurrent density reported in the literature, to the best of our knowledge, for undoped hematite (as nano-net) was 1.6 mA/cm^2 at 1.23 V_{RHE} and 2.7 mA/cm^2 at 1.53 V_{RHE}.[50] In the case of iron oxide prepared by thermal oxidation, Vincent et al[51] reported a photocurrent density of 0.9 mA/cm^2 at 1.8 V_{RHE} for the sample oxidized at 600 ^oC, and 2.6 mA/cm^2 for the 700 ^oC oxidized sample. These authors also reported a photocurrent density of about 0.35 mA/cm^2 at 1.7 V_{RHE} for the samples oxidized at 400-450 ^oC in a box furnace without any gas flow for 24 h, a similar experimental condition followed in this investigation but with a constant set temperature at 450 ^oC and shorter dwelling time (2 h) that resulted similar nano-leaf oxide morphology. However, much higher photocurrent density was observed in this investigation at a relatively lower bias potential (1.53 V_{RHE}). The reason for the increased photocurrent density of the current investigation could be attributed to the thinner oxide layer compared to the samples studied by Vincent et al[51] which could have resulted in smaller recombination losses. The photocurrent densities of the Nd doped oxide samples were lower than the unalloyed oxide samples. Doping of Nd in TiO_2 was observed to improve the photocatalytic properties by decreasing the band gap and introducing mid band gap states as electron states.[52] However, incorporation of Nd and B in the Fe_2O_3 structure was found to have a negative impact on the photocurrents which could be attributed to the polaron effect introduced by the Nd^{3+}. In case of TiO_2, the substitutional Nd^{3+} introduced oxygen vacancies for charge neutralization. The additional oxygen vacancies introduced by alloying of Nd^{3+} acted as shallow electron traps and extended the lifetime of holes.[21] This feature would be very helpful for α-Fe_2O_3 in which the light-to-current conversion efficiency is limited by hole diffusion lengths of 2-4 nm and hence shorter hole lifetimes. However, since Nd^{3+} is isovalent with Fe^{3+}, alloying will not introduce additional oxygen vacancies for electron trapping, and therefore no beneficial effect of hole lifetime could be expected. Furthermore, distortions introduced by the Nd^{3+} substitution would negatively affect the transfer of charge carriers based on the small polaron model.[53] It is

interesting to note that the recorded current value of the anodic oxide of FeNdB alloy during the potentiostatic test at 0.5 V was different from that of the galvanodynamic test. This observation indicated that the kinetics of electron-hole separation occurred faster under a dynamically varying electric field than under a static electric field in case of the iron oxide. The dark current densities were much smaller under potentiostatic conditions. In order to understand the oxygen evolution reaction (OER) occurring on the oxide samples, galvanodynamic tests were carried out with and without illumination, and the results are reported in Figure A4 (a) and (b) (Appendix A). It was observed that the exchange current density of the OER was lower for the alloyed iron oxide samples than that of unalloyed iron oxide samples, as seen in Table A1 (Appendix A). The alloyed iron oxide samples showed larger electron transfer coefficient (or symmetry factor) for the intermediate steps of oxygen evolution reactions and lower Tafel slopes than that of unalloyed iron oxide samples.

2.4.6. Mott-Schottky behavior

Figure A5(a) and (b) (Appendix A) show the results of electrochemical impedance spectroscopy in the form of Bode plots of the thermally oxidized and anodized samples, respectively, with and without illumination. The impedance values decreased orders of magnitude under the illumination for all the samples when compared to the impedance of the dark (not illuminated) condition. The impedance data can be fitted into a Randel's type equivalent circuit consisting of one resistor connected in series with a parallel RC circuit (the capacitance replaced with a constant phase element) as shown in Figure A6. The fitted parameters are summarized in Table A2. Figure 2.8 (a) and (b) show the Mott-Schottky results of the thermally oxidized iron oxide and FeNdB oxide samples, respectively. For both samples, a typical n-type behavior could be observed because of the positive slopes of the linear regions at potentials in the range of -0.6 – 0 V. The illuminated pure iron oxide sample showed two distinct regions of different slopes. Similar type of result has been reported by Klahr et al.[54] The two different slopes could be attributed to ionization of defects present at two different energy levels separated by about 0.2 eV. The slope of the Mott-Schottky plot is considered for calculation of the defect or charge carrier density, N_D, based on the relation:

$$N_D = 2/e * \varepsilon * \varepsilon_0 * m \qquad [2.7]$$

Where e = elementary charge, ε = dielectric constant of the semiconductor, ε_0 = permittivity in vacuum, and m = slope of the Mott-Schottky plot. From the above relation, it could be noted that shallower the slope, the larger is the defect density. The illuminated sample showed a shallower slope than the non-illuminated sample, especially at negative or less positive potentials. At potentials higher than 0.2 V, a change in the slope, suggesting p-type semiconducting behavior, was observed for the FeNdB oxides. This p-type behavior could be attributed to accumulation of holes at the surface because of slower kinetics of OER on the FeNdB oxide surface.

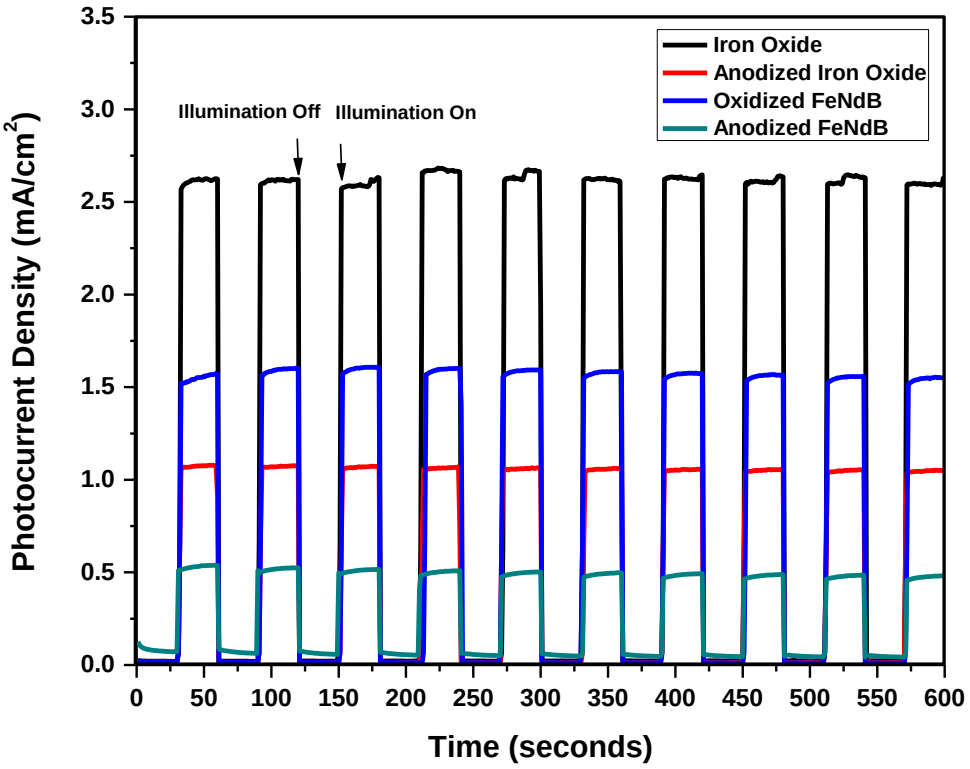

Figure 2.7. Photocurrent density vs. time plots of iron oxide and FeNdB samples in 1M KOH solution illuminated at 1-sun intensity using AM 1.5 filter. The samples were biased by an external potential of 0.5 $V_{Ag/AgCl}$.

Table 2.1 shows the summary of the Mott-Schottky plots of all the samples. The charge carrier density of the thermally oxidized iron oxide with nano-leaf morphology under dark condition was 3.9 x 10^{19} $cm^{-3.}$ Assuming that the charge carriers were oxygen vacancies, the oxide composition could be given as Fe_2O_{3-x}, where x = 6.5 x 10^{-4}. Under illumination, the

charge carrier density of the iron oxide sample increased by 33%. The flat band potential was -0.56 $V_{Ag/AgCl}$. The space charge width of the sample was 5-6 nm which is in the order of hole diffusion length of hematite. All these parameters contributed to the high photocurrent density of the iron oxide sample in this investigation. Similar Mott-Schottky results have been reported for thermally formed thin iron oxide films by Wielant et al.[55] The charge carrier density of the thermally oxidized FeNdB was about two orders of magnitude higher and the flat band potential was more negative than that of iron oxide. In spite of these positive attributes, the photocurrent density of the thermally oxidized FeNdB was about 40% lower than that of thermally oxidized iron oxide. The inferior photoactivity of the FeNdB oxide could be attributed to fast charge recombination due to the alloying additions possibly acting as recombination centers and only a thinner space layer available for charge separation. Since the width of the space layer was only about 1.2 nm, the photogenerated charges beyond the space charge layer were not effectively separated and therefore the relaxation of photogenerated electron-hole pairs lead to low photocurrent. Furthermore, observation of p-type behavior at higher potentials could also lead to increased relation due to formation of p-n junction at the photoanode.

Figures 2.9 (a) and (b) shows the Mott-Schottky plots of the anodized iron and FeNdB samples with and without illumination. The charge carrier density of the anodized FeNdB sample was the highest among the investigated samples. The defect density without illumination was 1.1 x 10^{22} cm^{-3} which increased to 1.6 x 10^{22} cm^{-3} upon illumination. The space charge layer was about 0.4 nm thick under a bias potential of 0.5 $V_{Ag/AgCl}$. This layer was shorter than the diffusion lengths of the holes. The flat band potential was -0.82 $V_{Ag/AgCl}$. Assuming that the flat band potential of a heavily doped semiconductor could be correlated with the position of conduction band minimum (CBM), the CBM of the anodized FeNdB sample was about 0.2 V below the H_2/H_2O level. The more negative flat potential indicates that the alloyed iron oxide samples require much smaller bias potential for photoelectrochemical water splitting. However, the electronic properties need to be improved for its potential use as an electrode for photoelectrolysis. Alloying of Nd and B in iron oxide resulted in lowering of the indirect bandgap, and higher charge carrier densities;

however, the photoconductivity was not significantly higher than that of the unalloyed iron oxide sample. Even though, the flatband potential of the alloyed iron oxide samples became more negative, the CBM of alloy oxides could be more positive with bandgap narrowing with alloying. Therefore, the apparent shifting of the flatband potential could be attributed to the surface catalysis of oxygen evolution reaction. This observation indicates that the mobility of the electrons was strongly impaired by the alloying of Nd^{3+} and B^{3+}. It is envisaged that the Nd^{3+} and B^{3+} sites functioned more as electron traps and recombination centers than enhancing the minority carrier life time.

Table 2.1. Summary of the Mott-Schottky analyses

Sample		**Flat band potential, $V_{Ag/AgCl}$**	**Charge carrier density, cm^{-3}**	**Calculated width of space charge layer at 0.5 V, nm**
Thermal iron oxide	Dark	-0.56	3.9×10^{19}	6.52
	Illuminated	-0.56	5.2×10^{19}	5.62
Oxidized FeNdB	Dark	-0.76	1.3×10^{21}	1.22
	Illuminated	-0.76	1.6×10^{21}	1.11
Anodized iron oxide	Dark	-0.66	6.6×10^{18}	16.6
	Illuminated	-0.66	1.3×10^{19}	11.7
Anodized FeNdB	Dark	-0.82	1.1×10^{22}	0.42
	Illuminated	-0.82	1.6×10^{22}	0.38

Recently, Chou et al discussed the higher limit of charge carrier density in hematite. It was suggested that too high a charge carrier density would increase the charge recombination and limit the photogenerated hole concentration within the hematite photoanode.[56] In this investigation, the observed p-type behavior at higher potential suggest possible accumulation of holes on the surface of the FeNdB photoanode due to slower OER kinetics and increased recombination losses due to the very high majority charge carrier density at the bulk. Even though, alloying of Nd and B ions favorably shifted the flat band potential of the hematite by about 0.2 V in the cathodic direction and decreased the band

gap, the charge transport properties need to be improved for utilization of the FeNdB oxide as an effective photoanode.

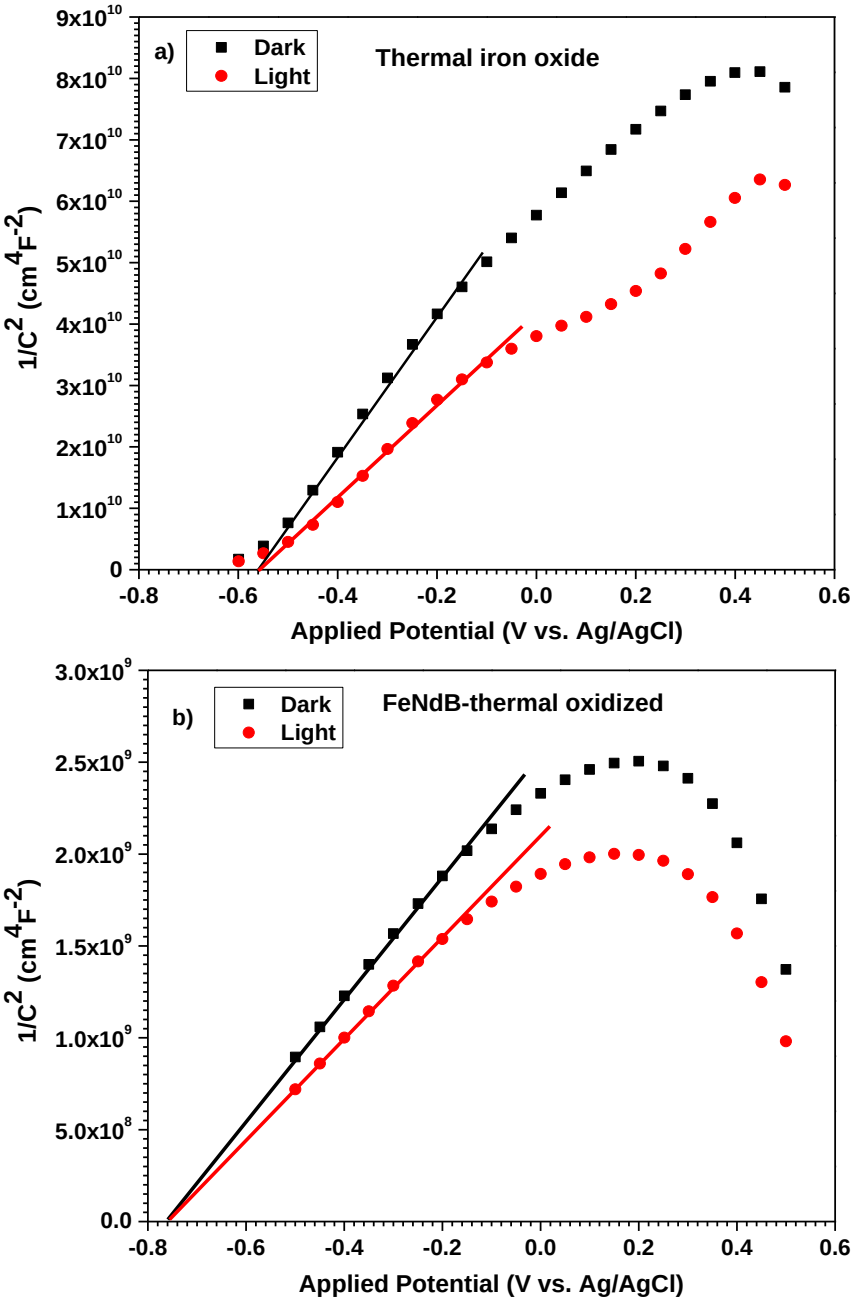

Figure 2.8. Mott-Schottky results of the thermally oxidized samples with and without illumination in 1 M KOH electrolyte: (a) thermal iron oxide; and (b) oxidized FeNdB.

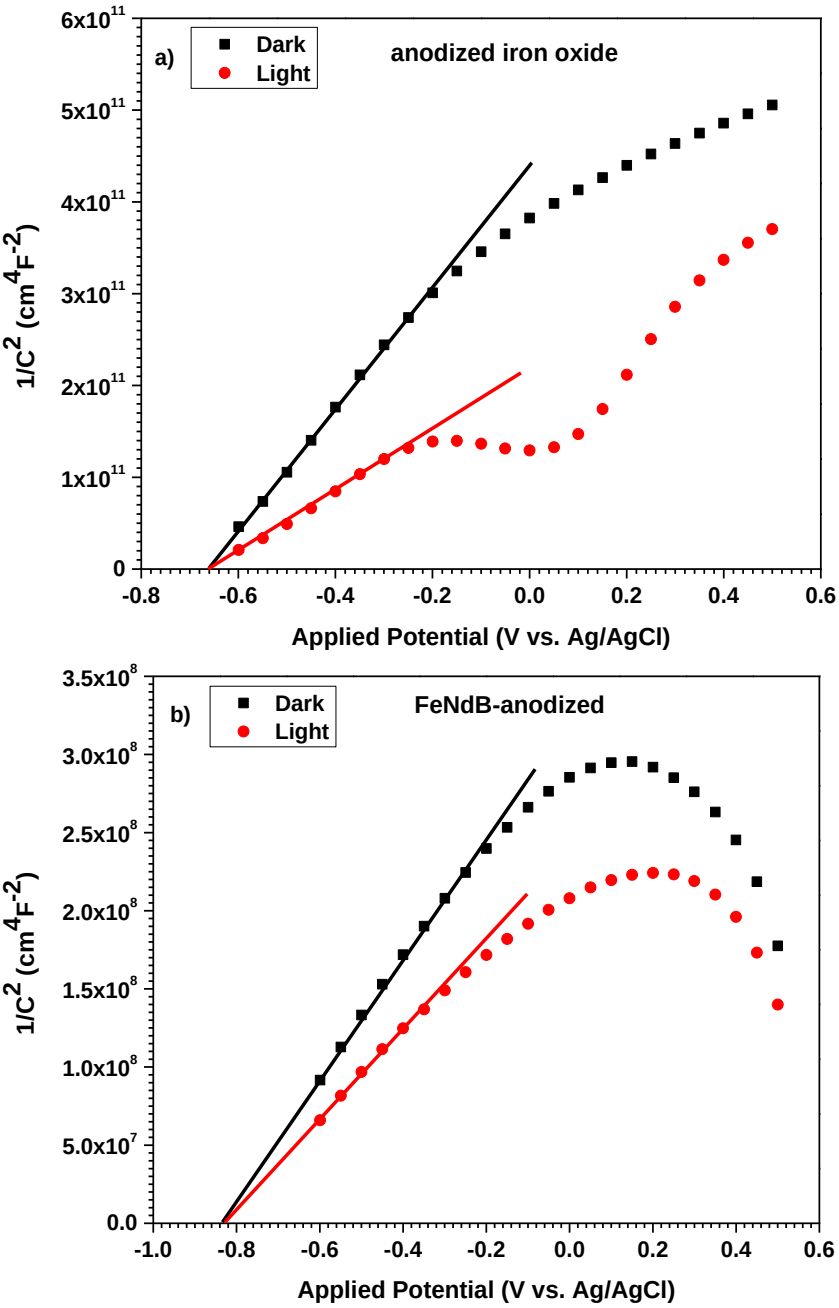

Figure 2.9. Mott-Schottky results of the anodized and annealed samples with and without illumination in 1 M KOH electrolyte: (a) anodic iron oxide; and (b) anodized FeNdB.

2.5. Conclusions

Based on the photoelectrochemical studies carried out on the surface modified $Fe_{14}Nd_2B$ alloy and pure iron foil samples, the following conclusions can be drawn:

1. Nanoporous α-Fe_2O_3 layer incorporated with Nd^{3+} and B^{3+} was obtained by electrochemical anodization of sintered FeNdB permanent magnet.

2. Thermal oxidation of the permanent magnet in air at 450 ^{o}C for two hours resulted in predominantly α-Fe_2O_3 surface layer with a nano-grain morphology.
3. Thermal oxidation of pure iron foil in air at 450 ^{o}C for 2 h resulted in nano-leaf α-Fe_2O_3 surface layer. Based on the charge carrier density determination using Mott-Schottky analysis the iron oxide can be described as Fe_2O_{3-x}, where x = 6.5 x 10^{-4}.
4. The unalloyed anodized Fe2O3 showed a direct bandgap of 2.35 eV and a flatband potential of –0.66 $V_{Ag/AgCl}$ in 1M KOH.
5. Incorporation of Nd^{3+} and B^{3+} in the iron oxide showed a direct bandgap of 2.05 eV and an indirect bandgap of 1.9 eV and shifted the flatband potentials to –0.8 $V_{Ag/AgCl}$ in 1 M KOH solution.
6. The FeNdB oxide showed marginally better catalytic activity for the oxygen evolution reaction than pure iron oxide under dark conditions.
7. The photocurrent densities of the thermally oxidized iron oxide, anodized iron oxide, oxidized FeNdB, and anodized FeNdB were 2.6, 1.1, 1.58, and 0.5 mA/cm^2, respectively at 0.5 $V_{Ag/AgCl}$ in 1 M KOH under 1-sun light simulated illumination.
8. The oxide layers obtained by thermal oxidation showed better photo activity than the anodized oxide layers in the cases of both the pure iron and alloyed iron.
9. The photoactivity of FeNdB oxide was lower than that of iron oxide. The low photocurrent density of the Nd and B alloyed iron oxide could be attributed to very high charge carrier density than that of pure iron oxide that resulted in increased recombination of photogenerated charge carriers.

2.6. References

1. Tartaj, P.; Morales, M. P.; Gonzalez-Carreño, T.; Veintemillas-Verdaguer, S.; Serna, C. J., The Iron Oxides Strike Back: From Biomedical Applications to Energy Storage Devices and Photoelectrochemical Water Splitting. *Advanced Materials* **2011,** *23* (44), 5243-5249.

2. Lin, Y.; Yuan, G.; Sheehan, S.; Zhou, S.; Wang, D., Hematite-based solar water splitting: challenges and opportunities. *Energy & Environmental Science* **2011,** *4* (12), 4862-4869.

3. Li, Z.; Luo, W.; Zhang, M.; Feng, J.; Zou, Z., Photoelectrochemical cells for solar hydrogen production: current state of promising photoelectrodes, methods to improve their properties, and outlook. *Energy & Environmental Science* **2013,** *6* (2), 347-370.

4. Macak, J. M.; Tsuchiya, H.; Ghicov, A.; Yasuda, K.; Hahn, R.; Bauer, S.; Schmuki, P., TiO2 nanotubes: Self-organized electrochemical formation, properties and applications. *Current Opinion in Solid State and Materials Science* **2007,** *11* (1–2), 3-18.

5. Albu, S. P.; Ghicov, A.; Macak, J. M.; Hahn, R.; Schmuki, P., Self-Organized, Free-Standing TiO2 Nanotube Membrane for Flow-through Photocatalytic Applications. *Nano Letters* **2007,** *7* (5), 1286-1289.

6. Chakrapani, V.; Thangala, J.; Sunkara, M. K., WO3 and W2N nanowire arrays for photoelectrochemical hydrogen production. *International Journal of Hydrogen Energy* **2009,** *34* (22), 9050-9059.

7. Sunkara, S.; Vendra, V. K.; Kim, J. H.; Druffel, T.; Sunkara, M. K., Scalable synthesis and photoelectrochemical properties of copper oxide nanowire arrays and films. *Catalysis Today* **2013,** *199* (0), 27-35.

8. Zhao, B.; Kaspar, T. C.; Droubay, T. C.; McCloy, J.; Bowden, M. E.; Shutthanandan, V.; Heald, S. M.; Chambers, S. A., Electrical transport properties of Ti-doped Fe_2O_3(0001) epitaxial films. *Physical Review B* **2011,** *84* (24), 245325.

9. Ling, Y.; Wang, G.; Wheeler, D. A.; Zhang, J. Z.; Li, Y., Sn-Doped Hematite Nanostructures for Photoelectrochemical Water Splitting. *Nano Letters* **2011,** *11* (5), 2119-2125.

10. Liu, J.; Liang, C.; Zhang, H.; Tian, Z.; Zhang, S., General Strategy for Doping Impurities (Ge, Si, Mn, Sn, Ti) in Hematite Nanocrystals. *The Journal of Physical Chemistry C* **2012,** *116* (8), 4986-4992.

11. Wheeler, D. A.; Wang, G.; Ling, Y.; Li, Y.; Zhang, J. Z., Nanostructured hematite: synthesis, characterization, charge carrier dynamics, and photoelectrochemical properties. *Energy & Environmental Science* **2012,** *5* (5), 6682-6702.

12. Boris, D. C.; Harry, B. R.; Uros, C.; Jacek, B. J.; Vivekanand, K.; Todd, D.; Mahendra, K. S., Photoelectrochemical activity of as-grown, α-Fe_2O_3 nanowire array electrodes for water splitting. *Nanotechnology* **2012,** *23* (19), 194009.

13. Macak, J. M.; Tsuchiya, H.; Taveira, L.; Aldabergerova, S.; Schmuki, P., Smooth Anodic TiO2 Nanotubes. *Angewandte Chemie International Edition* **2005,** *44* (45), 7463-7465.

14. Macák, J. M.; Tsuchiya, H.; Ghicov, A.; Schmuki, P., Dye-sensitized anodic TiO2 nanotubes. *Electrochemistry Communications* **2005,** *7* (11), 1133-1137.

15. Macak, J. M.; Zlamal, M.; Krysa, J.; Schmuki, P., Self-Organized TiO2 Nanotube Layers as Highly Efficient Photocatalysts. *Small* **2007,** *3* (2), 300-304.

16. Sahana, M. B.; Sudakar, C.; Setzler, G.; Dixit, A.; Thakur, J. S.; Lawes, G.; Naik, R.; Naik, V. M.; Vaishnava, P. P., Bandgap engineering by tuning particle size and crystallinity of SnO2–Fe2O3 nanocrystalline composite thin films. *Applied Physics Letters* **2008,** *93* (23), 231909.

17. Saremi-Yarahmadi, S.; Wijayantha, K. G. U.; Tahir, A. A.; Vaidhyanathan, B., Nanostructured α-Fe2O3 Electrodes for Solar Driven Water Splitting: Effect of Doping Agents on Preparation and Performance. *The Journal of Physical Chemistry C* **2009,** *113* (12), 4768-4778.

18. Liu, Y.; Yu, Y.-X.; Zhang, W.-D., Photoelectrochemical properties of Ni-doped Fe2O3 thin films prepared by electrodeposition. *Electrochimica Acta* **2012,** *59* (0), 121-127.

19. Munetoshi, S.; Hiroyasu, Y.; Hitoshi, T., Enhanced Photocurrent in Rh-Substituted α-Fe_2O_3 Thin Films Grown by Pulsed Laser Deposition. *Applied Physics Express* **2012,** *5* (11), 115801.

20. Meng, X. Y.; Qin, G. W.; Li, S.; Wen, X. H.; Ren, Y. P.; Pei, W. L.; Zuo, L., Enhanced photoelectrochemical activity for Cu and Ti doped hematite: The first principles calculations. *Applied Physics Letters* **2011,** *98* (11), 112104.

21. Zhang, Y. G.; Wang, Y. X., Calculations show improved photoelectrochemical performance for N, Ce, and Ce + N doped anatase TiO2. *Journal of Applied Physics* **2011,** *110* (3), 033519.

22. Li, W.; Wang, Y.; Lin, H.; Ismat Shah, S.; Huang, C. P.; Doren, D. J.; Rykov, S. A.; Chen, J. G.; Barteau, M. A., Band gap tailoring of Nd3+-doped TiO2 nanoparticles. *Applied Physics Letters* **2003,** *83* (20), 4143-4145.

23. Xu, Y.-H.; Chen, C.; Yang, X.-L.; Li, X.; Wang, B.-F., Preparation, characterization and photocatalytic activity of the neodymium-doped TiO2 nanotubes. *Applied Surface Science* **2009,** *255* (20), 8624-8628.

24. Goyal, G.; Dogra, A.; Rayaprol, S.; Kaushik, S. D.; Siruguri, V.; Kishan, H., Structural and magnetization studies on nanoparticles of Nd doped α-Fe2O3. *Materials Chemistry and Physics* **2012,** *134* (1), 133-138.

25. Yang, X.; Lian, X.; Liu, S.; Tian, J.; Jiang, C.; Wang, G.; Chen, J.; Wang, R., Investigation of Enhanced Photoelectrochemical Property of Cerium Doped Hematite Film Prepared by Sol-Gel Route. *International Journal of Electrochemical Science* **2013,** *8* (3), 3721-3730

26. Zhang, Y.; Das, G. K.; Xu, R.; Yang Tan, T. T., Tb-doped iron oxide: bifunctional fluorescent and magnetic nanocrystals. *Journal of Materials Chemistry* **2009,** *19* (22), 3696-3703.

27. Bloemen, M.; Vandendriessche, S.; Goovaerts, V.; Brullot, W.; Vanbel, M.; Carron, S.; Geukens, N.; Parac-Vogt, T.; Verbiest, T., Synthesis and Characterization of Holmium-Doped Iron Oxide Nanoparticles. *Materials* **2014,** *7* (2), 1155-1164.

28. Liao, P.; Keith, J. A.; Carter, E. A., Water Oxidation on Pure and Doped Hematite (0001) Surfaces: Prediction of Co and Ni as Effective Dopants for Electrocatalysis. *Journal of the American Chemical Society* **2012,** *134* (32), 13296-13309.

29. Valdés, Á.; Kroes, G.-J., First principles study of the photo-oxidation of water on tungsten trioxide (WO3). *The Journal of Chemical Physics* **2009,** *130* (11), 114701.

30. Rossmeisl, J.; Qu, Z. W.; Zhu, H.; Kroes, G. J.; Nørskov, J. K., Electrolysis of water on oxide surfaces. *Journal of Electroanalytical Chemistry* **2007,** *607* (1–2), 83-89.

31. Man, I. C.; Su, H.-Y.; Calle-Vallejo, F.; Hansen, H. A.; Martínez, J. I.; Inoglu, N. G.; Kitchin, J.; Jaramillo, T. F.; Nørskov, J. K.; Rossmeisl, J., Universality in Oxygen Evolution Electrocatalysis on Oxide Surfaces. *ChemCatChem* **2011,** *3* (7), 1159-1165.

32. Suntivich, J.; May, K. J.; Gasteiger, H. A.; Goodenough, J. B.; Shao-Horn, Y., A Perovskite Oxide Optimized for Oxygen Evolution Catalysis from Molecular Orbital Principles. *Science* **2011,** *334* (6061), 1383-1385.

33. Gaudillère, C.; Vernoux, P.; Mirodatos, C.; Caboche, G.; Farrusseng, D., Screening of ceria-based catalysts for internal methane reforming in low temperature SOFC. *Catalysis Today* **2010,** *157* (1–4), 263-269.

34. Cui, Y.-H.; Feng, Y.-J.; Liu, J.; Ren, N., Comparison of various organic compounds destruction on rare earths doped Ti/Sb-SnO2 electrodes. *Journal of Hazardous Materials* **2012,** *239–240* (0), 225-232.

35. Iwamoto, T.; Komorida, Y.; Mito, M.; Takahara, A., Chemical and physical characterizations of spinel ferrite nanoparticles containing Nd and B elements. *Journal of Colloid and Interface Science* **2010,** *345* (2), 143-148.

36. Chitrada, K.; Raja, K. S.; Pesic, B.; Charit, I., Corrosion Behavior of Surface Modified NdFeB Permanent Magnet in Dilute Chloride Environments. *Electrochimica Acta* **2014,** *123* (0), 23-32.

37. Li, Y.; Aindow, M.; Evans, H.; Harris, I. R., Electron microscopy studies of the oxidation of Nd-Fe-B magnets. In *Electron Microscopy and Analysis 1999: Proceedings of the Institute of Physics Electron Microscopy and Analysis Group Conference, University of Sheffield, 24-27 August 1999.* Kiely, C. J., Ed. Taylor & Francis: 1999; pp 483-486.

38. Rangaraju, R. R.; Panday, A.; Raja, K. S.; Misra, M., Nanostructured anodic iron oxide film as photoanode for water oxidation. *Journal of Physics D: Applied Physics* **2009,** *42* (13), 135303.

39. Büchler, M.; Schmuki, P.; Böhni, H.; Stenberg, T.; Mäntylä, T., Comparison of the Semiconductive Properties of Sputter-Deposited Iron Oxides with the Passive Film on Iron. *Journal of The Electrochemical Society* **1998,** *145* (2), 378-385.

40. Ayyub, P.; Multani, M.; Barma, M.; Palkar, V. R.; Vijayaraghavan, R., Size-induced structural phase transitions and hyperfine properties of microcrystalline Fe 2 O 3. *Journal of Physics C: Solid State Physics* **1988,** *21* (11), 2229.

41. Deka, S.; Joy, P. A., Enhancement of the phase transformation temperature of [gamma]-Fe2O3 by Zn2+ doping. *Journal of Materials Chemistry* **2007,** *17* (5), 453-456.

42. Lai, J.; Shafi, K. V. P. M.; Loos, K.; Ulman, A.; Lee, Y.; Vogt, T.; Estournès, C., Doping γ-Fe2O3 Nanoparticles with Mn(III) Suppresses the Transition to the α-Fe2O3 Structure. *Journal of the American Chemical Society* **2003,** *125* (38), 11470-11471.

43. T. I. Bhuiyan; M. Nakanishi; T. Fujii; Takada, J., Structure, morphology, and color tone properties of the Nd substituted hematite. *Memoirs of the Faculty of Engineering, Okayama University* **2007,** *41*, 93-98.

44. Chamritski, I.; Burns, G., Infrared- and Raman-Active Phonons of Magnetite, Maghemite, and Hematite: A Computer Simulation and Spectroscopic Study. *The Journal of Physical Chemistry B* **2005,** *109* (11), 4965-4968.

45. Hanesch, M., Raman spectroscopy of iron oxides and (oxy)hydroxides at low laser power and possible applications in environmental magnetic studies. *Geophysical Journal International* **2009,** *177* (3), 941-948.

46. Umesh, B.; Eraiah, B.; Nagabhushana, H.; Sharma, S. C.; Nagabhushana, B. M.; Shivakumara, C.; Rao, J. L.; Chakradhar, R. P. S., Structural, EPR, optical and Raman studies of Nd2O3:Cu2+ nanophosphors. *Spectrochimica Acta Part A: Molecular and Biomolecular Spectroscopy* **2012,** *94* (0), 365-371.

47. Mashiko, H.; Oshima, T.; Ohtomo, A., Band-gap narrowing in α-(CrxFe1-x)2O3 solid-solution films. *Applied Physics Letters* **2011,** *99* (24), -.

48. Wang, Y.; Doren, D. J., First-principles calculations on TiO2 doped by N, Nd, and vacancy. *Solid State Communications* **2005,** *136* (3), 186-189.

49. Magnan, H.; Stanescu, D.; Rioult, M.; Fonda, E.; Barbier, A., Enhanced photoanode properties of epitaxial Ti doped α-Fe2O3 (0001) thin films. *Applied Physics Letters* **2012,** *101* (13), -.

50. Lin, Y.; Zhou, S.; Sheehan, S. W.; Wang, D., Nanonet-Based Hematite Heteronanostructures for Efficient Solar Water Splitting. *Journal of the American Chemical Society* **2011,** *133* (8), 2398-2401.

51. Vincent, T.; Gross, M.; Dotan, H.; Rothschild, A., Thermally oxidized iron oxide nanoarchitectures for hydrogen production by solar-induced water splitting. *International Journal of Hydrogen Energy* **2012,** *37* (9), 8102-8109.

52. Minchitha, K. U.; Geetha Balakrishna, R., Structural modification and property tailoring in titania for high efficiency in sunlight. *Materials Chemistry and Physics* **2012,** *136* (2–3), 720-728.

53. Liao, P.; Toroker, M. C.; Carter, E. A., Electron Transport in Pure and Doped Hematite. *Nano Letters* **2011,** *11* (4), 1775-1781.

54. Klahr, B.; Gimenez, S.; Fabregat-Santiago, F.; Bisquert, J.; Hamann, T. W., Electrochemical and photoelectrochemical investigation of water oxidation with hematite electrodes. *Energy & Environmental Science* **2012,** *5* (6), 7626-7636.

55. Wielant, J.; Goossens, V.; Hausbrand, R.; Terryn, H., Electronic properties of thermally formed thin iron oxide films. *Electrochimica Acta* **2007,** *52* (27), 7617-7625.

56. Chou, J.-C.; Lin, S.-A.; Lee, C.-Y.; Gan, J.-Y., Effect of bulk doping and surface-trapped states on water splitting with hematite photoanodes. *Journal of Materials Chemistry A* **2013,** *1* (19), 5908-5914.

3. Enhanced Photoelectrochemical Performance of Anodic Nanoporous β-Bi_2O_3[†]

3.1. Abstract

Bismuth oxide has well-dispersed valence bands that show enhanced mobility of charge carriers, high refractive index, and large dielectric constant. These properties are attractive for photo catalysis. Thin films of bismuth oxide containing vertically oriented and uniformly distributed nanopores of controllable dimensions were synthesized by a simple electrochemical anodization of a bismuth metal substrate in citric acid solution at 3 – 60 V. Annealing the anodic nanoporous Bi_2O_3 at 200 °C for 2 h resulted in stabilization of the metastable β-Bi_2O_3 phase at room temperature. The nanoporous anodic oxides showed an energy band gap of 2.48 eV, and n-type semiconductivity. Scanning electron microscopy and electrochemical impedance spectroscopy resulted suggested a dual layered structure of the anodic oxide with a nanoporous outer layer and a planar inner layer. Thickness of the inner layer predominantly influenced the impedance of the anodic oxide. Under simulated 1-sun intensity, a maximum photo current density of 0.97 mA/cm^2 was observed in 1 M KOH at a potential of 1.53 V_{RHE} for the sample anodized at 10 V. A positive shift in the flat band potential upon illumination suggested accumulation of photo generated holes due to low catalytic activity of the anodic bismuth oxide for oxygen evolution reaction. The observed photo current density of the nanoporous anodic oxide of bismuth was an order of magnitude higher than that of the planar anodic oxide, and twice that of thin film β-Bi_2O_3 prepared by reactive sputtering.

3.2. Introduction

Synthesis of ordered arrays of nanoporous and nanotubular oxides of Al, Ti, and other valve metals has been investigated extensively because of their potential applications in solar energy conversion, energy storage, photocatalysts, sensors, and as templates for nanowire growth.[1-8] Enhanced photo catalytic, electrical, and electrochemical properties were reported

[†] This chapter has been published: Kalyan Chitrada, Krishnan S. Raja, Ruchi Gakhar and Dev Chidambaram, Journal of The Electrochemical Society 162 (6), H380-H391 (2015)

for the nanoporous and nanotubular oxides, particularly TiO_2 and Fe_2O_3, when compared to their bulk crystalline counterparts. [9-14] Bismuth is different from regular valve metals such as Al, Ti, Nb etc., because of its semi-metallic nature and high atomic number with the electron configuration [Xe]$4f^{14}5d^{10}6s^26p^3$. The large nucleus charge of bismuth increases the velocity of the 1*s* electrons to such an extent that the relativistic effect becomes significant which increases the mass of 1s electron by 26% and decreases the Bohr radius by 20%. Furthermore, the 6s electrons are less available for bonding. The normally degenerate *p* orbitals are split in to one spherically symmetric $p_{1/2}$ and two doughnut shaped $p_{3/2}$ orbitals because of the high degree of spin-orbit interaction. Since the $p_{3/2}$ orbitals have higher energy than $p_{1/2}$, the $p_{3/2}$ electron is removed during first ionization of Bi resulting in an electron configuration of Bi(I) as $6s^26p^2{}_{1/2}6p^0{}_{3/2}$. The major relativistic effects of bismuth are its lowest tendency to form a hybrid orbital and increasing tendency to form pyramidal structure.[15] The lone electron pairs of Bi(III) $6s^2$ induces intrinsic polarizabilities which facilitate separation of photo generated electron-hole pairs and their transport.[16] Recently, bismuth based ternary oxides such as $BiVO_4$, and $BiFeO_3$ are being actively investigated as promising high efficiency photocatalysts for solar water splitting applications.[17-19] However very few research efforts have been focused on understanding photo electrochemical behavior of the binary bismuth oxide which is the building block for the more advanced complex bismuth based oxides.

Bismuth oxide (Bi_2O_3) exists as six different polymorphs depending on the synthesis route and thermal treatment. These polymorphs are a) α – monoclinic, b) β – tetragonal, c) γ – body centered cubic, d) δ – face centered cubic, e) ε – orthorhombic and f) ω – triclinic. Out of these α and δ phases are stable and others are metastable phases. The monoclinic α-Bi_2O_3 shows a band gap of 2.8 eV with p-type semiconductivity and the tetragonal β-Bi_2O_3 shows a band gap of ~2.5 eV with an n-type semiconductivity.[20] The photo activity of β-Bi_2O_3 was reported to be higher than other polymorphs.[21] The metastable β-Bi_2O_3, that is stable in the temperature range of 650-303^{o}C, could be stabilized at room temperature by doping with cations that introduce excess oxygen sublattices within the tunnel structures of the β-Bi_2O_3.[22, 23] So far, many different nanostructures of β-Bi_2O_3 photocatalysts have been successfully prepared by techniques like magnetron sputtering,[24] sol-gel,[25] spin coating,[26] solution

based,[27, 28] electrochemical anodization,[29-38] electrospinning,[39] vapor deposition,[40] but in contrast, the photoelectrochemical testing of β-Bi_2O_3 has not received much attention.

Yang et al.[25] prepared β-Bi_2O_3 on FTO substrate via sol-gel process. While the films showed photoactivity, the band gap was only reduced to 2.7 eV in the optimal case. The same authors then utilized thin films of Bi (formed on FTO using sputtering) and oxidized it in air at high temperature to obtain Bi_2O_3 films.[24] This preparation resulted in a slightly better band gap 2.63-2.82eV. Kanazirski et al. obtained Bi_2O_3 via anodization in phosphoric acid electrolyte medium at various voltages from 100-160 V.[32] The band gap was found to be 2.8 eV for samples anodized at 100-120 V and 2.6 eV for samples anodized at 120-160 V. In comparison, the present study reports a band gap of 2.48 eV that is characteristic of β-Bi_2O_3. Lv et al,[36] formed Bi_2O_3 films through anodization of bismuth foil at 20V in electrolytes containing glycol and ammonium sulfate. While the study did not report a band gap for the films, it did report that the photocurrent generated was as large as 2.893 and 6.980 μA/cm^2 under 0 and 0.5 V bias voltage, respectively. While, the results from that study cannot be directly compared to the results from the present study, it is pertinent to note that in the present study, potentiostatic tests of different samples at -0.45 and 0.5 V vs Ag/AgCl, resulted in photo current densities of ranging from 0.10 mA/cm^2 to 0.97 mA/cm^2. Thus, the photo current generated from the samples prepared in the present study is about two orders of magnitude higher than that reported by Lv et al.[36]

To our best knowledge, very few studies on photoelectrochemical performances are reported [24, 25, 32, 36] and the maximum photocurrent reported for nanoporous thin film of β-Bi_2O_3, with a thickness of 210 nm deposited by a radio frequency magnetron sputtering system[24] was 0.45mA/cm^2. In this investigation, we report preparation of nanoporous layers of bismuth oxide via electrochemical anodization of bismuth substrate in citrate based electrolyte at different potentials in the range of 3 – 60 V. We will discuss the formation of these anodized nanoporous layers and how the effect of the anodization potential influenced the morphology of the pores, along with the superior photo electrochemical behavior of these materials.

3.3. Experimental Methods

3.3.1. Materials and methods

Circular discs of 3 mm thickness were machined out of a pure bismuth rod (99.99% purity, Alfa Aesar) of 12.7 mm diameter and were metallographically polished before electrochemical anodization. The polished bismuth samples were encapsulated in a sample holder exposing only 1 cm^2 of the active surface area and a platinum electrode was used as counter electrode. The anodization was carried out at room temperature in 0.3 M citric acid (Macron Fine Chemicals™) at potentials ranging from 3 – 60 V for 30mins and the distance between cathode and anode was about 1 cm. After anodization the samples were thoroughly rinsed with DI water, air dried and were subjected to thermal annealing for 2 h at 200 °C.

3.3.2. Characterization

The samples were characterized for surface morphology using scanning electron microscopy (LEO SUPRA 35VP & FEI Quanta 200F). Grazing angle XRD studies were carried out using a Bruker-AXS D8-Discover diffractometer equipped with parallel incident beam (Göbel mirror), vertical θ-θ goniometer, XYZ motorized stage and with a GADDS (General Area Diffraction System). X-ray photoelectron spectroscopy (PHI Quantum 2000) was employed to evaluate the surface valence states and electron density of states at the surface of the samples. Mono-chromated Al-Kα (1488.6 eV) radiation was used as the source with an acceptance angle of ±23° and take-off angle of 45°. Charge correction was carried out by considering the C 1s peak at 284.8 eV. Thermo Scientific DXR Raman microscope was used to characterize the Raman active components present in the surface films. The DXR system was fitted with a 532 nm laser of 5 mW power. Data was collected from a spot diameter of 0.7µm utilizing 32 exposures at an exposure time of 5 seconds. Absorbance spectra were recorded using a Shimadzu UV-2401PC spectrometer equipped with tungsten lamp. The scans were recorded over a range of 250-900 nm. Barium sulfate was used as standard reference. The step size and slit width used were 1 nm and 5 nm, respectively.

3.3.3. Photoelectrochemical studies

Photo electrochemical studies were carried out using a three-electrode configuration with a 7.5 cm^2 platinum flag counter electrode, and a home-made AgCl coated silver wire immersed in saturated KCl + AgCl solution contained in a Luggin probe that acted as a reference electrode (calibrated as 199 mV vs. standard hydrogen electrode). A home-made polyether ether ketone (PEEK) sample holder was used to electrically connect the sample with a potentiostat (Gamry Instruments, model: Reference 600) by exposing 1 cm^2 of the active surface. The samples were illuminated using a solar simulator (SOLAR Light, Glenside, PA, USA, Model: 16S-300) with a 300 W xenon lamp, and an air mass global 1.5 filter that gave 1-sun intensity (100 mW/cm^2) at appropriate settings. The samples were polarized at 0.5 V in 1 M KOH solution for constructing the Tauc plots. Band pass filters (Edmund Optics) in the range of 400-700 nm at 50 nm intervals were used to obtain the action spectra. Potentiodynamic, potentiostatic, electrochemical impedance spectroscopy (EIS), and Mott-Schottky analysis studies were carried out with and without illuminated conditions. Potentiostatic measurements were carried out in 1 M KOH solution at 0.2 V and 0.5 $V_{Ag/AgCl}$. Potential Vs current plots were constructed by scanning the potential of the sample from the open circuit potential to 0.5 V at a scan rate of 2.5 mV/s in 1 M KOH solution. EIS measurements were carried out under potentiostatic condition of 0.5 $V_{Ag/AgCl}$ by super imposing a *ac* signal of 10 mV and scanning the frequency from 0.1 MHz down to 0.1 Hz. Mott-Schottky type measurements were carried out at a frequency (*f*) of 1000 Hz by scanning the potential of the sample from 0.2 V to -0.6 V at 50 mV steps for every two seconds. All potentials were applied with reference to an Ag/AgCl reference electrode.

3.4. Results and Discussion

3.4.1. Potentiodynamic polarization

Figure 3.1 shows the anodic polarization of bismuth in 0.3 M citric acid solution with and without illumination of simulated solar light. The open circuit potential of the bismuth was about 52 mV more negative under illumination which could be attributed to the accumulation of electrons on the surface due to the photoelectric extraction of electrons from the Fermi level of the metal by the light.[41] Increase in the anodic polarization increased

the current density until a critical current density was reached, which was about 12 µA/cm^2 (at 0.126 V) without illumination, and 966 µA/cm^2 (at 0.312 V) with illumination. At potentials more positive than 0.22 V, the sample showed passivation under the dark condition.

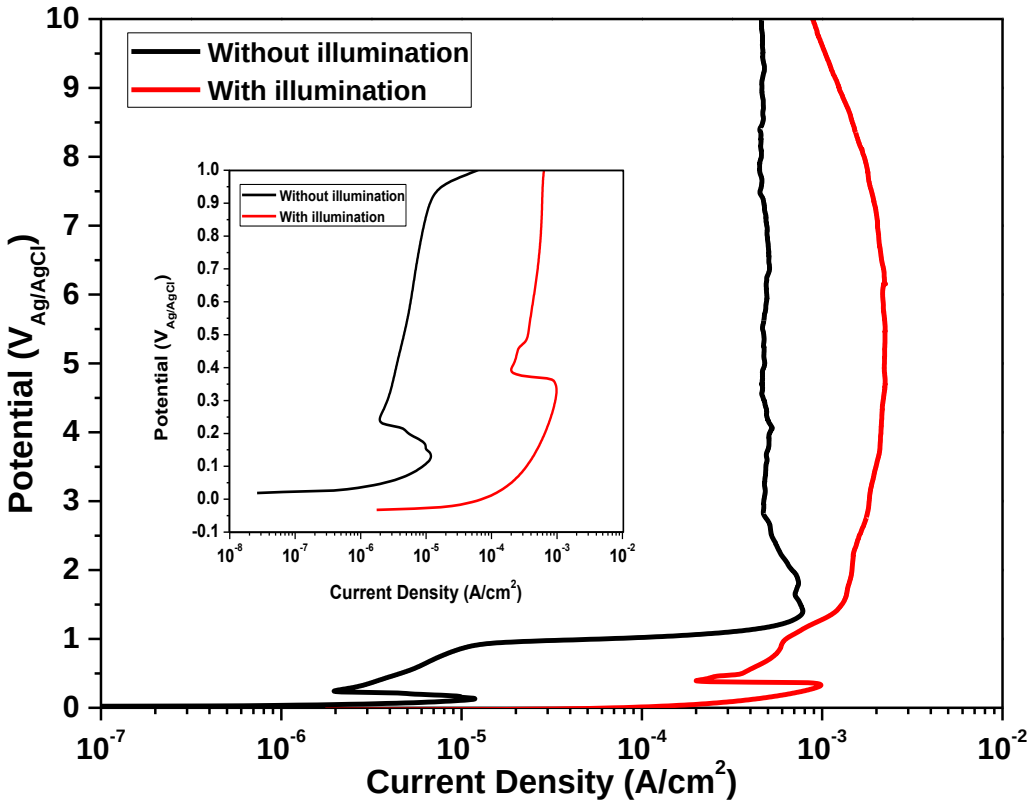

Figure 3.1. Anodic polarization of bismuth in 0.3 M citric acid solution with and without illumination of simulated solar light. The inset shows the polarization at lower potentials

The illuminated sample attained 'passivity' or field assisted growth of a surface layer at a constant current density only above 0.375 V. The large current densities recorded for the illuminated samples could be interpreted in two ways, viz, 1) illumination caused formation of a highly defective surface layer on the bismuth which made the passivation difficult which required higher potential and larger current density to grow a surface layer on the illuminated sample; or 2) a surface layer that was photo active was formed at the early stages of passivation and the increased anodic current density could be attributed to the photo generated electron-hole pairs. If the pseudo constant current density regions below 1 V were considered the passive regions, then the passive current density was in the range of 2.5-9.5 µA/cm^2 for the sample without illumination. When illuminated the passive current density

increased to 500-630 μA/cm^2. The anodic current density of non-illuminated sample increased sharply after reaching 1.16 V which could be attributed to the oxygen evolution reaction (OER) in the 0.3 M citric acid solution (pH: ~2). The OER was observed to initiate at about 0.95 V in case of the illuminated samples. The current density remained as constant at potentials higher than 1.3 V for the non-illuminated condition. The constant current densities implied field assisted growth of anodic oxide or surface layers on the samples. The illuminated sample showed a current density of about 2.2 mA/cm^2 and the sample without illumination exhibited 0.5 mA/cm^2. The difference in the current densities became smaller as the potential increased above 7 V. The composition of anodic oxide film is discussed later.

3.4.2. Potentiostatic anodization

Transients of anodization current densities recorded at different anodization potentials during potentiostatic anodization are shown in Figure 3.2. All the anodization experiments were carried out without illuminating the samples. The anodization current could be expressed as a function of anodization time as:

$$i_a = i_o t^n \qquad [3.1]$$

Where, i_a = anodization current, i_0 = instantaneous (initial) current at the time of application of a constant potential, t = time, and n = current transient exponent (slope of log t vs. log i).

Since the anodization current decayed with time because of the thickening of the oxide layer, the value of '*n*' would have negative values. It was observed that the rate of current decay in log-log scale was not constant throughout the anodization process. Three different stages of anodization could be delineated based on the variations of the slopes. The stage 1 occurred within one second of anodization. The current decay was slower at the stage 1 of the anodization, where the *n* value was in the range of -0.1 to -0.14 for the anodization potentials 3 – 10 V, as summarized in Table 3.1. Similar '*n*' values were reported for the stage-1 of the anodization of titanium in fluoride containing ethylene glycol solution.[42] The values of the '*n*' increased in the negative direction (implying steeper decay kinetics) as the anodization potential increased. It was observed that higher the anodization potential, larger

was the initial anodization current. For example, the current density recorded at 0.1 s after applying 60 V was an order of magnitude higher than that of 3 V. The anodization current was the result of ionization of bismuth as given in the reaction [3.2][43]:

$$Bi + 3H_2O \rightarrow Bi_2O_3 + 6H^+ + 6e^- \qquad [3.2]$$

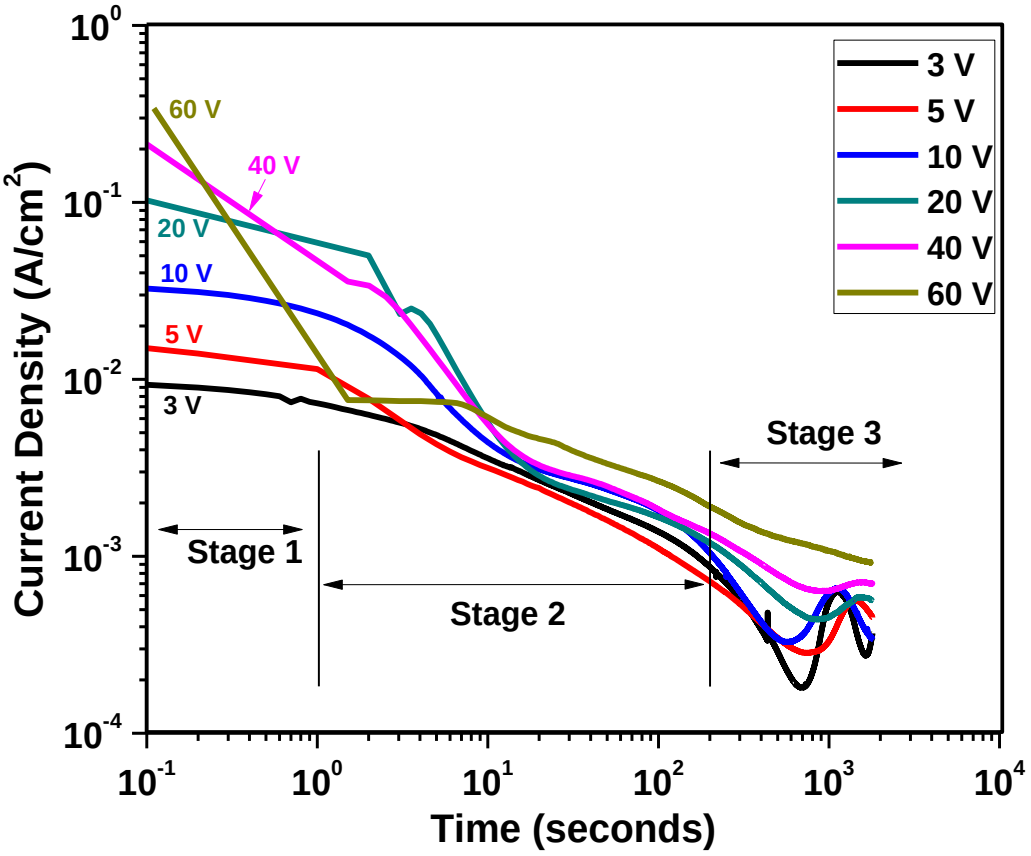

Figure 3.2. Transients of anodization current densities recorded at different anodization potentials during potentiostatic anodization

Formation of a thicker Bi_2O_3 film could be visualized when the current density was high. The pure bismuth sesquioxide film was the barrier type inner layer. Figure 3.3(a) shows the morphology of the oxide layer formed on the bismuth after 3 s of anodization at 60 V. When the anodization continued, accumulation H^+ ions near the oxide surface from the reaction [3.2] possibly initiated chemical dissolution of the oxide as given in the reaction [3.3]:

$$Bi_2O_3 + 6H^+ \rightarrow 2Bi^{3+}(aq) + 3H_2O \qquad [3.3]$$

If no other species were present in the electrolyte, the reactions [3.2] and [3.3] would continue during the anodization process until a steady state was reached that would result in a constant thickness of anodic oxide. In such case, the anodization current may not decay after reaching a steady state. In this investigation, citrate ions were present in the electrolyte which modified the passivation kinetics. A complex formation reaction could be proposed between the citrate and Bi^{3+} as given in [4]

$$Bi^{3+} + C_6H_5O_7^{3-} \rightarrow Bi(C_6H_5O_7) \qquad [3.4]$$

Table 3.1. Summary of the current transient exponents at different stages of the anodization

Anodization potential (V)	**Current transient exponent, *n***		
	Stage 1	**Stage 2 (a)**	**Stage 2 (b)**
3	-0.11	-0.22	-0.41
5	-0.12	-0.65	-0.45
10	-0.14	-0.90	-0.32
20	-0.24	-1.62	-0.31
40	-0.66	-1.23	-0.33
60	-1.45	---	-0.34

Evidence of formation of bismuth citrate layer will be discussed in the later based on the results of the XPS analysis. Presence of the citrate layer on top of the Bi_2O_3 layer resulted in a large potential drop across the surface layer, and in effect the potential drop across the film/electrolyte, which was driving the dissolution reaction, became smaller. Therefore, thickening of the inner layer continued. The rate of growth of the inner oxide layer was controlled by the high field conduction mechanism as discussed by Bojinov et al.[32] The formation of citrate layer, decreased dissolution of Bi_2O_3, and thickening of the inner layer resulted in the steeper anodic current decay as observed in the stage 2. Two different slopes were observed in the stage 2, referred to as stage 2(a) and (b). The stage 2 (a) corresponded to the anodization period up to 20 seconds, and the stage 2 (b) started afterwards. The slopes of stage 2 (a) were much steeper than those of stage 2 (b). The slopes observed in the stage 2 (b) were almost similar and independent of the anodization potential. This observation

indicated that the oxide growth mechanism in stage 2 (b) was similar for all the anodization potentials and possibly a constant electric field was maintained for the conduction of ions during this stage. Figure 3.3(b) shows the morphology of the surface layer after 30 s of anodization at 60 V. The surface layer consisted of several nanopores. It is interesting to note that in spite of presence of nanopores, the current continued to decay. Later it will be shown that these nanopores are, in fact, partial coverage of a secondary layer that grew on top of the inner barrier layer. During the stage 3 of the anodization that occurred about 200 seconds of application of potential, a fluctuation in the current density was observed in all the samples. The current decay stopped and an increase in the current was observed. This type of 'current decay and current raise' behavior was reported for anodization of titanium and iron that resulted in the nanotubular or nanoporous structures.[44, 45] Figure 3.3(c) shows the morphology of the anodized surface after 300 s at 60 V. Large size and high density of pores were observed after 300 s of anodization when compared to the morphology after 30 s (Figure 3.3(b)). When the anodization was continued for 600 s, the dissolution of the top layer was evident that exposed the underlying nanoporous oxide layer as seen in Figure 3.3(d). Figure 3.3(e) shows the surface morphology observed in some patches of the anodized surface that clearly revealed the nanoporous layer present underneath a top re-precipitated layer.

The fluctuations in the anodization current during the stage-3 signified the instability of the thin anodic oxide formed on the bismuth surface under the electric field. Self-assembled nanostructured patterns have been observed on the interface between two dielectric media when exposed to an electrostatic field.[46] The inner anodic oxide layer, top precipitated layer (presumably consisting of bismuth citrate), and the electrolytes are dielectrics, and the nanoporous structure observed on the inner oxide layer could be the result of the instability of the interface induced by the electric field of the anodization potential. The elastic, viscous, and capillary forces counteract the electrical forces that destabilize the interface.[47] Higher the elastic modulus and surface energy of the dielectric film, larger is the required electric field to induce instability. In case of the nanoporous anodic oxides, the electric field alone could not be accounted for the observed nanoporous structure

because specificity of the electrolyte played a critical role. Therefore, field assisted processes of oxide dissolution specific to the electrolyte, and migration of ions were attributed to the formation of nanoporous anodic oxides.[48, 49] Hebert et al related the morphological instability that resulted in the porous anodic oxide to the oxide formation efficiency.[50] These authors carried out a linear stability analysis of the thin film oxide by considering oxide dissolution and ion migration processes as controlling steps. In addition to field assisted ion transport, plastic flow of oxide during anodization was also attributed to the ionic flow that promoted nanoporous oxide structure.[51, 52] The nanoporous anodic oxide of valve metals such as Al and Ti consisted of a scalloped base and pore walls that consisted of a duplex layer of metal oxide outer wall and electrolyte ions (such as phosphate, fluoride etc.) incorporated oxyhydroxide inner wall [53, 54]. The diameter of the nanopores of the anodic oxide of Al and Ti was a strong function of anodization potential, which increased with the increase in the potential.[55] The cross sectional morphology of the bismuth anodic oxide prepared in citric acid solution was different from that of conventional valve metal anodic oxides and the size of the nanopores was not influenced by the anodization potential.

3.4.3. Material characterization

The morphologies of the nanoporous oxide layer prepared at different anodization potential in the range of 3 – 60 V are shown in figures 3.4(a) – (f). It is observed that the diameter of the nanopores was in the range of 30 - 70 nm for all the anodization potentials. The pore size distribution of the nanoporous oxide of the samples anodized at 60 V for 30 minutes is given in Figure B1 (Appendix B). It was observed that 80% of the pores were having diameter in the range of 50 - 60 nm. Similar type of a tight pore size distribution was noted for other anodization conditions as well. Even though the pore diameter did not vary significantly with the anodization potential, the pore wall thickness was found to increase with the increase in the anodization potential. Since the nanopores were not completely ordered, it was difficult to exactly quantify the increase in the wall thickness. The anodization potential lower than 20 V typically revealed wall thicknesses in the range of 10 – 25 nm; whereas anodization at 60 V exhibited wall thickness in the range of 30-60 nm. In other

words, the number of nanopores per unit area decreased with increase in the anodization potential in the citric acid solution.

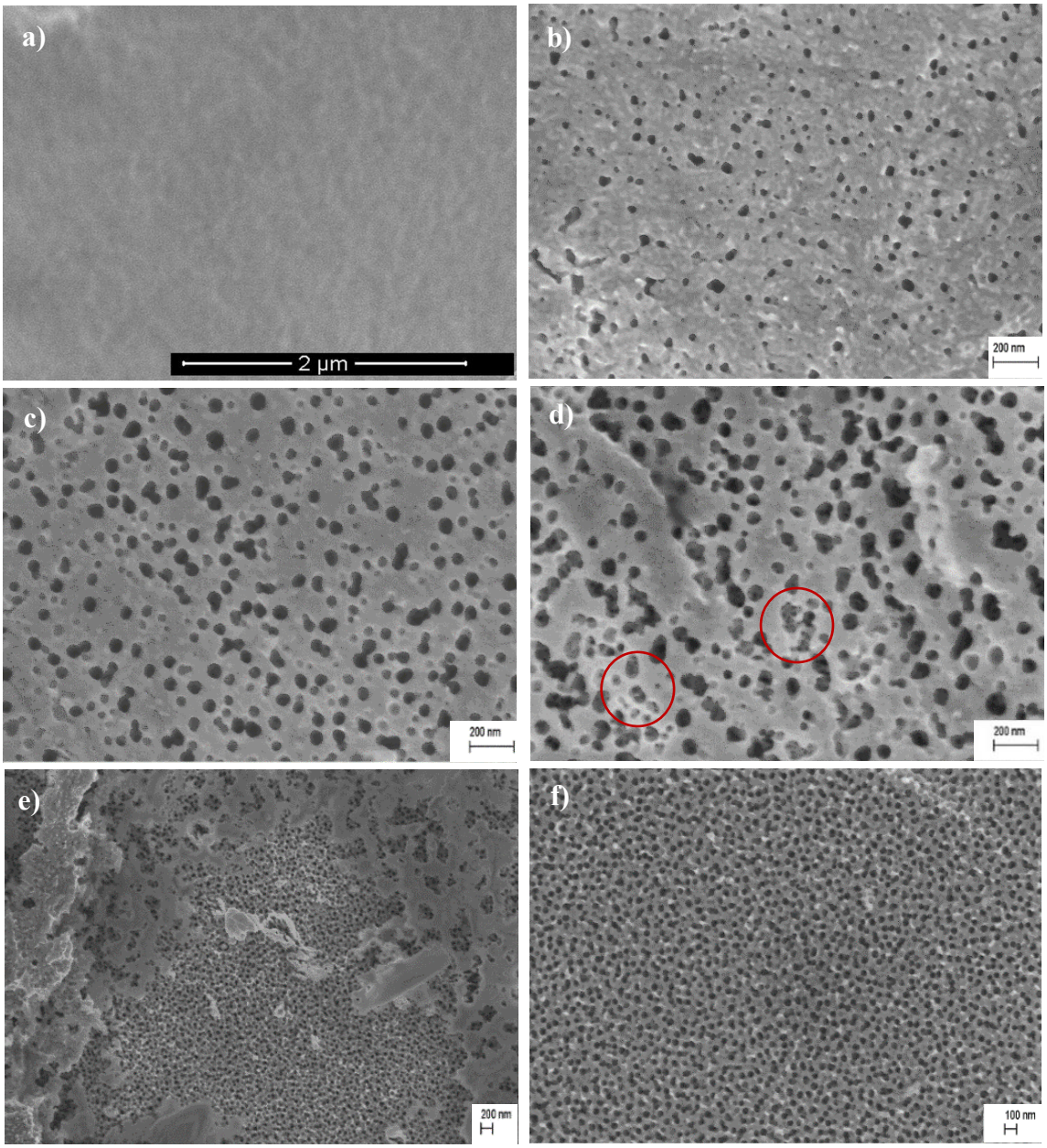

Figure 3.3. FESEM images of the nanoporous morphology of the bismuth oxide synthesized by anodization of bismuth at 60 V for a) 3s, b) 30s, c) 300s, d) 600s, e) & f) 1800s

Figure B2 (Appendix B) shows the cross sectional images of the oxides anodized at various anodization potentials. A dual layered structure of the anodic oxide is clearly seen. The bottom layer (inner layer) did not reveal any porosity. This layer was considered

impervious barrier type layer. On top of this layer a porous structure was observed. It should be noted that the inner barrier type layer was considerably thicker than the similar layers reported for the conventional valve metals. Table 3.2 summarizes the thicknesses of the oxides prepared at different anodization potentials. The reported thickness values were average measurements of two or three samples on multiple locations. The tabulated values exhibited a general trend even though the variation in the thicknesses between two samples of the same anodization conditions was as high as 20%. The total thickness of the anodic oxide and the thickness of the nanoporous component increased with the increase in the anodization potential. The thickness of the barrier type layer also increased with the increase in the anodization potential. The ratio of inner oxide thickness to total oxide thickness increased at higher anodization potentials (>20 V). The higher fraction of the inner oxide layer could possibly be a result of the increased dissolution of the outer nanoporous oxide layer at high anodization potentials. This phenomenon could be explained based on the high concentration of cation vacancies generated at the oxide/electrolyte interface by oxide dissolution. These vacancies were transported by electric field to the metal/oxide interface and are made available for the metal cation to occupy and grow as the inner oxide layer.[56] The thickness of the inner oxide layer played a major role in determining the photo activities as shown in a later section.

Based on the current transients measured during the anodization, and electron microscopic images the mechanism of the formation of nanoporous anodic bismuth oxide could be outlined as followed: The nanoporous anodic oxide formation was observed to be electrolyte specific. For example, anodization in NaOH solution or fluoride containing electrolytes did not result in the nanoporous oxide. Addition of glycerol to the citric acid solution was observed to improve the nanoporous morphology. It was considered that addition of glycerol would decrease the surface tension of the electrolyte and also modify the surface energy of the oxide by adsorption of the carbonaceous species. These observations indicated that surface energy of the anodic layer played a significant role on the nanopore formation.

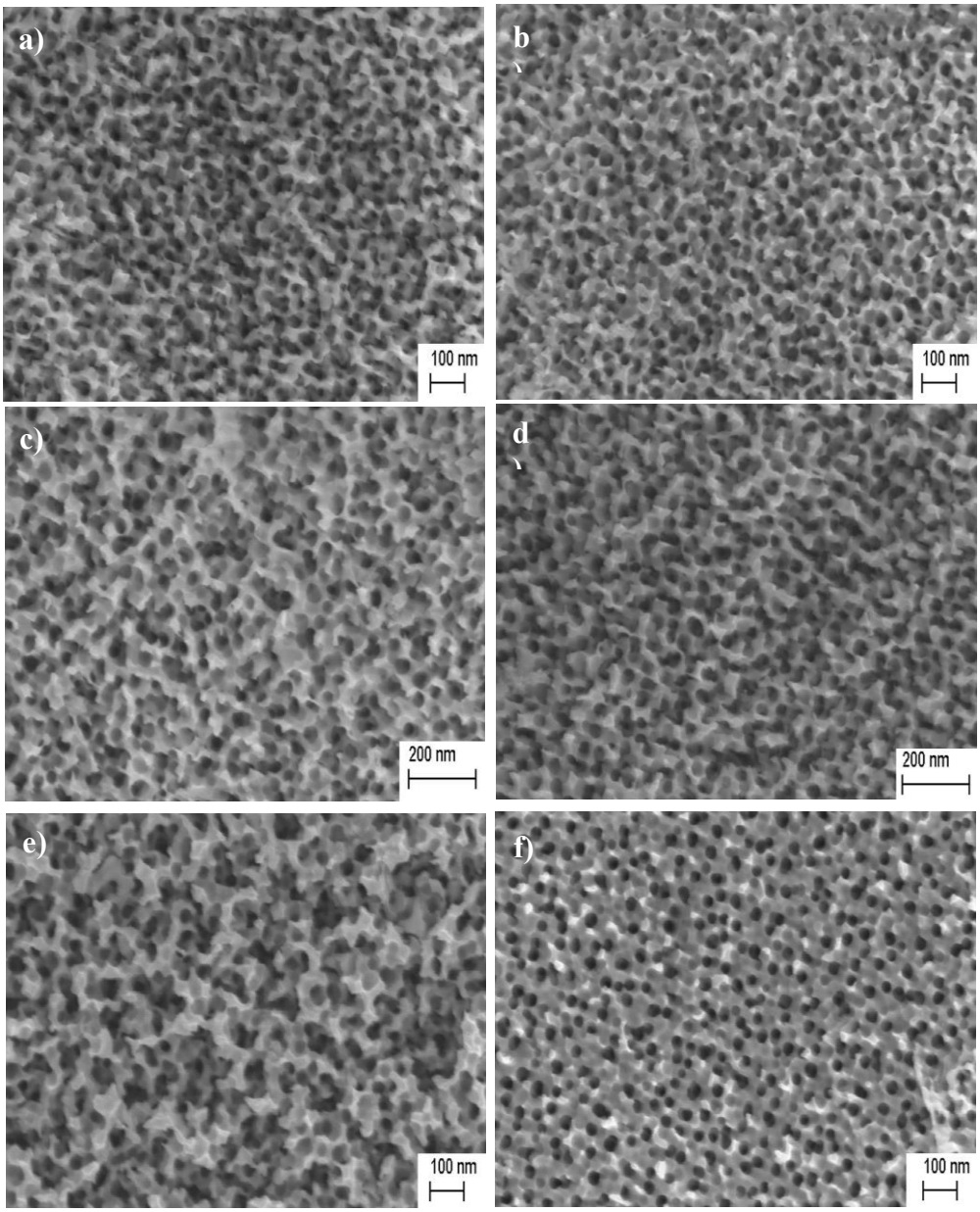

Figure 3.4 FESEM images of the bismuth oxide nanoporous oxide layer prepared at various anodization potentials, a) 3 V, b) 5 V, c) 10 V, d) 20 V, e) 40 V and f) 60 V for 30mins

The nanoporous pattern formation during anodization of bismuth in citric acid could be explained by an external field-induced interfacial instability of the oxide layer. In this case, the external fields causing the instability were the applied electric field, the stress field causing plastic flow, and the concentration field causing ionic flow. The stabilizing force acting against the external fields was considered to be the interfacial energy. Here no attempt is being made to develop a quantitative model to describe the nanoporous oxide formation.

However, the possible contributions of these forces while forming the nanopores are qualitatively described. The solubility of oxygen in bismuth at 1273 K is less than 2.4 at%.[57] The oxygen solubility of bismuth at room temperature will be much smaller than the reported value of the superheated liquid metal. On the other hand valve metals such Ti and Zr show considerably high oxygen solubility at room temperature (34 at%[58] and 28.6 at%, respectively). During the anodization of Ti or Zr, the metal substrate just underneath the oxide layer can accommodate a significant amount of oxygen as solid solution without forming oxide. The incorporation of oxygen in the metal limits the thickness of the barrier type oxide layer which has been reported by several investigators. [9, 13] Furthermore, the metal beneath the oxide layer is strengthened by the incorporation of oxygen as solid solution and therefore, the plastic deformation by growth stresses is small. Whereas, in bismuth these phenomena are absent due to its very limited solid solubility to oxygen. The thicker barrier type layer observed in the anodized bismuth as seen in Figure B2 (Appendix B) could be attributed to the lower solubility of oxygen in the pure metal that made all oxygen available for oxide formation. Since the metal substrate was not solid solution strengthened by the oxygen, it was subjected to significant plastic deformation by the stress field. It is well documented that bismuth oxides (δ-Bi_2O_3, in particular) show very high diffusivities for oxygen.[59] It could be argued that enhanced mass flow (in terms of plastic deformation, and ionic transport) accompanied by the reduction in the interfacial energy (because of the specific species in the electrolyte) helped enhance the instability of the interface under the electric field that resulted in the nanoporous pattern of the anodic oxide.

Table 3.2. Average thicknesses of anodic oxides prepared at different potentials for 30 minutes of anodization

Anodization potential, V	Total thickness of oxide, nm	Nanoporous layer thickness, nm
3	310	240
5	430	350
10	770	680
20	890	720
40	1150	850
60	1420	960

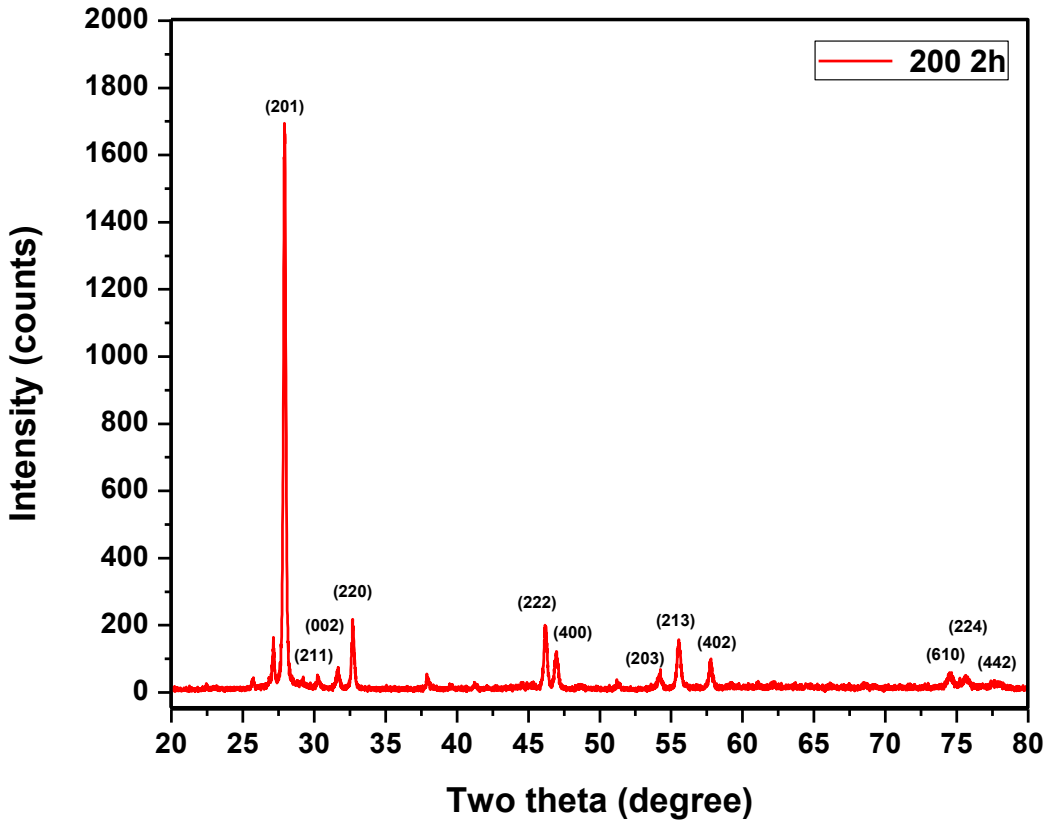

Figure 3.5. X-ray diffraction pattern of the nanoporous bismuth oxide synthesized by anodization of bismuth at 10 V for 30 minutes and annealed at 200 ^{o}C for 2h

The anodic oxide was predominantly amorphous in the as-anodized condition. Annealing the samples at 200 °C resulted in the crystalline structure. During annealing in ambient air, the inner layer (amorphous Bi_2O_3) was converted into β-Bi_2O_3, and the outer nanoporous layer that presumably consisted of a mixture of Bi_2O_3 + $Bi(C_6H_5O_7)$ was also converted to β-Bi_2O_3 as observed from the XRD analyses. Figure 3.5 shows the XRD pattern of the samples anodized at 10 V and annealed at 200 °C for 2 h. All the samples showed a predominantly β-Bi_2O_3 structure. The following reactions are considered for the conversion of bismuth citrate in to bismuth carbonate oxide and bismuth oxide. During annealing at 200 °C in air:

$$2[Bi(C_6H_5O_7 + 9O_2 \rightarrow Bi_2(CO_3)O_2 + 11CO_2 + 5H_2O \qquad [3.5]$$

Annealing at 200 ^{o}C for 2 h resulted in decomposition of bismuth carbonate oxide phase and formation of predominantly the β-Bi_2O_3 phase, given by the reaction:

$$Bi_2(CO_3)O_2 \rightarrow Bi_2O_3 + CO_2 \qquad [3.6]$$

As discussed in the introduction, it is documented that calcination of bismuth carbonate oxide precursor stabilizes the tetragonal β-Bi_2O_3 at room temperature[60].

Bi-*4f* spectra obtained from the as-anodized and annealed anodic bismuth oxide are provided in Figures 3.6 (a) and (b), respectively. The spectrum obtained from the as-anodized sample was observed to be wider than the spectrum obtained from the annealed sample. Peak-fitting of the Bi-*4f* spectra of the as-anodized sample showed the presence of two components, at 157.7 and 163.0 eV, corresponding to bismuth carbonate (labeled as B and E)[61] and at 158.6 and 163.9 eV, corresponding to bismuth oxide (labeled as C and F)[62]. The binding energy of Bi-$4f_{7/2}$ at 158.6 eV is associated with the tetragonal polymorph of the bismuth oxide.[27] Figures 3.6 (c) and (d) show the O-*1s* spectra of the as-anodized and annealed anodic bismuth oxide, respectively. The shoulders of the O-1s spectra could be attributed to the Bi-O in $(BiO)_2CO_3$ (labeled as A), O^{2-} (labeled as B)and adsorbed water (labeled as C) on the surface.[63] The predominant shoulders present on the O-*1s* spectra also indicated the possibility of significant concentration of oxygen vacancies present in the anodic oxides.[64]

The Raman spectra of the anodic nanoporous Bi_2O_3 annealed at 200 ^oC for 2 h before and after the photo electrochemical (PEC) testing are shown in Figure 3.7. The spectrum consisted of three major Raman features at ~457, 312, 122, 91 and 70 cm^{-1}. Hardcastle et al[65] reported the Raman frequencies of the displacements of oxygen atoms with respect to the bismuth atom that resulted in stretching of Bi-O bonds in the BiO_6 octahedra to be 462, 311, and 124 cm^{-1}. The Raman features associated with α-Bi_2O_3 are reported to be 212, 278, 335, 410, 445 and 538 cm^{-1}. Based on the reported Raman frequencies, the Raman spectrum of Figure 3.7 could be associated with the β-Bi_2O_3 phase. The Raman bands observed at lower frequencies such as 90 and 70 cm^{-1} could be assigned to the E_g and A_{1g} vibration modes of Bi respectively.[40]

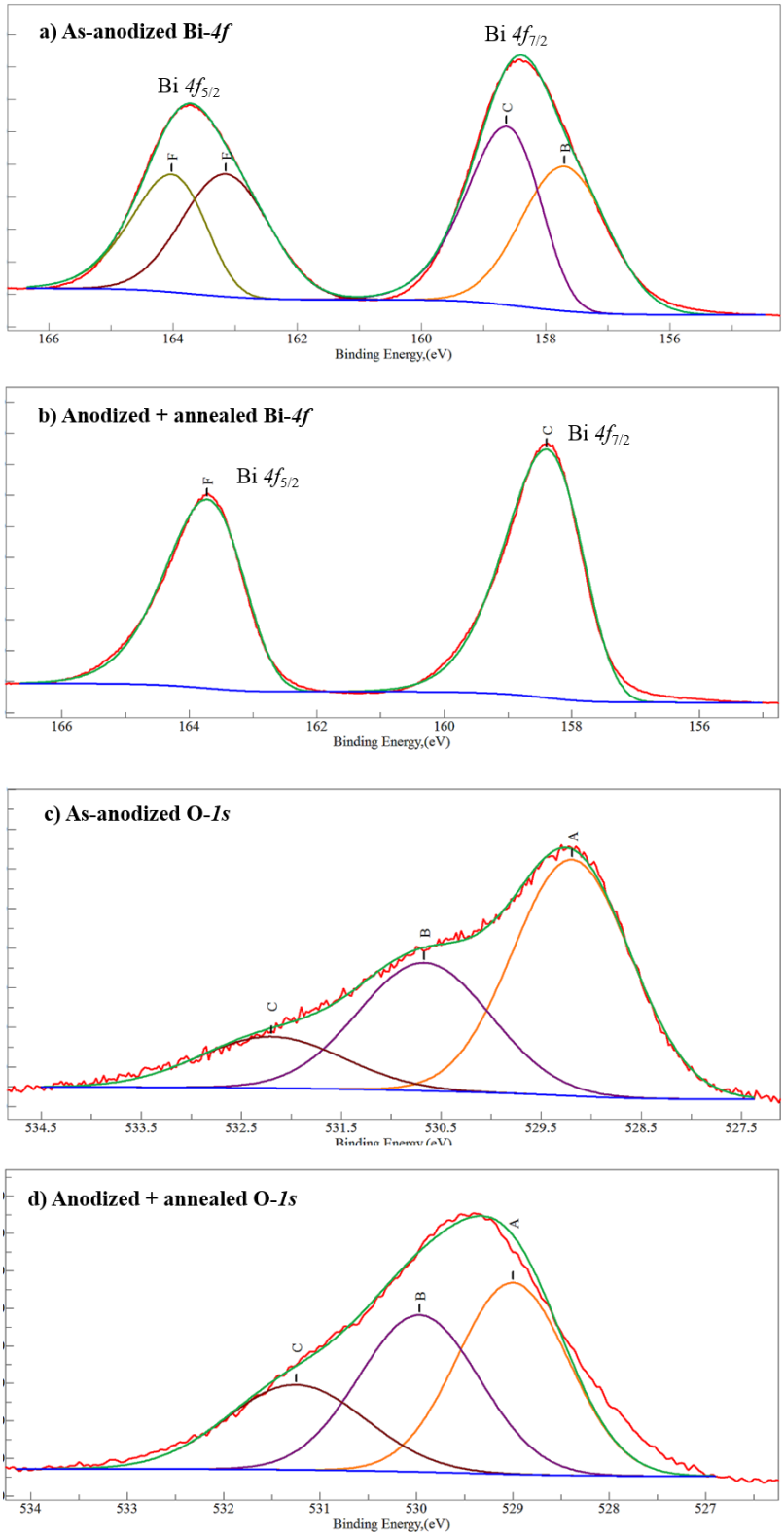

Figure 3.6. XPS spectra of (a) as anodized bismuth oxide surface- Bi 4f; (b) anodized and annealed bismuth oxide surface- Bi 4f. where B and E: bismuth carbonate, C and F: bismuth oxide, (c) as anodized bismuth oxide surface- O 1s ; and (d) anodized and annealed bismuth oxide surface- O 1s. Where A: carbonate, B: Oxide, C; Water

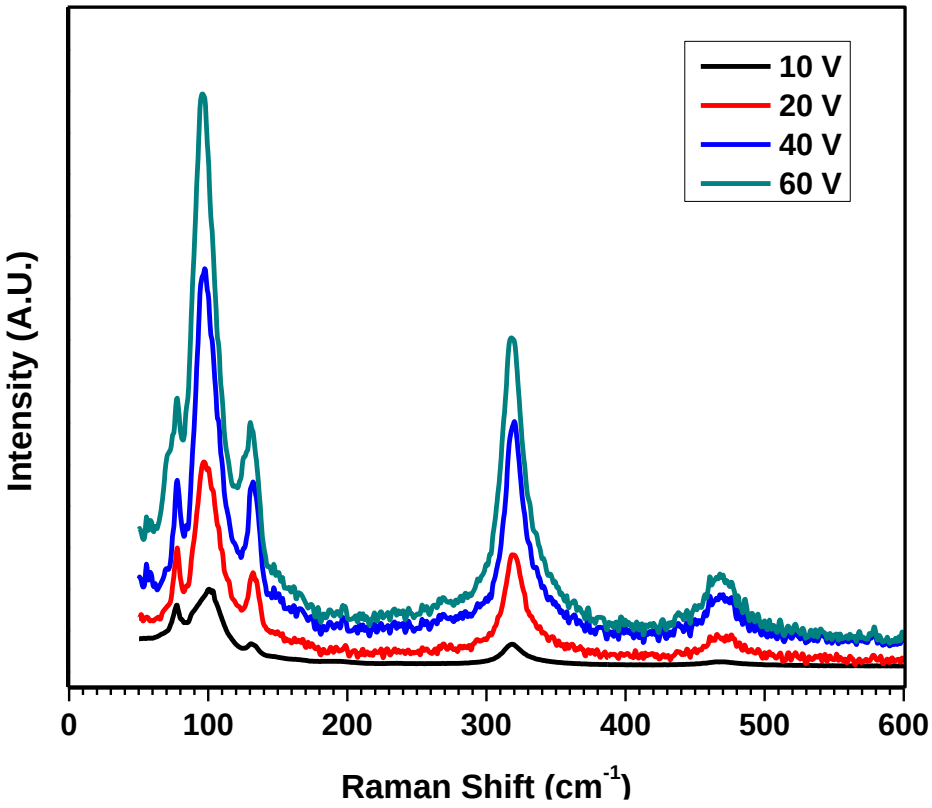

Figure 3.7. Raman spectra of the bismuth oxide nanoporous oxide layer prepared at anodization potentials, 10-60 V for 30 mins and annealed at 200 ^{o}C for 2h

Figure 3.8 (a) shows the UV-VIS diffuse reflectance spectroscopic results of the nanoporous Bi_2O_3 annealed at 200 ^{o}C for 2 h. A sharp absorbance shoulder was observed to take off at a wave length of 500 nm corresponding to an energy level of 2.48 eV. This energy level is associated with the band gap of β-Bi_2O_3. There were additional absorbance shoulders observed at energy levels of 2.7 eV and 2.95 eV. The absorbance at energy levels of 2.2 – 3.1 eV is usually attributed to the Bi^{3+} intra-ionic electronic transitions and charge transfer transitions between oxygen ligands and Bi^{3+} ions.[66] The minor absorbance shoulder observed at 2.7 eV could be attributed to the possible presence of sub carbonate phase in the sample. The optical absorption coefficient of Bi_2S_3 has been reported to be around 2 x 10^5 cm^{-1} in the wavelength of 400-700 nm.[67] Similarly, the optical absorption coefficient of Bi_2O_3 has been reported to be in the range of 2 x 10^4 – 1 x 10^5 cm^{-1} in the wavelengths range of 600 – 400 nm.[68] Based on the absorption coefficient, the required thickness of the Bi_2O_3 thin film to harvest the light having wavelengths of 600 nm and 400 nm would be about 5 µm and 1 µm respectively.

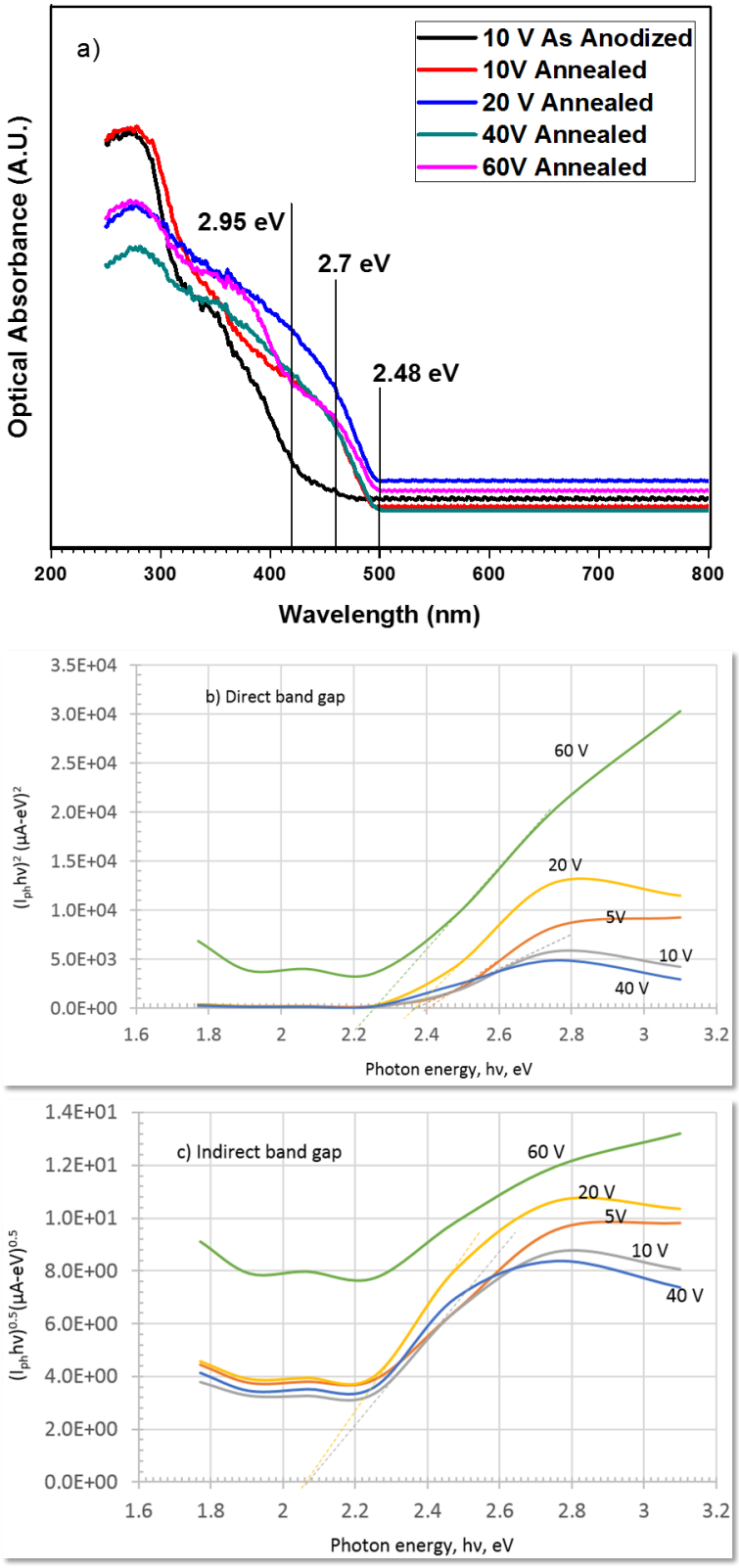

Figure 3.8. Energy band gap of the bismuth oxide nanoporous oxide layer prepared at various anodization potentials based on: (a) the UV-VIS diffuse reflectance measurements; (b) Tauc plots of the annealed Bi_2O_3 samples corresponding to a direct transition; and (c) Tauc plot of indirect transition

Presence of oxygen vacancies has been reported to shift the absorption spectra to longer wavelengths due to excitation of electrons from the donor levels of reduced Bi^{3+} to the conduction band.[66] It was observed that the sample anodized at 20 V showed better optical absorbance of light in the wavelengths of 400-500 nm than other samples. The as-anodized sample showed wider band gap than the annealed samples. Figures 3.8 (b) and (c) show the Tauc plots of the annealed anodic Bi_2O_3 samples that were anodized at different potentials associated with direct and indirect transitions, respectively. It was observed that increasing the anodization potential resulted in marginal red shift in the direct band gap values. For example, the sample anodized at 60 V showed a direct band gap of 2.26 eV as against 2.42 eV for the sample anodized at 5 V. On the other hand, the indirect band gap of the anodic Bi_2O_3 remained at 2.08 eV irrespective of the anodization potential. Overall, the results of XRD, Raman spectroscopy, and the UV-Vis photo spectroscopy confirm that the annealed anodic oxide was predominantly β-Bi_2O_3 irrespective of the anodization potential. As discussed in the introduction section, the tetragonal phase of the bismuth oxide shows the highest photo activity among the different polymorphs of Bi_2O_3.

3.4.4. Photoelectrochemical behavior

Figure 3.9 (a) shows photocurrent densities of the samples anodized at 3 V, 5 V and 10 V under interrupted illumination conditions during an anodic potential scan from the open circuit potential to 0.5 $V_{Ag/AgCl}$. The onset of the photo current was observed at around -0.45 $V_{Ag/AgCl}$. The increase in the bias potential increased the photo current and the dark current remained almost a constant after an initial increase during the potential scan from -0.55 to -0.38 V. During the potentiodynamic test, the maximum dark current value recorded was less than 0.10μA/cm^2 for all the samples. The maximum photo current densities recorded at 1-sun intensity (100 mW/cm^2) during the potentiodynamic test at 0.5 V were 0.58, 0.61, 0.79 mA/cm^2 for the samples anodized at 3, 5, 10 V, respectively. Figure 3.9 (b) shows the I-V plots of the samples anodized at 20, 40, and 60 V and annealed at 200 ^oC, for 2 h. The samples anodized at 20 V and higher potentials showed similar trends of the photo activities as those of the samples anodized at lower than 20 V. The sample anodized at 60 V showed higher photo current density than other samples at lower bias potentials (from OCP to +50 mV Vs

Ag/AgCl). However, at higher bias potentials (> 0.1 $_{VAg/AgCl}$), the sample anodized at 20 V showed the highest photo current. The maximum photo current densities recorded at 0.5 $V_{Ag/AgCl}$ were 1.0, 0.85, and 0.65 mA/cm^2 for the samples anodized at 20, 40, and 60 V respectively. The higher photo activity of the sample anodized at 20 V could be associated with the thicker nanoporous oxide layer (620 nm Vs ~400 nm) that harvested a large portion of light and relatively thinner nanopore walls that facilitated faster hole transport to the electrolyte interface. Surface area of the sample is considered to play a critical role in the photo catalytic activity. Table B1 (Appendix B) gives an estimation of the surface area of the nanoporous anodic bismuth oxide samples per 1 cm^2 of the projected area. The estimated surface areas of the samples prepared by anodization at 10 – 60 V were almost similar. However, significantly different maximum current densities were measured at a bias potential of 0.5 $V_{Ag/AgCl}$. The decrease in the photocurrent densities with increase in the anodization potentials of the samples could be correlated to the thicker walls of the nanopores. The increase in the anodization potentials resulted in the increased wall thickness of the nanopores. It is envisaged that the thicker walls of the nanoporous structure promoted recombination of the photo generated electron-hole pairs.

Figure 3.10 (a) shows the current transients during the potentiostatic tests of different samples at 0.2 and 0.5 $V_{Ag/AgCl}$ (1.53 V_{RHE}). The recorded photo current densities of the 3 V, 5 V and 10 V are 0.57, 0.60, 0.97 mA/cm^2 respectively at 0.5 $V_{Ag/AgCl}$ (1.53V_{RHE}). The sample anodized at 10 V showed higher photo current density than the samples anodized at 3 and 5 V at all the bias potentials. It is interesting to note that the recorded current values during the potentiostatic test at 0.5 V were slightly different from that of the potentiodynamic test as seen in the Figure 3.10 (a). This observation indicated that the kinetics of electron-hole separation occurred faster under a dynamically varying electric field than under a static electric field. The dark current densities were much smaller under potentiostatic conditions. Otherwise, no significant difference in total current densities of the samples was noted under illumination between the potentiodynamic polarization to 0.5 V and potentiostatic test at 0.5 V. The photo current was observed to decay almost exponentially.

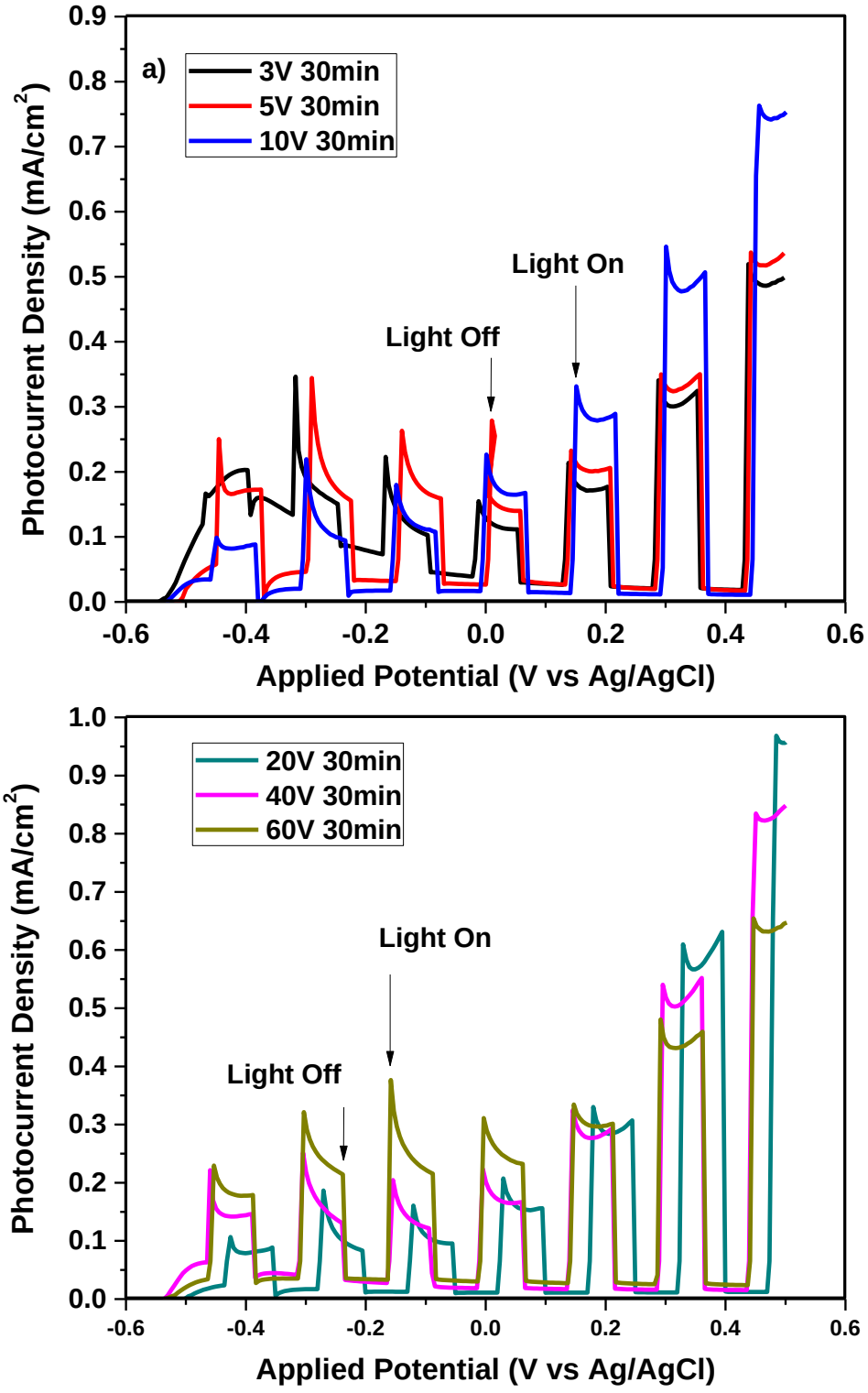

Figure 3.9. Potential vs current density plots of the anodic Bi_2O_3 prepared at different anodization potentials: (a) 3-10 V; and (b) 20-60 V. Thermal oxidation was carried out at 200 ºC for 2 h. The potentials were scanned at a rate of 2.5 mV/s in 1 M KOH solution and illuminated with a 1-sun intensity simulated solar light. The light was interrupted at regular intervals to record the dark current.

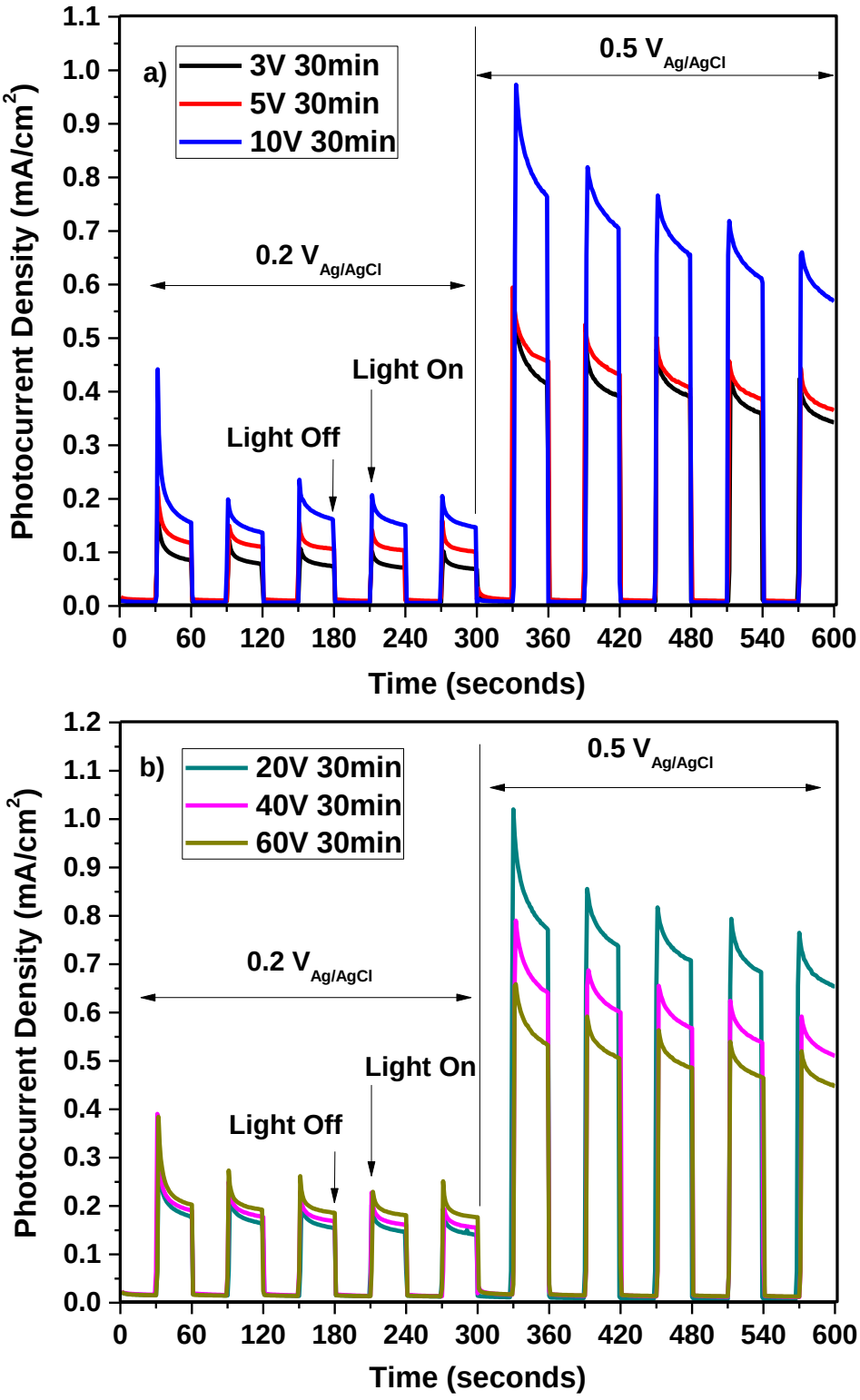

Figure 3.10. Photo current and dark current densities of the anodic Bi_2O_3 prepared at different anodization potentials: (a) 3-10 V; and (b) 20-60 V. Thermal oxidation was carried out at 200 ºC for 2 h. in 1 M KOH solution and illuminated with a 1-sun intensity simulated solar light. The light was interrupted at regular intervals to record the dark current.

The exponential decay of the photo current during the illumination conditions could be attributed to the following reasons: a) faster recombination of electron and holes; b) accumulation of H^+ ions within the nanoporous surface of the oxide layer due to the water oxidation reaction as given in the reaction [7]; c) possible accumulation of the holes at the surface of the nanoporous oxide electrode due to low catalytic activity of the Bi_2O_3 for the oxygen evolution reaction; and (d) adhesion of the oxygen bubbles on the nanoporous surface that caused scattering of the light.

It is known that the photo generated electrons and holes are separated by the electric field at the space charge layer. The electrons are extracted at the backside of the electrode and available for the hydrogen reduction reaction. The flow of these electrons is recorded as the photo current. The holes are consumed at the surface of the nanoporous Bi_2O_3 photo anode through the reaction:

$$2H_2O + 4h^+ \rightarrow 4H^+ + O_2 \qquad [3.7]$$

However, it is well established that bismuth based oxides have low catalytic activity for oxygen evolution reaction.[69] The slower oxygen evolution kinetics of bismuth oxide resulted in accumulation of holes at the surface and lead to recombination losses. Figure 3.10 (b) shows the photo currents recorded at constant potentials as a function of time for the samples anodized at 20 – 60 V. The recorded photo current densities of the 20 V, 40 V and 60 V are 0.96, 0.82, 0.65 mA/cm^2 respectively at 0.5 $V_{Ag/AgCl}$ (1.53V_{RHE}). The sample anodized at 60 V showed higher photo current density at 0.2 V than other two samples. The trend was different at higher bias potentials (0.5 $V_{Ag/AgCl}$), where the sample anodized at 20 V showed the highest photo current density. It is interesting to note that the sample anodized at 10 V showed better photo activity under all the bias potentials than any other sample. This could be attributed to the relatively thinner oxide layer observed in this anodization condition, where the recombination losses occurred in the inner oxide was minimum. Furthermore, the difference in photo activities of the samples under different bias potentials indicated that the photo activity was strongly influenced by the electric field within the oxide layer that separated the photo generated electron-hole pairs. The thickness of nanopore walls, and

length of nanopores of the anodic oxide layer prepared at 10 V were smaller than those prepared at higher anodization potentials. Thinner the wall, higher will be the probability of the holes reaching the oxide/electrolyte surface and participating in the water oxidation reaction. If the thickness of the oxide is small, then the electric field available for charge separation for a given bias potential will be high. Overall, the sample anodized at 10 V was found to have the optimum thickness of the oxide for a better photo activity. The observed photo current density of the nanoporous anodic oxide of bismuth was an order of magnitude higher than that of the planar anodic oxide,[32] and 100% higher than that of thin film β-Bi_2O_3 prepared by reactive sputtering [24] under the similar experimental conditions.

In order to evaluate the stability of the nanoporous β-Bi_2O_3 photo electrodes, potentiostatic polarization studies were carried out under illuminated conditions at 0.5 VAg/AgCl for 1 h. During this test, the hydrogen evolution at the platinum electrode was measured by the electrolyte displacement method using an inverted pipette. Figure B3 (Appendix B) shows the photocurrent density as a function of time. During the start of the test, the photo current density was as high as 4 mA/cm^2, which decayed abruptly to 0.6 mA/cm^2 within 600 seconds and decreased further slowly to less than 0.2 mA/cm^2 at the end of the 1 h test. Figure B4 (Appendix B) shows the volume of hydrogen evolution as a function of time. The total volume of hydrogen collected in the pipette was 115 microliters. The theoretically calculated volume of hydrogen accumulation based on the charge calculation by integrating the photocurrent transient plot was 142 microliters. This difference in the values could be attributed to the dissolved hydrogen in the KOH electrolyte column of the 2 ml pipette. The solubility of hydrogen in 1 M KOH at room temperature was reported to be 12 cc/l.[70] Therefore, about 24 microliters of hydrogen would be dissolved in the pipette solution. The unaccounted 3 microliters of hydrogen could have been lost by leaking out or by other unaccounted parasitic reactions. Overall, the average rate of hydrogen evolution using the β-Bi_2O_3 was about 0.115 ml/cm^2 area of the electrode in 1 M KOH electrolyte at 0.5 $V_{Ag/AgCl}$ bias potential under the simulated 1-sun intensity illumination. After the hour long potentiostatic photoelectrochemical tests, the samples were analyzed under the SEM and XRD. Figures B5 and B6 (Appendix B) show the SEM image and XRD of the photo electrode

samples, respectively, after the long term illumination. No significant change in the nanoporous morphology of the anodic bismuth oxide after the one-hour long photo electrochemical test as seen in the Fig B5. The XRD results did not reveal formation any new phases and all the peaks were identified as β-Bi_2O_3. The results indicated that in spite of the significant photo current decay, the nanoporous bismuth oxide showed stability of the morphology and phase content.

3.4.5. Electrochemical impedance spectroscopy

Figures 3.11 (a) and (b) shows the results of electrochemical impedance spectroscopy in the form of Bode plots with and without illumination of the samples. The impedance data of the samples anodized in different conditions, in the form of Nyquist and Bode plots, are given in the Appendix B as Figures B7 and B8. The impedance data could be fitted with an equivalent circuit model consisting of two parallel RC circuits as shown in the Figure 3.12. The entire Bi_2O_3 anodic oxide was represented by a resistor, R_1, and a leaky capacitor (constant phase element) Q_1. Within the oxide layer, the nanoporous part was represented by another resistor R_2 and a constant phase element Q_2. The impedance of a constant phase element is given as:

$$Z(\omega) = \frac{1}{(j\omega)^m Q} \qquad [3.8]$$

Where, Z = impedance, ω = frequency, j = √-1, Q represents interfacial capacitance and has a unit of capacitance when *m* = 1, surface heterogeneity or continuously distributed time constants for charge-transfer reaction are represented by *m* <1.

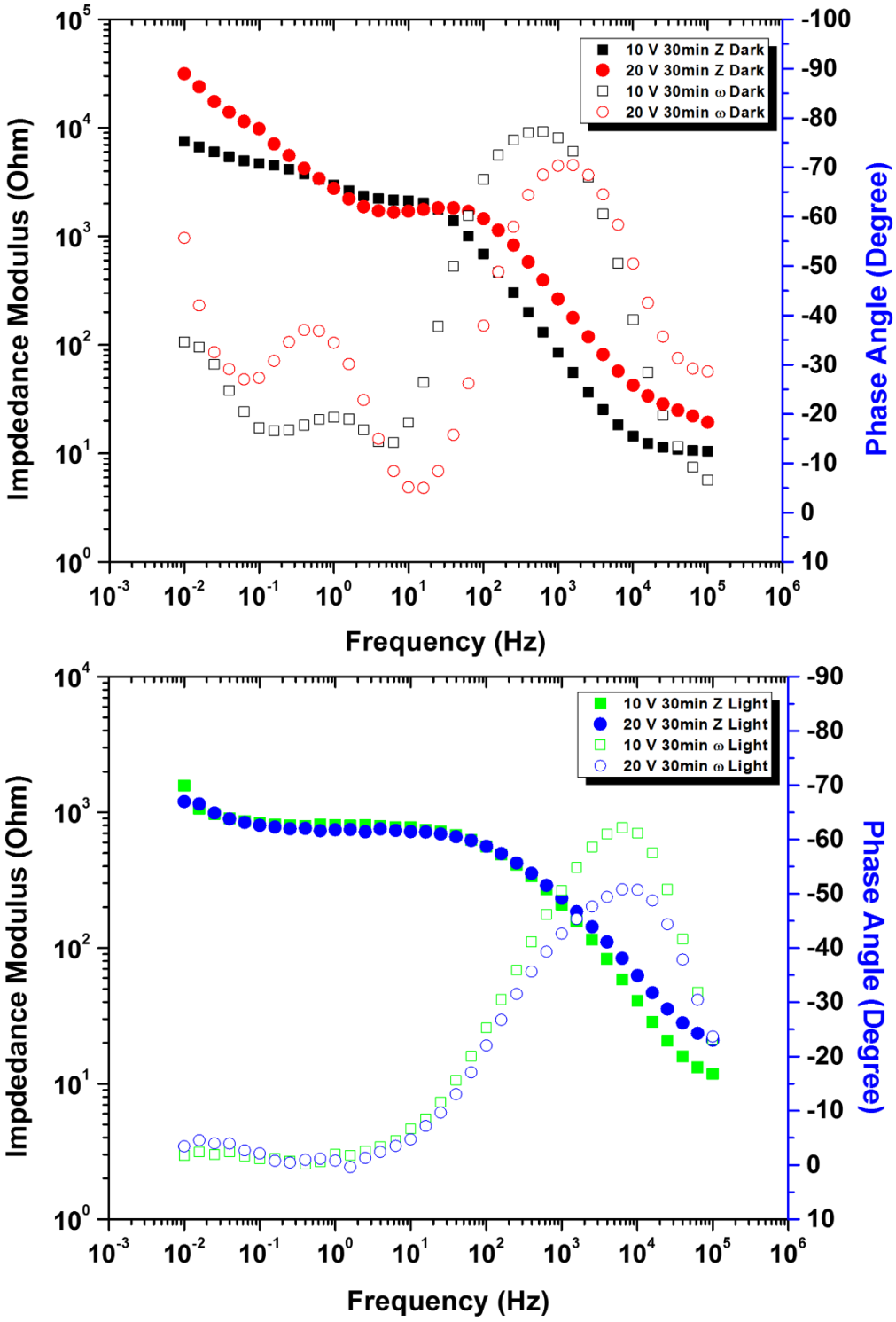

Figure 3.11. Electrochemical impedance spectroscopy (Bode plots) of the anodic nanoporous Bi_2O_3 samples anodized at 10 V for 30 min and 20 V 30min and annealed at 200 ^{o}C for 2 h in 1 M KOH with applied potential of 0.5 V without (a) and with (b) illumination. Z (filled markers) - refers to impedance modulus and ω (unfilled markers) refer to phase angle.

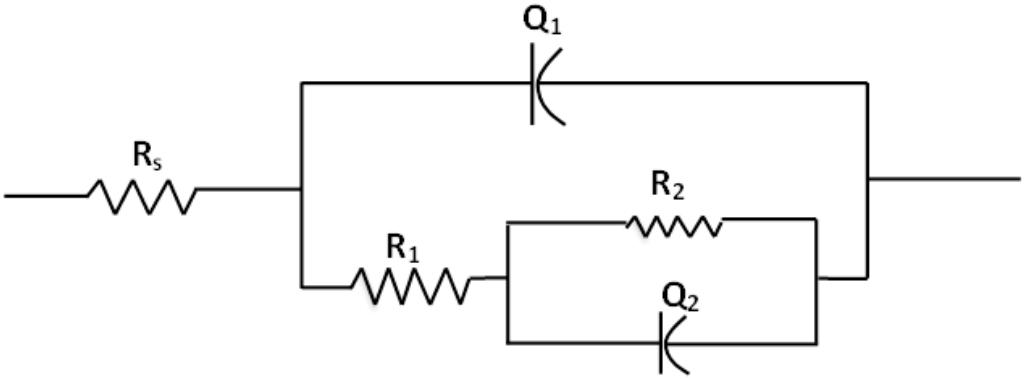

Figure 3.12. Equivalent circuit for the EIS data in Table 3.3

Table 3.3 summarizes the values of the circuit components. The resistance, R_s corresponds to the resistance of the solution. In spite of employing similar concentration of the solution for all the sample, the sample anodized at lower potentials showed relatively higher resistance than the samples anodized at potentials higher than 20 V. This could be attributed to the tortuous path of the electrolyte penetrating the less ordered nanoporous anodic oxide. The R_1 was assumed predominantly to be determined by the resistance of the inner oxide layer. Thicker the inner oxide layer, larger was resistance. Therefore, the samples anodized at 40 and 60 V showed higher values of the R_1 than other samples. The resistance values were high in the dark (not-illuminated) condition. Upon illumination, the resistance became smaller. This observation implied that the inner oxide layer was effectively harvesting the light. The component Q_1 considered predominantly to represent the capacitance like behavior of the inner oxide layer and Q_2 represents the capacitance of the nanoporous layer. It was observed that the capacitance of the nanoporous oxide was larger, for most of the samples, than that of the inner oxide layer, as expected, because of the increased surface area. The values of Q_1 and Q_2 increased significantly under illumination, which could be attributed to the photo generated charge carriers. The value of 'm' was larger (closer to unity) than the value of 'n' for each sample, especially under dark condition, signifying that the inner oxide layer was more homogeneous than the outer layer. The capacitance values of nanoporous layer (Q_2) of the samples anodized at 10 V and 20 V were significantly higher than

that of samples anodized at 40 V and 60 V. Klahr et al [71] correlated the interfacial capacitance of surface states of the hematite photo electrodes to the DOS by the relation:

$$Capacitance\ \left(\frac{F}{cm^2}\right) = q^2 * DOS \qquad [3.9]$$

Where q= elementary charge (Coulomb), DOS = density of states having units as $cm^{-2}eV^{-1}$.

High electron density of states indicates better charge transport. The increased photo activities of the samples anodized at 10 and 20 V, therefore, could be attributed to the possible high density of states available at the nanoporous structure.

Table 3.3. Summary of the values of the equivalent circuit elements describing electrochemical impedance of anodized Bi_2O_3 oxide samples in 1 M KOH solution with and without illumination at 0.5 $V_{Ag/AgCl}$.

Sample	R_{sol} Ωcm²	R_1 Ωcm²	R_2 Ωcm²	Q_1 $(\Omega cm^2)^{-1}s^m$	M	Q_2 $(\Omega cm^2)^{-1}s^m$	n
5V-dark	18.23	$1.18x10^3$	$25.7x10^3$	$3.5x10^{-9}$	0.90	$3.22x10^{-4}$	0.64
5V- light	12.4	905.8	593	$5.68x10^{-6}$	0.81	$7.3x10^{-3}$	0.81
10V-dark	12.6	$2.4\ x10^3$	$2.3x10^3$	$5.8x10^{-6}$	0.88	$7.3x10^{-4}$	0.76
10V-Light	8.86	780	346	$4.8x10^{-6}$	0.78	$11.5x10^{-3}$	0.76
20V-Dark	18.6	$1.66x10^3$	$50.4x10^3$	$1.2x10^{-6}$	0.91	$1.74x10^{-4}$	0.68
20V-Light	12.8	755.3	303.9	$8.6x10^{-6}$	0.70	$15.9x10^{-3}$	0.98
40V-dark	9.2	$35x10^3$	$58.3x10^3$	$4.26x10^{-6}$	0.71	$1.38x10^{-4}$	0.75
40V-light	5.1	428	$1.2x10^3$	$1.2x10^{-7}$	0.92	$1x10^{-6}$	0.81
60V-Dark	6.9	$32.5x10^3$	$8.78x10^3$	$6.37x10^{-7}$	0.87	$4.2x10^{-6}$	0.82
60V-Light	6.8	1067	$1.34x10^3$	$1.5x10^{-6}$	0.80	$39x10^{-6}$	0.39

3.4.6. Mott-Schottky analysis

Mott-Schottky results of the sample anodized at 20 V for 30 min with and without illumination is shown in Figure 3.13. The Mott-Schottky results of other samples are given in the supporting information as Figure B9. The slope of the Mott-Schottky plot is considered for calculation of the defect or charge carrier density, N_D, based on the relation:

$$N_D = 2/e * \varepsilon * \varepsilon_0 * m \qquad [3.10]$$

where e = elementary charge, ε = dielectric constant of the semiconductor, ε_0 = permittivity in vacuum, and m = slope of the Mott-Schottky plot. From the above relation, it could be noted that shallower the slope larger will be the defect density. From the positive slope of the Mott-Schottky plots it can be concluded that the anodic nanoporous Bi_2O_3 showed n-type behavior. Therefore, the majority charge carriers will be electrons. The charge carrier densities of the annealed anodic Bi_2O_3 samples anodized at 3 – 10 V under the dark condition were in the range of 1.5 - 4.8 x 10^{18} cm^{-3}. On the other hand the samples anodized at 20 – 60 V showed an order of magnitude lower charge carrier density in the range of 1.4 – 2.4 x 10^{17} cm^{-3}. Upon illumination, the charge carrier densities of the samples anodized between 3 and 10 V were in the range of 4.6 x 10^{18} – 1.9 x 10^{19} cm^{-3}. The samples anodized at 20 – 60 V showed more than an order of increase in the charge carrier densities upon illumination. The increase in the charge carrier density could be attributed to the decrease in the impedance as noted in the previous section. The charge carries could be associated with the oxygen vacancies that were inherently formed during anodization. It should be noted that the β-Bi_2O_3 has a distorted fluorite structure with 25% of ordered vacant oxygen sites along (001) planes. [72]

The samples anodized at potentials higher than 5 V showed two distinct regions of different slopes in the Mott-Schottky plots. The two different slopes could be attributed to ionization of defects possibly present at two different energy levels separated by about 0.2 eV under the dark conditions. Furthermore, the different slopes also could be associated with the presence of dual layers of the anodic oxide with distinctly different morphologies. Table 3.4 shows the summary of the Mott-Schottky results of all the samples. The charge carrier densities for the dark conditions only for the low band bending conditions (from OCP to -0.2 $V_{Ag/AgCl}$) are reported. The increased photo current density of the sample anodized at high potentials could be attributed to the higher charge carrier density upon illumination than that of the sample anodized at low potentials.

The flat band potential of the samples was determined from the intercept of potential axis of the Mott-Schottky plots where $1/C^2 = 0$. The flat band potential for an n-type material can be expressed as:[73]

$$E_{FB} = E_C + \Delta E_F + V_H + E_O \qquad [3.11]$$

Where, E_{FB} is the flat band potential with respect to a reference electrode (Ag/AgCl in this case), ΔE_F is the difference between the Fermi level and majority carrier band edge (E_C), V_H is the potential drop across the Helmholtz layer, and E_O is the scale factor relating the reference electrode redox level to the absolute vacuum scale (-4.7 V for saturated Ag/AgCl). ΔE_F can be calculated using the standard relation:

$$\Delta E_F = kTln\left(\frac{N_D}{N_C}\right) \qquad [3.12]$$

Where, k = Boltzmann constant, T = temperature, N_D = charge carrier density determined from the Mott-Schottky plot, and N_c = effective density of states in conduction band given by the relation[74]:

$$N_C = 2\left(\frac{2\pi m_e^* kT}{h^2}\right)^{3/2} \qquad [3.13]$$

Where, m^*_e = equivalent mass of electrons, h = Planck's constant, k = Boltzmann's constant, and T = temperature. The effective mass of electrons in α-Bi_2O_3 is considered as 0.68 times the mass of electron.

Considering the effective density of states in conduction band to be around 1.4 x10^{25} m^{-3} and charge carrier densities of 1.6 x 10^{24} m^{-3} under dark condition, the ΔE_F of the sample anodized at 10 V can be calculated in the potential scale as: -0.056 V in the dark condition. Using the relation [11], one can calculate the position of the conduction band edges of the anodic nanoporous Bi_2O_3 and analyze the energetics of the electrochemical water splitting process. If the flat band potential is measured at a pH corresponding to zero point of charge (pH_{ZPC}), then the V_H will be zero because of the absence of the absorption at the electrode interface. In case of the Bi_2O_3, the pH_{ZPC} has been reported[75] as 6.2. Therefore, significant

adsorption of OH^- would be expected on the surface of the nanoporous oxide layer and the potential drop across the Helmholtz layer should be considered. Since the magnitude of V_H was a strong function of electrolyte and all the experiments were carried out in the same electrolyte, the contribution of V_H was not considered in the calculation of the band edges in this work. This is justifiable because the band edge variation were compared between different annealing conditions of similar material.

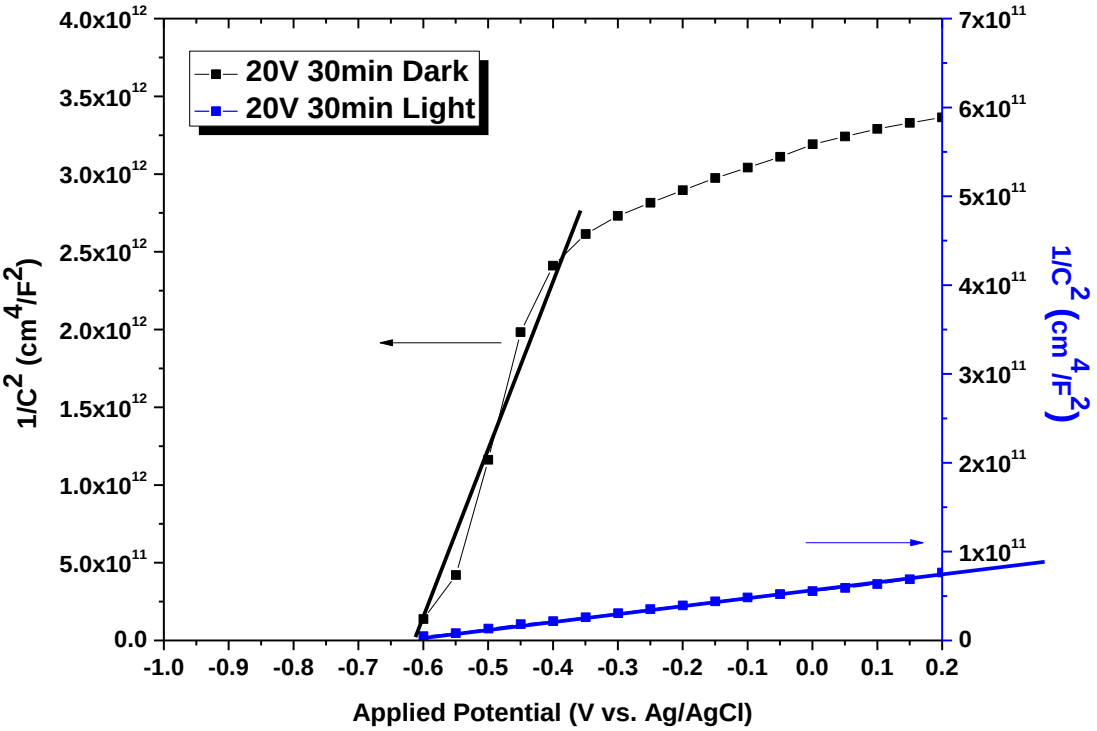

Figure 3.13. Mott-Schottky of the anodic nanoporous Bi_2O_3 anodized at 20 V for 30 min and annealed at 200 ºC for 2 h in 1 M KOH with and without illumination.

Figure 3.14 shows the schematic of a simplified potential level diagram illustrating the positions of the Fermi level, and conduction band edge of the anodic nanoporous Bi_2O_3 with reference to the Ag/AgCl electrode. The Fermi level of the material was determined from the flat band potential. The conduction band minimum was observed to be at -3.94 eV with reference to the absolute vacuum scale. The valence band maximum was positioned at 1.44 eV below the energy level of H_2O/O_2, and thus providing energetic holes for oxygen evolution reaction. The potentials of the hydrogen and oxygen evolution reactions pertain to pH:14. It was observed that the conduction band edge of the sample was about 0.27 V below the

hydrogen reduction potential indicating requirement of an external bias to split water. Since the valence band was well below the oxygen evolution potential, the holes were energetic for participating in the water oxidation reaction.

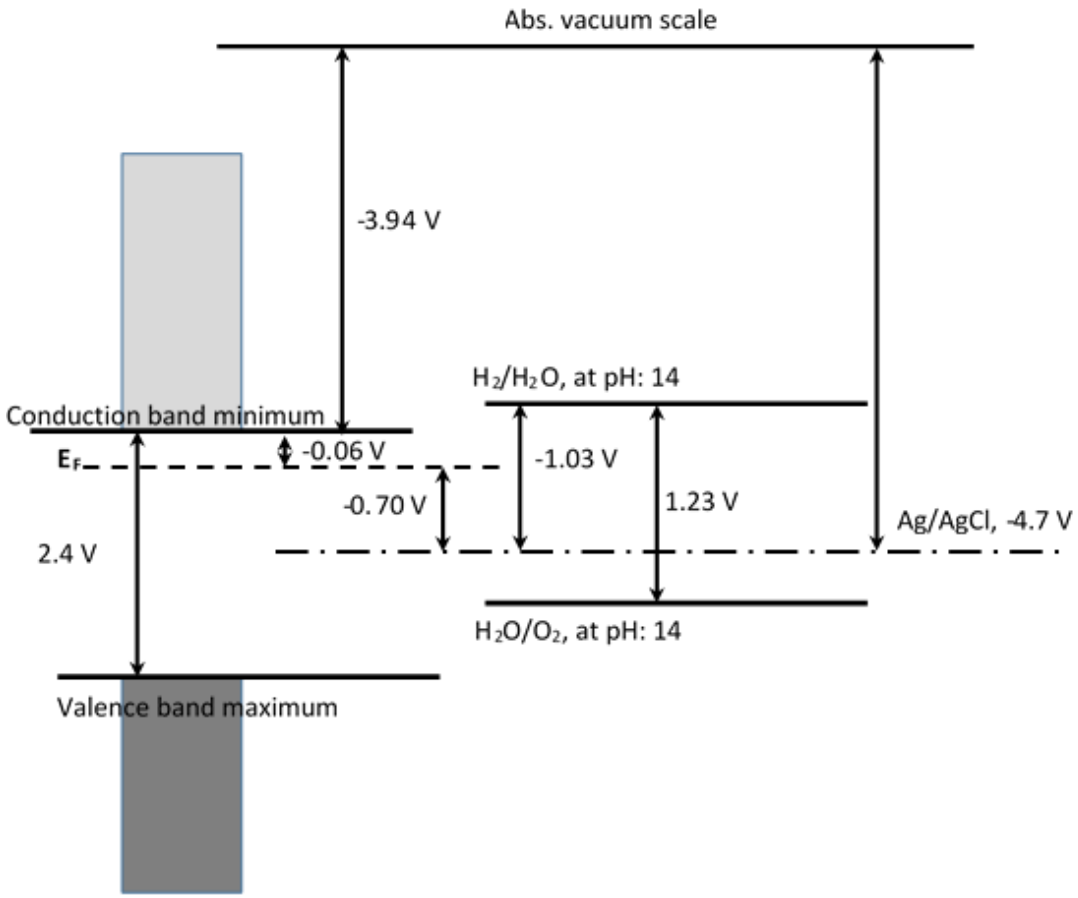

Figure 3.14. Schematics of the potential levels of anodic (anodized at 10 V) nanoporous Bi_2O_3 in pH:14 solution with reference to absolute vacuum scale and saturated Ag/AgCl electrode (Not to scale). All energy scales were converted to potential scale (1 eV corresponds to 1 V).

It is interesting to note that the flat band potentials of most of the samples shifted to more positive potentials upon illumination than that of dark conditions (Table 3.4). The positive shift of the potentials indicated accumulation of the photo generated holes on the surface of the anodic oxides This could be attributed to the low activity of the nanoporous bismuth oxide for the oxygen evolution reaction, similar to the behavior reported for $BiVO_4$.[76] In order to make the anodic nanoporous bismuth oxide layer a practically useful electrode material for water splitting, two modifications could be implemented which are the directions for further research and beyond the scope of this manuscript. These modifications are: 1)

addition of hole scavengers such as hydrogen peroxide, methanol etc. The hole scavengers may potentially mitigate accumulation of holes on the nanoporous surface which could increase the photo current and hinder photo oxidation of Bi^{3+} to higher valence states. However, the drawback of this approach would be difficulty in controlling the electrolyte chemistry in a practical device. Furthermore, addition of hole scavenger would not lead to stoichiometric hydrogen and oxygen evolution by water splitting reaction since the oxygen evolution would still be retarded. 2) The next approach could be provision of a layer of catalyst that promotes oxygen evolution reaction (OER) such as cobalt phosphate, FeOOH, NiOOH, nickel borate etc. Deposition of a transparent OER catalyst on the anodic nanoporous bismuth oxide layer would help not only stabilize the photo current but also enhance the photo activity.[74]

Table 3.4. Summary of the Mott-Schottky analyses

Sample		Flat band potential, $V_{Ag/AgCl}$	Charge carrier density, cm^{-3}
3 V 30 min	Dark	-0.10	4.82×10^{18}
	Illuminated	-0.74	1.10×10^{19}
5 V 30 min	Dark	-0.70	4.00×10^{18}
	Illuminated	-0.54	4.56×10^{18}
10 V 30 min	Dark	-0.70	1.57×10^{18}
	Illuminated	-0.85	1.89×10^{19}
20 V 30 min	Dark	-0.62	1.33×10^{17}
	Illuminated	-0.60	2.68×10^{19}
40 V 30 min	Dark	-0.62	1.40×10^{17}
	Illuminated	-0.61	2.68×10^{19}
60 V 30 min	Dark	-0.64	1.44×10^{17}
	Illuminated	-0.63	1.40×10^{19}

3.5. Conclusions

Thin films of nanoporous bismuth oxide were synthesized by a simple electrochemical anodization of bismuth substrate at constant potentials in the range of 3 – 60 V in 0.3 M citric acid solution. The anodic oxides exhibited a dual layered structure having a planar inner oxide and nanoporous outer oxide. The thickness of the oxides increased with the anodization potentials up to 10 V and then decreased after 20 V. The diameter of the nanopores was not affected by the anodization potential but the nanopore wall thickness increased with the anodization potential. Annealing the anodic nanoporous Bi_2O_3 at 200 °C for 2 h resulted in stabilization of the metastable β-Bi_2O_3 phase that showed tetragonal symmetry and n-type semiconductivity. A maximum photo current density of 0.97 mA/cm^2 was observed for the sample anodized at 10 V at 1.53 RHE. The nanoporous anodic oxides showed a charge carrier density in the range of $1.2 \times 10^{17} – 4.8 \times 10^{18}$ cm^{-3} without illumination and about 60% increase in the charge carrier density upon illumination. The flat potentials shifted to positive values upon illumination which indicated accumulation of holes on the surface that did not participate in the water oxidation reaction.

3.6. References

1. Masuda, H.; Fukuda, K., Ordered Metal Nanohole Arrays Made by a Two-Step Replication of Honeycomb Structures of Anodic Alumina. *Science* **1995,** *268* (5216), 1466-1468.

2. Parkhutik, V. P.; Shershulsky, V. I., Theoretical modelling of porous oxide growth on aluminium. *Journal of Physics D: Applied Physics* **1992,** *25* (8), 1258.

3. Gong, D.; Grimes, C. A.; Varghese, O. K.; Hu, W.; Singh, R. S.; Chen, Z.; Dickey, E. C., Titanium oxide nanotube arrays prepared by anodic oxidation. *Journal of Materials Research* **2001,** *16* (12), 3331-3334.

4. Gu, D.; Baumgart, H.; Namkoong, G.; Abdel-Fattah, T. M., Atomic Layer Deposition of ZrO2 and HfO2 Nanotubes by Template Replication. *Electrochemical and Solid-State Letters* **2009,** *12* (4), K25-K28.

5. Guo, Y.; Quan, X.; Lu, N.; Zhao, H.; Chen, S., High Photocatalytic Capability of Self-Assembled Nanoporous WO3 with Preferential Orientation of (002) Planes. *Environmental Science & Technology* **2007,** *41* (12), 4422-4427.

6. Zhao, Z.-G.; Miyauchi, M., Nanoporous-Walled Tungsten Oxide Nanotubes as Highly Active Visible-Light-Driven Photocatalysts. *Angewandte Chemie International Edition* **2008,** *47* (37), 7051-7055.

7. Macak, J. M.; Tsuchiya, H.; Taveira, L.; Aldabergerova, S.; Schmuki, P., Smooth Anodic TiO2 Nanotubes. *Angewandte Chemie International Edition* **2005,** *44* (45), 7463-7465.

8. Macák, J. M.; Tsuchiya, H.; Ghicov, A.; Schmuki, P., Dye-sensitized anodic TiO2 nanotubes. *Electrochemistry Communications* **2005,** *7* (11), 1133-1137.

9. Zhang, Z.; Wang, P., Optimization of photoelectrochemical water splitting performance on hierarchical TiO2 nanotube arrays. *Energy & Environmental Science* **2012,** *5* (4), 6506-6512.

10. Macak, J. M.; Tsuchiya, H.; Ghicov, A.; Yasuda, K.; Hahn, R.; Bauer, S.; Schmuki, P., TiO2 nanotubes: Self-organized electrochemical formation, properties and applications. *Current Opinion in Solid State and Materials Science* **2007,** *11* (1–2), 3-18.

11. Albu, S. P.; Ghicov, A.; Macak, J. M.; Hahn, R.; Schmuki, P., Self-Organized, Free-Standing TiO2 Nanotube Membrane for Flow-through Photocatalytic Applications. *Nano Letters* **2007,** *7* (5), 1286-1289.

12. Macak, J. M.; Zlamal, M.; Krysa, J.; Schmuki, P., Self-Organized TiO2 Nanotube Layers as Highly Efficient Photocatalysts. *Small* **2007,** *3* (2), 300-304.

13. Cho, I. S.; Chen, Z.; Forman, A. J.; Kim, D. R.; Rao, P. M.; Jaramillo, T. F.; Zheng, X., Branched TiO2 Nanorods for Photoelectrochemical Hydrogen Production. *Nano Letters* **2011,** *11* (11), 4978-4984.

14. Sivula, K.; Le Formal, F.; Grätzel, M., Solar Water Splitting: Progress Using Hematite (α-Fe2O3) Photoelectrodes. *ChemSusChem* **2011,** *4* (4), 432-449.

15. Norman, N. C., *Chemistry of arsenic, antimony, and bismuth*. Blackie Academic & Professional: London; New York, 1998.

16. Lin, X.; Huang, F.; Wang, W.; Shi, J., Photocatalytic activity of Bi24Ga2O39 for degrading methylene blue. *Scripta Materialia* **2007,** *56* (3), 189-192.

17. Berglund, S. P.; Flaherty, D. W.; Hahn, N. T.; Bard, A. J.; Mullins, C. B., Photoelectrochemical Oxidation of Water Using Nanostructured BiVO4 Films. *The Journal of Physical Chemistry C* **2011,** *115* (9), 3794-3802.

18. Cao, D.; Wang, Z.; Nasori; Wen, L.; Mi, Y.; Lei, Y., Switchable Charge-Transfer in the Photoelectrochemical Energy-Conversion Process of Ferroelectric BiFeO3 Photoelectrodes. *Angewandte Chemie* **2014,** *53* (41), 11027-31.

19. Zhu, A.; Zhao, Q.; Li, X.; Shi, Y., BiFeO3/TiO2 Nanotube Arrays Composite Electrode: Construction, Characterization, and Enhanced Photoelectrochemical Properties. *ACS Applied Materials & Interfaces* **2013,** *6* (1), 671-679.

20. Hou, J.; Yang, C.; Wang, Z.; Zhou, W.; Jiao, S.; Zhu, H., In situ synthesis of α–β phase heterojunction on Bi2O3 nanowires with exceptional visible-light photocatalytic performance. *Applied Catalysis B: Environmental* **2013,** *142–143* (0), 504-511.

21. Qiu, Y.; Yang, M.; Fan, H.; Zuo, Y.; Shao, Y.; Xu, Y.; Yang, X.; Yang, S., Nanowires of [small alpha]- and [small beta]-Bi2O3: phase-selective synthesis and application in photocatalysis. *CrystEngComm* **2011,** *13* (6), 1843-1850.

22. Miyayama, M.; Terada, H.; Yanagida, H., Stabilization of β-Bi2O3 by Sb2O3 Doping. *Journal of the American Ceramic Society* **1981,** *64* (1), C-19-C-19.

23. Horiuchi, S.; Izumi, F.; Mitsuhashi, T.; Uchida, K.; Shimomura, T.; Ogasahara, K., Structural studies of β-Bi2O3 stabilized by the addition of PbF2. *Journal of Solid State Chemistry* **1988,** *74* (2), 247-255.

24. Xin, Y.; Xiaojuan, L.; Shangjun, L.; Gang, W.; Chunping, J.; Jing, T.; Jinwei, C.; Ruilin, W., Enhanced photocatalytic performance: a β -Bi 2 O 3 thin film by nanoporous surface. *Journal of Physics D: Applied Physics* **2013,** *46* (3), 035103.

25. Yang, X.; Lian, X.; Liu, S.; Jiang, C.; Tian, J.; Wang, G.; Chen, J.; Wang, R., Visible light photoelectrochemical properties of β-Bi2O3 nanoporous films: A study of the dependence on thermal treatment and film thickness. *Applied Surface Science* **2013,** *282* (0), 538-543.

26. Brezesinski, K.; Ostermann, R.; Hartmann, P.; Perlich, J.; Brezesinski, T., Exceptional Photocatalytic Activity of Ordered Mesoporous β-Bi2O3 Thin Films and Electrospun Nanofiber Mats. *Chemistry of Materials* **2010,** *22* (10), 3079-3085.

27. Cheng, H.; Huang, B.; Lu, J.; Wang, Z.; Xu, B.; Qin, X.; Zhang, X.; Dai, Y., Synergistic effect of crystal and electronic structures on the visible-light-driven photocatalytic performances of Bi2O3 polymorphs. *Physical Chemistry Chemical Physics* **2010,** *12* (47), 15468-15475.

28. Yang, B.; Mo, M.; Hu, H.; Li, C.; Yang, X.; Li, Q.; Qian, Y., A Rational Self-Sacrificing Template Route to β-Bi2O3 Nanotube Arrays. *European Journal of Inorganic Chemistry* **2004,** *2004* (9), 1785-1787.

29. Williams, D. E.; Wright, G. A., Nucleation and growth of anodic oxide films on bismuth—II. *Electrochimica Acta* **1977,** *22* (5), 505-508.

30. Ammar, I. A.; Khalil, M. W., Anodic oxidation of bismuth in H2SO4 solutions. *Electrochimica Acta* **1971,** *16* (9), 1379-1394.

31. Bojinov, M.; Kanazirski, I.; Girginov, A., Impedance measurements of the relaxation phenomena in the bismuth/anodic film/electrolyte system. *Electrochimica Acta* **1992,** *37* (13), 2415-2420.

32. Kanazirski, I.; Bojinov, M.; Girginov, A., Electrical properties of the barrier layer/solution interface and its role during breakdown of anodic bismuth oxide films. *Electrochimica Acta* **1993,** *38* (4), 511-517.

33. Bojinov, M.; Kanazirski, I.; Girginov, A., Barrier oxide film vs. salt layer formation on bismuth in tartaric acid solutions. *Electrochimica Acta* **1995,** *40* (5), 591-598.

34. Shimizu, K.; Kobayashi, K.; Skeldon, P.; Thompson, G. E.; Wood, G. C., The direct observation of anodic Bi2O3 formed on bismuth in ammonium dihydrogen phosphate solution. *Corrosion Science* **1996,** *38* (3), 431-441.

35. Chitrada, K. C.; Raja, K. S., Nanoporous Anodic Bismuth Oxide Photo-Anodes. *ECS Transactions* **2014,** *61* (22), 1-12.

36. Lv, X.; Zhao, J.; Wang, X.; Xu, X.; Bai, L.; Wang, B., Novel Bi2O3 nanoporous film fabricated by anodic oxidation and its photoelectrochemical performance. *J Solid State Electrochem* **2013,** *17* (4), 1215-1219.

37. Chitrada, K. C.; Raja, K. S., Nanoporous Anodic Bismuth Oxide for Electrochemical Energy Storage. *ECS Transactions* **2014,** *61* (18), 55-67.

38. Chitrada, K.; Raja, K. S., Stability of the Nanoporous Bismuth Oxide Photoanodes for Solar Water Splitting. In *Materials and Processes for Solar Fuel Production*, Viswanathan, B.; Subramanian, V.; Lee, J. S., Eds. Springer New York: 2014; Vol. 174, pp 173-199.

39. Wang, C.; Shao, C.; Wang, L.; Zhang, L.; Li, X.; Liu, Y., Electrospinning preparation, characterization and photocatalytic properties of Bi2O3 nanofibers. *Journal of Colloid and Interface Science* **2009,** *333* (1), 242-248.

40. Latha, K.; Jin-Han, L.; Yuan-Ron, M., Synthesis of bismuth oxide nanostructures by an oxidative metal vapour phase deposition technique. *Nanotechnology* **2007,** *18* (29), 295605.

41. Williams, D. E.; Wright, G. A., Structure and electronic properties of bismuth anodic oxide films—I. Photoeffects. *Electrochimica Acta* **1979,** *24* (11), 1179-1187.

42. Raja, K. S.; Gandhi, T.; Misra, M., Effect of water content of ethylene glycol as electrolyte for synthesis of ordered titania nanotubes. *Electrochemistry Communications* **2007,** *9* (5), 1069-1076.

43. Pourbaix, M., *Atlas of electrochemical equilibria in aqueous solutions*. Pergamon Press: Oxford; New York, 1966.

44. Raja, K. S.; Misra, M.; Paramguru, K., Formation of self-ordered nano-tubular structure of anodic oxide layer on titanium. *Electrochimica Acta* **2005,** *51* (1), 154-165.

45. Rangaraju, R. R.; Raja, K. S.; Panday, A.; Misra, M., An investigation on room temperature synthesis of vertically oriented arrays of iron oxide nanotubes by anodization of iron. *Electrochimica Acta* **2010,** *55* (3), 785-793.

46. Schaffer, E.; Thurn-Albrecht, T.; Russell, T. P.; Steiner, U., Electrically induced structure formation and pattern transfer. *Nature* **2000,** *403* (6772), 874-877.

47. Bandyopadhyay, D.; Sharma, A.; Thiele, U.; Reddy, P. D. S., Electric-Field-Induced Interfacial Instabilities and Morphologies of Thin Viscous and Elastic Bilayers. *Langmuir* **2009,** *25* (16), 9108-9118.

48. Hoar, T. P.; Mott, N. F., A mechanism for the formation of porous anodic oxide films on aluminium. *Journal of Physics and Chemistry of Solids* **1959,** *9* (2), 97-99.

49. O'Sullivan, J. P.; Wood, G. C., The Morphology and Mechanism of Formation of Porous Anodic Films on Aluminium. *Proceedings of the Royal Society of London. A. Mathematical and Physical Sciences* **1970,** *317* (1531), 511-543.

50. Hebert, K. R.; Albu, S. P.; Paramasivam, I.; Schmuki, P., Morphological instability leading to formation of porous anodic oxide films. *Nat Mater* **2012,** *11* (2), 162-166.

51. Jessensky, O.; Müller, F.; Gösele, U., Self-organized formation of hexagonal pore arrays in anodic alumina. *Applied Physics Letters* **1998,** *72* (10), 1173-1175.

52. Li, A. P.; Müller, F.; Birner, A.; Nielsch, K.; Gösele, U., Hexagonal pore arrays with a 50–420 nm interpore distance formed by self-organization in anodic alumina. *Journal of Applied Physics* **1998,** *84* (11), 6023-6026.

53. Regonini, D.; Satka, A.; Jaroenworaluck, A.; Allsopp, D. W. E.; Bowen, C. R.; Stevens, R., Factors influencing surface morphology of anodized TiO2 nanotubes. *Electrochimica Acta* **2012,** *74* (0), 244-253.

54. Regonini, D.; Jaroenworaluck, A.; Stevens, R.; Bowen, C. R., Effect of heat treatment on the properties and structure of TiO2 nanotubes: phase composition and chemical composition. *Surface and Interface Analysis* **2010,** *42* (3), 139-144.

55. Su, Z.; Zhou, W., Pore diameter control in anodic titanium and aluminium oxides. *Journal of Materials Chemistry* **2011,** *21* (2), 357-362.

56. Macdonald, D. D., On the formation of voids in anodic oxide films on aluminum. *Journal of the Electrochemical Society* **1993,** *140* (3), L27-L30.

57. Risold, D.; Hallstedt, B.; Gauckler, L. J.; Lukas, H. L.; Fries, S. G., The bismuth-oxygen system. *JPE* **1995,** *16* (3), 223-234.

58. Okamoto, H., O-Ti (Oxygen-Titanium). *J. Phase Equilib. Diffus.* **2011,** *32* (5), 473-474.

59. Punn, R.; Feteira, A. M.; Sinclair, D. C.; Greaves, C., Enhanced Oxide Ion Conductivity in Stabilized δ-Bi2O3. *Journal of the American Chemical Society* **2006,** *128* (48), 15386-15387.

60. Mansour, S. A. A., Thermal decomposition of anhydrous bismuth citrate. *Thermochimica Acta* **1994,** *233* (2), 257-268.

61. Zhang, Y.; Li, D.; Zhang, Y.; Zhou, X.; Guo, S.; Yang, L., Graphene-wrapped Bi2O2CO3 core-shell structures with enhanced quantum efficiency profit from an ultrafast electron transfer process. *Journal of Materials Chemistry A* **2014,** *2* (22), 8273-8280.

62. Sarma, B.; Jurovitzki, A. L.; Smith, Y. R.; Mohanty, S. K.; Misra, M., Redox-Induced Enhancement in Interfacial Capacitance of the Titania Nanotube/Bismuth Oxide Composite Electrode. *ACS Applied Materials & Interfaces* **2013,** *5* (5), 1688-1697.

63. Li, Q.; Liu, H.; Dong, F.; Fu, M., Hydrothermal formation of N-doped (BiO)2CO3 honeycomb-like microspheres photocatalysts with bismuth citrate and dicyandiamide as precursors. *Journal of Colloid and Interface Science* **2013,** *408* (0), 33-42.

64. Whitman, S. R.; Raja, K. S., Formation and electrochemical characterization of anodic ZrO2–WO3 mixed oxide nanotubular arrays. *Applied Surface Science* **2014,** *303* (0), 406-418.

65. Hardcastle, F. D.; Wachs, I. E., The molecular structure of bismuth oxide by Raman spectroscopy. *Journal of Solid State Chemistry* **1992,** *97* (2), 319-331.

66. Vila, M.; Díaz-Guerra, C.; Piqueras, J., Laser irradiation-induced α to δ phase transformation in Bi2O3 ceramics and nanowires. *Applied Physics Letters* **2012,** *101* (7), -.

67. Sirimanne, P. M.; Takahashi, K.; Sonoyama, N.; Sakata, T., Photocurrent enhancement of wide bandgap Bi2O3 by Bi2S3 over layers. *Solar Energy Materials and Solar Cells* **2002,** *73* (2), 175-187.

68. Evan Tariq Al Waisy, M. S. A. W., Structural, Surface Morphology and Optical Properties of Bi2O3 Thin Film Prepared By Reactive Pulse Laser Deposition. *Journal of university of Anbar for Pure science* **2013,** *7* (2).

69. Dutta, D. P.; Roy, M.; Tyagi, A. K., Dual function of rare earth doped nano Bi2O3: white light emission and photocatalytic properties. *Dalton Transactions* **2012,** *41* (34), 10238-10248.

70. Ruetschi, P.; Amlie, R. F., Solubility of Hydrogen in Potassium Hydroxide and Sulfuric Acid. Salting-out and Hydration. *The Journal of Physical Chemistry* **1966,** *70* (3), 718-723.

71. Klahr, B.; Gimenez, S.; Fabregat-Santiago, F.; Hamann, T.; Bisquert, J., Water Oxidation at Hematite Photoelectrodes: The Role of Surface States. *Journal of the American Chemical Society* **2012,** *134* (9), 4294-4302.

72. Wang, Y.; Wen, Y.; Ding, H.; Shan, Y., Improved structural stability of titanium-doped β-Bi2O3 during visible-light-activated photocatalytic processes. *J Mater Sci* **2010,** *45* (5), 1385-1392.

73. Nozik, A. J.; Memming, R., Physical Chemistry of Semiconductor−Liquid Interfaces. *The Journal of Physical Chemistry* **1996,** *100* (31), 13061-13078.

74. Kasap, S. O., *Principles Of Electronic Materials And Devices (without Cd)*. Tata Mcgraw-Hill Publishing Company Limited: 2006.

75. Xu, Y.; Schoonen, M. A. A., The absolute energy positions of conduction and valence bands of selected semiconducting minerals. *American Mineralogist* **2000,** *85* (3-4), 543-556.

76. Kim, T. W.; Choi, K.-S., Nanoporous BiVO4 Photoanodes with Dual-Layer Oxygen Evolution Catalysts for Solar Water Splitting. *Science* **2014,** *343* (6174), 990-994.

4. Enhanced Performance of β-Bi_2O_3 by in-situ Photo-conversion to Bi_2O_3-BiO_{2-x} Composite Photoanode for Solar Water Splitting[‡]

4.1. Abstract

Ordered nanoporous bismuth oxide layer consisting of metastable β-Bi_2O_3 phase that showed n-type semiconductivity was synthesized by a simple electrochemical anodization of bismuth substrate. When the anodic nanoporous β-Bi_2O_3 samples were tested as photoanodes for solar water splitting application in 0.5 M Na_2SO_4 (pH:5.8), and 1 M KOH (pH:13.7), the photocurrent decayed continuously with time from an initial value of 0.95 mA/cm^2 under 1-sun illumination at a bias potential of 1.5 V_{RHE}. Accumulation of photo generated holes at the photoanode/ electrolyte was attributed to the photocurrent decay. Addition of methanol as sacrificial hole scavenger was not found to be effective for the bismuth oxide photoanodes. When hydrogen peroxide was added to the 0.5 M Na_2SO_4 electrolyte, the photocurrent density increased to ~4 mA/cm^2 and was stable for more than 1 h of illumination of AM1.5 global light at 1.5 V_{RHE}. Addition of hydrogen peroxide to the 0.3 M KOH solution showed a gradual increase in the photocurrent density for the first 300 seconds of light illumination to a maximum value of ~ 10 mA/cm^2 at 0.65 V_{RHE} and then it decreased continuously. The high photocurrent density of nanoporous β-Bi_2O_3 in 1 M KOH + 0.3 M H_2O_2 was be attributed to the presence of photo-converted Bi_2O_{4-x} phase which harvested more light in the visible wavelengths.

4.2. Introduction

Bismuth based mixed oxides such as $BiVO_4$, $BiFeO_3$, $BiWO_6$, Bi_3NbO_7, and Bi_2MoO_6 are being actively investigated as promising high efficiency photocatalysts for solar water splitting applications.[1-11] These bismuth based oxides show predominantly n-type semiconductivity and therefore function as photoanodes in the photoelectrochemical water splitting process. A significant amount of literature is available on the photoelectrochemical behavior of

[‡] This chapter has been published: Kalyan Chitrada, Ruchi Gakhar, Dev Chidambaram, Eric Aston, Krishnan S. Raja, Journal of The Electrochemical Society 163 (7), H546-H558 (2016)

bismuth based ternary oxides, however very few studies have reported the performance of the binary Bi_2O_3 which is the elementary constituent of the advanced bismuth mixed oxides. The photocatalytic behavior of the bismuth based oxides is well documented and the factors that limit their performance is well understood. Most importantly they exhibit low catalytic activity for oxygen evolution, which results in hole accumulation at the electrode/electrolyte interface. In order to overcome this limitation, a thin layer of oxygen evolution catalysts such as Co-Pi, FeOOH, $Ni(OH)_2$ or $CoPO_4$ is usually coated on the photoanodes.[12-17] The binary and ternary bismuth oxides show more or less similar electronic structures, where the valence bands of both binary Bi_2O_3, and mixed bismuth oxides are considered to be formed by O-*2p* and Bi-*6s* orbitals.[18, 19] The top of the Bi-6s orbital is positioned at more negative potential than that of O-*2p*.[20-22] The conduction band of Bi_2O_3 is predominantly formed by Bi-*6p* orbitals. Whereas, the conduction band of mixed bismuth oxide is determined by the d-orbitals of transitions metals present in the mixed oxide. Bismuth oxide shows enhanced mobility of charge carriers because of its well-dispersed valence bands and it has high refractive index and large dielectric constant due to lone electron pairs of Bi(III) $6s^2$ that induces intrinsic polarizabilities.[19, 21, 22] These properties make it attractive for photocatalysis. Bismuth oxide is available in six different polymorphs.[23, 24] Among these polymorphs, monoclinic α and face centered cubic δ phases are the stable phases at room temperature and at above 730 ^oC respectively. The other phases are metastable that are stabilized either by relevant doping or synthesis conditions. The metastable tetragonal β-Bi_2O_3 is of interest to the photocatalysis community because of its superior photo activity with a band gap of ~2.5 eV and an n-type semi-conductivity.[25]

Recently the present authors reported formation of nanoporous anodic oxide of bismuth by a facile anodization process.[26-29] The nanoporous β-Bi_2O_3 showed relatively high initial photocurrent density, yet the photocurrent decayed upon continuous illumination. The photocurrent decay could predominantly be attributed to accumulation of holes. It was envisaged that addition of hole scavengers would help stabilize the photocurrent by mitigating surface recombination of charges. Dotan et al evaluated the photoelectrochemical properties of hematite using hydrogen peroxide as a hole scavenger.[30] The addition of

hydrogen peroxide was found to remove the barrier for charge injection at the electrode/electrolyte interface and shift the onset potential of photocurrent to more negative values. No current doubling effect was observed in the hematite with the addition of H_2O_2. On the other hand, current doubling effect has been reported in case of InP electrode.[31] The current doubling was explained by the following reactions with the formation of a HO_2^* radical intermediate in the first step (reaction [1]) and electron injection in to the conduction band in the second step (reaction [2]):

$$H_2O_2 + h^+ \rightarrow HO_2^* + H^+ \qquad [4.1]$$

$$HO_2^* \rightarrow O_2 + H^+ + e^- \qquad [4.2]$$

In the absence of current doubling, the radical intermediate could capture another hole and the reaction [2] could be modified as:

$$HO_2^* + h^+ \rightarrow O_2 + H^+ \qquad [4.3]$$

Current doubling was observed with the addition of organic hole scavengers such as alcohols, formate, and aldehydes in other semiconductor electrodes like ZnO, CdS, and TiO_2.[32] Sayama et al reported enhanced photo activity of $BiVO_4$ either by surface modification with $AgNO_3$ or by addition of methanol as hole scavenger.[17] The current density increased more than 80% with the implementation of either one of the modifications. Interestingly, the effect was not additive when the surface modified BiVO4 with Ag^+ was tested in the electrolyte with the methanol addition. Similar observation was reported by Long et al for the $BiVO_4$ electrode surface modified with a p-type Co_3O_4 layer.[14] Addition of 10 vol% methanol as hole scavenger did not increase the photo activity because the holes were considered to have been trapped by the Co_3O_4 layer at a potential not positive enough to oxidize the methanol. Similar to the Ag^+, Co_3O_4 catalyzed only the oxygen evolution reaction. Most of the available literature mainly focused on the approaches to improve the photocatalytic behavior of bismuth based ternary oxides, especially on bismuth vanadate. It is not clear if the reported strategies for bismuth vanadate will be suitable for the binary bismuth oxide photocatalysts because of different electronic structures.

In this manuscript, we report exclusively the strategies implemented to understand and improve photoelectrochemical behavior of β-Bi_2O_3 nanoporous thin films. We will discuss the decaying photocurrent behavior of β-Bi_2O_3 as a function of pH. Also, adherence of oxygen bubbles and occlusion of H^+ ions at electrode/electrolyte as possible reasons for the observed photocurrent decay are discussed. Likewise, the effect of sacrificial reagent additions as hole scavengers on the photoelectrochemical behavior of β-Bi_2O_3 will be discussed to minimize accumulation of hole at electrode/electrolyte interface. The effect of addition of hole scavengers on the morphology, chemical composition and photoelectrochemical behavior of β-Bi_2O_3 nanoporous photo-anodes will be examined in detail.

4.3. Experimental Methods

4.3.1. Fabrication of nanoporous oxide films

Disc samples (3 mm thick) were sliced out of 12.5 mm diameter bismuth rods (99.99% purity, Alfa Aesar) and then the surfaces were metallographically polished, washed thoroughly using acetone, distilled water and dried in a stream of air. The polished bismuth samples were encapsulated in a sample holder exposing only 1 cm^2 of the active surface area to the anodization electrolyte. The anodization was carried out at room temperature in 0.3M citric acid (Macron Fine Chemicals™) at 20 V for 30 minutes using a two-electrode configuration with a platinum flag as a counter electrode. The distance between the Pt-cathode and bismuth anode was maintained constant at about 1 cm. A DC power source (Sorensen XPF-60-20 dual DC power supply) was used for applying the required anodization potential. After anodization the samples were thoroughly rinsed with DI water, air dried and thermal annealed at 200 °C for 2 h.

4.3.2. Material characterization

The surface morphology of the anodic oxide layer was evaluated using a scanning electron microscope (LEO SUPRA 35VP). The phase analyses of the anodic oxides before and after photo electrochemical testing were carried out using XRD and Raman spectroscopy. X-ray diffraction pattern were recorded using a Rigaku Smartlab 3kW X-ray diffractometer using

Cu Kα wavelength (λ = 1.541 Å; 40 kV, 44 mA). The measurements were recorded in the 2θ range from 10^o to 80^o in Parallel Beam (PB) mode, with a scan speed of 1^o/min and step width of 0.06^o. Thermo Scientific DXR Raman microscope fitted with a 532 nm laser was used for Raman spectroscopic analyses. The analyses were carried out using two power levels such as 1 mW and 5 mW at multiple locations in each samples. Data were collected from a spot diameter of 0.7 µm utilizing 32 exposures at an exposure time of 5 seconds. Optical absorbance spectra were recorded using a Shimadzu UV- 2401PC spectrometer equipped with a tungsten lamp. The scans were recorded over a range of 250–900 nm. Barium sulfate was used as standard reference. The step size and slit width used were 1 nm and 5 nm, respectively.

4.3.3. Photoelectrochemical testing

Photo electrochemical studies were carried out using a three-electrode configuration. A Pt wire spiral with a surface area of 7.5 cm^2 was used as a counter electrode. A graded pipette with a least count of 10 µL was placed over the Pt electrode to collect and measure the hydrogen evolving on the counter electrode by the electrolyte displacement method. The reference electrode was a home-made Ag/AgCl in saturated KCl + AgCl solution (199 mV vs. standard hydrogen electrode). Freshly prepared reference electrodes were used for each test because Ag/AgCl electrode was not very stable when immersed in high pH solutions for long time. A home-made polyether ether ketone (PEEK) sample holder was used to electrically connect the sample with a potentiostat (Gamry Instruments, model: Reference 600) by exposing 1 cm^2 of the active surface. A solar simulator (SOLAR Light, Glenside, PA, USA, Model: 16S-300-002, Class A Spectrum) with a 300 W xenon lamp, and an air mass global 1.5 filter that gave 1-sun intensity (100 mW/cm^2) at appropriate settings was used for illumination of the samples. The light intensity was measured using a radiometer (SOLAR Light, Model: PMA 2100) in combination with a pyranometer (SOLAR Light, Model: PMA2144 Class II). Tauc plots were constructed by illuminating the samples using different band pass filters (Edmund Optics) in the range of 400 -700 nm at 50 nm intervals and polarizing the samples at a constant potential of 1.5 V_{RHE} in 1 M KOH. Even though the potentials were listed with reference to RHE for clarity in order to consider the pH effect, during the experiments

the potentials were applied with reference to an Ag/AgCl reference electrode. The conversion of potentials to RHE scale was carried using the relation:

$$V_{RHE} = V_{Ag/AgCl} + 0.199 + (0.059 \times pH) \qquad [4.4]$$

Potentiodynamic, potentiostatic, electrochemical impedance spectroscopy (EIS), and Mott-Schottky analysis studies were carried out with and without illuminated conditions in 1 M KOH (pH ~ 13.7) and 0.5M Na_2SO_4 (pH: 5.8) with and without addition of hole scavengers. Two types of hole scavengers were investigated: a) methanol and b) hydrogen peroxide (H_2O_2). The electrolyte was either 1 M KOH or 0.5 M Na_2SO_4 with 10 vol% methanol or 0.15M H_2O_2 or 0.3M H_2O_2 in deionized water. Potential Vs current plots were constructed by scanning the potential of the sample from the open circuit potential to 1.53 V_{RHE} at a scan rate of 2.5 mV/s. The current recorded under the solar-light illuminated condition is termed as 'photo current' and the current recorded without illumination is termed as 'dark current' in this report. In order to justify the term 'dark current' that was recorded under the room light, some experiments were carried out by blocking all the light on the sample and the recorded the current densities were about 60-70% of the values recorded with the room light on. Since the current densities were in the same order of magnitude in both the room light on and off conditions, all the experiments were carried out with room light on and still denoted as 'dark current' if the sample was not illuminated by the solar simulator. The gas (hydrogen) collected from the counter electrode pipette compartment was sampled out and analyzed using a gas chromatography (Shimadzu GC-17A; Coulmn: CP MolSieve 5A, 0.53mm ID x 50mL). EIS measurements were carried out under potentiostatic condition of 1.5 V_{RHE} by super imposing an ac signal of 10 mV and scanning the frequency from 0.1 MHz down to 0.1 Hz. The EIS data were fitted with appropriate equivalent circuit models. The goodness of fitting (χ^2) was smaller than 1 x 10^{-3} for the calculated values of the components of the equivalent circuits that typically represented less than 10% error in the model fitting. Mott-Schottky measurements were carried out at different frequencies (f) in the range of 100 - 3000 Hz by scanning the potential of the sample from 1.5 V_{RHE} to the open circuit potentials at 50 mV steps for every two seconds. The capacitance (C) of the space charge layer of the

bismuth oxide was calculated from the measured imaginary impedance (*Z'*), and applied frequency (*f*), using the relation:

$$C = \frac{1}{2\pi f Z'} \qquad [4.5]$$

The slope of the Mott-Schottky plot ($1/C^2$ Vs potential) is considered for calculation of the defect or charge carrier density (N_D), based on the relation:

$$N_D = \frac{2}{e.\varepsilon.\varepsilon_o.m} \qquad [4.6]$$

Where e = elementary charge, ε = dielectric constant of the semiconductor, ε_0 = permittivity in vacuum, and m = slope of the Mott-Schottky plot.

4.4. Results and Discussion

4.4.1. Morphology and structural characterization

Figures 4.1 (a) and (b) shows the surface morphology of the nanoporous bismuth oxide obtained after anodizing the bismuth in 0.3 M citric acid at 20 V for 30 minutes and thermally annealed at 200 ^{o}C for 2 h. The inner diameter of the pores was in the range of 30 - 42 nm with a pore wall thickness in the range of 10-25 nm. The thickness of the oxide layer was typically about 900 nm with a dual layered structure with a barrier type continuous bottom layer of about 150 nm thick and a nanoporous layer on the top.[26] XRD pattern of the thermally annealed anodic oxide layer exhibit a predominant tetragonal β-Bi_2O_3 associated with the JCPDS card # 027- 0050 (Figure 4.1 (c)) and also the Raman spectrum (Figure 4.1(d)) of the sample reveals peaks at 126, 313, and 468 cm^{-1} indicating the presence of β-Bi_2O_3 based on the previous literature values.[26, 27, 33, 34] The direct band gap of the nanoporous oxide sample was 2.37 eV as observed from the Tauc plot given as Figure C1 (supporting information). The Bi^{3+} intra-ionic electronic transitions and charge transfer transitions between oxygen ligands and Bi^{3+} ions could be assigned to the observed band gaps.[35] The reported band gap of the tetragonal β-Bi_2O_3 is ~2.5 eV and the monoclinic α-Bi_2O_3 shows a band gap of 2.8 eV.[19] The lower band gap of the nanoporous Bi_2O_3 indicated that the samples did not contain other

high band gap phases such as α (2.8 eV) or δ (3.1 eV),[36] and thus validating the XRD and Raman analysis data of the nanoporous oxide. It was observed that the indirect band gap of the nanoporous sample was 1.9 eV.

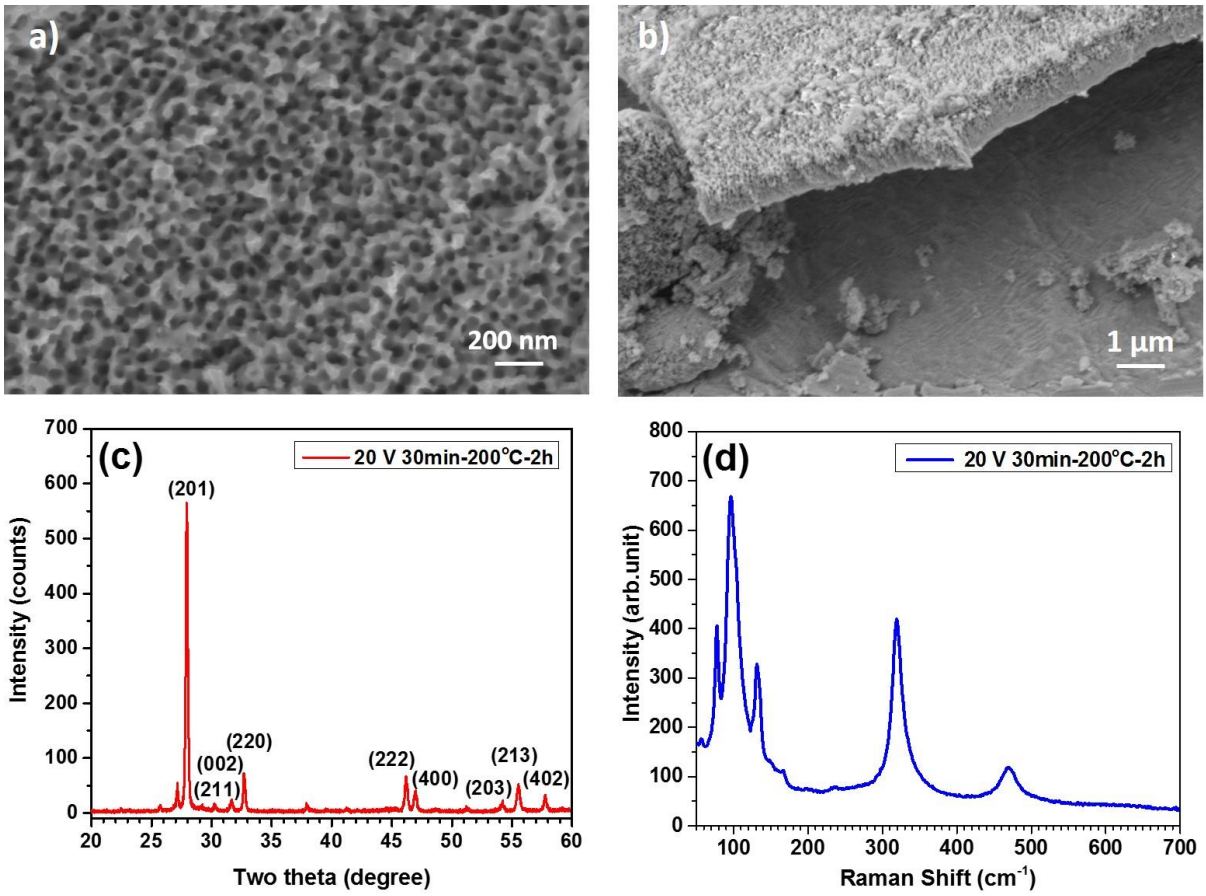

Figure 4.1. (a) & (b) SEM image of the surface morphology of the nanoporous β-Bi_2O_3, c) XRD pattern and d) Raman spectrum of the nanoporous β-Bi_2O_3.

4.4.2. Photoelectrochemical Behavior

4.4.2.1. Effect of pH of the Electrolyte

Figure 4.2(a) shows the current Vs potential characteristics of the nanoporous bismuth oxide in two different pH conditions. The maximum photocurrent densities recorded at 1.5 V_{RHE} were 0.94 and 0.91 mA/cm^2 in 1 M KOH and 0.5 M Na_2SO_4, respectively. The maximum (dark) current density recorded without illumination of the simulated solar light was 12 and 4 µA/cm^2 at 1.5 V_{RHE} in 1 M KOH and 0.5 M Na_2SO_4, respectively. Chopping the illumination at low bias potentials showed cathodic current transients. The positive current

during anodic bias of the sample represented electrons flowing from the bismuth oxide (photoanode) to the Pt counter electrode. According to Dotan et al the negative current spike observed during the interruption of light was due to back reaction of electrons in the conduction band with the photo generated holes accumulated at the interface of the electrode/electrolyte interface.[30] The accumulation of holes at the oxide surface was due to high barrier to charge injection into the electrolyte.[37] Increasing the bias potential in the anodic direction decreased the cathodic current transient upon interruption of the illumination and after a certain potential the cathodic current transient disappeared and only the anodic current was observed as seen in the Figure 4.2(a). The photocurrent transients at a constant potential of 1.53 V_{RHE} of the nanoporous Bi_2O_3 with interrupted illumination are shown in the Figure 4.2 (b). The photocurrent density in 1 M KOH was about 20% higher than that of 0.5 M Na_2SO_4. The photocurrent was observed to decay continuously with time in both the electrolytes. This photocurrent decay could be caused by several factors such as: a) accumulation of the photo generated holes at the electrode/electrolyte interface, b) adherence of oxygen bubbles on the nanoporous surface that effectively decreased the photo active surface area, and c) occlusion of H^+ ions that were generated by the reaction [4.7] not reaching the counter electrode but reacting with the bismuth oxide and dissolving the photo active material through the reaction [4.8]:

$$2H_2O + 4h^+ \rightarrow 4H^+ + O_2 \qquad [4.7]$$

$$Bi_2O_3 + 2H^+ \rightarrow 2BiO^+ + H_2O \qquad [4.8]$$

The detrimental effect of oxygen bubbles sticking to the surface and occlusion of H^+ ions would be more pronounced in the nanoporous surface than a planar surface. It is envisaged that the shadowing effect of oxygen bubbles and occlusion of H^+ ions could have influenced the photocurrent decay behavior of the nanoporous bismuth oxide samples. If the photocurrent decay was influenced by the occlusion of the H^+ ions, then steeper photocurrent decay was expected in the low pH electrolyte. In contrast, the photocurrent at a constant potential decayed much faster in the 1 M KOH electrolyte (Figure 4.2(b)) than in the 0.5 M Na_2SO_4, even though the oxygen evolution in high pH electrolyte is given by

$4OH^- + 4h^+ \rightarrow 2H_2O + O_2$. Therefore, the shadowing effect created by the oxygen bubbles by sticking to the nanoporous surface of the electrode could be predominant.

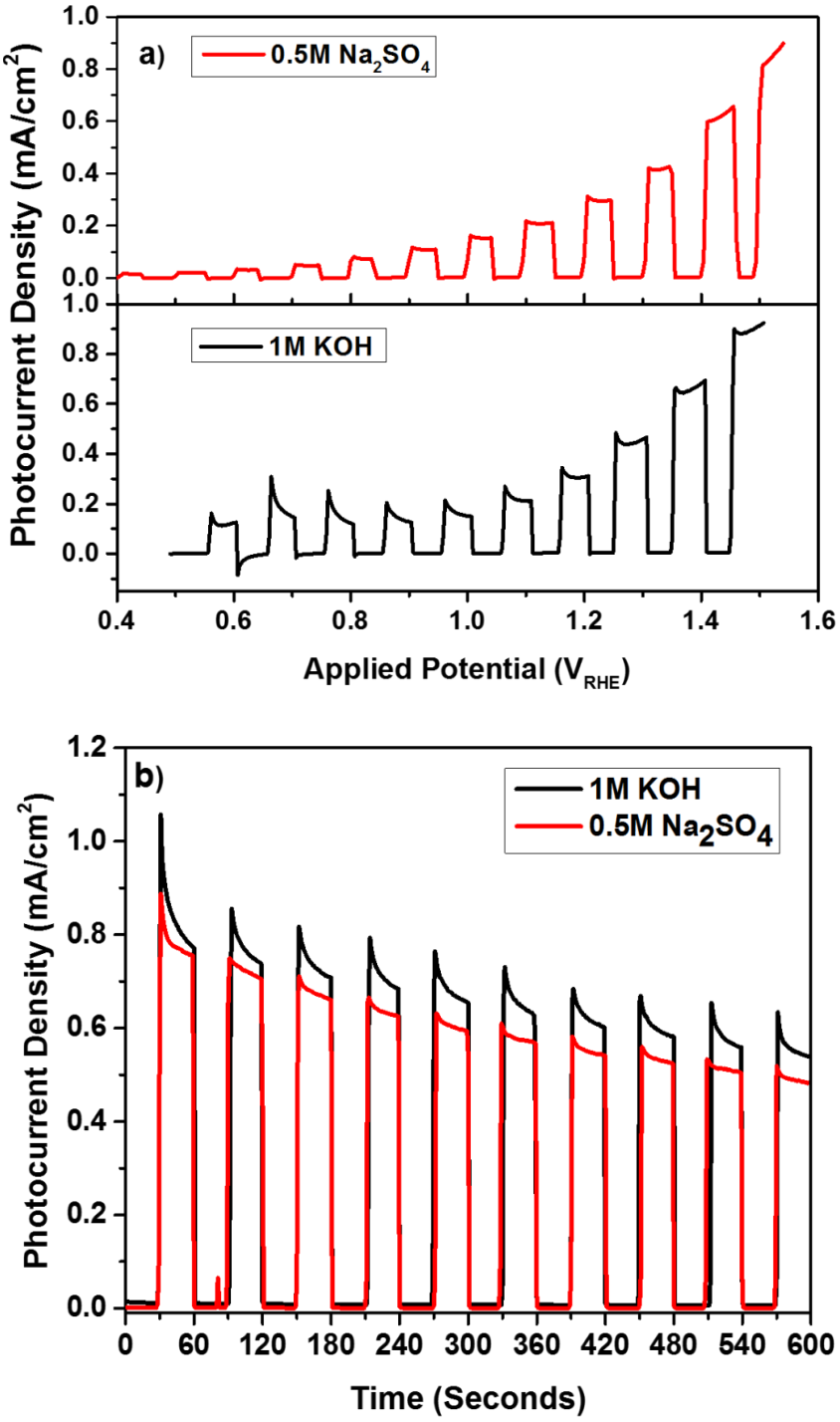

Figure 4.2. (a) I-V characteristics and (b) Potentiostatic current transients of nanoporous Bi_2O_3 in 1 M KOH and 0.5 M Na_2SO_4 under chopped illumination

4.4.2.2. Effect of Stirring

In order to understand the shadowing effect of oxygen bubble, photoelectrochemical experiments were carried out on the nanoporous samples under vigorously agitated condition using a mechanical stirrer in 1 M KOH. The results are shown in Figure 4.3(a). The stirring of the electrolyte for forceful removal of oxygen bubbles from the nanoporous surface was not effective since there was no noticeable change in the photocurrent densities between these two experimental conditions. The effect of occlusion of H^+ ions within the nanopores of the bismuth oxide should be more pronounced when the pH of the electrolyte is low. However, comparison of the photocurrent Vs time plots in 1 M KOH solution (pH: 13.7) and 0.5 M Na_2SO_4 (pH: 5.8) indicated that the pH of the electrolyte did not significantly affect the current decay as seen in Figure 4.2. The current decay was more abrupt in 1 M KOH than in the 0.5 M Na_2SO_4 electrolyte. In order to mitigate the photocurrent decay of the nanoporous bismuth oxide the next strategy adopted was to minimize the accumulation of the photo generated holes at the electrode/electrolyte interface. As indicated in the experimental section, two types of hole scavengers were investigated, viz., 1) methanol, and 2) hydrogen peroxide.

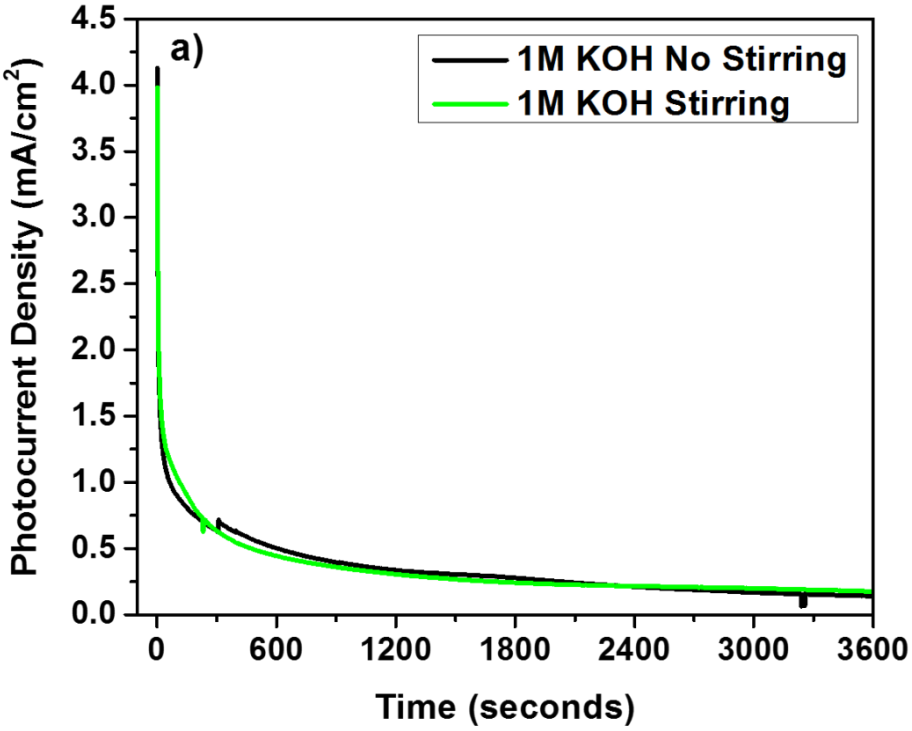

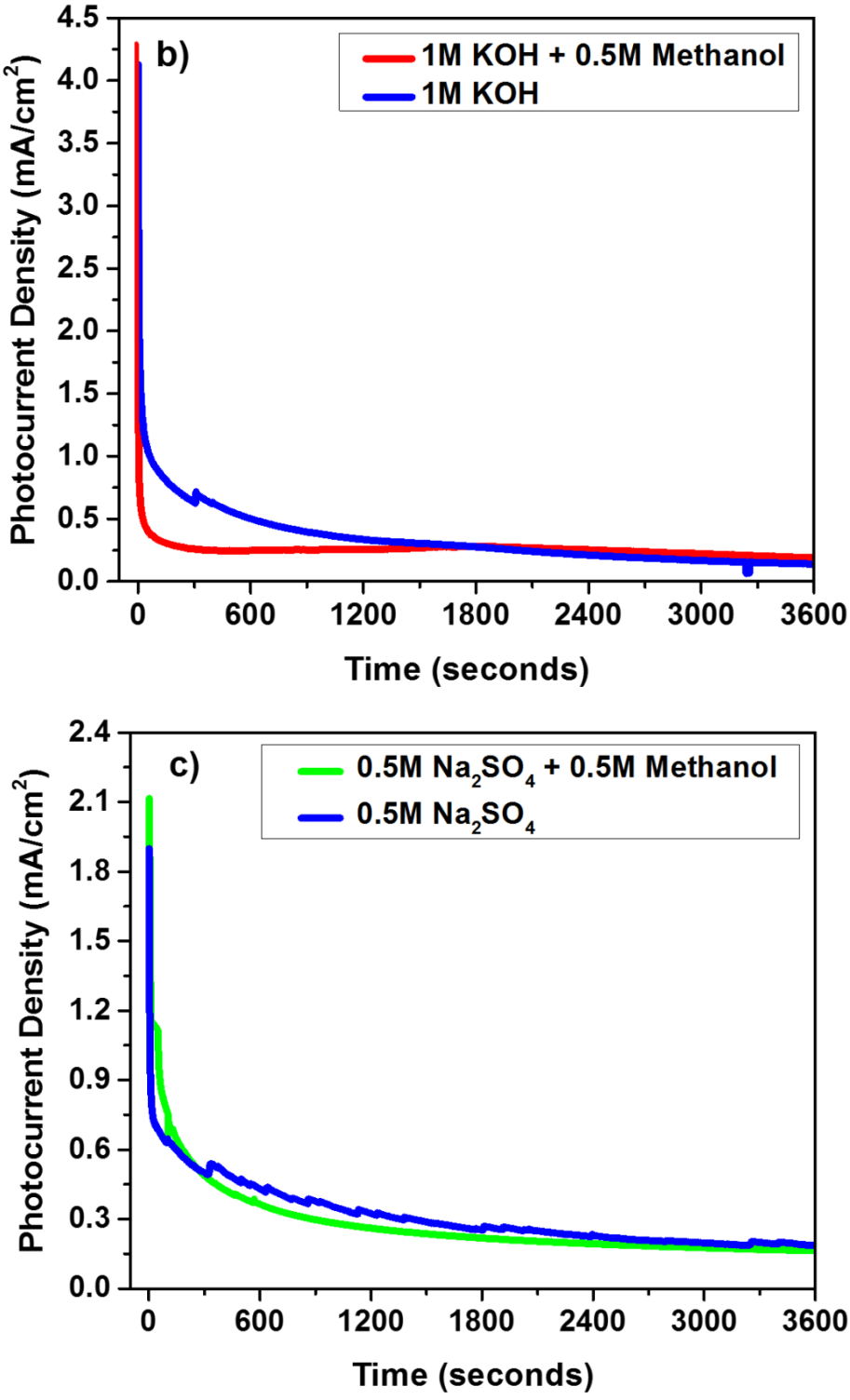

Figure 4.3. (a) Potentiostatic current transients of nanoporous Bi_2O_3 at 1.5 V_{RHE} in 1 M KOH under continuous illumination with and without stirring. Potentiostatic current transients with the addition of 10 vol % methanol as hole-scavenger for the nanoporous Bi_2O_3 at 1.5 V_{RHE} in (b) 1 M KOH solution; and (c) 0.5 M Na_2SO_4 solution.

4.4.2.3. Effect of Hole Scavengers

Methanol addition:

The results of the addition of 10 vol% methanol in 1 M KOH and 0.5 M Na_2SO_4 solutions are given in Figure 4.3 (b) and (c), respectively. The potentiostatic tests at 1.53 V_{RHE} did not show increase in the photocurrent with the addition of methanol in both the pH conditions on the nanoporous bismuth oxide samples. The absence of hole scavenging effect of methanol on the nanoporous β-Bi_2O_3 electrodes was in contrast to the result observed on the $BiVO_4$ by Sayama et al.[17] However, Long et al reported no increase in the photato conversion efficiency with the addition of methanol for the $BiVO_4$/Co_3O_4 composite electrodes. Trapping of holes by the Co_3O_4 layer at a potential that was not positive enough to oxidize methanol was attributed to the ineffectiveness of the methanol addition.[14] The methanol oxidation occurs by the following steps with the TiO_2 photoelectrodes in basic electrolytes[38]:

$$OH^- + h^+ \rightarrow OH_s^* \qquad [4.9]$$

$$CH_3OH + OH_s^* \rightarrow CH_2OH^* + H^+ + OH^- \qquad [4.10]$$

$$CH_2OH^* \rightarrow HCHO + H^+ + e^- \qquad [4.11]$$

The redox potential for CH_2OH^*/HCHO was at -0.95 V_{NHE} that was above the conduction band edge of the TiO_2 and thus directly injected electrons in to the conduction band of the TiO_2 resulting in the photocurrent enhancement.[39] However, in order to observe the current enhancement, the required intermediate was the formation of hydroxymethyl radical. In addition, the semiconductor should have a strong adsorption constant for the CH_2OH^* radical and a high electronic coupling for easy charge transfer. The absence of current enhancement with the addition of methanol for the nanoporous β-Bi_2O_3 indicated that dehydrogenation of methanol to CH_2OH^* did not occur. Campbell and Parsons reported that submonolayer coverage of Bi^{3+} on to Pt electrode inhibited oxidation of methanol.[40] On the other hand Bi^{3+} coverage on Pt improved the oxidation of formic acid. Similar observations were made by other researchers as well.[41, 42] Yang observed that bismuth was not a good catalyst for the

adsorption and dehydrogenation of methanol molecules. Therefore, the absence of the enhancement of photocurrent with methanol addition could be due to the poor catalytic behavior of bismuth species for methanol dehydrogenation.[42]

Addition of Hydrogen Peroxide: I-V Characteristics

The addition of hydrogen peroxide as hole scavenger enhanced the photocurrent densities of the nanoporous bismuth oxide samples. Figures 4.4 (a) and (b) show the current density Vs applied potential plots (*I-V* plots) of nanoporous Bi_2O_3 with and without the addition of 0.15 M and 0.3 M H_2O_2 to 1 M KOH electrolyte. Adding hydrogen peroxide to 1 M KOH lead to a steep increase in the photocurrent density as the applied potential increased from OCP to 0.6 V_{RHE} before reaching almost a plateau value of 6 and 10 mA/cm^2 in 0.15 M H_2O_2 and 0.3 M H_2O_2 additions, respectively. Further increase in the applied potential increased the photocurrent at a lower rate and the observed maximum current densities were 8 and 13 mA/cm^2 at 1.53 V_{RHE} in presence of 0.15 M and 0.3 M H_2O_2, respectively. The I-V behavior in the absence of H_2O_2 was different, where the rate of increase in the photocurrent was higher in the potential range of 0.9 to 1.5 V_{RHE} even though the maximum current was only about 1 mA/cm^2 at 1.5 V_{RHE} in 1 M KOH. The plateau like *I-V* plots observed above 0.6 V_{RHE} potential range in the hydrogen peroxide containing electrolytes could be attributed to the saturation of band bending[43]. It is envisaged that the band bending occurred across the nanopore walls of the anodic oxide during the application of bias potential. The presence of an electric field due to the band bending separated the photo generated electrons and holes, and caused a steep increase in the photocurrent in addition to other factors as discussed below. When the space charge layer thickness was equal to the thickness of the nanopore walls at about 0.6 V_{RHE}, the increase in the bias potential did not contribute to the band bending. Therefore, the photocurrent increased only marginally. The maximum dark current density (current recorded without illumination of the samples) is less than 15 µA/cm^2 in the 1 M KOH electrolyte and increased to 24 and 31 µA/cm^2 at 1.53 V_{RHE} in both the concentrations of H_2O_2. Therefore, the observed high photo current densities cannot be accounted for the thermodynamic dissociation of hydrogen peroxide alone. This significant increase in the photo current density with the addition of H_2O_2 could be attributed to the

following reasons, viz., (a) hydrogen peroxide acts as hole scavenger and minimizes the hole accumulation at the photoanode/electrolyte interface that results in more electrons to flow to the counter electrode; (b) the onset potential of the photo current moves to a less positive potential (0.29 V_{RHE} Vs 0.50 V_{RHE}) because of the shift in the redox potential of the O_2/H_2O_2 system to 0.66 V_{RHE} from 1.23 V_{RHE} for O_2/H_2O system; (c) The addition of hydrogen peroxide in high pH electrolyte is associated with the following redox reactions: [44]

$$H_2O_2 \leftrightarrow HO_2^- + H^+; pH > 11.63 \qquad [4.12]$$

$$HO_2^- + h^+ \rightarrow HO_2^* \qquad [4.13]$$

$$HO_2^* \rightarrow O_2 + H^+ + e^- \qquad [4.14]$$

$$HO_2^* + h^+ \rightarrow O_2 + H^+ \qquad [4.15]$$

$$E^0 = 0.67\ V_{RHE} \text{ for } 0.3\ M\ H_2O_2$$

The HO_2* radical is formed by scavenging a hole at the surface of the photoanode by reaction [4.13] and this radical can inject an electron into the conduction band of the β-Bi_2O_3 causing a current doubling effect.[31] Alternately, the HO_2* radical can capture another hole from the photoanode surface as given in the reaction [4.15] and minimize the charge recombination loss which in turn results in the increased photo current; and (d) combination of high pH, highly oxidizing environment created by the H_2O_2 addition, and light illumination resulted in photo conversion of the β-Bi_2O_3 into the BiO_{2-x} phase. The BiO_{2-x} has a lower band gap of ~1.4 eV due to the presence of Bi^{5+} that has a low lying $6s^0$ state and thus moving the conduction band minimum to lower energy level.[45] The composite structure of β-Bi_2O_3-BiO_{2-x} harvests more light in the visible region and enhances the photo current. The formation of BiO_{2-x} phase could have occurred by oxidation of Bi^{3+} to higher valence states following the reactions [4.16] and [4.17].

$$2Bi_2O_3 + H_2O_2 + hv \rightarrow 2Bi_2O_4 + 2H^+ + 2e^- \qquad [4.16]$$

$$2Bi_2O_4 + H_2O_2 + hv \rightarrow 2Bi_2O_5 + 2H^+ + 2e^- \qquad [4.17]$$

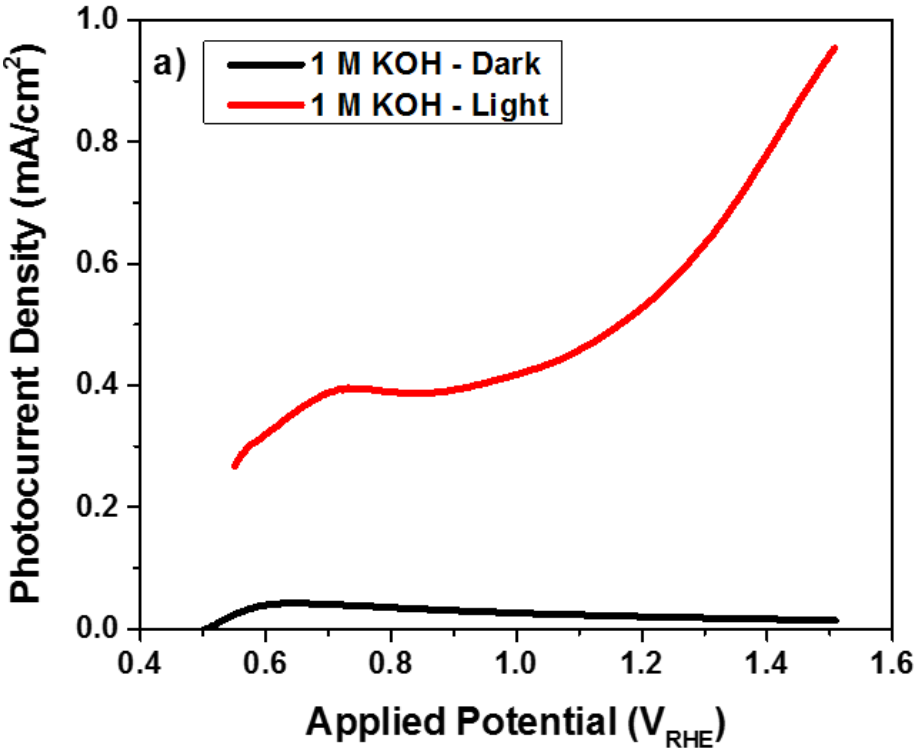
a)
1 M KOH - Dark
1 M KOH - Light
Photocurrent Density (mA/cm^2)
Applied Potential (V_{RHE})
1.0
0.8
0.6
0.4
0.2
0.0
0.4
0.6
0.8
1.0
1.2
1.4
1.6

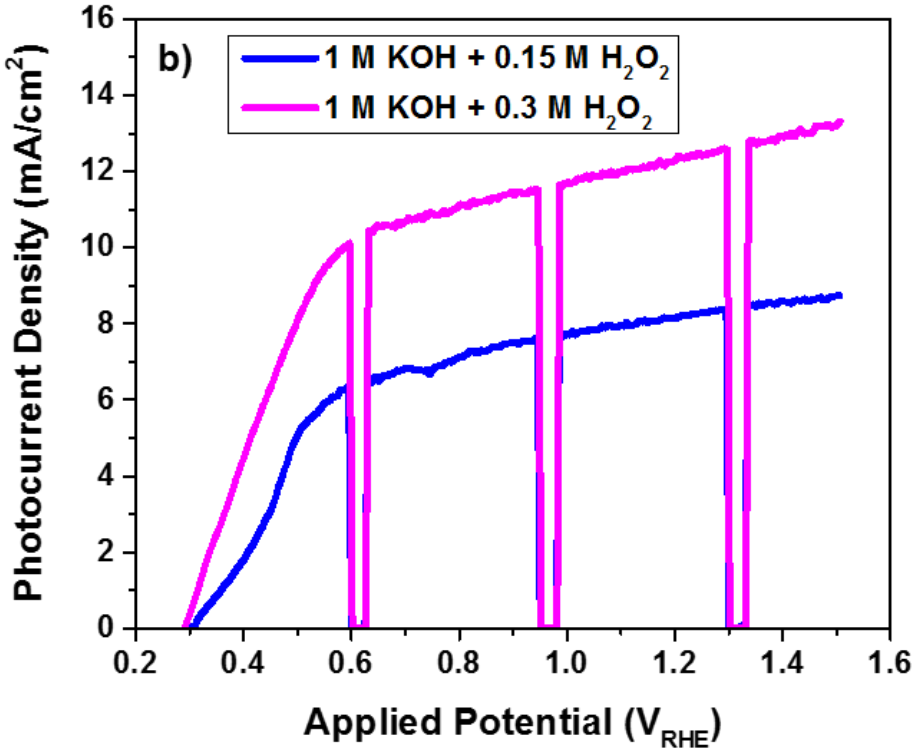
b)
1 M KOH + 0.15 M H_2O_2
1 M KOH + 0.3 M H_2O_2
Photocurrent Density (mA/cm^2)
Applied Potential (V_{RHE})
16
14
12
10
8
6
4
2
0
0.2
0.4
0.6
0.8
1.0
1.2
1.4
1.6

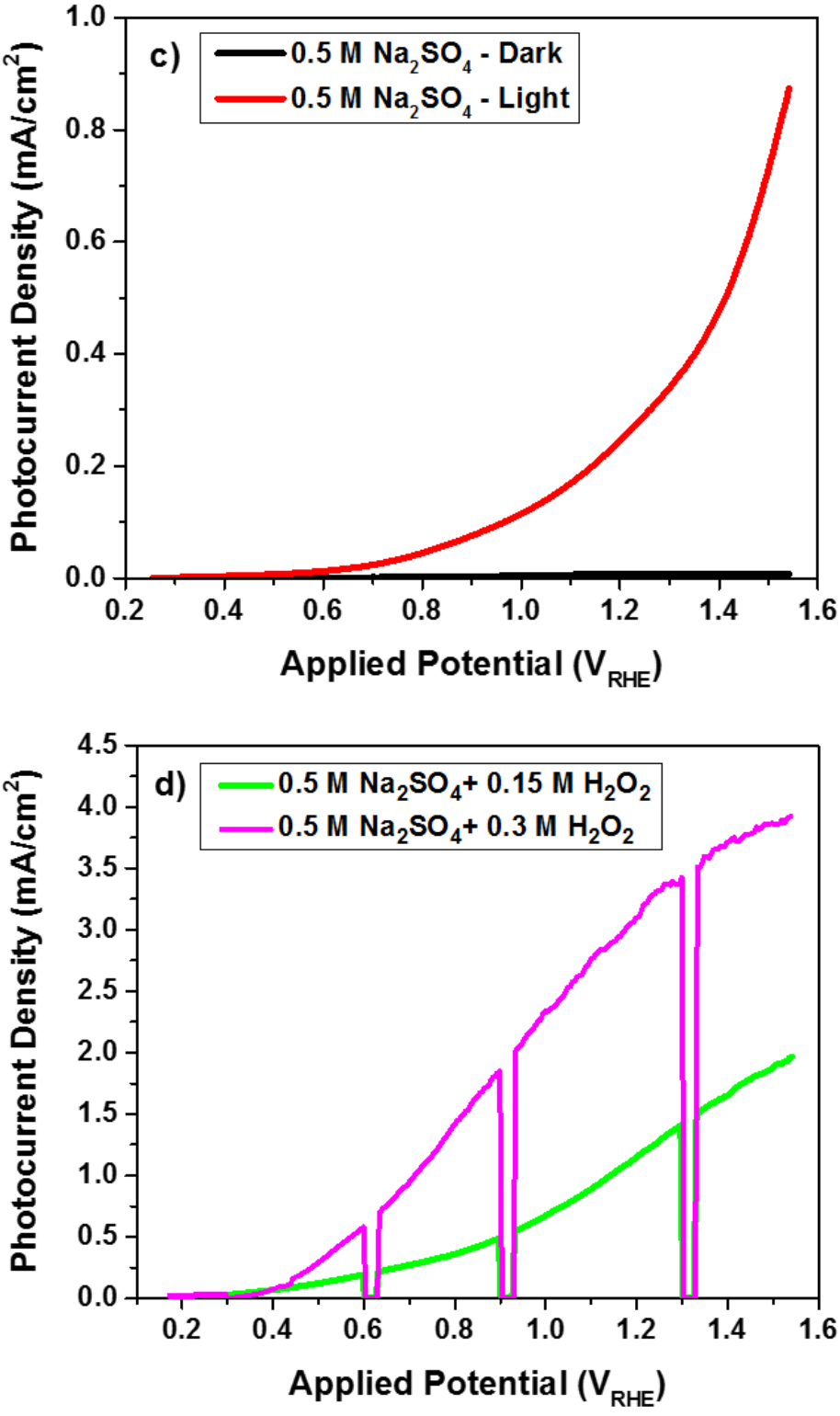

Figure 4.4. I-V characteristics of nanoporous Bi_2O_3 in (a) 1 M KOH (b) 1 M KOH with H_2O_2, (c) 0.5 M Na_2SO_4 and (d) 0.5 M Na_2SO_4 with H_2O_2 under continuous illumination.

The above reactions would result in the current flow through the potentiostat. It was observed that the reactions [4.16] and [4.17] did not result in significant increase in the current without light illumination since the measured dark current was very low.

Moreover, formation of higher valence bismuth ions could be possible by other acid-base reactions as given in the reactions [4.18] – [4.22].

$$Bi_2O_3 + 4H^+ \rightarrow 2BiOH^+ + H_2O \qquad [4.18]$$

$$Bi_2O_3 + 2H^+ \rightarrow 2BiO^+ + H_2O \qquad [4.19]$$

$$2BiO^+ + OH^- \rightarrow BiOOH \qquad [4.20]$$

$$BiOOH + OH^- \rightarrow BiO_2^- + H_2O \qquad [4.21]$$

$$2BiO_2^- + 2OH^- \rightarrow Bi_2O_5 + H_2O + 4e^- \qquad [4.22]$$

$$Bi_2O_3 + Bi_2O_5 \rightarrow 2Bi_2O_4 \qquad [4.23]$$

Presence of mixed valence states of Bi^{3+} and Bi^{5+} could be considered as formation of Bi_2O_{4-x} or BiO_{2-x} type oxide structures on the photoanode surface. The partial transformation of the stoichiometry of the oxide would alter the electronic and photo catalytic behavior of the photoanode. The morphological and structural changes occurring on the photoanode will be discussed in later sections of this paper.

Figures 4.4 (c) and (d) show the current Vs potential plots of nanoporous bismuth oxide samples in 0.5 M Na_2SO_4 solution with and without the addition of 0.15 M and 0.3 M H_2O_2. The photocurrent densities increased with increase in the concentration of H_2O_2 and with the increase in the applied potentials. There was no current plateau behavior observed in this electrolyte. The dissociation of hydrogen peroxide electrolytes with a pH lower than 11.63 can be expressed by the reaction [4.24]:

$$H_2O_2 \rightarrow O_2 + 2H^+ + 2e^- \qquad [4.24]$$

The photo current density of nanoporous Bi_2O_3 in 0.5 M Na_2SO_4 with the addition of H_2O_2 was much lower than that of the 1 M KOH with hydrogen peroxide addition. The maximum photo current density was about 4 mA/cm^2 at 1.5 V_{RHE} in 0.5 M Na_2SO_4 with the addition of 0.3 M H_2O_2, which was about 30% of the photo current recorded in the 1 M KOH + 0.3 M H_2O_2 at the same bias condition. Addition of 0.15 M H_2O_2 to the 0.5 M Na_2SO_4 solution showed a maximum photo current density of only about 2 mA/cm^2 which is just 100% higher than the current density recorded without addition of the hydrogen peroxide.

Addition of Hydrogen Peroxide: I-t Characteristics

Figure 4.5 (a) shows the photocurrent transients (*I-t* plots) recorded in 1 M KOH at a constant potential of 0.65 V_{RHE} with addition of H_2O_2 at two different concentrations. The photocurrent densities were at about 2 and 7 mA/cm^2 at the start of the tests which increased to about 7 and 10 mA/cm^2 in about 150 seconds for the 0.15 M and 0.3 M H_2O_2 additions respectively. After reaching these peak values, the photocurrent was stabilized for 60 seconds and thereafter, approximately after 300 seconds, the current started dropping steadily to around 3 and 4.5 mA/cm^2 by the end of the 1 hour illumination in both concentrations of H_2O_2. The current density at the end of 1-h test was about 40% of the maximum recorded current density. It was observed that under dark condition (without light illumination but with the same bias potential), the current density was about ~32 μA/cm^2 indicating that the observed high current density was only due to the photocatalytic reaction. Similar kind of behavior was observed when the photo current density was recorded at 1.53 V_{RHE} as a function of time in the KOH solution with the additions of H_2O_2 as shown in Figure C2 (a). Applying higher bias potential increased the photo current following the trend observed during the potentiodynamic test. The high current density observed during illumination of the samples in the presence of hydrogen peroxide was attributed predominantly to the high photo activity of the in-situ transformed Bi_2O_{4-x} phases. The contribution from the oxidative current due to transformation of Bi^{3+} to Bi^{4+} was considered to be less significant. A conservative estimation of charge passed through the Bi^{3+} oxidation reaction would be only about 0.4 Coulomb (assuming that the entire (~1.9 μmol) Bi_2O_3 photo anode converted to Bi_2O_5). This value was only about 13% of the total charge accumulated during the first 300

seconds of illumination of the sample at 0.65 V_{RHE}. When the light illumination was interrupted, the current dropped to less than 50 μA/cm^2. These observations clearly indicated that the high current density recorded during the illumination was due to photo catalytic behavior and not photo degradation of the photoanode.

Figure 4.5 (b) shows the hydrogen evolution at the Pt-counter electrode as a function of time. The volume of hydrogen was measured by the water displacement method using a graduated pipette. The hydrogen volume collected in the pipette was compared with the values of charge accumulated by integrating the photo current density recorded during the photo electrochemical experiments as a function of time. The addition of 0.15 and 0.3 M H_2O_2 to the 1 M KOH electrolyte increased the hydrogen evolution rate to 1.7 and 2.6 ml/h per 1 cm^2 area of the photoanode at 0.65 V_{RHE}. Analysis of the collected gas in the pipette using gas chromatography confirmed only the presence of hydrogen. Initially the samples were of pale yellow in color indicative of the β-Bi_2O_3 phase. The color of the sample did not change when tested in the 1 M KOH solution without H_2O_2 addition. The samples tested in the 1 M KOH + H_2O_2 turned into yellowish-brown, typical of the BiO_{2-x} phase indicating occurrence of the phase transformation. Hydrogen evolution rate for samples tested in presence and absence of H_2O_2 at 1.53 V_{RHE} is shown in Figure C2 (b). It is noted that the hydrogen evolution rate was about 0.030 ml/h per 1 cm^2 area of the β-Bi_2O_3 photoanode in the KOH solution (Figure C2 (b)).

Figures 4.5 (c) and (d) show the photo current density vs time plots at 0.80 V_{RHE} and hydrogen evolution rates, respectively for the pH 5.8 electrolyte (0.5 M Na_2SO_4) with different H_2O_2 concentrations. The measured volume of hydrogen was compared with the charge calculated from the integration of the photo current Vs time plot. The amounts of hydrogen collected in various electrolytes at a bias potential of 1.53 V_{RHE} are listed in the Table 4.1. Photo current density was recorded at 1.53 V_{RHE} as a function of time in the 0.5 M Na_2SO_4 solution with the additions of H_2O_2 and hydrogen evolution rate is shown in Figures C2 (c) and (d). The amount of hydrogen evolved per unit surface area of the electrode per hour was almost the same for both the pH conditions without the addition of hole scavengers. When

hydrogen peroxide was added, the rate of hydrogen evolved increased by an order of magnitude in both pH conditions, and the KOH (pH 13.7) electrolyte showed higher hydrogen evolution rate than the Na_2SO_4 (pH 5.8) electrolyte. The Faradaic efficiency was low without the addition of hole scavengers which could be attributed to the limitation of the experimental arrangement to measure very low volume of hydrogen evolution. When the solubility of hydrogen in the electrolyte column was taken into account, the Faradaic efficiency was comparable to that of the hole scavenger additions. Figure 4.6 (a) shows long term stability of samples tested in Na_2SO_4 and pH 7 buffer in H_2O_2 at 0.80 V_{RHE}.

Table 4.1. Hydrogen collected at the Pt counter electrode compartment by water displacement method using nanoporous bismuth oxide as photo electrode at an applied bias of 1.53 V_{RHE}.

Electrolyte	Hydrogen collected by water displacement method, (ml/cm^2.h)	Hydrogen evolution calculated by photo current integration, (ml/cm^2.h)	Faradaic Efficiency, %
1 M KOH	0.115	0.142	80.98
1 M KOH + 0.15 M H_2O_2	2.04	2.07	98.55
1 M KOH + 0.3 M H_2O_2	2.12	2.17	97.69
0.5 M Na_2SO_4	0.115	0.13	88.46
0.5 M Na_2SO_4 + 0.15 M H_2O_2	0.76	0.78	97.43
0.5 M Na_2SO_4 + 0.3 M H_2O_2	1.412	1.438	98.19

Table 4.2. Cathodic charge accumulation due to surface states on the nanoporous Bi_2O_3 at different potentiostatic conditions with chopped illumination.

Potential range, V_{RHE}	No H_2O_2, (A.s)	0.15 M H_2O_2, (A.s)	0.3 M H_2O_2, (A.s)
0.5	-1.4×10^{-4}	-5.2×10^{-5}	-4.2×10^{-5}
0.7	-8.5×10^{-5}	-2.8×10^{-5}	-4.3×10^{-6}
0.9	-8.7×10^{-6}	-3.7×10^{-6}	
1.1	-3.0×10^{-6}		

In order to understand the reason for the increase in the photo current densities with the addition of hydrogen peroxide, current transient measurements were carried out by chopping the illumination at quick successions. Figure 4.6 (b) shows the current transients at different applied potentials under chopped illumination with various H_2O_2 additions. At lower

bias potentials cathodic current transients were observed in all the electrolytes. Table 4.2 summarizes the cathodic charge accumulation at the surface states of the samples. The results show that the addition of hydrogen peroxide decreased the cathodic charge accumulation. Furthermore, the potential at which no cathodic current transients observed shifted to less noble values with the addition of hydrogen peroxide. The absence of negative current transient when the light was interrupted at less anodic potentials implied that the accumulation of holes at the surface of the photoanode was absent and the electrons from the conduction band flowed through the potentiostat to the counter electrode suppressing recombination with holes. Furthermore, when the illumination was on, the positive current transients showed exponential type decay in KOH without H_2O_2 addition. This exponential type decay was clearly absent and almost a plateau current behavior was noticed with the addition of hydrogen peroxide, except for the instantaneous current spike when the illumination was on. This plateau anodic current indicated that all the photo generated holes reached the electrode/electrolyte interface and participated in the oxygen evolution reaction:

$$HO_2^- + 2h^+ \rightarrow O_2 + H^+ \qquad [4.25]$$

At low pH, the oxygen evolution reaction can be given as:

$$H_2O_2 + 2h^+ \rightarrow O_2 + 2H^+ \qquad [4.26]$$

The photo current results in two different pH conditions revealed that reaction [4.25] could occur at a faster rate than that of reaction [4.26] on the nanoporous Bi_2O_3 samples because partial dissociation of hydrogen peroxide had already occurred in the high pH condition as noted from the reaction [4.12].

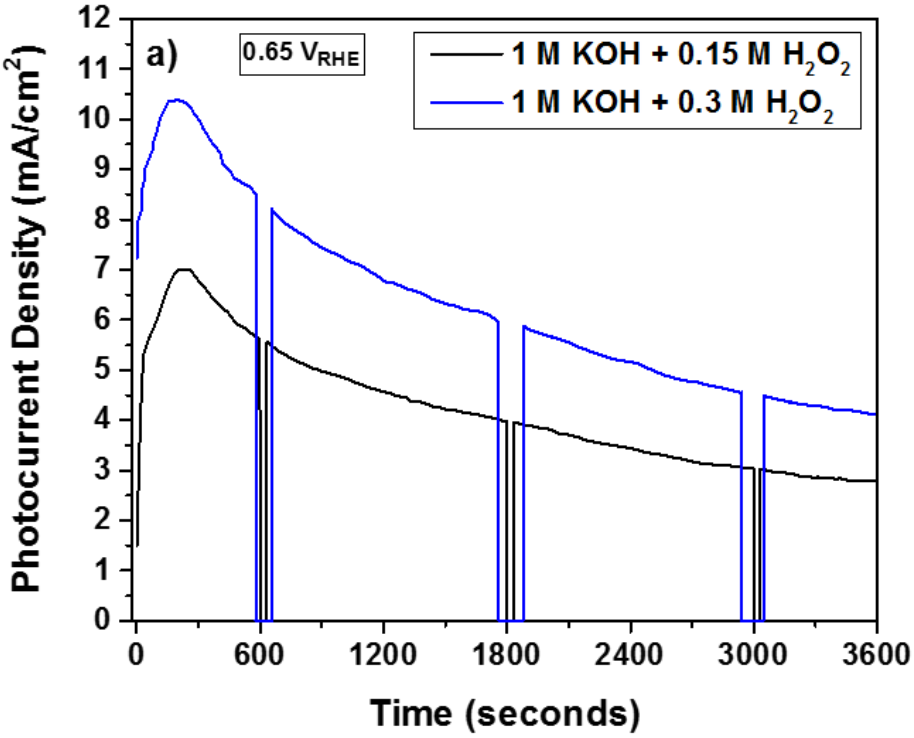
a)
0.65 V$_{RHE}$
1 M KOH + 0.15 M H$_2$O$_2$
1 M KOH + 0.3 M H$_2$O$_2$
Photocurrent Density (mA/cm^2)
Time (seconds)
0
1
2
3
4
5
6
7
8
9
10
11
12
0
600
1200
1800
2400
3000
3600

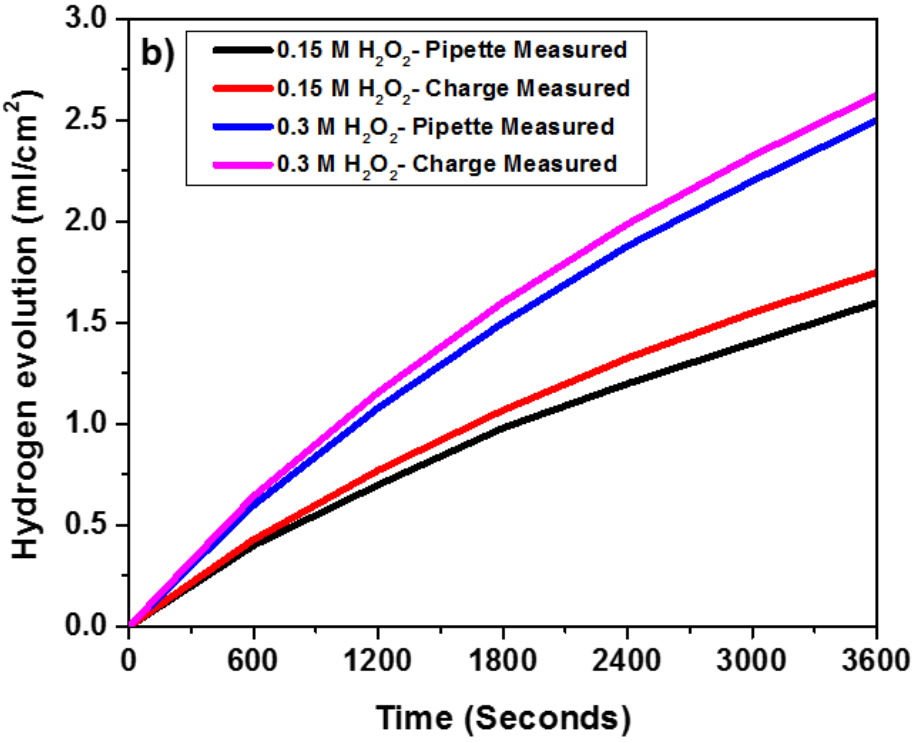
b)
0.15 M H$_2$O$_2$- Pipette Measured
0.15 M H$_2$O$_2$- Charge Measured
0.3 M H$_2$O$_2$- Pipette Measured
0.3 M H$_2$O$_2$- Charge Measured
Hydrogen evolution (ml/cm^2)
Time (Seconds)
0.0
0.5
1.0
1.5
2.0
2.5
3.0
0
600
1200
1800
2400
3000
3600

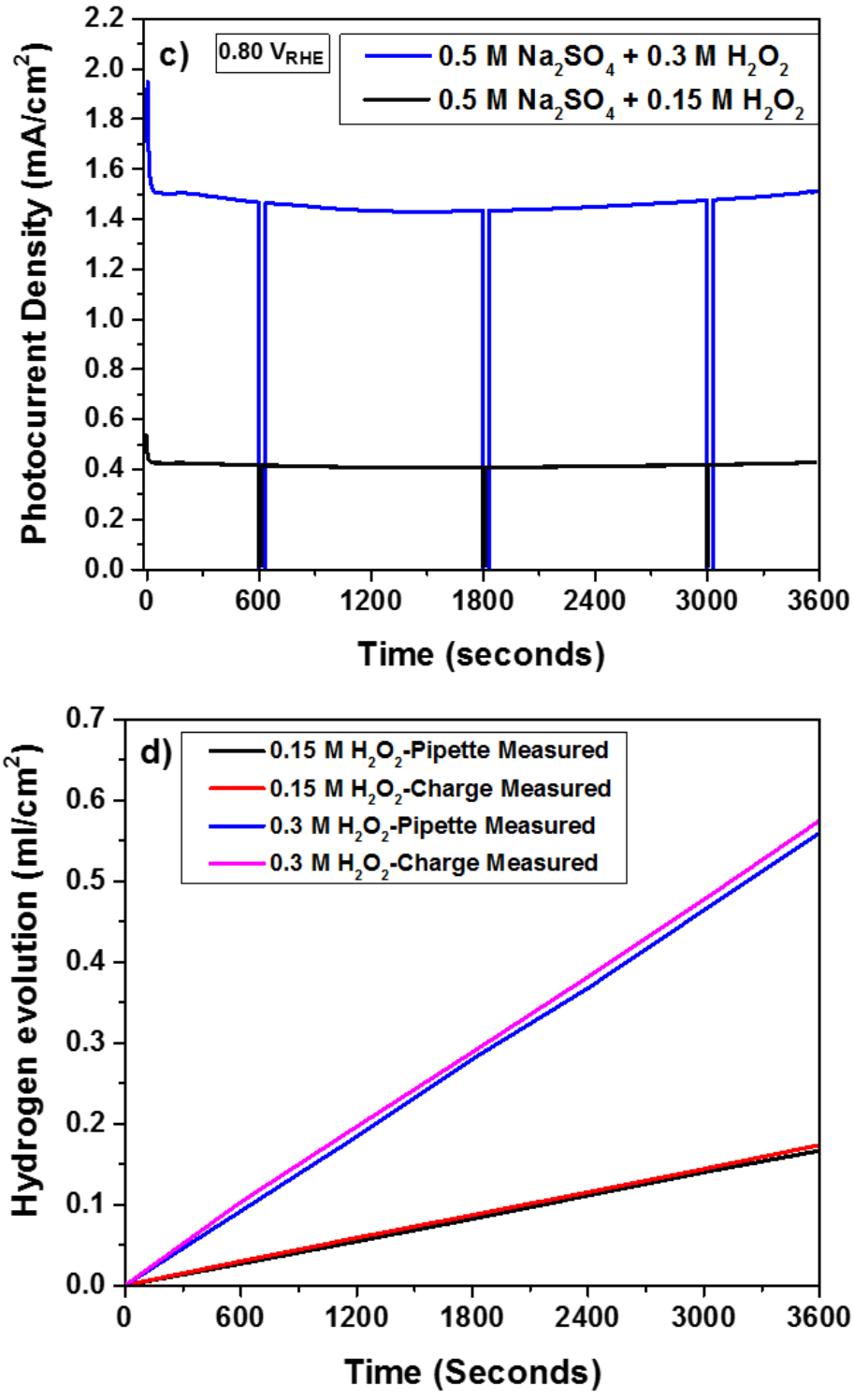

Figure 4.5. (a) Potentiostatic current transients with the addition of H_2O_2 as hole-scavenger for the nanoporous Bi_2O_3 at 0.65 V_{RHE} in 1 M KOH solution; (b) Cumulative hydrogen evolution as a function of time measured by water displacement using a pipette in comparison with the charge accumulation. (c) Potentiostatic current transients with the addition of H_2O_2 as hole-scavenger for the nanoporous Bi_2O_3 at 0.8 V_{RHE} in 0.5 M Na_2SO_4 solution; (d) Cumulative hydrogen evolution as a function of time measured by water displacement using a pipette in comparison with the charge accumulation.

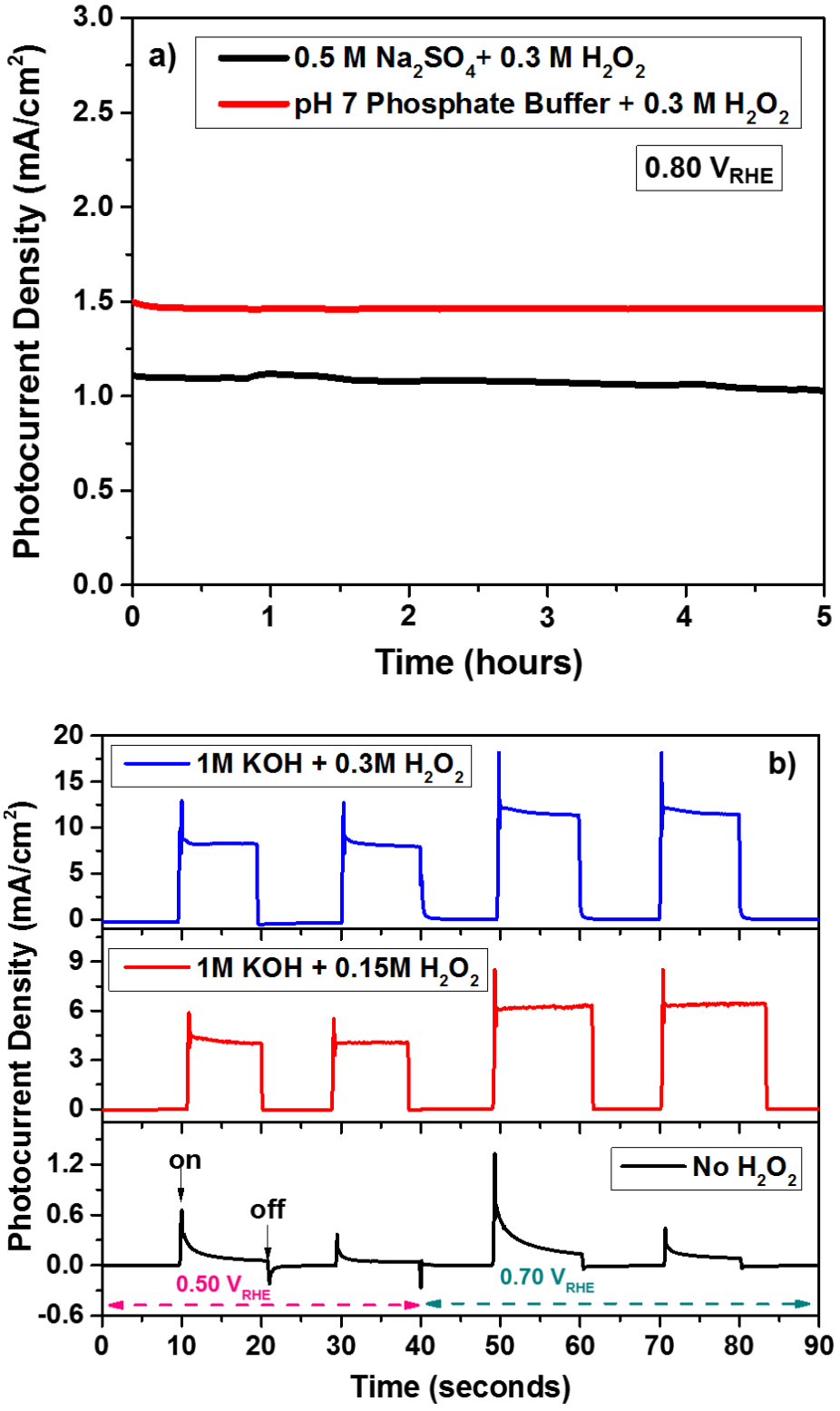

Figure 4.6. (a) Potentiostatic current transients with the addition of H_2O_2 as hole-scavenger for the nanoporous Bi_2O_3 at 0.80 V_{RHE} in 0.5 M Na_2SO_4 and pH 7 Phosphate buffer solution. (b) Current transients at different bias potentials with chopped illumination conditions in presence of H_2O_2 as hole-scavenger for the nanoporous Bi_2O_3 in 1 M KOH solution.

4.4.3. Material testing after photoelectrochemical testing

In order to understand the distinctive behavior of the photoanode in the presence of H_2O_2 in KOH, potentiostatic tests were interrupted at 200 and 300 seconds to characterize the samples for morphological and compositional changes using tools like SEM, XRD, XPS and Raman spectroscopy. Morphology of the sample removed at 200 seconds exhibited presence of both nanoporous and agglomerated structure indicating loss of high surface nanoporous morphology (Figure 4.7 (a)). After reaching 300 seconds, the sample demonstrated a complete loss of the nanoporous morphology as observed in Figure 4.7 (b). This agglomerated morphology was further stabilized thereafter till the end of the experiment. Correspondingly, the morphology of the sample tested in dark condition in 1 M KOH + 0.3 M H_2O_2 also changed to agglomerated microstructure, however no increase in dark current density was observed as seen in Figure 4.5 (a). It was observed that the nanoporous morphology was not effected when tested in the 1 M KOH under dark and illuminated conditions.[26] These observations indicated that addition of H_2O_2 caused β-Bi_2O_3 to BiO_{2-x} phase transformations that resulted in morphological changes. These morphological changes due to nucleation and growth of new BiO_{2-x} phase from the nanoporous β-Bi_2O_3 decreased the effective surface area of the photoanode and caused decrease in the photocurrent density. The sample obtained at 300 seconds interruption was characterized using UV-DRS and XRD. The results confirmed the presence of the BiO_{2-x} phase in addition to β-Bi_2O_3. Figure 4.7(c) shows the results of optical absorbance as a function of wavelength. The sample prior to the photo electrochemical testing (labeled as β-Bi_2O_3) absorbs light with wavelengths shorter than 530 nm, corresponding to a bandgap of 2.34 eV. The sample photo electrochemical tested in 1 M KOH + 0.3 M H_2O_2 solution at 0.65 V_{RHE} for 300 seconds (labeled as β-Bi_2O_3/BiO_{2-x} composite) shows increased light absorbance and absorbance of longer wavelength light as well. A small absorbance shoulder taking off at 680 nm is observed indicating the presence of a narrow band gap phase. The band gap of the composite structure is considered to be 2.19 eV. Similar results are observed from the Tauc plots constructed using the β-Bi_2O_3/BiO_{2-x} composite sample as shown in Figure C3 (supporting information). Figure 4.7 (d) shows the XRD pattern of the sample after photo electrochemical testing in the 1 M KOH + 0.3 M H_2O_2 solution at

0.65 V_{RHE} for 300 s. The sample shows XRD peaks associated with β-Bi_2O_3 (JCPDS card # 027-0050), BiO_{2-X} (JCPDS 047-1057), and bismuth from the substrate. The peak at 2θ = 29.5 is considered to be a characteristic peak of BiO_{2-x} by Hameed et al,[46] which is observed in this study also. The XRD results substantiates the formation of BiO_{2-x} phase in the photo electrochemical tested sample. In order to determine the valence states of bismuth, X-ray photoelectron spectroscopy was carried out on samples tested in 1 M KOH + 0.3 M H_2O_2 solution at 0.65 V_{RHE} with and without illumination and the results are presented in Figure 4.7 (e) and (f). The high resolution peaks of Bi *4f* showed peaks at 158.4 eV and 164 eV corresponding to Bi $4f_{7/2}$ and Bi $4f_{5/2}$, respectively. The broader signals of the 4f orbitals and the shoulders observed at higher binding energies can be deconvoluted into two couplets corresponding to Bi^{3+} and Bi^{5+} as seen in Figure 4.7 (e). The larger couplets of Bi $4f_{5/2}$ and $4f_{7/2}$ centered around binding energies of 158.4 and 163.8 eV could be assigned to the Bi^{3+}.[47] The resolved smaller couplets at higher binding energies at 159.3 and 165.1 eV could be assigned to the Bi^{5+} that were present to the formation of the new BiO_{2-X} phase.[48] It is interesting to note that presence of Bi^{5+} could be observed in the sample tested in the dark condition. However, the intensities of the higher binding energy couplet were much smaller than those observed on the sample tested under illuminated condition. Figure 4.7 (f) shows the O 1s spectra of the samples tested in dark and light conditions in 1 M KOH + 0.3 M H_2O_2. The peak is centered around 530.2 eV with a significant shoulder at higher binding energies and the shoulder centered around 532 eV could be attributed to the presence of oxygen vacancies and the presence of BiO_{2-x} phase.[48] Figures 4.8 and 4.9 compare the surface morphologies of the β-Bi_2O_3 photoanodes after 1 hour long photoelectrochemical testing at 1.5 V_{RHE} in the 1 M KOH and 0.5 M Na_2SO_4 electrolytes, respectively, with and without H_2O_2 additions. The surface morphology of the photoanode was not altered when tested in the 0.5 M Na_2SO_4 electrolyte with and without H_2O_2 additions. No phase transformation was observed in the low pH electrolyte. On the other hand, significant surface morphology was observed when tested in the 1 M KOH electrolyte with the addition of H_2O_2. This morphological change was attributed to the transformation of the β-Bi_2O_3 to Bi_2O_{4-x} phase.

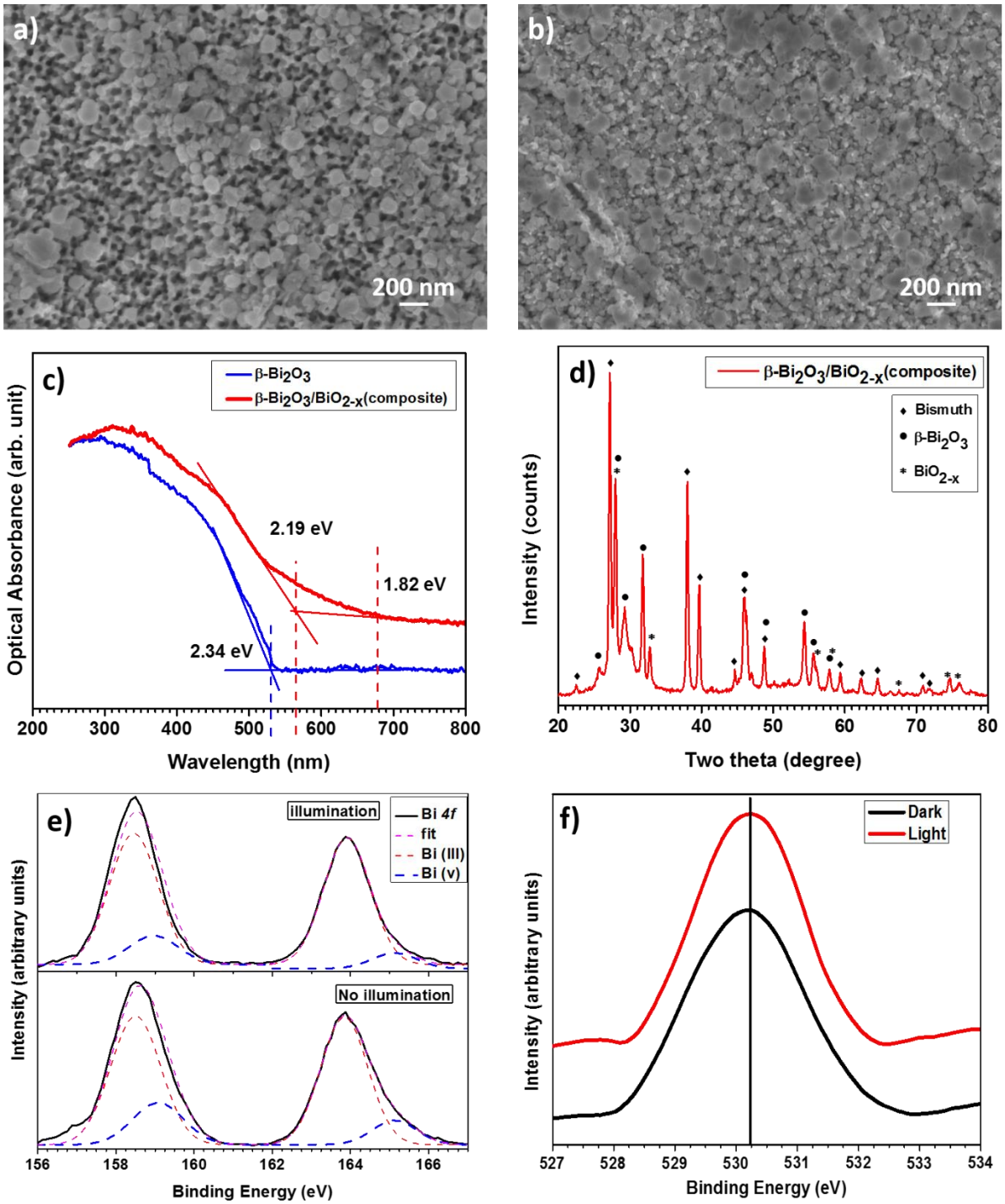

Figure 4.7. Characterization results of the β-Bi_2O_3 photoanode after initial illumination in 1 M KOH + 0.3 M H_2O_2 at 0.65 V_{RHE}. (a) surface morphology after 200 s testing; (b) surface morphology after 300 s testing; (c) UV-Vis diffuse reflectance spectra before and after testing for 300 s in 1 M KOH + 0.3 M H_2O_2 at 0.65 V_{RHE}, (d) XRD pattern of the sample after photo electrochemical testing in the 1 M KOH + 0.3 M H_2O_2 solution at 0.65 V_{RHE} for 300 s; (e) X-ray photoelectron spectroscopy of samples tested in 1 M KOH + 0.3 M H_2O_2 solution at 0.65 V_{RHE} with and without illumination: Bi 4f spectra; and (f) O-1s spectra

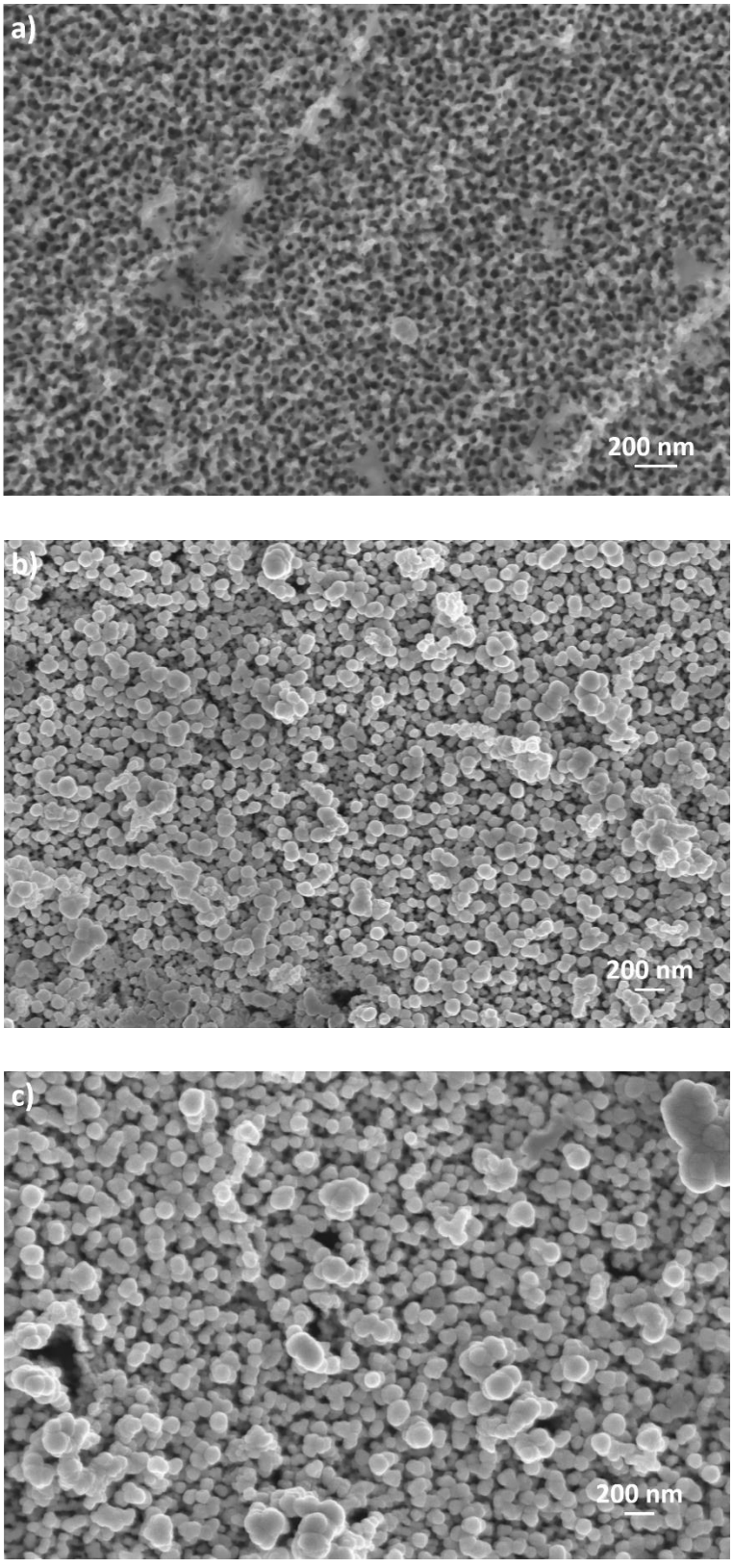

Figure 4.8. Surface morphology of the nanoporous Bi_2O_3 after 1 hour PEC testing in 1 M KOH at 1.5 V_{RHE}, (a) No H_2O_2 addition, (b) 0.15 M H_2O_2 addition, and (c) 0.3 M H_2O_2 addition.

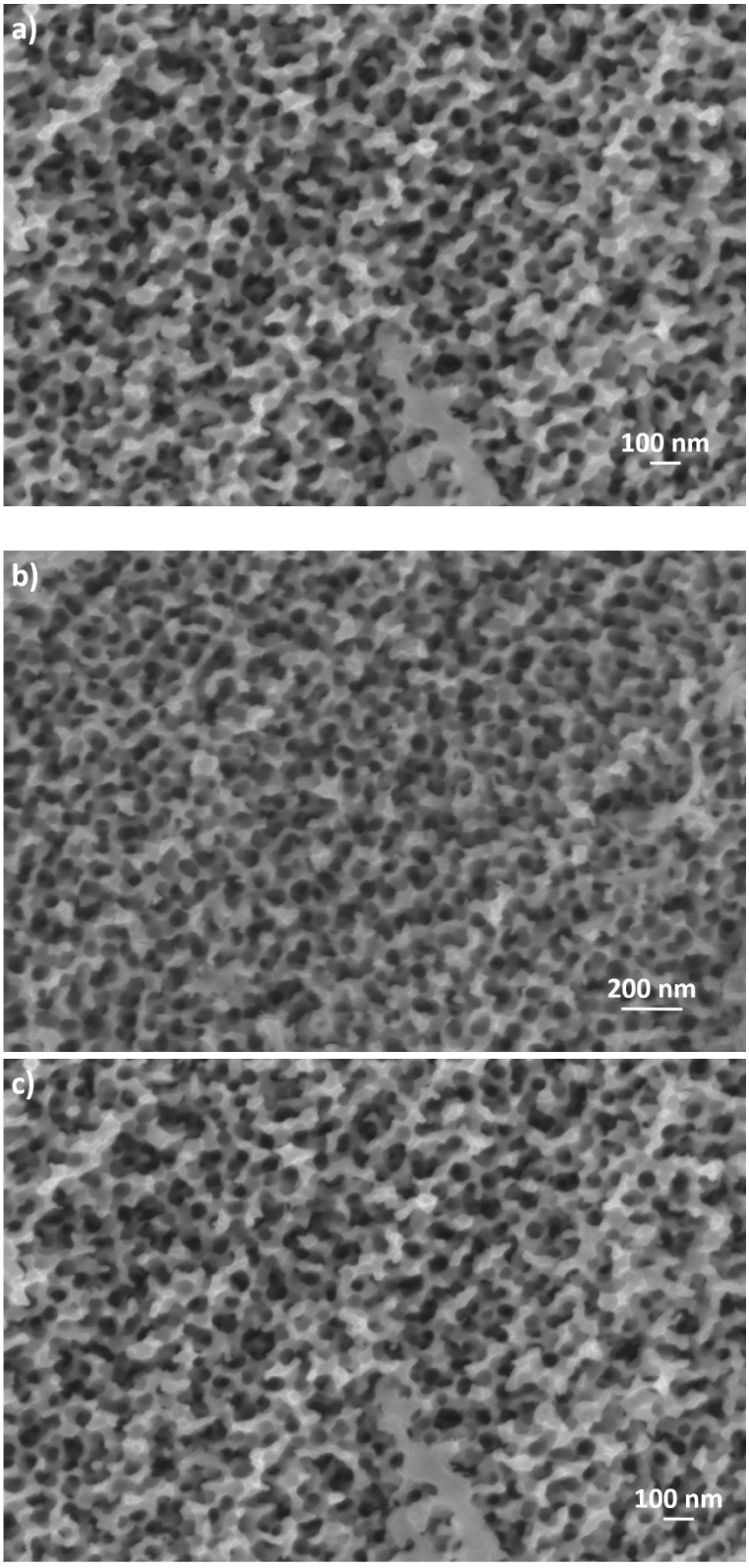

Figure 4.9. Surface morphology of the nanoporous Bi_2O_3 after 1 hour PEC testing in 0.5 M Na_2SO_4 at 1.5 V_{RHE}, (a) No H_2O_2 addition, (b) 0.15 M H_2O_2 addition, and (c) 0.3 M H_2O_2 addition.

4.4.4. Electrochemical impedance spectroscopy

An equivalent circuit for fitting the impedance spectra is given in Figure C4 and the typical electrochemical impedance spectra (EIS) of the nanoporous Bi_2O_3 samples at 1.5 V_{RHE} are given in Figure C5 and C6 (supporting information). The charge transfer is considered to occur through surface states of the top porous film represented by a parallel resistor (R_t)– constant phase element (Y_{top}) components. The other parallel *RC* circuit elements, resistor R_b and leaky capacitor Y_b represent the properties of the barrier layer of the dual layered nanoporous oxide sample. The impedance of a constant phase element or leaky capacitor is given as:

$$Z = \frac{1}{(j.\omega)^{\alpha} Y} \qquad [4.27]$$

Where, Z = impedance, ω = angular frequency, j = √-1, Y represents capacitance due to the space charge layer or interfacial capacitance and has a unit of capacitance when α = 1, surface heterogeneity or continuously distributed time constants for charge-transfer reaction are represented by α <1. The values of the different components of the equivalent circuit are summarized in Tables C1 – C2 (supporting information). The results of the EIS can be summarized as followed: When compared the results of dark and illuminated conditions of the same sample, the resistivity of the surface states (R_{top}) of sample decreased significantly for the illuminated case, and the barrier resistivity (R_b) decreased by orders of magnitude. This could be due to transfer of the photo generated electrons to the back contact of the sample. Mott-Schottky results as given in Tables C3-C5 (supporting information) also corroborated this observation with the increase in the majority carrier densities upon illumination. The dispersed capacitance due to the surface states of the porous layer (Y_{top}) and space charge layer (Y_b) increased significantly after illumination. Since the variations of the impedance values did not follow a particular trend, it was difficult to compare the values of the individual components between different experimental conditions and develop a meaningful insight in order to explain the photo electrochemical behavior of the samples. Figures C7 shows the result of the electrochemical impedance spectroscopy of the

nanoporous bismuth oxide samples after photo electrochemical testing in 1 M KOH + 0.3 M H_2O_2 electrolyte. The impedance results are fitted with an equivalent circuit shown in Figure C8 and the fitted values are summarized in Table C6. The impedance values of the sample tested in the hydrogen peroxide containing electrolytes were considerably smaller and the charge storage capacity was about 100% higher than the sample tested in 1 M KOH. The increased conductivity of the sample tested in the H_2O_2 containing solution is attributed to the formation of BiO_{2-x} phase that has a narrow band gap and charge transfer defects due to non-stoichiometry. However, the results of Mott-Schottky plots were more useful in understanding the photo electrochemical behavior of the samples.

4.4.5. Mott-Schottky analysis

The charge carrier densities of the nanoporous Bi_2O_3 samples were evaluated at different frequencies in 1 M KOH solution without the addition of H_2O_2 and summarized in Table C3 (supporting information). The charge carrier density was not significantly influenced by the test frequency under dark condition. However, when illuminated the charge carrier density increased with decrease in the test frequency. This could be attributed to the ionization of deep level defects present as band gap states. These defects could act as traps for charge carriers or recombination centers. The flat band potential shifted to less negative potentials with the decrease in the frequency under the dark condition while the flat potential of the illuminated condition remained constant at all frequencies and less negative than that of the dark condition. The less negative flat band potential implied accumulation of holes at the electrode surface under the illuminated condition. Addition of 0.15 M H_2O_2 as hole scavenger to 1 M KOH also showed a similar Mott-Schottky behavior as that of 1 M KOH without H_2O_2 for the nanoporous bismuth oxide sample as illustrated in the Table S4 (supporting information). However, with the addition of H_2O_2, the flat band potential was shifted to more negative potentials when illuminated. This observation, clearly indicated that presence of H_2O_2 acted as surface hole scavenger. Furthermore, higher charge carrier density values were observed with the addition of H_2O_2 than the sample tested in the solution without H_2O_2 under the illuminated condition. This could be attributed to the decreased electron-hole recombination losses in the presence of hole scavengers.

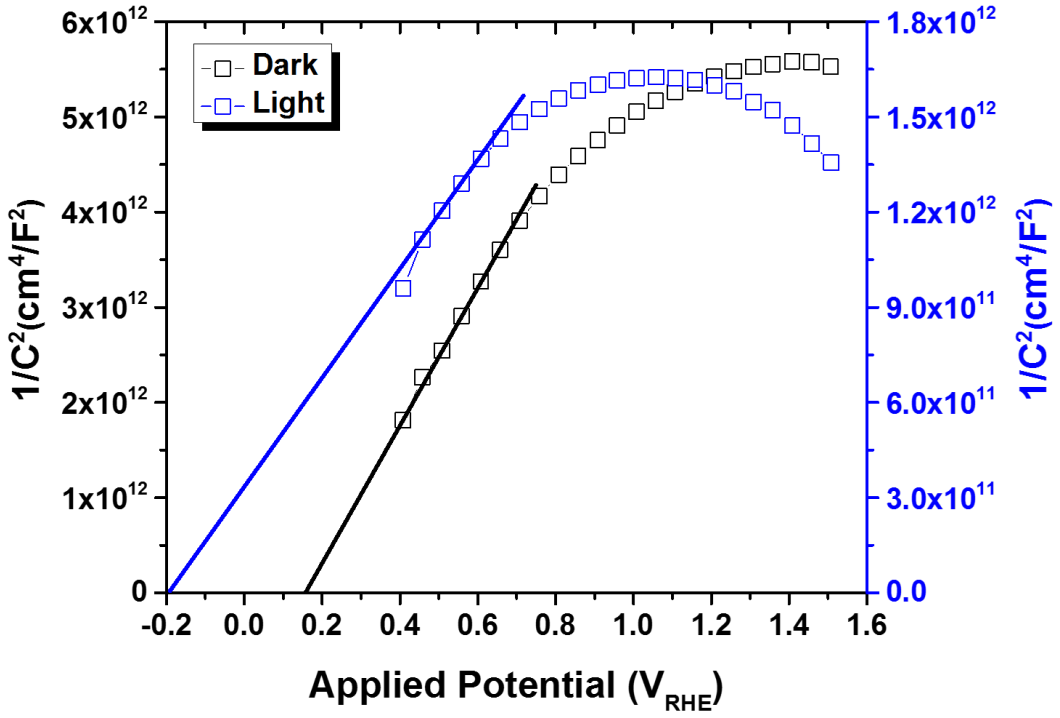

Figure 4.10. Mott-Schottky plots of of nanoporous bismuth oxide in 1 M KOH + 0.3 M H_2O_2 with and without illumination

Table C5 summarizes the Mott-Schottky results of all the samples in different electrolytes at a frequency of 1000 Hz. The charge carrier density values can be correlated to the observed photo current densities. The nanoporous bismuth oxide sample tested in 1 M KOH + 0.3 M H_2O_2 showed the highest photo current density which could be associated with the presence of BiO_{2-x} phase. Apparently, for spontaneous hydrogen evolution without any external bias, the flat band potential should be more negative than 0 V_{RHE}. It is observed that the presence of H_2O_2 shifted the flat band potentials to more negative potentials in the dark and illuminated conditions than those of the β-Bi_2O_3. The negative flat band potentials of the samples under illuminated condition indicated the possibility of having a spontaneous hydrogen evolution reaction without applying bias potential, and absence of hole accumulation at the electrode surface. Figure 4.10 shows the typical Mott-Schottky plots of the nanoporous bismuth oxide in 1 M KOH + 0.3 M H_2O_2 with and without illumination. The values of the flat band potentials, and defect concentrations derived from the Mott-Schottky results are summarized in the Table 4.3. The flat band potential of the samples indicates the position of conduction edge. It is seen that the defect concentration of the sample tested in

the 1 M KOH + 0.3 M H_2O_2 (labeled as β-Bi_2O_3/BiO_{2-x} composite) was higher than that of pure β-Bi_2O_3 sample in the dark condition. The defects are considered to be oxygen vacancies because of the *n*-type semiconducting character. The higher oxygen vacancies observed in the composite electrode in the dark condition could be attributed to the presence of the non-stoichiometric BiO_{2-x} phase. However, the defect concentration was significantly less in the composite electrode than in the β-Bi_2O_3 electrode under the illuminated condition. In spite of showing less defect concentration upon illumination, the composite electrode showed much better conductivity and higher photo current density initially compared to the β-Bi_2O_3 sample, which could be attributed to the low band gap energy of the BiO_{2-x} phase.

Table 4.3. Summary of the Mott-Schottky results of nanoporous bismuth oxide in 1 M KOH + 0.3 M H_2O_2 with and without illumination (Figure 10)

Sample	Condition	Flat band potential (V_{RHE})	Defect concentration (cm^{-3})
β-Bi_2O_3	Dark	0.38	1.33×10^{17}
	Light	0.40	2.68×10^{19}
β-Bi_2O_3/BiO_{2-x} Composite	Dark	0.15	4.23×10^{17}
	Light	-0.19	4.16×10^{18}

4.5. Conclusions

Based on the photo electrochemical experiments carried out on the anodic bismuth oxide samples having two morphologies (planar and nanoporous) in two pH conditions (5.8 and 13.7) with and without addition of sacrificial hole scavengers, the following conclusions are drawn:

1. The nanoporous samples containing a β-Bi_2O_3 phase after thermal annealing at 200 ^oC for 1 h were prepared by electrochemical anodization in 0.3 M citric acid. These nanoporous sample showed a photo current density of 0.9 mA/cm^2 at 1.5 V_{RHE} that was decaying continuously with time.
2. Photoelectrochemical testing in two different pH conditions (for a possible occlusion of H^+ ions) and stirring the electrolyte (for a possible adherence of oxygen bubbles on the

nanoporous surface) did not have an effect on the photo current density of the nanoporous oxide sample.

3. The photo current decay of the nanoporous oxide sample was associated with the photo generated hole accumulation at the electrode surface.
4. Methanol addition as a sacrificial hole scavenger was not effective due to probable poor catalytic activity of bismuth for CH_2OH^* intermediate formation reaction.
5. Addition of hydrogen peroxide as hole scavenger increased the photo current density by about 4 times in 0.5 M Na_2SO_4 (pH: 5.8) electrolyte. The photo current density initially decayed and remained plateau at ~ 4 mA/cm^2 for 1 h with a bias potential of 1.5 V_{RHE}
6. Addition of H_2O_2 in 1 M KOH (pH: 13.7) showed an increase-decrease behavior and high photo current density of ~10 mA/cm^2.
7. The high photo activity observed in the 1M KOH + 0.3 M H_2O_2 electrolyte was attributed to the *in-situ* formation of Bi_2O_{4-x} phase by the photo-conversion of the β-Bi_2O_3 at the surface. The photo-converted Bi_2O_{4-x} has a smaller band gap and therefore harvested more light in the visible region.
8. Future efforts will be rendered to stabilize the nanoporous structure of the β-Bi_2O_3/BiO_{2-x} composite photoanode for long term stability.

4.6. References

1. Park, Y.; McDonald, K. J.; Choi, K.-S., Progress in bismuth vanadate photoanodes for use in solar water oxidation. *Chemical Society Reviews* **2013,** *42* (6), 2321-2337.

2. Chen, L.; Toma, F. M.; Cooper, J. K.; Lyon, A.; Lin, Y.; Sharp, I. D.; Ager, J. W., Mo-Doped BiVO4 Photoanodes Synthesized by Reactive Sputtering. *ChemSusChem* **2015,** *8* (6), 1066-1071.

3. Chen, Y.-S.; Manser, J. S.; Kamat, P. V., All Solution-Processed Lead Halide Perovskite-BiVO4 Tandem Assembly for Photolytic Solar Fuels Production. *Journal of the American Chemical Society* **2015,** *137* (2), 974-981.

4. Pihosh, Y.; Turkevych, I.; Mawatari, K.; Uemura, J.; Kazoe, Y.; Kosar, S.; Makita, K.; Sugaya, T.; Matsui, T.; Fujita, D.; Tosa, M.; Kondo, M.; Kitamori, T., Photocatalytic generation

of hydrogen by core-shell WO3/BiVO4 nanorods with ultimate water splitting efficiency. *Scientific Reports* **2015,** *5*, 11141.

5. Abdi, F. F.; Han, L.; Smets, A. H. M.; Zeman, M.; Dam, B.; van de Krol, R., Efficient solar water splitting by enhanced charge separation in a bismuth vanadate-silicon tandem photoelectrode. *Nat Commun* **2013,** *4*.

6. Cao, D.; Wang, Z.; Nasori; Wen, L.; Mi, Y.; Lei, Y., Switchable Charge-Transfer in the Photoelectrochemical Energy-Conversion Process of Ferroelectric BiFeO3 Photoelectrodes. *Angewandte Chemie* **2014,** *53* (41), 11027-31.

7. Zhu, A.; Zhao, Q.; Li, X.; Shi, Y., BiFeO3/TiO2 Nanotube Arrays Composite Electrode: Construction, Characterization, and Enhanced Photoelectrochemical Properties. *ACS Applied Materials & Interfaces* **2013,** *6* (1), 671-679.

8. Saison, T.; Gras, P.; Chemin, N.; Chanéac, C.; Durupthy, O.; Brezová, V.; Colbeau-Justin, C.; Jolivet, J.-P., New Insights into Bi2WO6 Properties as a Visible-Light Photocatalyst. *The Journal of Physical Chemistry C* **2013,** *117* (44), 22656-22666.

9. Xu, Q. C.; Wellia, D. V.; Ng, Y. H.; Amal, R.; Tan, T. T. Y., Synthesis of Porous and Visible-Light Absorbing Bi2WO6/TiO2 Heterojunction Films with Improved Photoelectrochemical and Photocatalytic Performances. *The Journal of Physical Chemistry C* **2011,** *115* (15), 7419-7428.

10. Jiang, J.; Wang, M.; Chen, Q.; Shen, S.; Li, M.; Guo, L., Synthesis and characterization of nanoporous Bi3NbO7 films: application to photoelectrochemical water splitting. *RSC Advances* **2014,** *4* (21), 10542-10548.

11. Man, Y.; Zong, R.; Zhu, Y., Preparation and Photoelectrochemical Properties of Bi2MoO6 Films. *Acta Physico-Chimica Sinica* **2007,** *23* (11), 1671-1676.

12. Abdi, F. F.; van de Krol, R., Nature and Light Dependence of Bulk Recombination in Co-Pi-Catalyzed BiVO4 Photoanodes. *The Journal of Physical Chemistry C* **2012,** *116* (17), 9398-9404.

13. Kim, T. W.; Choi, K.-S., Nanoporous BiVO4 Photoanodes with Dual-Layer Oxygen Evolution Catalysts for Solar Water Splitting. *Science* **2014,** *343* (6174), 990-994.

14. Long; Cai; Kisch, H., Visible Light Induced Photoelectrochemical Properties of n-BiVO4 and n-BiVO4/p-Co3O4. *The Journal of Physical Chemistry C* **2008,** *112* (2), 548-554.

15. Pilli, S. K.; Furtak, T. E.; Brown, L. D.; Deutsch, T. G.; Turner, J. A.; Herring, A. M., Cobalt-phosphate (Co-Pi) catalyst modified Mo-doped BiVO4 photoelectrodes for solar water oxidation. *Energy & Environmental Science* **2011,** *4* (12), 5028-5034.

16. Zhong, M.; Hisatomi, T.; Kuang, Y.; Zhao, J.; Liu, M.; Iwase, A.; Jia, Q.; Nishiyama, H.; Minegishi, T.; Nakabayashi, M.; Shibata, N.; Niishiro, R.; Katayama, C.; Shibano, H.; Katayama,

M.; Kudo, A.; Yamada, T.; Domen, K., Surface Modification of CoOx Loaded BiVO4 Photoanodes with Ultrathin p-Type NiO Layers for Improved Solar Water Oxidation. *Journal of the American Chemical Society* **2015,** *137* (15), 5053-5060.

17. Sayama, K.; Nomura, A.; Arai, T.; Sugita, T.; Abe, R.; Yanagida, M.; Oi, T.; Iwasaki, Y.; Abe, Y.; Sugihara, H., Photoelectrochemical Decomposition of Water into H2 and O2 on Porous BiVO4 Thin-Film Electrodes under Visible Light and Significant Effect of Ag Ion Treatment. *The Journal of Physical Chemistry B* **2006,** *110* (23), 11352-11360.

18. Walsh, A.; Yan, Y.; Huda, M. N.; Al-Jassim, M. M.; Wei, S.-H., Band Edge Electronic Structure of BiVO4: Elucidating the Role of the Bi s and V d Orbitals. *Chemistry of Materials* **2009,** *21* (3), 547-551.

19. Cheng, H.; Huang, B.; Lu, J.; Wang, Z.; Xu, B.; Qin, X.; Zhang, X.; Dai, Y., Synergistic effect of crystal and electronic structures on the visible-light-driven photocatalytic performances of Bi2O3 polymorphs. *Physical Chemistry Chemical Physics* **2010,** *12* (47), 15468-15475.

20. Kudo, A.; Omori, K.; Kato, H., *J. Am. Chem. Soc.* **1999,** *121*, 11459.

21. Jiang, H.-Y.; Li, P.; liu, G.; Ye, J.; Lin, J., Synthesis and photocatalytic properties of metastable [small beta]-Bi2O3 stabilized by surface-coordination effects. *Journal of Materials Chemistry A* **2015,** *3* (9), 5119-5125.

22. Zhang, J.; Dang, W.; Yan, X.; Li, M.; Gao, H.; Ao, Z., Doping indium in [small beta]-Bi2O3 to tune the electronic structure and improve the photocatalytic activities: first-principles calculations and experimental investigation. *Physical Chemistry Chemical Physics* **2014,** *16* (42), 23476-23482.

23. Schlesinger, M.; Schulze, S.; Hietschold, M.; Mehring, M., Metastable [small beta]-Bi2O3 nanoparticles with high photocatalytic activity from polynuclear bismuth oxido clusters. *Dalton Transactions* **2013,** *42* (4), 1047-1056.

24. Drache, M.; Roussel, P.; Wignacourt, J.-P., Structures and Oxide Mobility in Bi−Ln−O Materials: Heritage of Bi2O3. *Chemical Reviews* **2007,** *107* (1), 80-96.

25. Hou, J.; Yang, C.; Wang, Z.; Zhou, W.; Jiao, S.; Zhu, H., In situ synthesis of α–β phase heterojunction on Bi2O3 nanowires with exceptional visible-light photocatalytic performance. *Applied Catalysis B: Environmental* **2013,** *142–143* (0), 504-511.

26. Chitrada, K. C.; Raja, K. S.; Gakhar, R.; Chidambaram, D., Enhanced Photoelectrochemical Performance of Anodic Nanoporous β-Bi2O3. *Journal of The Electrochemical Society* **2015,** *162* (6), H380-H391.

27. Chitrada, K. C.; Raja, K. S., Nanoporous Anodic Bismuth Oxide Photo-Anodes. *ECS Transactions* **2014,** *61* (22), 1-12.

28. Chitrada, K. C.; Raja, K. S., Nanoporous Anodic Bismuth Oxide for Electrochemical Energy Storage. *ECS Transactions* **2014,** *61* (18), 55-67.

29. Chitrada, K.; Raja, K. S., Stability of the Nanoporous Bismuth Oxide Photoanodes for Solar Water Splitting. In *Materials and Processes for Solar Fuel Production*, Viswanathan, B.; Subramanian, V.; Lee, J. S., Eds. Springer New York: 2014; Vol. 174, pp 173-199.

30. Dotan, H.; Sivula, K.; Gratzel, M.; Rothschild, A.; Warren, S. C., Probing the photoelectrochemical properties of hematite ([small alpha]-Fe2O3) electrodes using hydrogen peroxide as a hole scavenger. *Energy & Environmental Science* **2011,** *4* (3), 958-964.

31. Theuwis, A.; Vermeir, I. E.; Gomes, W. P., Chemical and electrochemical interaction of acidic H2O2 solutions with (100) InP. *Journal of Electroanalytical Chemistry* **1996,** *410* (1), 31-42.

32. Fujishima, A.; Kato, T.; Maekawa, E.; Honda, K., Mechanism of the Current Doubling Effect. I. The ZnO Photoanode in Aqueous Solution of Sodium Formate. *Bulletin of the Chemical Society of Japan* **1981,** *54* (6), 1671-1674.

33. In, J.; Yoon, I.; Seo, K.; Park, J.; Choo, J.; Lee, Y.; Kim, B., Polymorph-Tuned Synthesis of α- and β-Bi2O3 Nanowires and Determination of Their Growth Direction from Polarized Raman Single Nanowire Microscopy. *Chemistry – A European Journal* **2011,** *17* (4), 1304-1309.

34. Hardcastle, F. D.; Wachs, I. E., The molecular structure of bismuth oxide by Raman spectroscopy. *Journal of Solid State Chemistry* **1992,** *97* (2), 319-331.

35. Vila, M.; Díaz-Guerra, C.; Piqueras, J., Laser irradiation-induced α to δ phase transformation in Bi2O3 ceramics and nanowires. *Applied Physics Letters* **2012,** *101* (7), -.

36. Agasiev, A. A.; Zeinally, A. K.; Alekperov, S. J.; Guseinov, Y. Y., Photoelectrical properties of δ-Bi2O3 thin films. *Materials Research Bulletin* **1986,** *21* (7), 765-771.

37. Memming, R., *Semiconductor Electrochemistry*. Wiley: 2015.

38. Villarreal, T. L.; Gómez, R.; Neumann-Spallart, M.; Alonso-Vante, N.; Salvador, P., Semiconductor Photooxidation of Pollutants Dissolved in Water: A Kinetic Model for Distinguishing between Direct and Indirect Interfacial Hole Transfer. I. Photoelectrochemical Experiments with Polycrystalline Anatase Electrodes under Current Doubling and Absence of Recombination. *The Journal of Physical Chemistry B* **2004,** *108* (39), 15172-15181.

39. Kho, Y. K.; Iwase, A.; Teoh, W. Y.; Mädler, L.; Kudo, A.; Amal, R., Photocatalytic H2 Evolution over TiO2 Nanoparticles. The Synergistic Effect of Anatase and Rutile. *The Journal of Physical Chemistry C* **2010,** *114* (6), 2821-2829.

40. Campbell, S. A.; Parsons, R., Effect of Bi and Sn adatoms on formic acid and methanol oxidation at well defined platinum surfaces. *Journal of the Chemical Society, Faraday Transactions* **1992,** *88* (6), 833-841.

41. Jeyabharathi, C.; Mathiyarasu, J.; Phani, K. L. N., Methanol tolerant oxygen-reduction activity of carbon supported platinum–bismuth bimetallic nanoparticles. *J Appl Electrochem* **2009,** *39* (1), 45-53.

42. Yang, M., Catalytic activities of PtBi nanoparticles toward methanol electrooxidation in acid and alkaline media. *Journal of Power Sources* **2013,** *229* (0), 42-47.

43. Liu, Z.; Pesic, B.; Raja, K. S.; Rangaraju, R. R.; Misra, M., Hydrogen generation under sunlight by self ordered TiO2 nanotube arrays. *International Journal of Hydrogen Energy* **2009,** *34* (8), 3250-3257.

44. Pourbaix, M., *Atlas of electrochemical equilibria in aqueous solutions*. Pergamon Press: Oxford; New York, 1966.

45. Wang, W.; Chen, X.; Liu, G.; Shen, Z.; Xia, D.; Wong, P. K.; Yu, J. C., Monoclinic dibismuth tetraoxide: A new visible-light-driven photocatalyst for environmental remediation. *Applied Catalysis B: Environmental* **2015,** *176–177* (0), 444-453.

46. Hameed, A.; Montini, T.; Gombac, V.; Fornasiero, P., Surface Phases and Photocatalytic Activity Correlation of Bi2O3/Bi2O4-x Nanocomposite. *Journal of the American Chemical Society* **2008,** *130* (30), 9658-9659.

47. Hameed, A.; Aslam, M.; Ismail, I. M. I.; Salah, N.; Fornasiero, P., Sunlight induced formation of surface Bi2O4−x–Bi2O3 nanocomposite during the photocatalytic mineralization of 2-chloro and 2-nitrophenol. *Applied Catalysis B: Environmental* **2015,** *163*, 444-451.

48. Sajjad, S.; Leghari, S. A. K.; Zhang, J., Nonstoichiometric Bi2O3: efficient visible light photocatalyst. *RSC Advances* **2013,** *3* (5), 1363-1367.

5. Stability of the Nanoporous Bismuth Oxide Photoanodes for Solar Water Splitting[§]

5.1. Abstract

Bismuth oxide has well-dispersed valence bands that show enhanced mobility of charge carriers, high refractive index, and large dielectric constant. These properties are attractive for photo catalysis. Bismuth oxide has widely been investigated for photo degradation of dyes for safeguarding the environment. However, not much work has been reported on bismuth oxide as a photo electrode material for solar water splitting. Photodecomposition of Bi_2O_3 is a concern when used as a photocathode. However, Bi_2O_3 can be obtained as an n-type semiconductor by stabilizing other polymorph: β-Bi_2O_3, which is a metastable phase. Thin films of nanoporous bismuth oxide were synthesized by a simple electrochemical anodization of bismuth substrate. Annealing the anodic nanoporous Bi_2O_3 at 240 °C for 2 h resulted in stabilization of the β-Bi_2O_3 phase. Longer annealing times resulted in formation of the more stable α-Bi_2O_3 phase that showed monoclinic lattice structure and p-type semiconductivity. The photostability of these materials is discussed based on the photo electrochemical measurements.

5.2. Introduction

The search for semiconductor photocatalyts for commercially viable solar water splitting process still continues in spite of the multidisciplinary research efforts put worth by the international community since the publication of the first report by Fujishima and Honda.[1] The basic requirements of photocatalysts for spontaneous water splitting are: a) Electron energy band gap around 1.73 eV in order to absorb most of the visible light spectrum and drive the water splitting reaction, b) Appropriate band edge positions relative to the energy levels of the hydrogen and oxygen evolution reactions (OERs), and c) Stable against

[§] This chapter has been published: Kalyan Chitrada, Krishnan S Raja, "Stability of the β-Bi_2O_3 Nanoporous Photoanodes for Solar Water Splitting" Materials and Processes for Solar Fuel Production, Nanostructure Science and Technology, Vol. 174, 2014

environmental degradation. Furthermore, the material should have high charge transport properties and low electron-hole recombination losses in order to exhibit high solar-to-hydrogen conversion efficiency.

Several binary transition metal oxides such as TiO_2[2], Fe_2O_3[3], ZnO[4], and WO_3, and higher order mixed oxides[5,6,7], such as $CaBi_2O_4$, $BiVO_4$ etc have been investigated as photo-electrocatalysts for water splitting. Non-oxide based compound semiconductor materials such as CdTe, CdS, CdSe, PbS, etc. have been investigated widely as photo catalysts individually or as quantum dot sensitizers in combination with oxide materials[8,9]. If the energy level of the anodic or cathodic decomposition reaction of the semiconductor lies within the energy band gap, then the material will be prone to photo corrosion[10]. Compound semiconductors that show n-type behavior have higher tendency for photo corrosion than their p- type counterparts because. This phenomenon is attributed to the oxidation reaction of the holes at the surface of the n-type semiconductor that acts as a photo anode:

$$MX + zh^+ \rightarrow M^{Z+} + X \qquad [5.1]$$

On the other hand, p-type semiconductor materials act as photo cathode where the photo reaction is hydrogen ion reduction. Therefore, in general, the p-type material is cathodically protected during solar water splitting. TiO_2 shows higher photo stability than other metal oxide photo catalysts such as Fe_2O_3, ZnO, and WO_3. However, use of TiO_2 is limited by its wider band gap that absorbs light at wavelengths shorter than 400 nm. Iron oxide is impaired by its short diffusion lengths for holes, and the conduction band minimum positioned at lower than the H_2/H_2O energy level. WO_3 will not be stable in high pH electrolytes. Because no single material is found to possess all the required properties for functioning as a sustainable photo catalyst material for solar water splitting, materials with novel compositions, unique morphologies, and hybrid nanostructures are being investigated.

In order to have highly mobile charge carriers, the widths of the conduction and valence bands require being wide. The chance of scattering of the charge carrier is more when the band width is narrow. Recently the interest on bismuth based materials is increasing

because of the $6S^2$ configuration. Hybridization of Bi *6s* and O *2p* orbitals in bismuth oxides results in well-dispersed valence bands that show high mobility of holes[11]. Furthermore, bismuth oxide show high refractive index (2.9) and high dielectric constant that varies from 46 -190 [12-15]. The high refractive index of the material helps utilize the light effectively for conversion of electron and hole pairs. The high dielectric constant ensures low electrostatic forces between the charge and its trap. Thus, the charge transport properties will be better with a high dielectric material.

Bismuth sesquioxide exists in different polymorphs depending on the synthesis conditions and thermal history. The monoclinic α-Bi_2O_3 is a stable phase at room temperature that shows a band gap of 2.8 eV with p-type semiconductivity. The high temperature β-Bi_2O_3 becomes a metastable phase at room temperature with a tetragonal lattice structure, a band gap of ~2.5 eV and an n-type semiconductivity. In spite being a non-toxic material with appropriate band gap and valence band edge position (+3.13 V *vs.* NHE), Bi_2O_3 shows only a low hydrogen evolution rate due to its lower conduction band edge position (+0.33 V *vs.* NHE). The general strategies employed to overcome these limitations are simultaneous doping and nano-sizing of the material. Most of the investigations focused on the β-Bi_2O_3 because of its higher photoactivity than that of other polymorphs. However, being a metastable phase, the stability of the β-Bi_2O_3 is not investigated.

5.3. Synthesis and characterization of Bi_2O_3 polymorphs for photo-catalytic applications:

Yang et al[12] investigated the photoelectrochemical properties of β - Bi_2O_3 nanoporous films prepared by wet chemical process using $Bi(NO_3).5H_2O$ as bismuth source and triton X-100 and citric acid in ethanol as surfactant and complexing agent. The bismuth citrate complex was spin coated onto ITO and heat treated at different temperatures ranging from 350-550 ^oC. The optical absorption edges were observed: one at 2.7 eV and 3.26 eV. The conduction band minimum was composed of the hybridization of O *2p* and Bi *6p*. The two absorption edges could be attributed to the photon-electron excitation of O *2p* → Bi *6p* and Bi 6s → Bi 6p. Photocatalytic studies were carried out in 1M NaOH. IPCE and APCE were

calculated at 0 V Vs Ag/AgCl. No photocurrents were reported but the reported IPCE was 10.5% at 400 nm and 25.5% at 350 nm.

Bi_2O_3 thin films were obtained by air oxidizing of the magnetron sputtered pure Bi layer at 250 ^oC for 1-3 h by X. Yang et al[13]. The photo electrochemical studies were carried out in 0.5M Na_2SO_3 solution. The reported photocurrent density was 0.45 mA/cm^2 at 1.23 V_{NHE} for which the reported APCE was 30%. The onset of the photocurrent occurred at -0.15V_{NHE}. The band gap of the air oxidized Bi_2O_3 film increased with the decrease in the thickness (2.63 and 2.88eV for 500 and 12 nm thickness, respectively).

Nanoporous Bi_2O_3 films were synthesized by electrochemical anodization in 0.3 wt% ammonium sulfate + 5.0 wt% DI water in ethylene glycol at 30-50 ^OC by applying potentials in the range of 10-40V[14]. The anodization time was 40min. Water content of the ethylene glycol solution was observed to play a crucial role in the formation nanoporous structure. No regular nanoporous films were formed when the water content was below 4 wt%. The nanopores showed a diameter was a large as 400nm for 5 wt% water content at 30 ^oC. Increasing the anodization temperature increased the diameter of the nanopores. The optimized anodization conditions was reported to be 0.3 wt% $(NH_4)_2SO_4$ + 5 wt% water in EG, 20V, 40 ^OC, 40min. The nanoporous Bi_2O_3 film formed under these conditions showed the tetragonal β Bi_2O_3phase after annealing at 200 ^oC. (PFD card 74-1374). Photocurrent measurements were carried at in 0.5M Na_2SO_4 electrolyte. The observed dark currents were 0.013-0.032 $\mu A/cm^2$ at 0 V and 0.5 V_{SCE} respectively and photocurrents were 2.893 and 6.98 $\mu A/cm^2$ at 0 and 0.5 V_{SCE} respectively.

K. Brezensinski et al[15] synthesized β Bi_2O_3 in two different routes and compared their properties. Poly(ethylene-co butylene)-block- poly(ethylene oxide) diblock copolymer (referred as KLE) was used as template to grow the nanoporous β Bi_2O_3 film. Nanofibers of β Bi_2O_3 were prepared by electrospinning of $Bi(NO_3).5H_2O$ dissolved in acetylacetone and 2-methoxyethanol combined with polyvinyl butyral in methanol. All the materials were calcined at 400 ^oC. The KLE template β Bi_2O_3 film showed high phase purity and high BET surface area as compared to electrospun β Bi_2O_3 nanofiber mat. The nanostructure was found to be

retained up to 450 ^{o}C of calcination. Higher temperature than 450 ^{O}C resulted in restructuring of the nanowires and transformation of β to more stable α Bi_2O_3. Low temperature calcination at 250 ^{O}C required about 12h for cross linking of the amorphous structure JCPDS card for β Bi_2O_3: 27-0050. Crystallization was observed to occur at the temperature window of 380-385 ^{O}C. The KLE-templated β Bi_2O_3 showed an optical band gap of 3.4 eV (~360 nm light) for the samples calcined at 400 ^{o}C. The KLE template β Bi_2O_3 showed exceptional photocatalytic activity as compared to the TiO_2 thin film having similar band gap and similar BET area.

Li et al[16] reported the photoelectrochemical behavior of DC reactive magnetron sputtered Bi_2O_3 that was annealed at 300 ^{o}C for 2h. PEC studies were carried out using 0.2M Na_2SO_3 solution. It was observed that the electrode having Bi/Bi_2O_3 configuration showed better photoelectrochemical properties than the Bi_2O_3 electrode. It was suggested that the increased photocurrent density of Bi/Bi_2O_3 was due to the shift in the Fermi level of the Bi_2O_3. The work function of 6.23 eV. Therefore under equilibrium, the contact between Bi and Bi_2O_3 resulted in shift in the Fermi level of the Bi_2O_3. When the Bi_2O_3 was present without a BI substrate, no such Fermi level shift occurred and therefore photocurrent was low.

Qin et al[17] reported formation of template free nanotubes of β Bi_2O_3 by a hydrothermal process of dissolving 0.375 mmol of $Bi(NO_3)_3.5H_2O$ and urea (1.35mmol) in ethylene gylcol (25ml) and heating it to 150 ^{o}C for 12h. If the $Bi(NO_3)_3$/urea influences both the morphology of the final product (sheet vs nanotube) and the chemistry (stoichiometry). Moreover, ethylene glycol also was found to be critical in achieving the nanotubes. If water was the solvent, then the product was not nanotube. The Bi_2O_3 and $(BiO)_2CO_3$ nanotubes were investigated for their waste water treatment capacity in term of Cr(VI) ion removal. The Bi_2O_3 NTSs showed strong positive surface charge (zeta potential 38mV in deionized water). The Cr(VI) adsorption peak showed a maximum at pH 5.0 and decreased at higher and lower pH values. The adsorption was poor at lower pH values (pH <3.0) because of lower pH, the Cr 6+ was presented as uncharged H_2CrO_4. The nanotubular configuration showed higher

photocatalytic activity than nanoparticle configuration in terms of photocatalytic degradation of RhB dye.

Schlensinger et al[18] investigated the relation between the starting bismuth precursor materials and the final product. The starting bismuth precursor was in form of polynuclear bismuth oxide clusters composed of different numbers of $[Bi_6O_{8-X}]_{2(1+x)+}$ units. The polynuclear bismuth oxide clusters were hydrolyzed at room temperature and annealed at temperature lower than 400C. The beta-Bi2O3 prepared by this route showed energy band gaps between 2.36 - 2.53 eV. The photocatalyst showed promising results in the degradation of rhodamine B (RhB) dye.

Yu et al[19] reported a simple template free method for synthesis of flower like Bi_2O_3 microspheres though a solvothermal process at 200 C using $Bi(NO_3)_3.5H_2O$ dissolved in ethylene glycol. The Bi_2O_3 contained predominantly cubic delta phase. The band gap was 2.89 ev. The surface are of the nanopshere delta Bi_2O_3 was around 58.2m^2/g as compared to 0.368m^2/g of commercial Bi_2O_3 product.

Dutta et al[20] prepared alpha-bi_2O_3 by a simple wet chemical synthetic process by dissolving $Bi(NO_3)_3$ $6H_2O$ in pH 10 solution by NH_4OH addition by high power ultrasonication. The hydrolyzed precipitate was vacuum dried. Doping the Bi_2O_3 with 1.2% Eu^{3+} and/or 0.8% Tb^{3+} resulted in β Bi_2O_3 structure. Addition of PEG in the solution yielded nanorod structure [short chain polymer modified the morphology of final product]. The bandgap of the undoped α Bi_2O_3 was about 3.81 eV. Doping of two rare earths red shifted the band gap to 3.56 eV.

Li et al[21] reported the electronic structure of α Bi_2O_3 using XPS measurements and DFT calculations. The valence bands of α Bi_2O_3 showed and energy width of about 7 eV that contained three knee points at binding energies of 2.4, 3.5 and 6.2 eV. In addition to the valence band width, there was additional peak at 11.2 eV that was associated with Bi *6s* states. The Bi^{3+} possesses an electronic configuration of $5d^{10}\ 6s^2 6p^0$, which prefers asymmetric coordination environment referred to as lone-pair effect. The asymmetry charge

distribution was attributed to the interaction between *s* and *p* orbitals of cation and *p* orbitals of the anion.

Lei and chen[22] calculated surface energies of different termination configurations of α Bi_2O_3 using ab-inito calculations. It is proposed that (010) plane is the most stable and (110) plane is the least stable. The second most stable plane is (111). Matusumoto et al[23] investigated the electronic structures of sesquioxides such as As_2O_3, Sb_2O_3 and Bi_2O_3. These oxides form highly distorted structures with large open spaces. The distorted structures are attributed to the presence of "lone pair" electrons in the outer orbital (for Bi^{3+}, it is 6s). The electrons were the top of valence band considered to contribute to the localized charge distribution (formation of lone pair). The low symmetry as the result of lone pair formation resulted in the band gaps and semiconducting behavior of the sesquioxides.

Matsumoto et al[24] investigated the electronic structures of the Bi_2O_3 by considering different defective configurations of oxide-ion vacancies arranged in different plane. Three possible arrays of vacancy sites of oxygen sublattice were considered aligned along either the <100>, <110> or <111> direction. The symmetry was lowered by displacing the ions from their ideal lattice positions of cubic fluorite structure. Symmetry breaking in the <100> array model with 2X2X2 super cell of defective cubic fluorite structure represented the β Bi_2O_3 structure. The theoretical calculation of the band gap indicated a value of 1.75 eV. The band gap is of transition type.

H. Cheng et al[11] investigated the electronic structures of the Bi_2O_3 polymorphs. The beta-Bi2O3 was synthesized by dissolving $Bi(NO_3)_3.5H_2O$ in dilute HNO_3 and the solution was drop wise added to the excessive Na_2CO_3 solution to obtain $Bi_2O_2CO_3$ precipitates. The precipitate was calcined at 380C for 10min to transform the precipitate in to β Bi_2O_3. The BET surface area of the β Bi_2O_3 particles was 8.55m^2/g. the room temperature photoluminescent peaks of β Bi_2O_3 by excitation wavelength at 300nm were weak indicating efficient charge separation or low charge recombination, the UV-Vis photo spectrum indicated a direct band gap of 2.48 eV. The crystal structure of β Bi_2O_3 showed tunnel structure at the center of the

photogenerated electrons and holes. Moreover, the β Bi_2O_3 exhibited a dispersive band structure (the width of band was 6 eV) that resulted in faster transfer of electrons and holes.

Xu et al[25] prepared porous bismuth carbonate microflowers by urea assisted alcholysis of bismuth nitrate. The as prepared microflowers had surface area of 120 m^2/g. Upon thermal annealing at 500C for 1h, the bismuth carbonate transformed into α Bi_2O_3 whose surface area decreased to 25m^2/g. the morphology also changed from microflowers to micronuts. Since surface area plays a crucial in most of the catalytic reactions, a UV-irradiation process was developed to increase the surface area. UV irradiation was carried out to make Bi_2O_3 micronuts to rebloom for which the surface area increased from 25m^2/g to 95m^2/g. The calcined α Bi_2O_3 showed a band gap value of 2.7eV and UV irradiated materials showed a band gap of 2.4 eV. Furthermore, UV irradiation resulted in O (2p) – Bi^{3+} ($6p^0$) excitations and surface O(2p)-Bi^{5+} ($6s^0$) transitions.

The stability of the Bi_2O_3 photocatalyst is considered to be affected by the oxidation reaction of Bi^{3+}. The Bi^{5+} formation could be attributed to reaction with oxygen in the solution during UV light illumination.

$$Bi^{3+} + 2h^+ \rightarrow Bi^{5+} \qquad [5.2]$$

$$2H_2O + 4h^+ \rightarrow 4H^+ + O_2 \qquad [5.3]$$

$$Bi_2O_3 + \frac{1}{2}O_2 \rightarrow Bi_2)_{4-x} \qquad [5.4]$$

$$O_2 + e^- \rightarrow O^{2-} \qquad [5.5]$$

The photo generated super-oxide radicals with the strongest oxidation ability and sufficiently long life time can oxidize the Bi^{3+} to Bi^{5+} by forming Bi_2O_{4-x} at the surface.

5.4. Experimental

5.4.1. Materials and methods

In the present investigation, Bi_2O_3 nanoporous films were synthesized by electrochemical anodization of commercial purity bismuth metal in the form of circular discs of 3 mm thick and 12.7 mm diameter in the electrolyte solutions containing 0.3 M citric acid. Anodization was carried out at various potentials ranging from 3 V to 60 V for different time durations ranging from 0.5 to 2 h. Based on the morphology, thickness, and photo electrochemical behavior the nanoporous oxides obtained by anodization at 60V for 30 minutes were investigated further to evaluate the stability under continuous illumination. After anodization, the samples were thermally annealed at 200, 220, and 240 ^oC for 2- 6 h. The annealing temperature was limited to 240 ^oC because of the low melting temperature of the bismuth metal substrate which supported the nanoporous bismuth oxide layer. The oxide layer was not separated from the substrate since the bismuth substrate acted as a current collector for the Bi_2O_3 photo anode during the photoelectrochemical experiments. It was observed that annealing at 200 ^oC for up to 6 h showed presence of mixture of bismuth carbonate oxide ($Bi_2(CO_3)O_2$) and β-Bi_2O_3 phases. The proposed reactions of the formation of bismuth carbonate oxide during the anodization of bismuth in citric acid and further annealing in air can be given as:

Reactions on the anode:

$$Bi \rightarrow Bi^{3+} + 3e^- \qquad [5.6]$$

$$Bi^{3+} + C_6H_8O_7 \rightarrow Bi(C_6H_5O_7) + 3H^+ \qquad [5.7]$$

Reaction on the cathode:

$$3H^+ + 3e^- \rightarrow {}^3/_2\, H_2 \qquad [5.8]$$

$$2[Bi(C_6H_5O_7)] + 9O_2 \rightarrow Bi_2(CO_3)O_2 + 11CO_2 + 5H_2O \qquad [5.9]$$

During annealing at 200 ^oC in air:

Annealing at 220 ^{o}C for 4 h resulted in decomposition of bismuth carbonate oxide phase and formation of predominantly the β-Bi_2O_3 phase, given by the reaction:

$$Bi_2(CO_3)O_2 \rightarrow Bi_2O_3 + CO_2 \qquad [5.10]$$

Annealing at 240 ^{o}C resulted in complete disappearance of the bismuth carbonate oxide phase and formation of the metastable β-Bi_2O_3 and α-Bi_2O_3 phases. The effect of having only the β-Bi_2O_3 and mixtures α + β Bi_2O_3 phases on the photo stability will be discussed in this chapter.

5.4.2. Photoelectrochemical studies

Potentiodynamic, potentiostatic, electrochemical impedance spectroscopy (EIS), and Mott-Schottky analysis studies were carried out with and without illuminated conditions. Photo electrochemical studies were carried out using a three-electrode configuration with a 7.5 cm^2 flag shaped platinum counter electrode, and a home-made Ag/AgCl reference electrode (calibrated as 199 mV vs. standard hydrogen electrode). The saturated Ag/AgCl electrode was prepared by anodizing a 1 mm in diameter, 10 cm long silver wire at 5 V for 15 minutes in a saturated KCl solution. The AgCl coated silver wire was immersed in the saturated KCl solution contained in a plastic pipette. The tip of the saturated KCl solution filled pipette was sealed by a gel of agar. The agar gel was prepared by dissolving 1 gram of agar in 20 ml of saturated KCl solution (~ 4.83 M at 25 °C) and cooking it at around 80 °C until a gel consistency was obtained. All the potentials in this investigation were measured with reference to the Ag/AgCl electrode dipped in the saturated KCl salt bridge, whose potential was measured to be +46 mV vs saturated calomel electrode (SCE) at 24 °C and 199 mV Vs standard hydrogen electrode (SHE). A home-made polyether ether ketone (PEEK) sample holder was used to electrically connect the sample with a potentiostat (Gamry Instruments, model: Reference 600) by exposing 1 cm^2 of the active surface. The samples were illuminated using a solar simulator (SOLAR Light, Glenside, PA, USA, Model: 16S-300) with a 300 W xenon lamp, and an air mass global 1.5 filter that gave 1-sun intensity (100 mW/cm^2) at appropriate settings. Band pass filters (Edmund Optics) in the range of 400 -700 nm at 50 nm intervals were used to obtain an action spectra. The intensity of the light was measured using a

pyranometer probe (SOLAR Light, USA, model: PMA 2144) and a radiometer (SOLAR Light, USA, model: PMA 2100). The samples were polarized at 0.2 V in 1 M KOH solution for constructing the Tauc plots. Potentiostatic measurements were carried out in 1 M KOH solution at 0.2 V. The photocurrents were recorded by illuminating the samples for 20 minutes. After 20 minutes of illumination, electrochemical impedance spectroscopy (EIS) measurements were carried out under light and dark (by interrupting the light and equilibrating the samples under dark condition for 20 minutes) conditions. EIS measurements were carried out under potentiostatic condition of 0.2 V by super imposing an *ac* signal of 10 mV and scanning the frequency from 0.1 MHz down to 0.1 Hz. Mott-Schottky (M-S) measurements were carried out at a frequency (*f*) of 3000 Hz by scanning the potential of the sample from 0.5 V to -0.6 V at 50 mV steps for every two seconds. The capacitance (*C*) of the space charge layer was calculated from the imaginary impedance (*Z"*) using the relation $C = -1/(2\pi f Z")$. All potentials were applied with reference to an Ag/AgCl reference electrode. After completing the EIS and M-S measurements, the illumination of the sample resumed for another 20 minutes and the EIS and M-S measurements were repeated. Each 20 minutes of illumination constituted one cycle. Multiple illumination cycles were carried out on each annealing condition until the photo current density decreased to less than 0.05 mA/cm^2.

5.5. Results and Discussion

5.5.1. Morphology and structural characterization

Figure 5.1 (a) shows the nanoporous morphology of the oxide layer formed at 60 V for 30 minutes in citric acid electrolyte in the as-anodized condition. The diameters of the pores were in the range of 20 -50 nm and total thickness of the film was less than 500 nm. It was observed that pore diameter and film thickness changed with the annealing at 240 ^{o}C for 2 h, as seen in Figure 5.1 (b). Annealing at 240 ^{o}C resulted in growth of a thin planar oxide layer. The formation of the top planar layer was considered to occur in three stages: Stage 1. Widening of the rim of the nanopores and formation of oxide ridges; Stage 2. Coalescence of oxide ridges in to islands (Figure 2.1 (b)); and Stage 3. Spreading of the islands in to a thin continuous top layer. Occurrence of the stages 1 and 2 were observed in the samples annealed for 2 and 4 h. The area coverage of the oxide islands increased with annealing time

and almost 50% of the nanoporous oxide layer was covered with a thin top layer after 6 h of annealing. Ultrasonication of the samples in methanol for about 30 seconds was observed to remove the top oxide layer. The nanoporous oxide layer after removal of the top oxide layer showed almost similar dimensions as that of as anodized condition. Figures 5.2 (a) and (b) show the morphologies of the nanoporous oxide layer after removal of the top planar layer by ultrasonication.

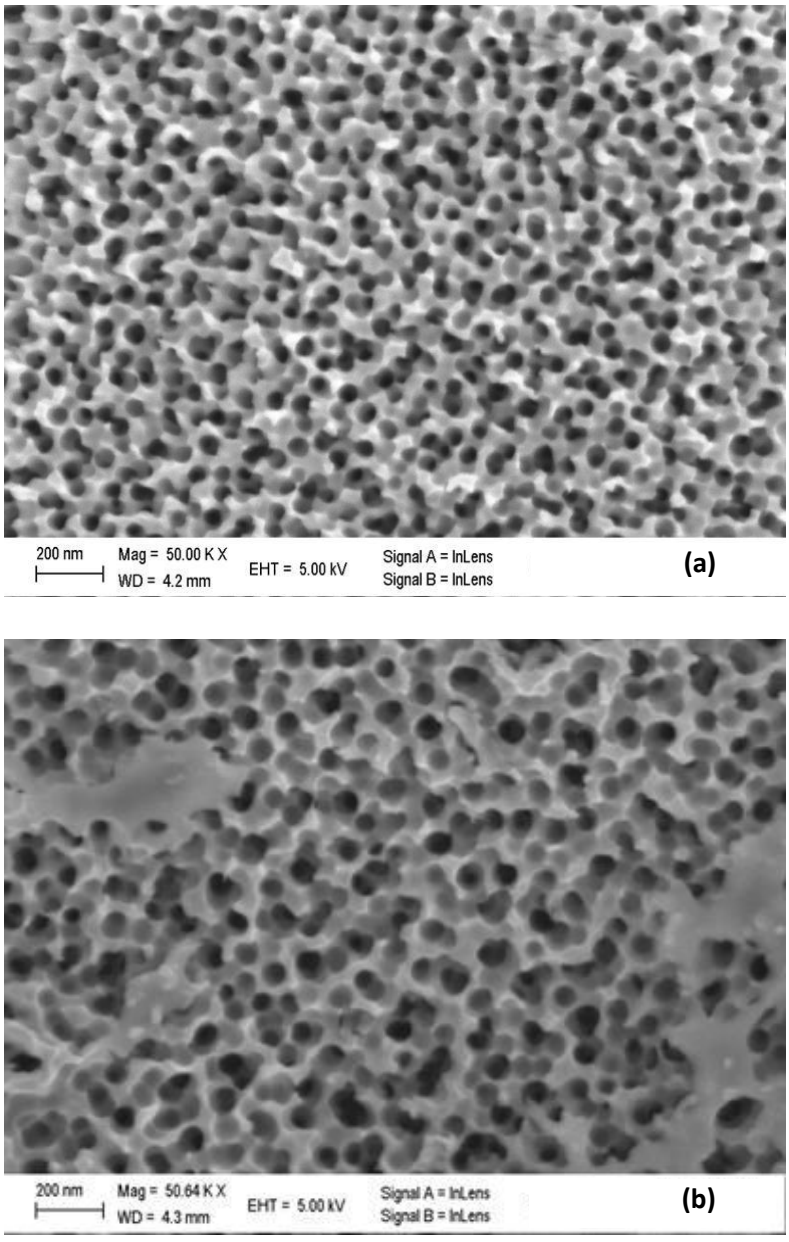

Figure 5.1. FESEM images of the nanoporous morphology of the bismuth oxide synthesized by anodization of bismuth at 60 V for 30 minutes: (a) as-anodized condition; and (b) annealed at 240 ^{o}C for 2 h

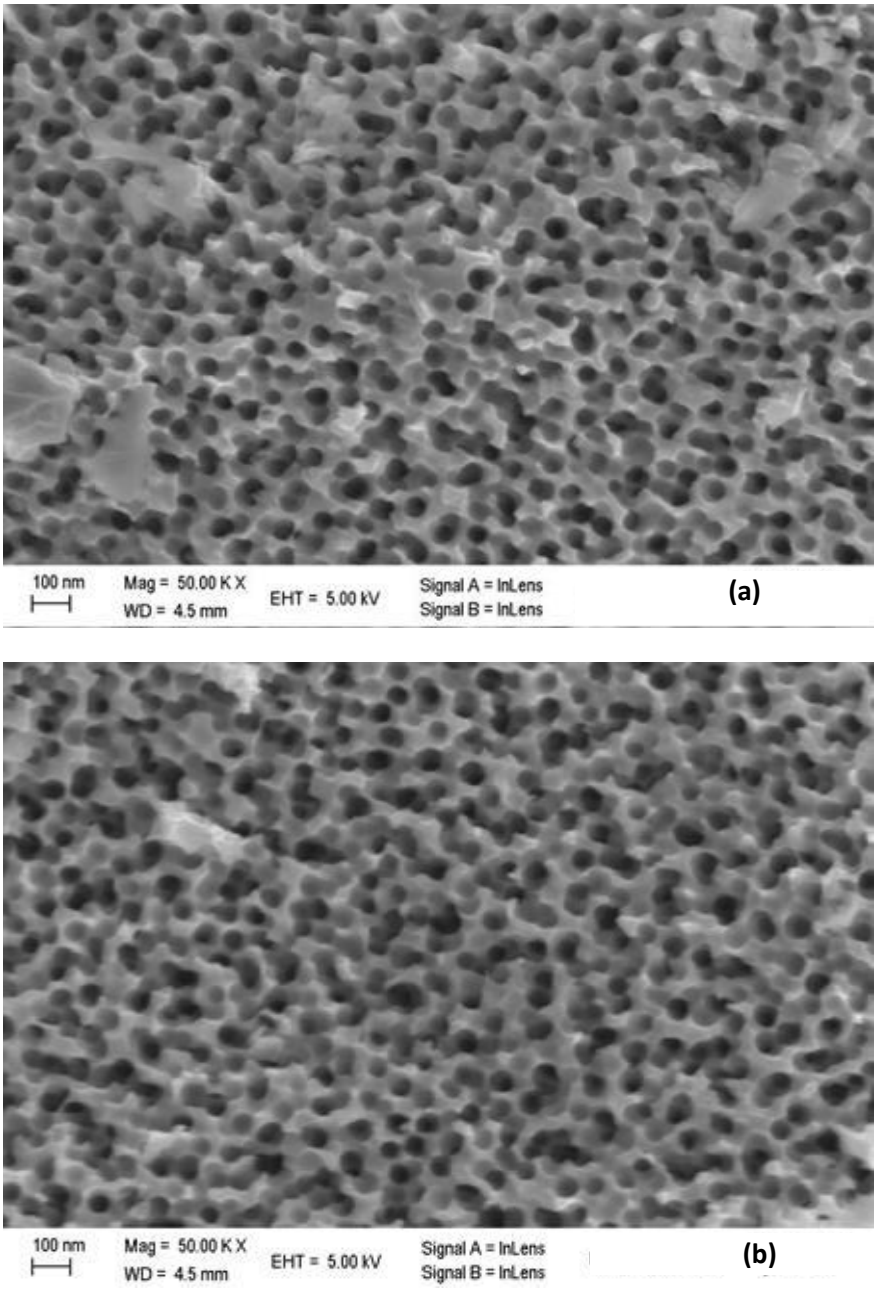

Figure 5.2. FESEM images of the nanoporous morphology of the bismuth oxide synthesized by anodization of bismuth at 60 V for 30 minutes: (a) annealed at 240 ^{o}C for 4 h; and (b) annealed at 240 ^{o}C for 2 h

Figure 5.3 shows the X-ray diffraction patterns of the nanoporous oxide layers after different annealing conditions. The samples annealed at 240 ^{o}C for 2 and 4 h showed predominantly β-Bi_2O_3. Annealing for 6 hours showed a mixture of beta and alpha phases of Bi_2O_3. The XRD peaks corresponding to α-Bi_2O_3 were not predominant and the phase content was roughly estimated to be less than 15%. It should be noted that the α-Bi_2O_3 is considered

as a *p*-type semiconductor. The nanopores of Bi_2O_3 containing both α+β phases showed enhanced photocatalytic activity that was attributed to an efficient charge separation and charge transfer across the α-β phase junction.[26] However, it should be noted that the *p-n* junction of α-β phases is advantageous for charge separation when used as a photo-catalyst under open circuit conditions. When an external bias is applied to the photoelectrochemical cell, presence of the *p-n* junction within a photoelectrode (either photoanode or photocathode) may not be helpful. This is because of the fact that the inherent electric field formed across the p-n junctions would be modified by the external applied electric field. How does the presence of *p-type* α-Bi_2O_3 along with β-Bi_2O_3 affect the photoelectrochemical behavior of the will be discussed in the subsequent sections.

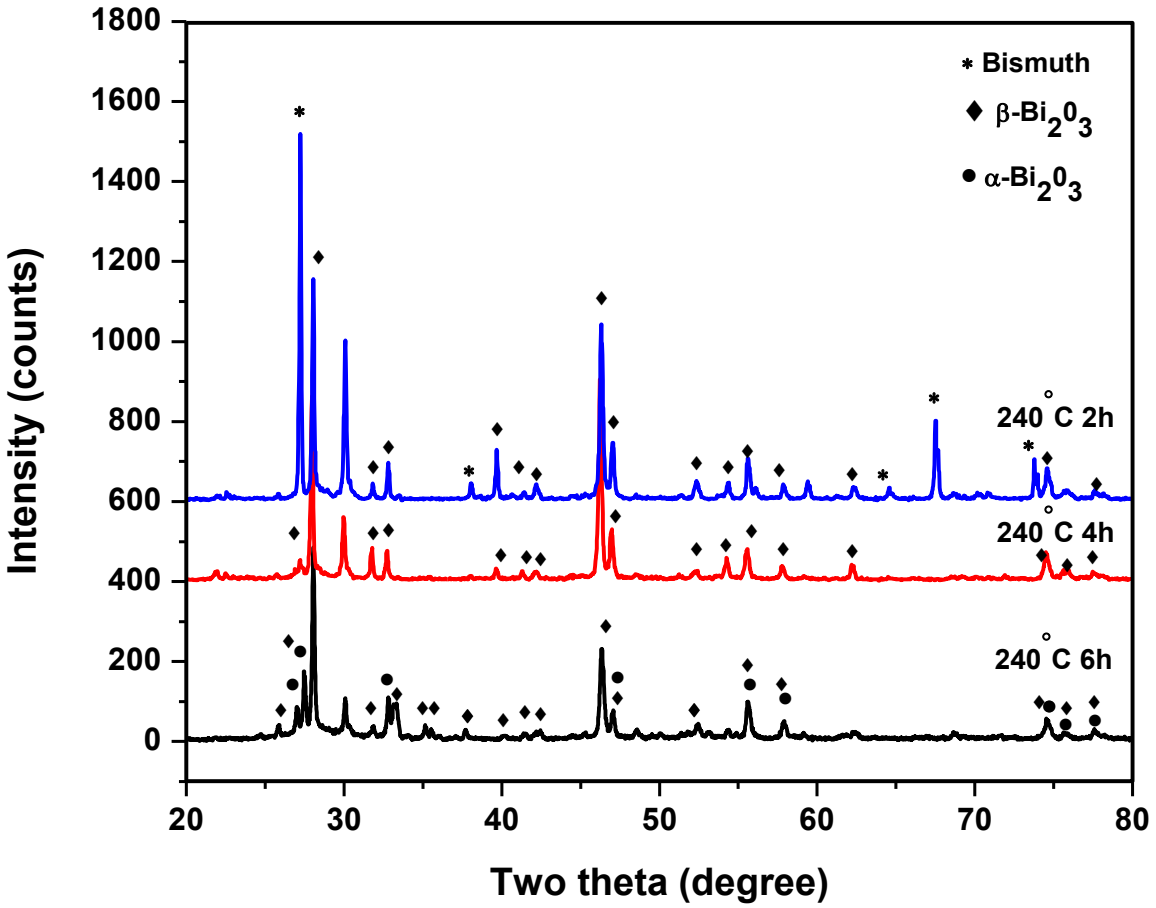

Figure 5.3. X-ray diffraction patterns of the nanoporous bismuth oxide synthesized by anodization of bismuth at 60 V for 30 minutes and annealed at 240 ^oC for 2, 4, and 6 h. Increasing the annealing time increased the volume fraction of monoclinic α-Bi_2O_3.

5.5.2. Optical characteristics

Figure 5.4 shows the UV-VIS diffuse reflectance spectroscopic results of the nanoporous Bi_2O_3 annealed at 240 ^oC for 4 and 6 h. A sharp absorbance shoulder was observed to take off at a wave length of 500 nm corresponding to an energy level of 2.48 eV. This energy level is associated with the band gap of β-Bi_2O_3. There were additional absorbance shoulders observed at energy levels of 2.8 eV and 3.02 eV. The absorbance at energy levels of 2.2 – 3.1 eV is usually attributed to the Bi^{3+} intra-ionic electronic transitions and charge transfer transitions between oxygen ligands and Bi^{3+} ions.[27] The minor absorbance shoulder observed at 2.8 eV could be attributed the presence of β-Bi_2O_3 phase in the sample annealed at 240 ^oC for 6 h. The optical absorption coefficient of Bi_2S_3 has been reported to be around 2 x 10^5 cm^{-1} in the wavelength of 400-700 nm.[28] Similarly, the optical absorption coefficient of Bi_2O_3 has been reported to be in the range of 2 x 10^4 – 1 x 10^5 cm^{-1} in the wavelengths range of 600 – 400 nm.[29] Based on the absorption coefficient, the required thickness of the Bi_2O_3 thin film to harvest the light having wavelengths of 600 nm and 400 nm would be about 5 µm and 1 µm respectively. Presence of oxygen vacancies has been reported to shift the absorption spectra to longer wavelengths due to excitation of electrons from the donor levels of reduced Bi^{3+} to the conduction band.[28]

Figure 5.5 shows the Raman spectra of the anodic nanoporous Bi_2O_3 annealed at 240 ^oC for 6 h before and after the photoelectrochemical (PEC) testing. The discussion in this section will focus on the Raman spectrum of the sample before the PEC testing. The spectrum consisted of three major Raman bands centered around 457, 312, and 91 cm^{-1}. Hardcastle et el reported the Raman frequencies of the displacements of oxygen atoms with respect to the bismuth atom that resulted in stretching of Bi-O bonds in the BiO_6 octahedra to be 462, 311, and 124 cm^{-1}.[30] The Raman frequencies associated with α-Bi_2O_3 are reported to be 212, 278, 335, 410, 445 and 538 cm^{-1}. Based on the reported Raman frequencies, the Raman spectrum of Figure 5.5 could be associated with the β-Bi_2O_3 phase. The Raman bands observed at lower frequencies such as 90 and 70 cm^{-1} could be assigned to the E_g and A_{1g} vibration modes of Bi respectively.[31]

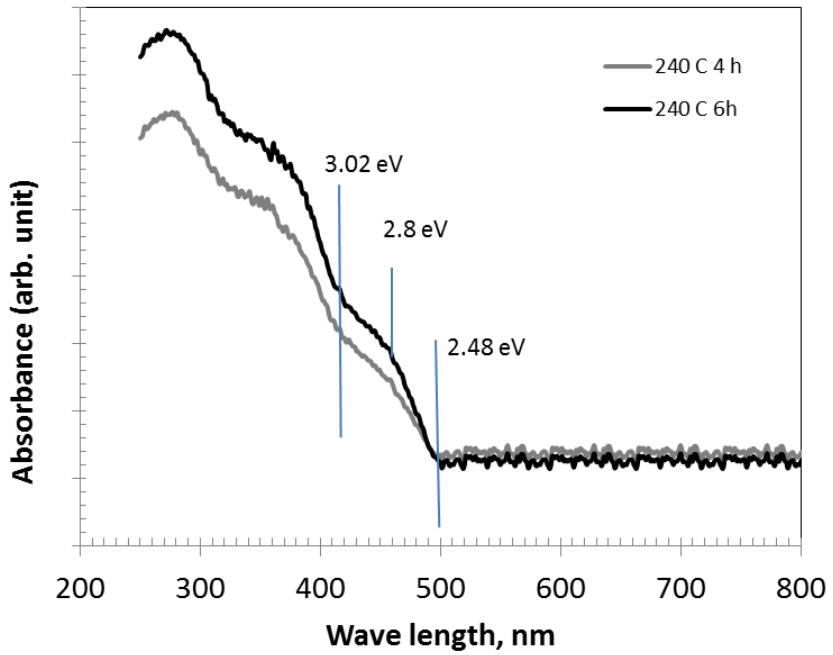

Figure 5.4. Optical absorbance spectra (obtained from the UV-VIS diffuse reflectance spectroscopy)of the nanoporous bismuth oxide synthesized by anodization of bismuth at 60 V for 30 minutes and annealed at 240 ^{o}C for 4, and 6 h. Inflections of optical absorbance were observed at three different energy levels indicating optical transitions occurred due to multiple phases. Baseline corrections were applied by comparing the spectrum obtained using barium sulfate.

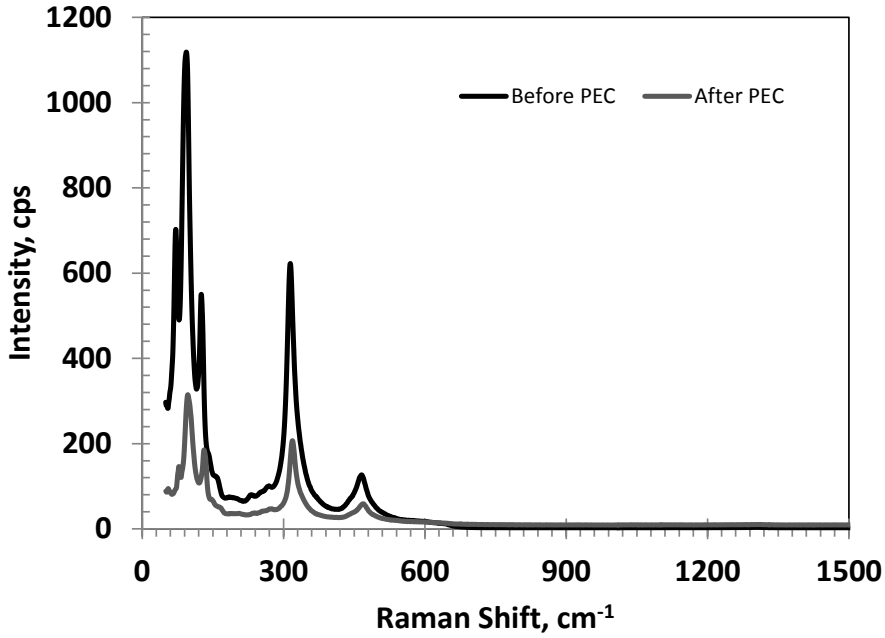

Figure 5.5. Raman spectra of the anodic nanoporous Bi_2O_3 annealed at 240 ^{o}C for 6 h before and after the photo electrochemical tests. The change in intensity implies decrease in the thickness of the oxide layer and modification of the surface morphology/roughness.

5.5.3. Photoelectrochemical behavior

Figure 5.6 (a) shows the photocurrent densities of the annealed samples as a function of time under an external bias of 0.2 $V_{Ag/AgCl}$ in 1 M KOH. The observed spikes of the photo current density are associated with the starting of a new illumination cycle for every twenty minutes. The photo current decayed exponentially during the first 20 minutes of illumination. The rate of photo current decay was relatively slower in the subsequent 20-minutes illumination cycle than that of the first 20-minutes cycle. The sample annealed at 240 ^{o}C for 2 h showed slightly better photo electrochemical activity than the other two annealed conditions. The samples annealed at 240 ^{o}C for 4 h and 6 h showed almost similar decay behavior of photo current density. The initial trend of the photo current decay of the sample annealed at 240 ^{o}C for 6 h is given in Figure 5.6 (b). It can be seen that the 'half-life' of the photo current (time taken to reach the 50% of the initial photo current density) of the sample was about 600 seconds.

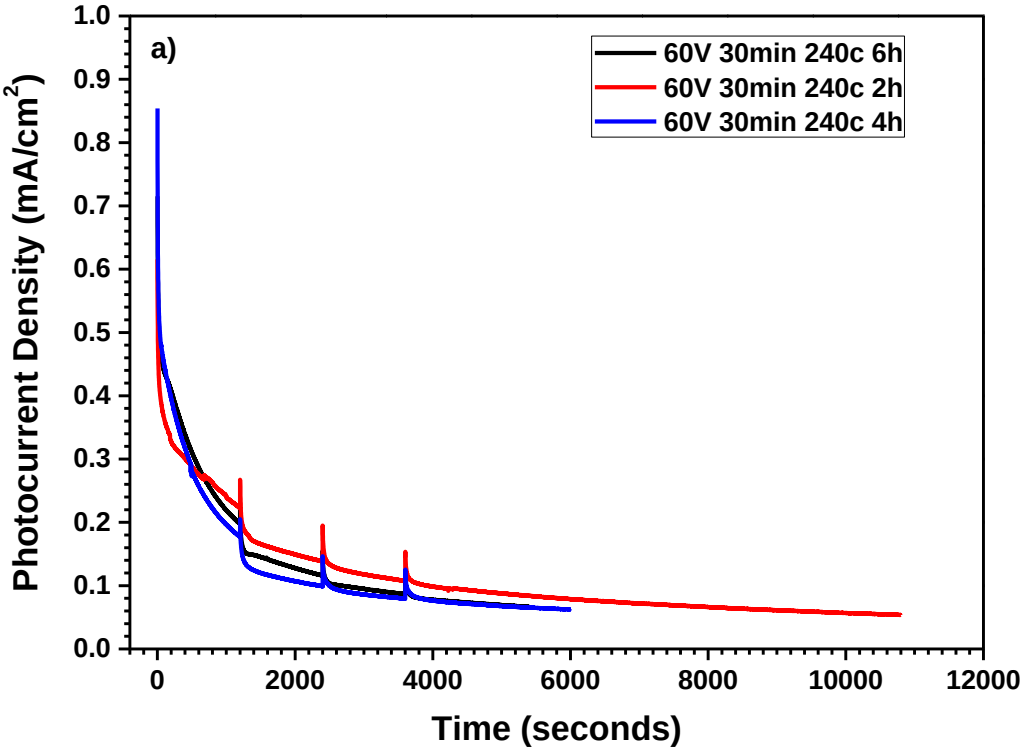

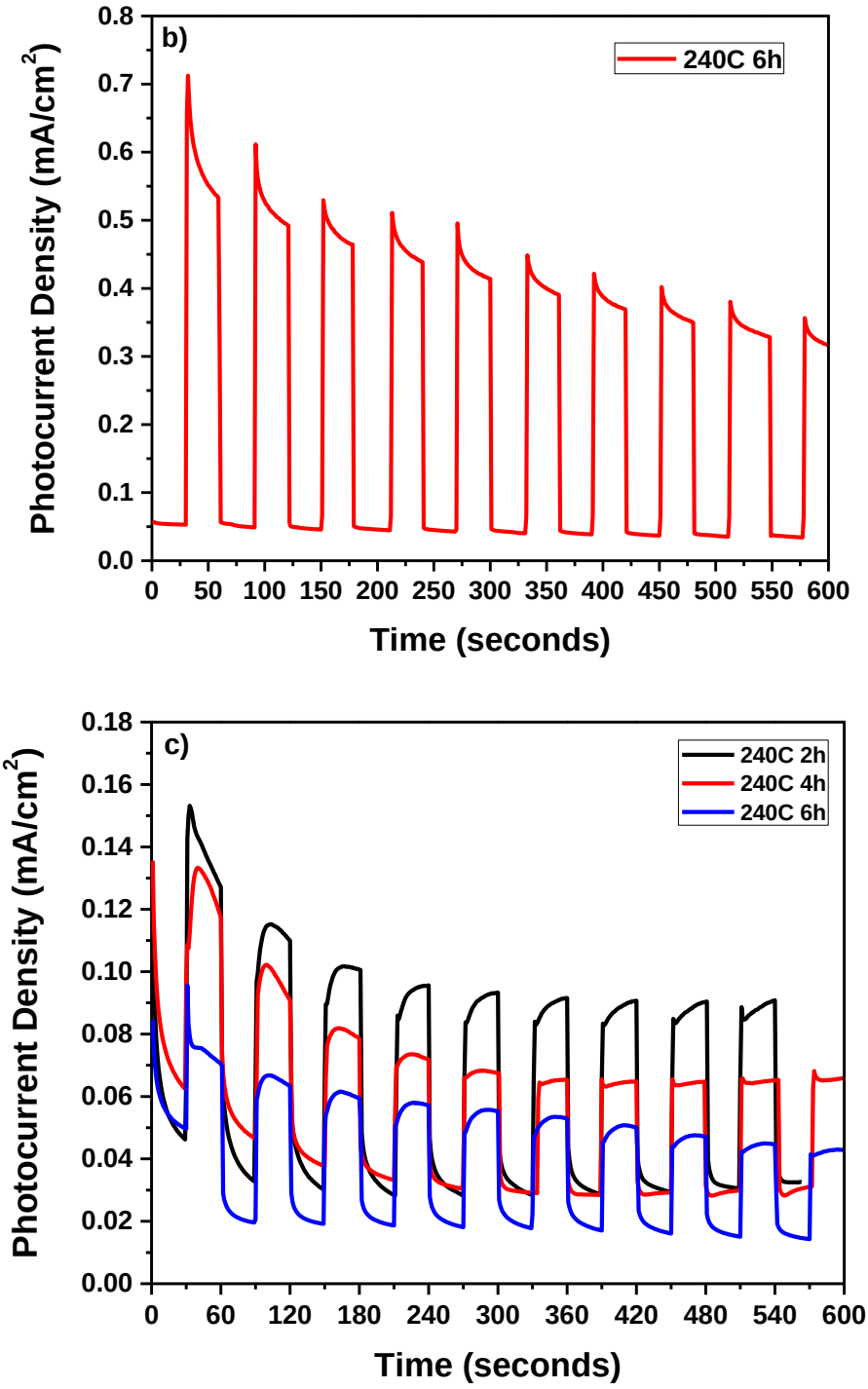

Figure 5.6.(a) Photo current density of the nanoporous anodic Bi_2O_3 annealed at 240 ^oC for different times. The samples were polarized at 0.2 V Ag/AgCl in 1 M KOH solution and illuminated with a 1-sun intensity simulated solar light. (b) Photo current and dark current densities of the nanoporous anodic Bi_2O_3 annealed at 240 ^oC for 6 h. The light was interrupted at regular intervals to record the dark current. (c) Photocurrent and dark current densities of the thermally oxidized Bi_2O_3. Thermal oxidation was carried out at 240 ^oC for 2, 4, and 6 h.

The exponential decay of the photocurrent during initial illumination conditions could be attributed to the faster recombination of electrons and holes. It is known that the photogenerated electrons and holes are separated by the electric field at the space charge layer. The electrons are extracted at the backside of the electrode and available for the hydrogen reduction reaction. The flow of these electrons is recorded as the photocurrent. The holes are consumed at the surface of the nanoporous Bi_2O_3 photoanode through the reaction [3] described in the earlier section. However, it is well established that bismuth-based oxides have low catalytic activity for OER. The slower oxygen evolution kinetics of bismuth oxide resulted in accumulation of holes at the surface and lead to recombination losses. The rate of decay of the photo current density observed with the anodic nanoporous Bi_2O_3 was much faster than that of transition metal oxide photo-electrodes such as TiO_2, Fe_2O_3 and WO_3. In order to understand the decay process several post-test measurements were carried out.

Since annealing of the nanoporous anodic Bi_2O_3 was carried out in air, it was likely that a thermally oxidized layer could have formed in addition to the anodic oxide layer. The oxide layer due to thermal annealing could form either at the metal/anodic oxide layer interface or on top of the already existing anodic layer, depending on the transport numbers of the Bi^{3+} and O^{2-}. If the growth of the oxide layer is cation transport controlled, then the oxide will grow at the oxide/air interface. It is well known that the δ-Bi_2O_3, a high temperature phase has very high oxygen ion conductivity. Therefore, the air-oxidized layer would be predominantly formed at the metal/oxide interface. This is also evidenced from the predominantly nanoporous morphology of the oxide after annealing. In order to isolate the effect of thermally formed film on the photoactivity of anodic oxide layer, bismuth metal samples were thermally oxidized in air at 240 ^oC for 2, 4, and 6 h and their photocurrents were measured using the similar procedure followed for the anodic nanoporous oxide samples. Figure 5.6 (c) shows the current densities of the samples with and without illumination when polarized at 0.2 $V_{Ag/AgCl}$ in 1 M KOH. The 2 h oxidized sample showed higher photocurrent density than the samples oxidized for longer time. Similar results were observed in the case of anodic oxide samples. The dark current density of the thermally

oxidized samples (oxidized for 2 and 4 h) plateaued at around 30 μA/cm^2 which was lower than that of anodic nanoporous oxide (~50 μA/cm^2). The initial photocurrent density of the 2 h thermal oxidized sample was about 0.10 mA/cm^2 which was much lower than that of its anodic oxide counterpart (~0.68 mA/cm^2). After 500 s of illumination, the photocurrent densities of the thermal and anodic oxides were ~0.06 and ~0.36 mA/cm^2, respectively. Initially, both the samples revealed exponential decay of the photocurrent that could be due to accumulation of holes due to poor oxygen evolution kinetics and subsequent recombination losses. Interestingly, after 100 s of exposure to the test solution, the current density increased parabolically after illumination before reaching a steady state or decreasing. The thermally formed bismuth oxide was very thin and planar. Therefore, the surface area available for accumulation of holes was much smaller than that of the anodic nanoporous oxide. Once all the hole trapping sites were occupied, the excess holes generated by continuous illumination were participating in the OER. On the other hand, sites for electron and hole trapping were always available in the anodic oxide because of its large surface area. It is well established that large concentrations of oxygen vacancies and metal cation vacancies are available on the anodic oxide that act as electron and hole trapping sites, respectively. It was observed that the contribution of thermally oxidized layer to the photoactivity of annealed nanoporous anodic oxide was significantly less.

Figures 5.7 (a) and (b) compare the surface morphologies of the anodic nanoporous Bi_2O_3 samples before and after the photo electrochemical (PEC) test. It is clear the nanoporous morphology of the oxide layer has significantly changed after the PEC test. Furthermore, selective dissolution of oxide layer could also be observed that manifested into formation of discrete pits. The porosity level of the oxide appeared to have decreased significantly and the morphology of the oxide layer was turning out to be of sintered flakes. Figure 5.8 shows the Tauc plots of the post-PEC tested samples. The band gap of the sample annealed at 240 ^oC for 4 h increased to 2.7 eV and the sample annealed at 240 ^oC for 6 h showed a band gap of 2.75 eV. The increase in the band gap of the samples suggested the possibility of increase in the volume fraction of α-Bi_2O_3.

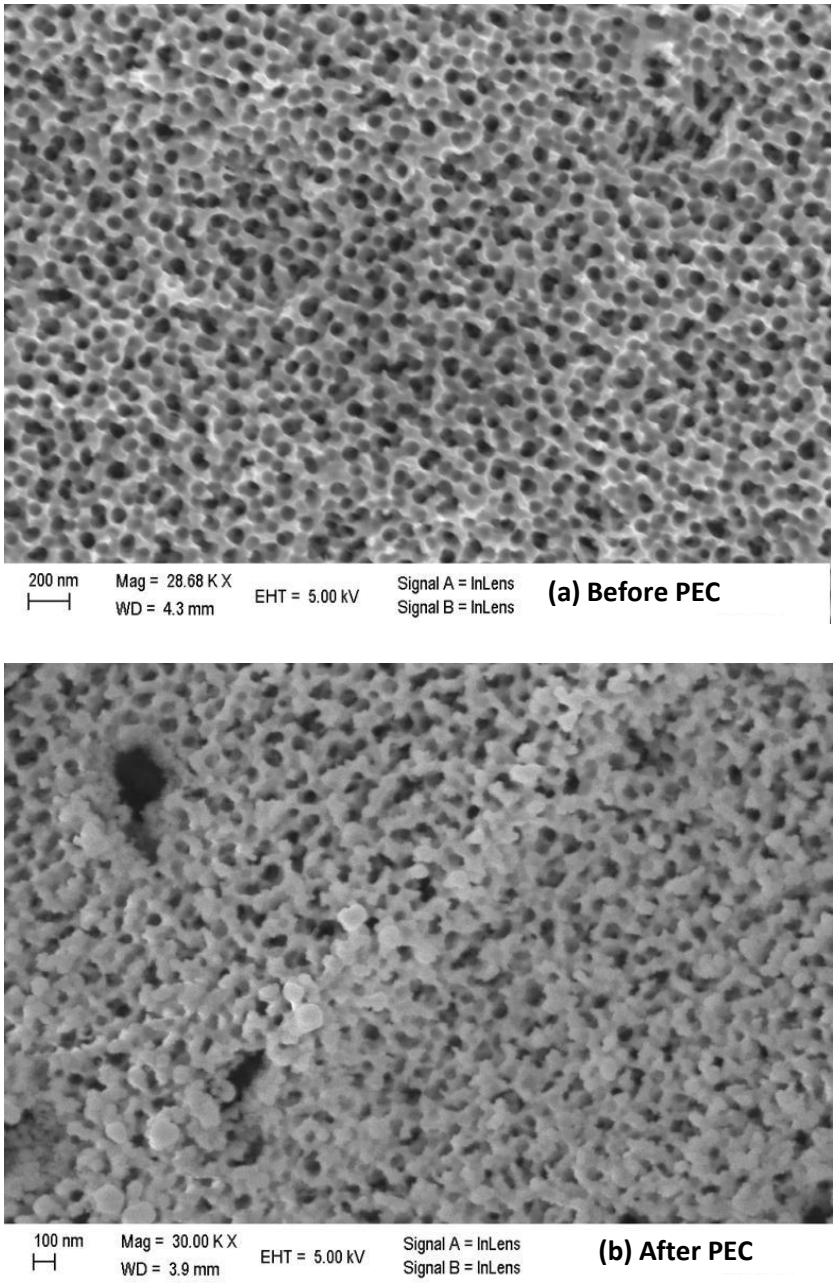

Figure 5.7. FESEM images of the nanoporous morphology of the bismuth oxide synthesized by anodization of bismuth at 60 V for 30 minutes and annealed at 240 ^{o}C for 2 h: (a) before the PEC testing, and (b) after the PEC testing at 0.2 $V_{Ag/AgCl}$ in 1 M KOH for ~ 3 h of illumination.

It should be noted that the α-Bi_2O_3 is the stable phase at room temperature whose band gap is 2.8 eV and that shows p-type semiconductivity. Therefore, the exponential decrease in the photo current density of the samples containing metastable β-Bi_2O_3 could be attributed the possible photo assisted transformation of the α-Bi_2O_3 that had higher band gap (therefore, harvesting smaller fraction of the simulated sunlight) and different semiconductivity. When

p-type semiconducting phases are present within the matrix of n-type material, several local p-n junctions would be formed. These junctions would alter the electric field of the space charge layer of the photo electrode and affect the electron-hole separation. Furthermore, the α-Bi_2O_3 present along with the β-Bi_2O_3 could possibly act as traps for the holes. It should be noted that the holes need to be transported to the surface of the photo anode and participate in the water oxidation reaction to evolve oxygen as given in reaction [3]. Trapping of holes by the α-Bi_2O_3 would manifest into decrease in the photo current. Figure 5.9 shows the XRD patterns of the post PEC tested samples. By comparing the XRD results of the samples before the PEC testing as given in Figure 5.3, it was observed that the volume fraction of the α-Bi_2O_3 phase increased significantly after the PEC testing. It can be seen that the sample annealed at 240 ^oC for 6 h showed about 40% of α-Bi_2O_3 after the long term illumination under an external bias potential.

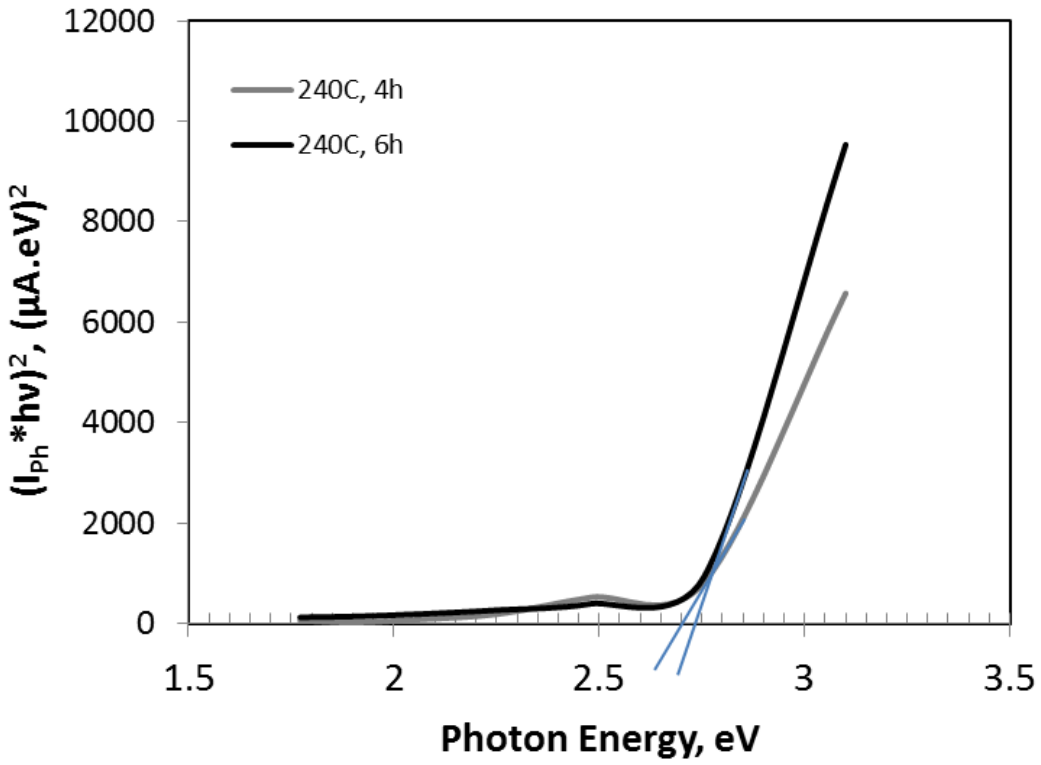

Figure 5.8. Tauc plots of the nanoporous anodic Bi_2O_3 annealed at 240 ^oC for 2 and 4 h after long term photo electrochemical experiments. The band gap values increased from 2.5 to > 2.7 eV after > 2 h of photo illumination.

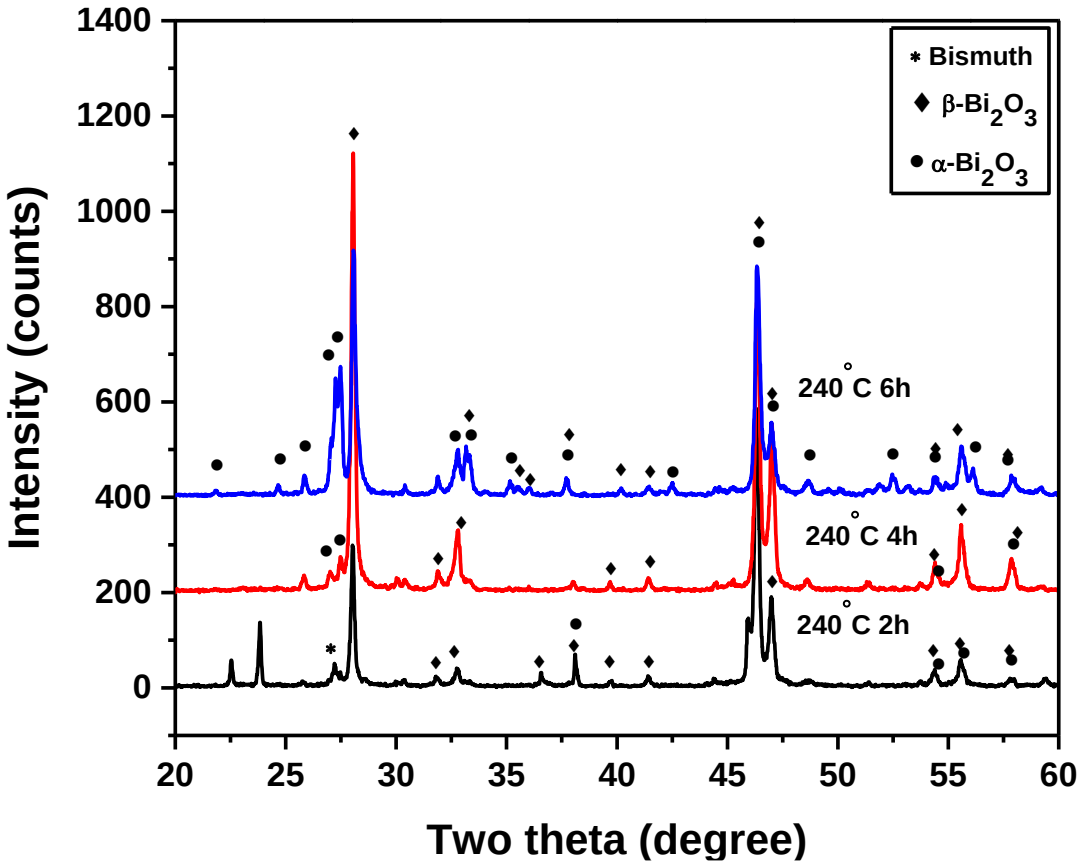

Figure 5.9. XRD patterns of the nanoporous anodic Bi_2O_3 annealed at 240 ^oC for 2, 4, and 6 h after long term photo electrochemical experiments.

5.5.4. Impedance spectroscopy

Figures 5. 10 (a) and (b) show the impedance modulus of the sample annealed at 240 ^oC for 4 h under dark and illuminated conditions after the end of each 20-minutes illumination cycles. For comparison, the impedance modulus at 0.01 Hz could be considered. After the first cycle the impedance under dark condition was about 5 x 10^4 Ohm-cm^2. When illuminated the impedance was about 1.7 x 10^3 Ohm-cm^2. The lower impedance under illumination could be attributed to the increased charge carrier density because of the photo generated electron-hole pairs. The impedance increased almost by an order of magnitude to 3 x 10^5 Ohm-cm^2 after the second cycle measured under dark condition. This increase in the impedance was commensurate with the significant decay in the photo current density between first and second 20-minutes illumination cycles. The impedance measured after subsequent illumination cycles increased with the number cycles even though the change

was not very significant for both dark and illuminated conditions as seen in Figures 5.10 (a) and (b) which followed the trend of the photo current decay.

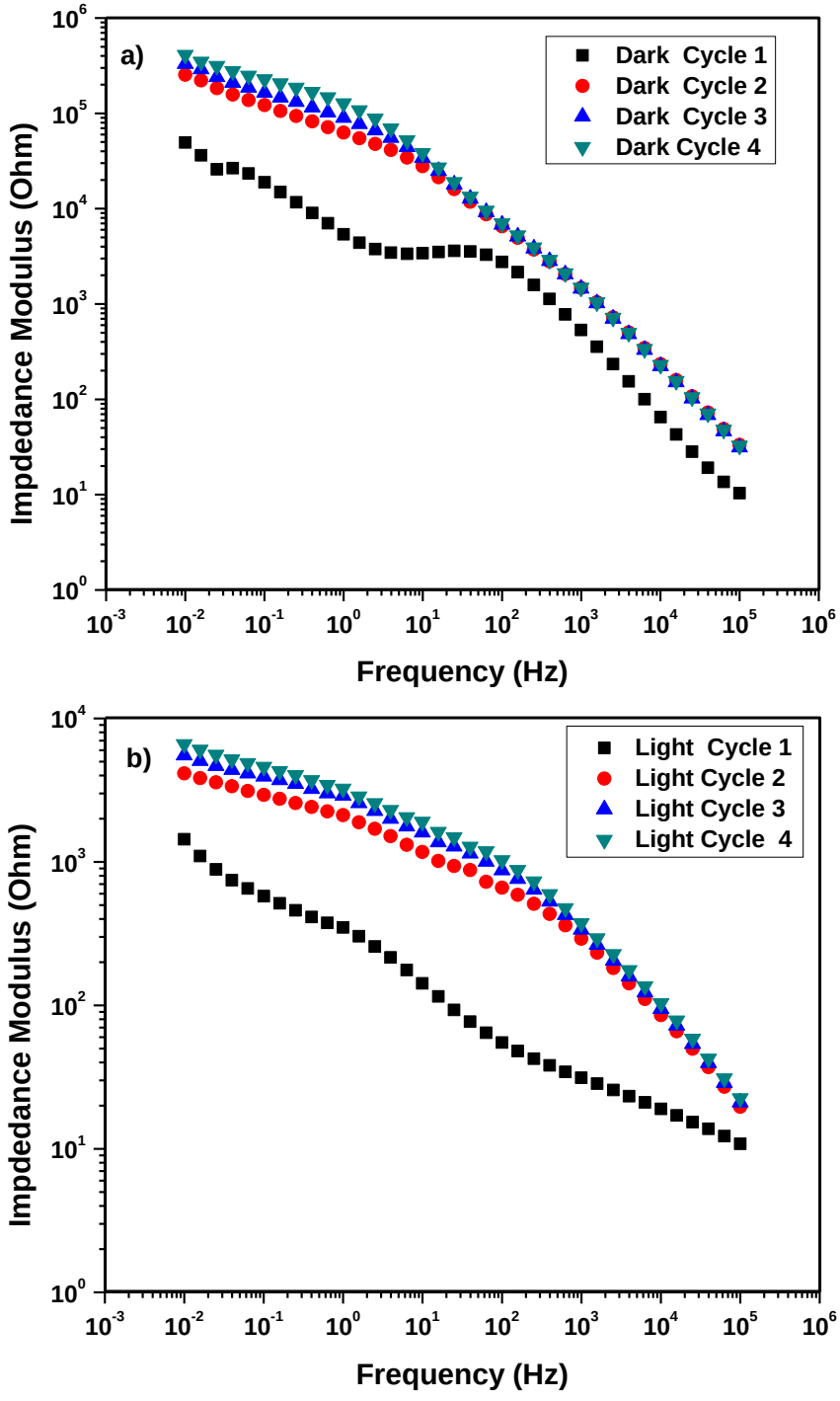

Figure 5.10. Electrochemical impedance spectroscopy (Bode plots) of the anodic nanoporous Bi_2O_3 annealed at 240 ^{o}C for 4 h in 1 M KOH without (a) and with (b) illumination.

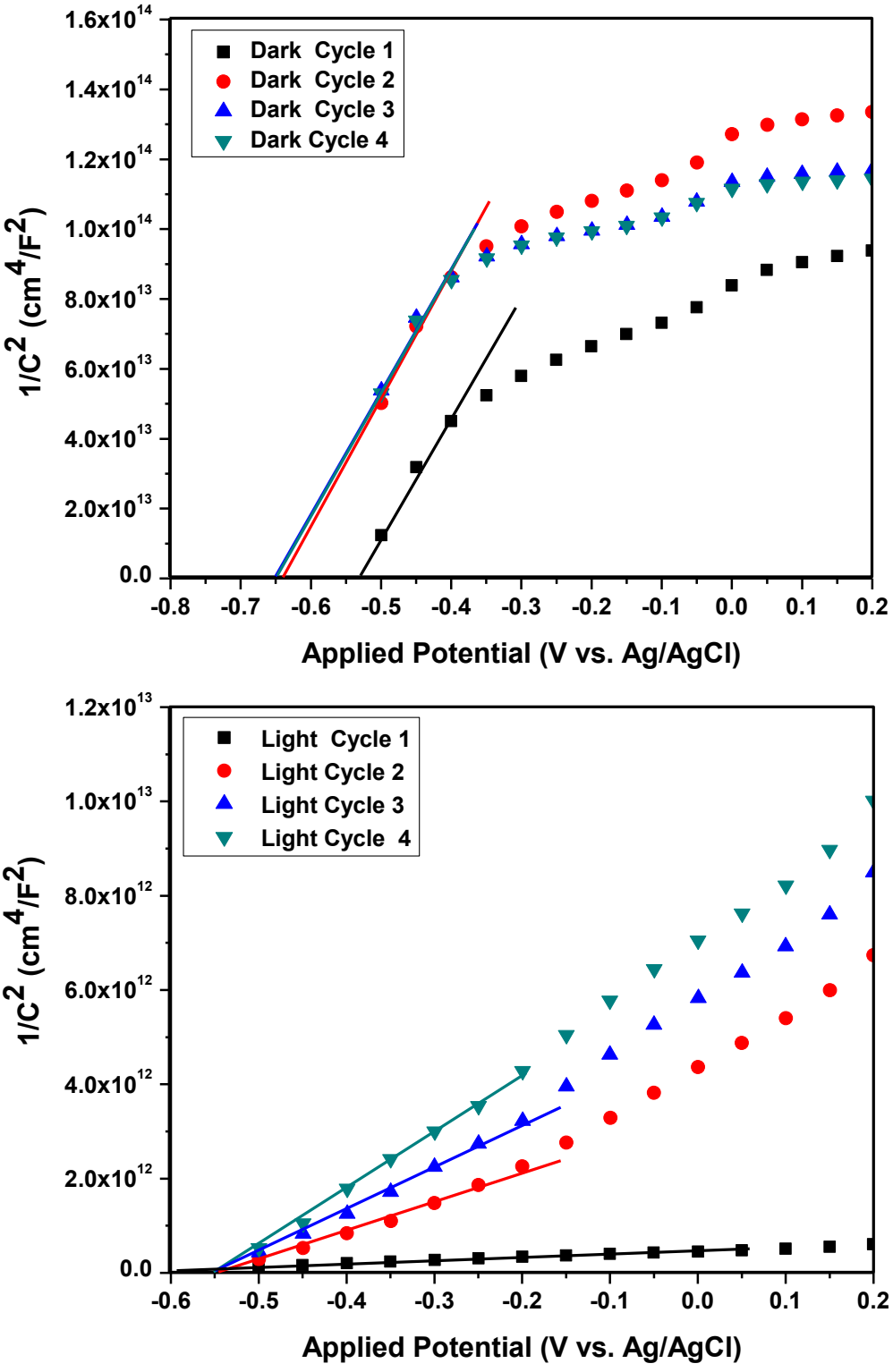

Figure 5.11. Mott-Schottky of the anodic nanoporous Bi_2O_3 annealed at 240 ^oC for 4 h in 1 M KOH without (a) and (b) with illumination

Figures 5.11 (a) and (b) show the Mott-Schottky plots of the sample annealed at 240 °C for 4 h under dark and illuminated conditions respectively. The plots showed two different regions. The region in the potential range of -0.5 to -0.3 V was considered as low band bending region that showed steeper slopes and hence lower charge carrier densities. The region at higher anodic potentials, considered as high band bending region, showed shallower slopes and therefore higher charge carrier densities. In order to compare the photo electrochemical behavior of the different annealed samples, only the low band bending region was considered. Table 5.1 summarizes the Mott-Schottky results of the sample annealed at 240 °C for 4h. The flat band potential after cycle 1 under dark condition was -0.53 $V_{Ag/AgCl}$ and the potential shifted to slightly negative potential -0.59 $_{V}Ag/AgCl$ under illuminated condition. It is interesting to note that the flat band potentials of subsequent cycles under illuminated condition were more positive than the flat band potentials of dark conditions. In fact, the flat band potentials did not change significantly with the increase in the number of illumination cycles.

Table 5.1. Summary of Mott-Schottky results of the anodic nanoporous Bi_2O_3 sample annealed at 240 °C for 4 h after different illumination cycles. Each cycle represents illumination of the sample using 1-sun intensity simulated solar light for 20 minutes under an applied potential of 0.2 $V_{Ag/AgCl}$ in 1 M KOH.

Cycle	Flat band potential $V_{Ag/AgCl}$	Charge carrier density, cm^{-3}
Dark cycle 1	-0.53	9.35×10^{15}
Dark cycle 2	-0.64	8.53×10^{15}
Dark cycle 3	-0.66	9.45×10^{15}
Dark cycle 4	-0.66	9.45×10^{15}
Light Cycle 1	-0.59	3.2×10^{18}
Light Cycle 2	-0.54	5.56×10^{17}
Light Cycle 3	-0.55	3.74×10^{17}
Light Cycle 4	-0.55	2.43×10^{17}

5.5.5. Significance of the flat band potential

The flat band potential was determined from the intercept of potential axis of the Mott-Schottky plots where $1/C^2 = 0$. The flat band potential for an n-type material can be expressed as:[31]

$$E_{FB} = E_C + \Delta E_F + V_H + E_O \qquad [5.11]$$

Where, E_{FB} is the flat band potential with respect to a reference electrode (Ag/AgCl in this case), ΔE_F is the difference between the Fermi level and majority carrier band edge (E_C), V_H is the potential drop across the Helmholtz layer, and E_O is the scale factor relating the reference electrode redox level to the absolute vacuum scale (-4.7 V for saturated Ag/AgCl). ΔE_F can be calculated using the standard relation:

$$\Delta E_F = kT \ln\left(\frac{N_D}{N_C}\right) \qquad [5.12]$$

Where, k = Boltzmann constant, T = temperature, N_D = charge carrier density determined from the Mott-Schottky plot, and N_c = effective density of states in conduction band given by the relation:

$$N_c = (7.54\pi)\left(\frac{m_c E}{h^2}\right)^{3/2} \qquad [5.13]$$

Where, m_e = equivalent mass of electrons, h = Planck's constant, ***E*** = energy range of the band considered. The effective mass of electrons in α-Bi_2O_3 is considered as 0.68 times the mass of electron. Considering the effective density of states in conduction band to be around 5 x10^{22} cm^{-3}, the ΔE_F can be calculated in potential scale as: 0.4 V in dark condition and about 0.3 V for the illuminated condition. Using the relation (6), one can calculate the position of the conduction band edges of the anodic nanoporous Bi_2O_3 and analyze the energetics of the PEC water splitting process. If the flat band potential is measured at a pH corresponding to zero point of charge (pH_{ZPC}), then the V_H will be zero because of the absence of the absorption at the electrode interface. In case of the Bi_2O_3, the pH_{ZPC} has been reported as 6.2.[32] Therefore, significant adsorption of OH^- would be expected on the surface of the nanoporous oxide layer and the potential drop across the Helmholtz layer should be considered. Since the magnitude of V_H was a strong function of electrolyte and all the experiments were carried out in the same electrolyte, the contribution of V_H was not considered in the calculation of the band edges in this work. This is justifiable because the band edge variation were compared

between different annealing conditions of similar material. From the positive slope of the Mott-Schottky plots it can be concluded that the anodic nanoporous Bi_2O_3 showed n-type behavior. Therefore, the majority charge carriers will be electrons. The charge carrier density under the dark condition was in the order of 10^{16} cm^{-3}. The charge carries could be associated with the oxygen vacancies that were inherently formed during anodization. It should be noted that the β-Bi_2O_3 has a distorted fluorite structure with 25% of ordered vacant oxygen sites along (001) planes.[33] When illuminated the charge carrier density increased by almost two orders of magnitude. The charge carrier densities of the samples under the dark and illuminated conditions could be directly correlated with the impedance values. The charge carrier density decreased with the number of cycles under the illuminated condition.

Figure 5.12 (a) and (b) illustrate the Bode plots of the anodic nanoporous Bi_2O_3 sample annealed at 240 °C for 6 h under dark and illuminated conditions after each 20-minutes illumination cycles, respectively. The results are almost similar to those of the samples annealed at 240 °C for 4 h. Figure 5.13 (a) and (b) show the Mott-Schottky results of the sample annealed at 240 °C for 6 under dark and illuminated conditions. Table 5.2 and 5.3 summarize the Mott-Schottky results of the sample annealed at 240 °C for 6 h and 2 h respectively. It was observed that the charge carrier density values remained almost similar in spite of different annealing times and variations in the phase contents. Even though the sample annealed for 6 h showed presence of relatively higher volume fraction of α-Bi_2O_3, the charge carrier density did not vary significantly. Comparing the photo current densities of the samples and correlating with the structural and electronic properties, it can be suggested that the charge carrier density influenced the photo current more than the phase content of the material. Among the three annealing times, higher photo current density was obtained from sample annealed for 2 h. This sample also had the highest charge carrier density and more negative flat band potential. The more negative is the flat band potential, better will be the photo electrochemical activity of the n-type electrode. This behavior can be explained using an energy level diagram.

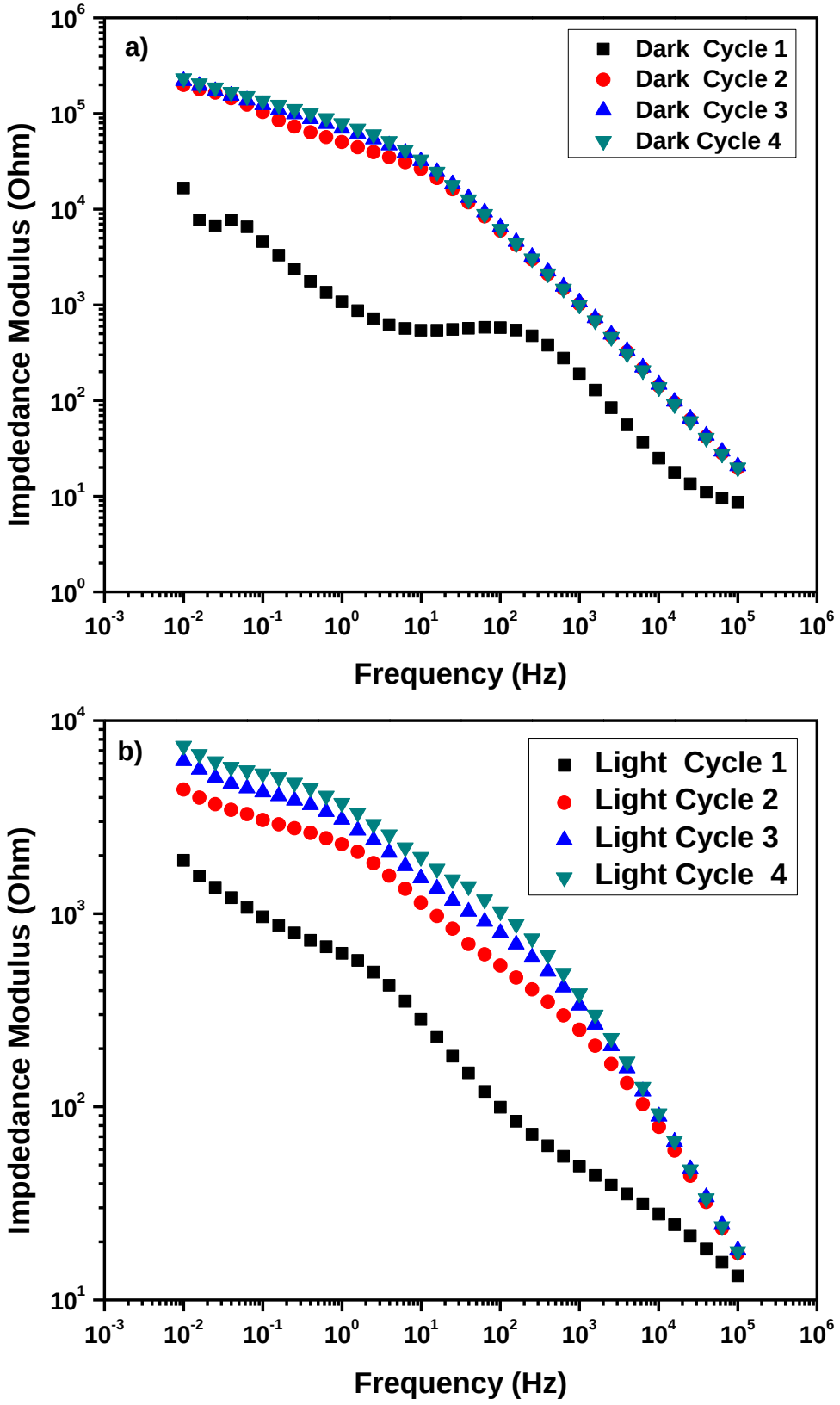

Figure 5.12. Electrochemical impedance spectroscopy (Bode plots) of the anodic nanoporous Bi_2O_3 annealed at 240 ^oC for 6 h in 1 M KOH without (a) and with (b) illumination.

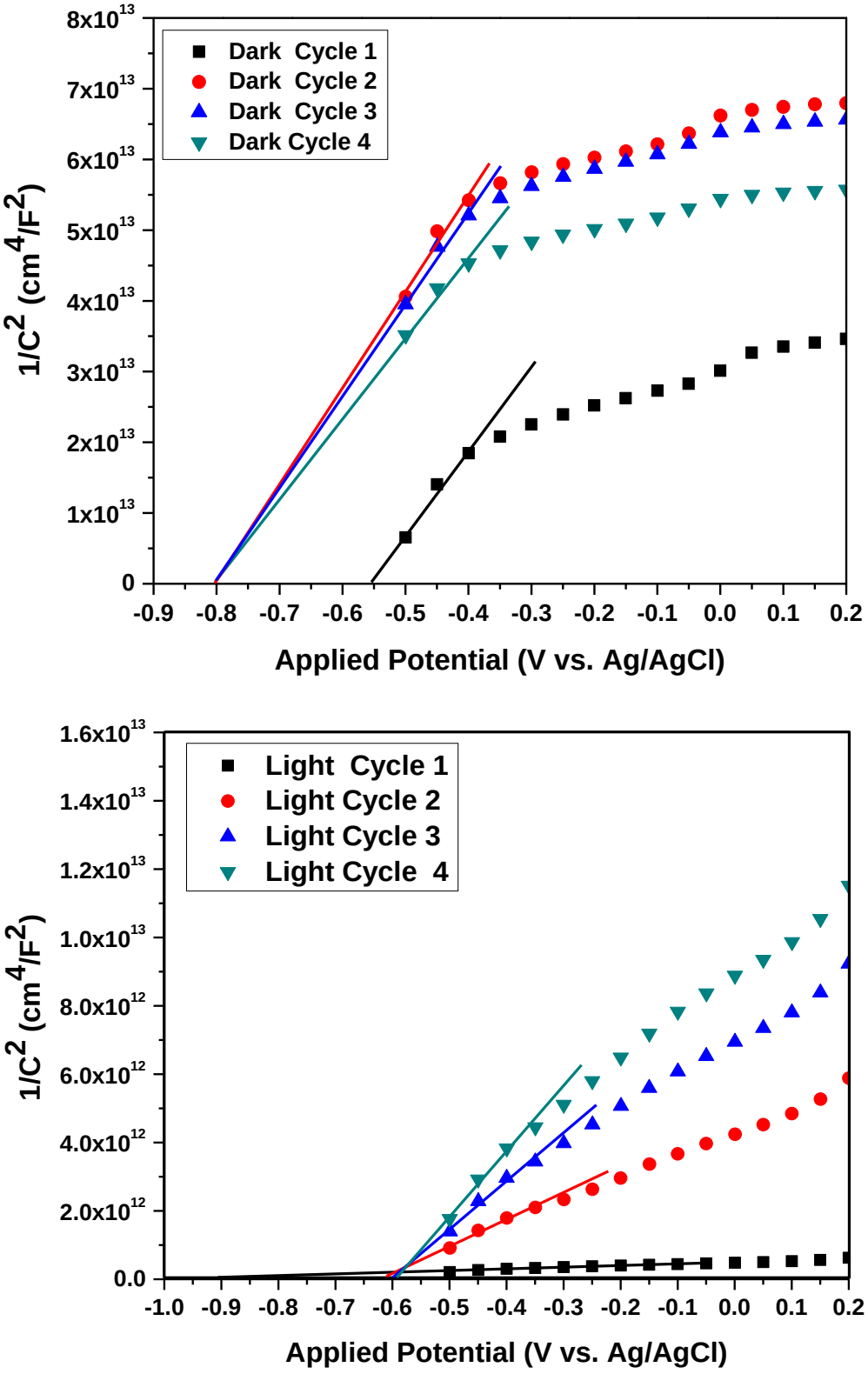

Figure 5.13. Mott-Schottky of the anodic nanoporous Bi_2O_3 annealed at 240 C for 6 h in 1 M KOH without (a) and (b) with illumination.

Table 5.2. Summary of Mott-Schottky results of the anodic nanoporous Bi_2O_3 sample annealed at 240 °C 6 h after different illumination cycles. Each cycle represents illumination of the sample using 1-sun intensity simulated solar light for 20 minutes under an applied potential of 0.2 $V_{Ag/AgCl}$ in 1 M KOH.

Cycle	Flat band potential $V_{Ag/AgCl}$	Charge carrier density, cm^{-3}
Dark cycle 1	-0.55	2.58×10^{16}
Dark cycle 2	-0.80	2.24×10^{16}
Dark cycle 3	-0.80	2.44×10^{16}
Dark cycle 4	-0.80	3.01×10^{16}
Light Cycle 1	-0.72	3.18×10^{18}
Light Cycle 2	-0.61	3.88×10^{17}
Light Cycle 3	-0.60	2.24×10^{17}
Light Cycle 4	-0.59	1.48×10^{17}

Table 5.3. Summary of Mott-Schottky results of the anodic nanoporous Bi_2O_3 sample annealed at 240 °C for 2 h after different illumination cycles. Each cycle represents illumination of the sample using 1-sun intensity simulated solar light for 20 minutes under an applied potential of 0.2 $V_{Ag/AgCl}$ in 1 M KOH.

Cycle	Flat band potential $V_{Ag/AgCl}$	Charge carrier density, cm^{-3}
Dark cycle 1	-0.53	1.32×10^{16}
Dark cycle 2	-0.78	2.14×10^{16}
Dark cycle 3	-0.86	2.61×10^{16}
Dark cycle 4	-0.90	3.16×10^{16}
Light Cycle 1	-1.26	3.93×10^{18}
Light Cycle 2	-0.89	6.40×10^{17}
Light Cycle 3	-0.80	3.36×10^{17}
Light Cycle 4	-0.75	2.90×10^{17}

Figure 5.14 shows the schematic of the potential level diagram illustrating the positions of the Fermi level, and conduction band edge of the anodic nanoporous Bi_2O_3 with reference to the Ag/AgCl electrode. The Fermi level of the material was determined from the flat band potential. The conduction band minimum was observed to be at -3.85 eV with reference to the absolute vacuum scale. The potentials of the hydrogen and OERs pertain to pH:14. It was observed after long term illumination, the conduction band edge of the sample was below the hydrogen reduction potential indicating requirement of an external bias to

split water. Since the valence band was well below the oxygen evolution potential, the holes were energetic for participating in the water oxidation reaction. It should be noted that during the initial period of illumination the flat band potential was negative enough for spontaneous hydrogen reduction reaction. For example, the sample annealed for 2 h (Table 5.3.) showed a flat band potential of -1.2 V during cycle 1. With the continuous illumination, the flat band potential shifted to more positive values. A correlation between the volume fraction of α-Bi_2O_3 and flat band potential could be observed. The flat band potential increased to more positive values with the increase in the α-Bi_2O_3 in the sample.

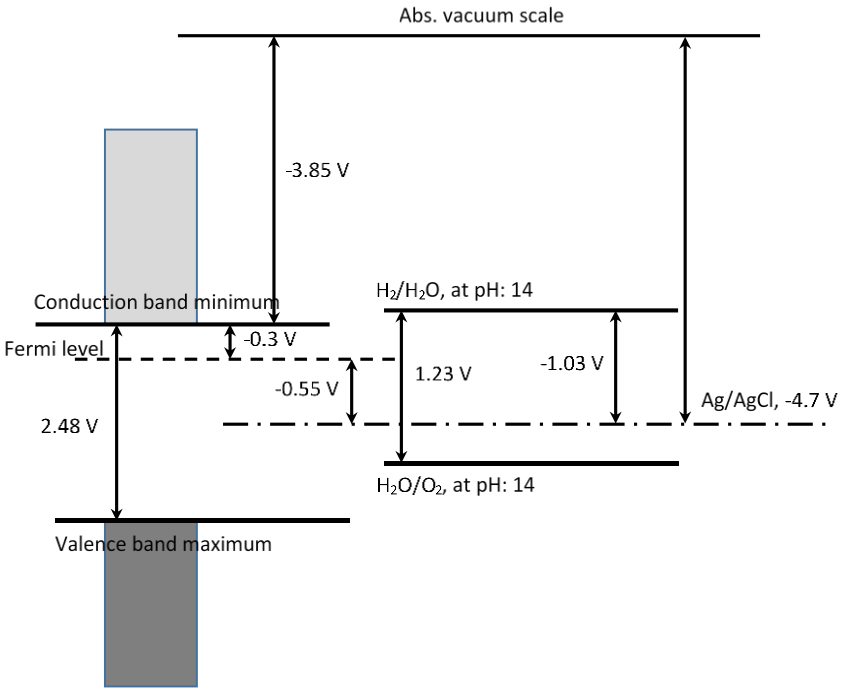

Figure 5.14. Schematics of the potential levels of anodic nanoporous Bi_2O_3 in pH:14 solution with reference to absolute vacuum scale and saturated Ag/AgCl electrode. All energy scales were converted to potential scale (1 eV corresponds to 1 V).

5.5.6. Photodecomposition

Cathodic decomposition of Bi_2O_3 has been proposed as a mechanism of instability in the photo activity.[34] The critical cathodic decomposition for Bi_2O_3 in 1 M KOH based on the reaction:

$$Bi_2O_3 + 3H_2O + 6e^- \rightarrow 2Bi(s) + 6OH^- \qquad E_O = -0.65\,V_{Ag/AgCl} \qquad [5.14]$$

It is observed that this critical potential is more positive than the observed flat band potentials during initial illumination cycles. Therefore, if the electrode was not anodically polarized, the cathodic decomposition could be a mechanism of instability under illumination at open circuit. In the present investigation, the samples were anodically polarized. Therefore, cathodic decomposition was not thermodynamically possible. The observed decay in the photocurrent density could be attributed to the formation of more stable α-Bi_2O_3 phase that showed p-type semiconductivity. In addition, the nanoporous anodic oxide showed possibly low activity for oxygen evolution similar to the behavior reported for $BiVO_4$. In order to make the anodic nanoporous bismuth oxide layer a practically useful electrode material for water splitting, two modifications could be implemented: (1) Addition of hole scavengers such as hydrogen peroxide and methanol. The hole scavengers may potentially mitigate accumulation of holes on the nanoporous surface which could increase the photocurrent and hinder photo oxidation of Bi^{3+} to higher valence states. However, the drawback of this approach would be difficult in controlling the electrolyte chemistry in a practical device. Furthermore, addition of hole scavenger would not lead to stoichiometric hydrogen and oxygen evolution by water splitting reaction since the oxygen evolution would still be retarded. (2) The next approach would be provision of a layer of catalyst that promotes OER such as cobalt phosphate, FeOOH, NiOOH, and nickel borate. Deposition of a transparent OER catalyst on the anodic nanoporous bismuth oxide layer would help not only stabilize the photocurrent but also enhance the photoactivity.[35]

5.6. Summary

Thin films of nanoporous bismuth oxide were synthesized by a simple electrochemical anodization of bismuth substrate. Annealing the anodic nanoporous Bi_2O_3 at 240 °C for 2 h resulted in stabilization of the metastable β-Bi_2O_3 phase that showed tetragonal symmetry and n-type semiconductivity. Longer annealing times resulted in formation of the more stable α-Bi_2O_3 phase that showed monoclinic lattice structure and p-type semiconductivity. The stability of the photo electrochemical behavior of the Bi_2O_3 nanoporous structure was observed to be affected by in-situ formation of the α-Bi_2O_3 phase during the illumination under an applied bias.

5.7. References

1. Fujishima, A.; Honda, K., Electrochemical Photolysis of Water at a Semiconductor Electrode. *Nature* **1972,** *238* (5358), 37-+.

2. Liu, Z.; Pesic, B.; Raja, K. S.; Rangaraju, R. R.; Misra, M., Hydrogen generation under sunlight by self ordered TiO< sub> 2</sub> nanotube arrays. *International Journal of Hydrogen Energy* **2009,** *34* (8), 3250-3257.

3. Rangaraju, R.; Panday, A.; Raja, K.; Misra, M., Nanostructured anodic iron oxide film as photoanode for water oxidation. *Journal of Physics D: Applied Physics* **2009,** *42* (13), 135303.

4. Yang, X.; Wolcott, A.; Wang, G.; Sobo, A.; Fitzmorris, R. C.; Qian, F.; Zhang, J. Z.; Li, Y., Nitrogen-Doped ZnO Nanowire Arrays for Photoelectrochemical Water Splitting. *Nano Letters* **2009,** *9* (6), 2331-2336.

5. Kudo, A.; Omori, K.; Kato, H., A Novel Aqueous Process for Preparation of Crystal Form-Controlled and Highly Crystalline BiVO4 Powder from Layered Vanadates at Room Temperature and Its Photocatalytic and Photophysical Properties. *Journal of the American Chemical Society* **1999,** *121* (49), 11459-11467.

6. Tang, J.; Zou, Z.; Ye, J., Efficient Photocatalytic Decomposition of Organic Contaminants over CaBi2O4 under Visible-Light Irradiation. *Angewandte Chemie International Edition* **2004,** *43* (34), 4463-4466.

7. Rao, P. M.; Cai, L.; Liu, C.; Cho, I. S.; Lee, C. H.; Weisse, J. M.; Yang, P.; Zheng, X., Simultaneously Efficient Light Absorption and Charge Separation in WO3/BiVO4 Core/Shell Nanowire Photoanode for Photoelectrochemical Water Oxidation. *Nano Letters* **2014,** *14* (2), 1099-1105.

8. Zhao, Z. B.; Wang, P.; Fan, L. B.; Chen, Z. F.; Yang, D. L., A PbS Film Synthesized by Ultrasonic Wave Assisted Chemical Bath Deposition Method and its Application in Photoelectrochemical Cell. *Advanced Materials Research* **2013,** *820*, 3-6.

9. Mandal, K. C.; Basu, S.; Bose, D. N., Surface-modified CdTe PEC solar cells. *Solar Cells* **1986,** *18* (1), 25-30.

10. Gerischer, H., On the stability of semiconductor electrodes against photodecomposition. *Journal of Electroanalytical Chemistry and Interfacial Electrochemistry* **1977,** *82* (1–2), 133-143.

11. Cheng, H.; Huang, B.; Lu, J.; Wang, Z.; Xu, B.; Qin, X.; Zhang, X.; Dai, Y., Synergistic effect of crystal and electronic structures on the visible-light-driven photocatalytic performances of Bi(2)O(3) polymorphs. *Physical chemistry chemical physics : PCCP* **2010,** *12* (47), 15468-75.

12. Yang, X.; Lian, X.; Liu, S.; Jiang, C.; Tian, J.; Wang, G.; Chen, J.; Wang, R., Visible light photoelectrochemical properties of β-Bi2O3 nanoporous films: A study of the dependence on thermal treatment and film thickness. *Applied Surface Science* **2013,** *282*, 538-543.

13. Yang, X.; Lian, X.; Liu, S.; Wang, G.; Jiang, C.; Tian, J.; Chen, J.; Wang, R., Enhanced photocatalytic performance: aβ-Bi2O3thin film by nanoporous surface. *Journal of Physics D: Applied Physics* **2013,** *46* (3), 035103.

14. Lv, X.; Zhao, J.; Wang, X.; Xu, X.; Bai, L.; Wang, B., Novel Bi2O3 nanoporous film fabricated by anodic oxidation and its photoelectrochemical performance. *J Solid State Electrochem* **2013,** *17* (4), 1215-1219.

15. Brezesinski, K.; Ostermann, R.; Hartmann, P.; Perlich, J.; Brezesinski, T., Exceptional Photocatalytic Activity of Ordered Mesoporous β-Bi2O3Thin Films and Electrospun Nanofiber Mats. *Chemistry of Materials* **2010,** *22* (10), 3079-3085.

16. Chunzhi Li, J. Z., Kejia Liu A New Method of Enhancing Photoelectrochemical Characteristics of Bi-Bi2O3 Electrode for Hydrogen Generation via Water Splitting. *International Journal of Electrochemical Science* **2012,** *74* (6), 5028-5034.

17. Qin, F.; Li, G.; Wang, R.; Wu, J.; Sun, H.; Chen, R., Template-free fabrication of Bi2O3 and (BiO)2CO3 nanotubes and their application in water treatment. *Chemistry* **2012,** *18* (51), 16491-7.

18. Schlesinger, M.; Schulze, S.; Hietschold, M.; Mehring, M., Metastable beta-Bi2O3 nanoparticles with high photocatalytic activity from polynuclear bismuth oxido clusters. *Dalton transactions* **2013,** *42* (4), 1047-56.

19. Yu, Z.; Zhang, J.; Zhang, H.; Shen, Y.; Xie, A.; Huang, F.; Li, S., Facile solvothermal synthesis of porous Bi2O3 microsphere and their photocatalytic performance under visible light. *Micro & Nano Letters* **2012,** *7* (8), 814.

20. Dutta, D. P.; Roy, M.; Tyagi, A. K., Dual function of rare earth doped nano Bi2O3: white light emission and photocatalytic properties. *Dalton transactions* **2012,** *41* (34), 10238-48.

21. Li, S.; Morasch, J.; Klein, A.; Chirila, C.; Pintilie, L.; Jia, L.; Ellmer, K.; Naderer, M.; Reichmann, K.; Gröting, M.; Albe, K., Influence of orbital contributions to the valence band alignment of Bi2O3, Fe2O3, BiFeO3, and Bi0.5Na0.5TiO3. *Physical Review B* **2013,** *88* (4).

22. Lei, Y. H.; Chen, Z. X., Density functional study of the stability of various alpha-Bi2O3 surfaces. *The Journal of chemical physics* **2013,** *138* (5), 054703.

23. Matsumoto, A.; Koyama, Y.; Togo, A.; Choi, M.; Tanaka, I., Electronic structures of dynamically stable As2O3, Sb2O3, and Bi2O3 crystal polymorphs. *Physical Review B* **2011,** *83* (21), 214110.

24. Matsumoto, A.; Koyama, Y.; Tanaka, I., Structures and energetics of Bi2O3 polymorphs in a defective fluorite family derived by systematic first-principles lattice dynamics calculations. *Physical Review B* **2010,** *81* (9).

25. Xu, Z.; Tabata, I.; Hirogaki, K.; Hisada, K.; Wang, T.; Wang, S.; Hori, T., UV-induced formation of activated Bi2O3 nanoflake: an enhanced visible light driven photocatalyst by platinum loading. *RSC Advances* **2012,** *2* (1), 103-106.

26. Hou, J.; Yang, C.; Wang, Z.; Zhou, W.; Jiao, S.; Zhu, H., In situ synthesis of α–β phase heterojunction on Bi2O3 nanowires with exceptional visible-light photocatalytic performance. *Applied Catalysis B: Environmental* **2013,** *142–143* (0), 504-511.

27. Vila, M.; Díaz-Guerra, C.; Piqueras, J., Laser irradiation-induced α to δ phase transformation in Bi2O3 ceramics and nanowires. *Applied Physics Letters* **2012,** *101* (7), -.

28. Sirimanne, P. M.; Takahashi, K.; Sonoyama, N.; Sakata, T., Photocurrent enhancement of wide bandgap Bi2O3 by Bi2S3 over layers. *Solar Energy Materials and Solar Cells* **2002,** *73* (2), 175-187.

29. Waisy, E. T. A.; Wazny, M. S. A., Structural, Surface Morphology and Optical Properties of Bi2O3 Thin Film Prepared By Reactive Pulse Laser Deposition. *Journal of university of Anbar for Pure science* **2013,** *7* (2).

30. Hardcastle, F. D.; Wachs, I. E., The molecular structure of bismuth oxide by Raman spectroscopy. *Journal of Solid State Chemistry* **1992,** *97* (2), 319-331.

31. Nozik, A. J.; Memming, R., Physical Chemistry of Semiconductor−Liquid Interfaces. *The Journal of Physical Chemistry* **1996,** *100* (31), 13061-13078.

32. Xu, Y.; Schoonen, M. A. A., The absolute energy positions of conduction and valence bands of selected semiconducting minerals. *American Mineralogist* **2000,** *85* (3-4), 543-556.

33. Wang, Y.; Wen, Y.; Ding, H.; Shan, Y., Improved structural stability of titanium-doped β-Bi2O3 during visible-light-activated photocatalytic processes. *J Mater Sci* **2010,** *45* (5), 1385-1392.

34. Metikoš-Huković, M., The photoelectrochemical properties of anodic Bi2O3 films. *Electrochimica Acta* **1981,** *26* (8), 989-1000.

35. Kim, T. W.; Choi, K.-S., Nanoporous BiVO4 Photoanodes with Dual-Layer Oxygen Evolution Catalysts for Solar Water Splitting. *Science* **2014,** *343* (6174), 990-994.

Appendix A. Supplementary Information for Chapter 2

Cross-sectional SEM

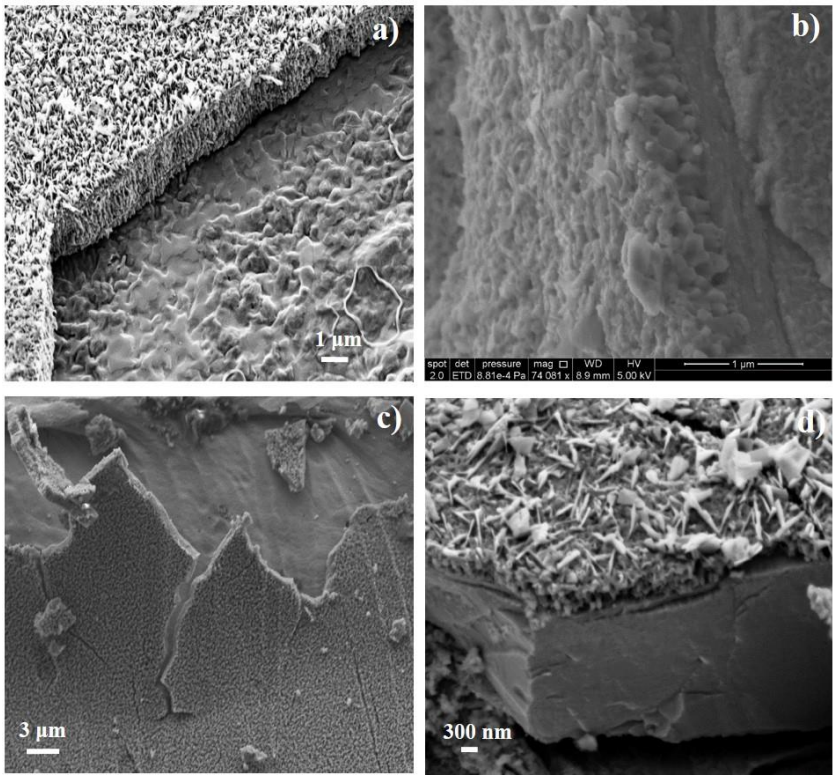

Figure A1. Cross-sectional FESEM images of (a) pure iron foil and (b) FeNdB samples thermally oxidized in air at 450 °C for 2 h. These samples are referred as thermal iron oxide and oxidized FeNdB respectively in the text. Cross-sectional FESEM images of the anodized surfaces of the (c) FeNdB and (d) iron foil samples electrochemically anodized in ethylene glycol solution containing 0.1 M NH_4F and 5 vol% water at 40 V for 15 minutes and thermally annealed at 450 °C for 2h. These samples are referred as anodized iron oxide and anodized FeNdB respectively in the text.

XPS Analysis

Figure A2 (a) shows the Fe-$2p_{3/2}$ X-ray photoelectron spectra of the FeNdB oxide samples in three different conditions. The binding energy of Fe $2p_{3/2}$ of the as-anodized sample was slightly less than that of other two samples indicating presence of large concentration of oxygen vacancies in the as-anodized condition. The Fe $2p_{3/2}$ spectrum of the oxidized FeNdB sample showed a small shoulder at the low binding energy side, which was characteristic of α-Fe_2O_3.[1] Larger multiplet splitting of the $2p_{3/2}$ peak has been observed for α-Fe_2O_3. Furthermore, the satellite peak to $2p_{3/2}$ observed at 719.2 eV is a characteristic of α-

Fe_2O_3. The XRD results also indicated that the oxidized FeNdB samples contained predominantly α-Fe_2O_3 phase.

Figure A2 (b) shows the Nd-*3d* spectra of FeNdB samples in as-anodized and anodized + annealed conditions. The $3d_{5/2}$ binding energy peak at 982.1 eV corresponds to Nd^{3+} ions in the material. The spectrum of Nd-*3d* is similar to the one reported for Nd_2O_3.[2] The $3d_{5/2}$ peak of the as-anodized sample showed a shoulder in the lower energy side indicating possible missing coordination with oxygen ions due to presence of oxygen vacancies. Significant concentration of Nd^{3+} observed in the anodized oxide layers of FeNdB samples could be associated with the field assisted oxidation of Fe and Nd at high voltages during anodization. During anodization, Fe^{3+} and Nd^{3+} ions migrate toward the oxide/electrolyte interface and O^{2-} ions migrate toward the metal/oxide interface. In spite of its large ionic radius, Nd^{3+} was observed to migrate two times faster than Al^{3+} in Al-10 at% Nd alloy.[3] Similar type of behavior could be expected in the FeNdB sample also.

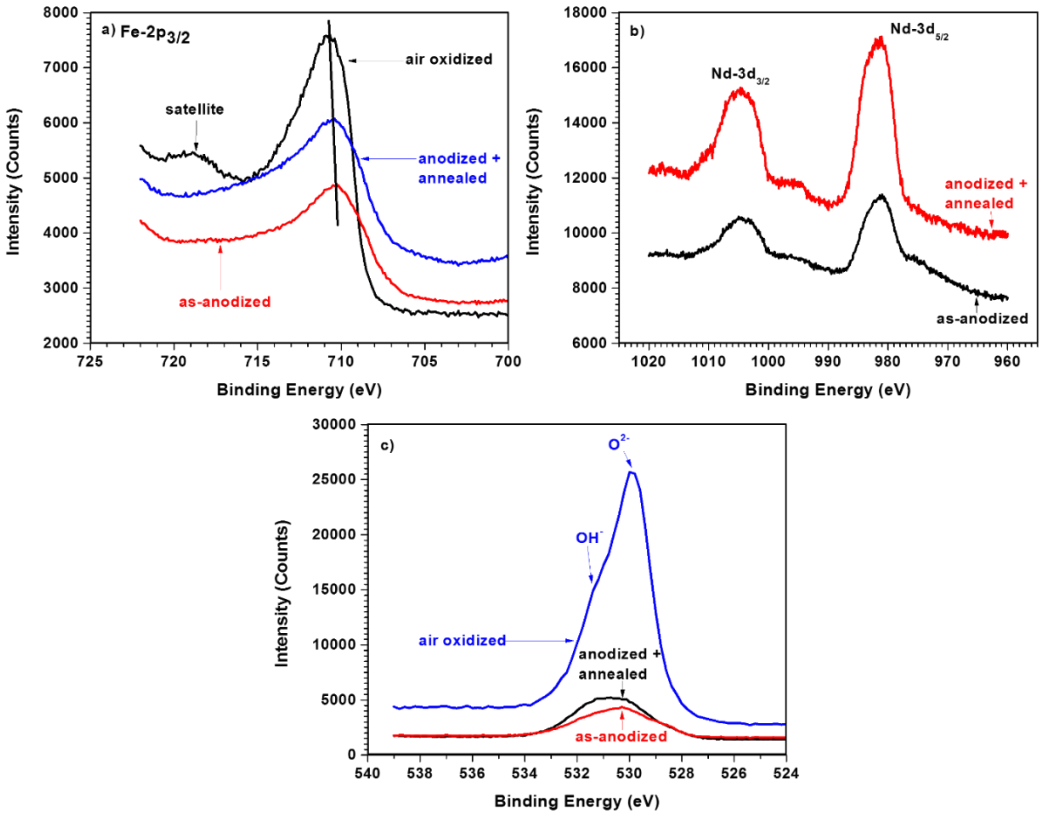

Figure A2. High resolution X-ray photo electron spectra of the FeNdB samples in three different surface conditions: air oxidized, as-anodized, and anodized + annealed. (a) Fe 2p spectra, (b) Nd 3d spectra, and (c) O 1s spectra

Figure A2 (c) shows the O 1s spectra of the three samples. The O *1s* peak at 530.1 eV of the oxidized FeNdB sample was associated with the O^{2-} ions present in the α-Fe_2O_3. A weak shoulder that started at 531.4 eV is associated with OH^-.[4] The O 1s peaks of the as-anodized, and anodized + annealed samples were broader than the oxidized FeNdB sample and no apparent shoulder corresponding to hydroxyl adsorption could be observed. The high energy peak at 531 eV could be attributed to the Nd-O bonding due to incorporation of Nd^{3+} ions in the Fe_2O_3 lattice. Similar results were reported for Nd^{3+} doping of TiO_2.[5] The broader could also be associated with the occluded carbonates on the nanotube walls of the oxides. The carbonaceous species with C-O or C=O bonding adsorbed on the oxide nanotubes during the anodization process in ethylene glycol solution. Thermal annealing was observed to convert part of these carbonaceous species in to diffusible carbon and get incorporated in the oxide which increased the conductivity of the iron oxide and titanium dioxide nanotubes.[6, 7]

Figure A3 shows the valence band structure of the oxide layers of pure iron and FeNdB alloy. Pure iron oxide in the as anodized and anodized + annealed conditions showed almost similar valance band structure near the Fermi energy level. The valence band of the anodized FeNdB sample was observed to have shifted by 0.1 eV to lower binding energies. The valence band structure of the pure iron oxide can be characterized by the combination of the partial electron density of states of O-*2p* and Fe-*3d*. In case of the oxide of FeNdB alloy, Nd-*3d* and Nd-*4f* partial density of states also contribute to the valence band making it wider than that of pure iron oxide. The increase in the band width could result in better charge transport properties because of minimized loss due to scattering. The shift in the valence band to lower binding energy could be attributed to the incorporation of Nd^{3+} in the hematite lattice structure. Magnan et al[8] reported shift of valence band of the Ti-doped hematite to higher binding energies because of the increase in the cation vacancy. The change in the valence band position was not considered to affect the energy band gap of the iron oxide but to move the Fermi level. If the same argument is applied to the present investigation, then the lowering the binding energy of the valence band should result in moving the Fermi level away from the conduction band and decrease in the conductivity.

The TEM, XRD, XPS, and Raman spectroscopic results indicate that in spite of a large difference in the ionic radii of Fe^{3+} and Nd^{3+} (0.0645 nm, and 0.0983 nm respectively for coordination number 6 with high spin configuration),[9] significant concentration of Nd^{3+} could be present in the solid solution.

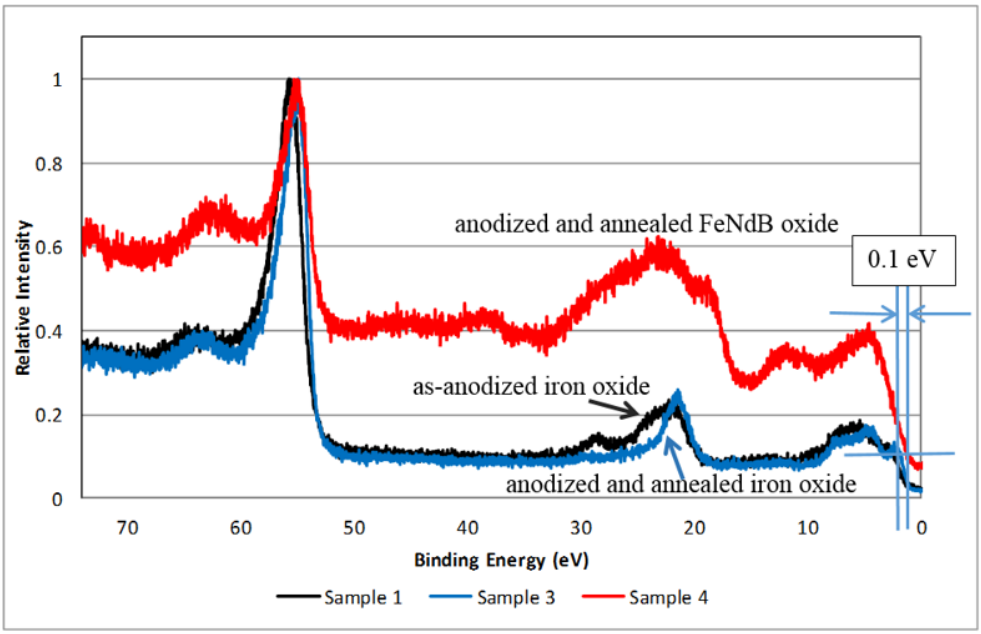

Figure A3. Valence band structure of the oxide layers of pure iron and $Fe_{14}Nd_2B$ alloy.

Galvanodynamic polarization

Figure A4 (a) shows the voltage vs current (V vs I) relation of the thermal iron oxide and oxidized FeNdB alloy with and without light illumination. Without light illumination (considered as dark condition), the oxygen evolution reaction (OER) initiated at a potential of 0.72 $V_{Ag/AgCl}$ (1.745 V_{RHE}), with an overpotential of 0.515 V, in case of the thermal iron oxide. The onset of OER on the oxidized FeNdB sample occurred at a potential of 0.68 $V_{Ag/AgCl}$, about 40 mV less than that of the iron oxide. Design of anode of a practical electrolyzer considers potential requirement at a current density of 10 mA/cm^2. If the data presented in Figure A4 (a) could be linearly extrapolated to a current density of 10 mA/cm^2, it is apparent that oxidized FeNdB sample alloy will perform better than the pure iron oxide. The Tafel slope and exchange current density for the OER could be determined by plotting the current density data in log scale and potential values in linear scale. Table A1 summarizes the pertinent data derived from the Figure A4 (a) and (b). The thermal iron oxide showed three orders of

magnitude higher exchange current density than oxidized FeNdB sample. However, the FeNdB oxide required much less potential to drive the OER because of its shallower Tafel slope of 68 mV/decade than the Tafel slope of the iron oxide (165 mV/decade). It should be noted that the calculated values are limited by the diffusion of the species because of the static experimental conditions. The Tafel slope can be expressed as:

$$\frac{dE}{d(\log i)} = \frac{2.303\,RT}{\alpha_a nF} \qquad (7)$$

Where, α_a is the charge transfer coefficient, n is number of electrons involved in the electrochemical reaction, and other notations bear the standard meanings. Even though four electrons are required for the overall oxygen evolution, the OER occurs in four steps as described in the introduction. It is well established that simultaneous involvement of more than one electron in a single step electrochemical reaction is highly improbable based on the absolute rate theory of Marcus.[10] Therefore, for the calculation of the transfer coefficient the value of n is considered to be one. For one electron transfer reaction, the transfer coefficient is similar to the symmetry factor. In general, the symmetry factor is considered (or assumed) to be 0.5, and number of electrons involved in a reaction is calculated from the Tafel slope and the assumed symmetry factor. Because the OER is considered a multistep reaction involving single electron in each step, the symmetry factor or transfer coefficient is considered a variable. In this investigation, the transfer coefficient or the symmetry factor is considered to be influenced by the surface morphology, oxygen vacancy sites, and nearest neighbors to the adsorption sites. Overall, the oxide layer of FeNdB showed higher transfer coefficient under dark condition than the iron oxide which is attributed to the incorporation of the Nd (III) and B(III) in the lattice. Liao et al., based on the first principle calculations, proposed that n-type dopants in the hematite that easily ionize to the highest valence state or promote covalent bonding with oxygen would render better charge transfer properties.[11] The incorporation of Nd^{3+} and B^{3+} ions in the hematite structure could satisfy the above conditions (easy and complete ionization, and more covalent bonding with oxygen, respectively) for better charge transfer characteristics.

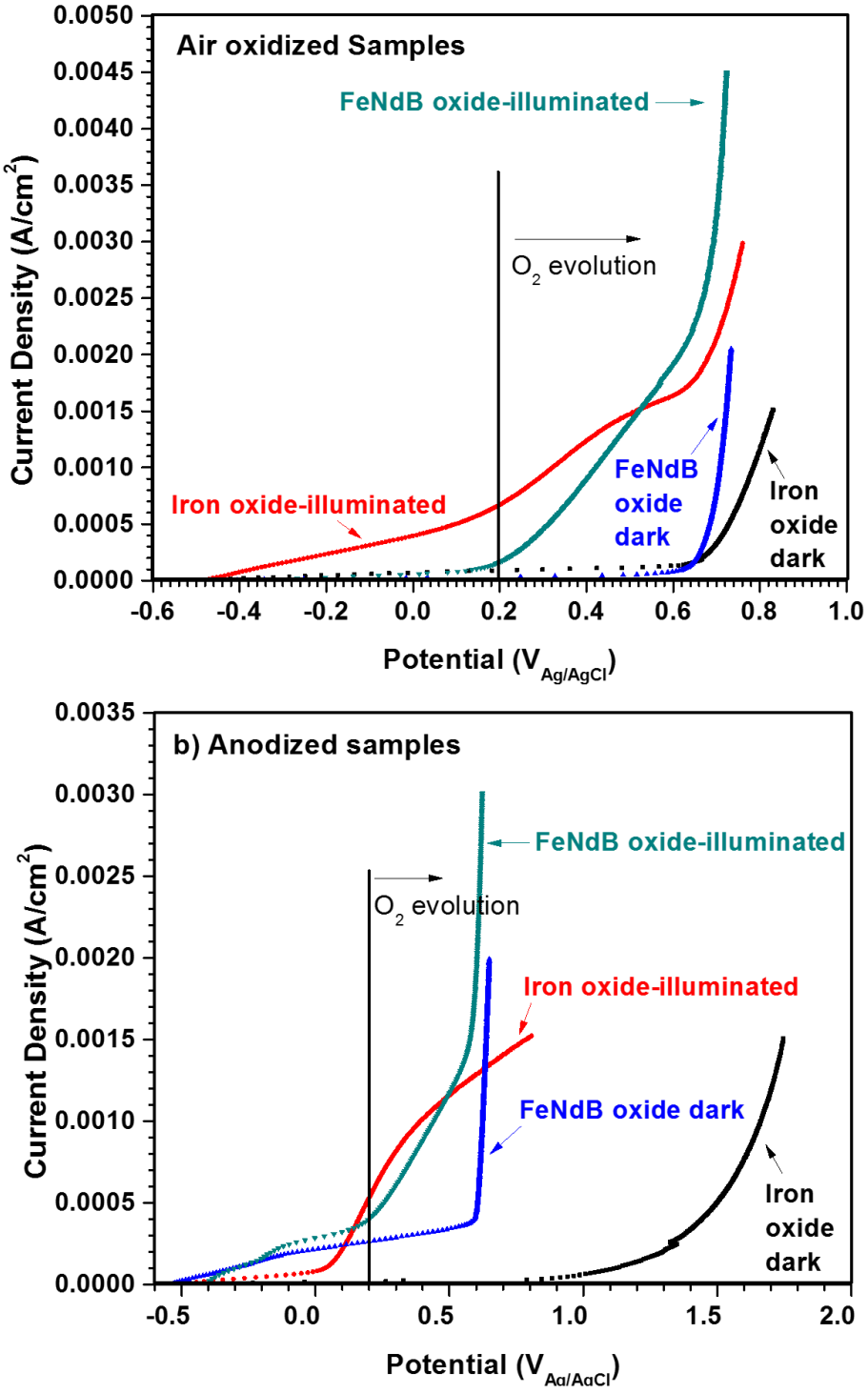

Figure A4. Galvanodynamic polarization results of the oxides of iron and FeNdB alloy in 1 M KOH solution with and without illumination: (a) Samples thermally oxidized in air; and (b) Samples anodized and annealed. The scan rate was 5 $\mu A cm^{-2} s^{-}$

The OER catalytic activities of the thermally oxidized surfaces under light illumination were different from that of dark condition. The OER initiated on the iron oxide at a more

negative potential (-0.4 $V_{Ag/AgCl}$) than that of FeNdB oxide. The exchange current density increased by three orders of magnitude when illuminated for both the oxides. The Tafel slopes also increased under illumination which lead to the decrease of the transfer coefficients, as seen in Table A1. Even though the iron oxide performed better at lower applied potentials, FeNdB oxide showed higher current density at potential higher than 0.52 $V_{Ag/AgCl}$. The reason for such behavior could be understood by considering the thickness of the oxide layer, thickness of the space charge layer, and charge carrier densities as described later.

The anodized oxide surfaces showed different OER catalytic behaviors as compared to that of thermally oxidized surfaces as seen in Figure A4 (b). The difference could be attributed to the difference in the morphologies of the anodic oxide and thermally oxidized surface. The anodic oxide had relatively larger surface area due to the nanoporous nature and was also thicker than the thermally oxidized layer. The morphology variation resulted in different electronic properties which will be quantified subsequently. It is interesting to note that the anodic oxide showed a large overpotential, about 1.2 V for the OER under dark condition. Though the exchange current density for OER on the anodized iron oxide was greater than that of thermally oxidized iron, very low transfer coefficients were observed on the anodic iron oxide. On the other hand, anodic oxide of FeNdB performed similar to or slightly better than its thermally oxidized counterpart in terms of transfer coefficient and exchange current density. The overpotential for the OER was similar for both the anodized and thermally oxidized FeNdB. When illuminated, the anodic iron oxide and FeNdB oxide showed almost similar photocatalytic behavior at lower potentials, and the FeNdB anodic oxide performed better at potentials more anodic to 0.5 $V_{Ag/AgCl}$. The anodic oxide of FeNdB showed higher dark current than any other sample. The onset of the photocurrent was observed at around -0.4 and -0.32 $V_{Ag/AgCl}$ for the thermally oxidized and anodized iron oxide samples, respectively. Similar values were reported by other researchers for hematite samples.[12-14] In case of the FeNdB samples, the onset of photocurrent occurred at potentials -0.15 and -0.1 $V_{Ag/AgCl}$ for the thermally oxidized and anodized samples, respectively.

Table A1. Exchange current densities and Tafel slopes of OER of the oxides of pure iron and FeNdB alloy

Sample	Condition	OER exchange current density ($i_{O(O2)}$, A/cm^2)	Tafel slope (V/decade)	Charge Transfer Coefficient
Thermal iron oxide	Dark	2×10^{-7}	0.165	0.36
	Illuminated	2×10^{-4}	0.245	0.24
Oxidized FeNdB	Dark	1×10^{-10}	0.0685	0.86
	Illuminated	9×10^{-6}	0.2	0.30
Anodized iron oxide	Dark	2×10^{-6}	0.55	0.11
	Illuminated	7×10^{-4}	0.57	0.10
Anodized FeNdB	Dark	1×10^{-9}	0.073	0.81
	Illuminated	3×10^{-7}	0.106	0.56

Electrochemical Impedance Characterization

Figures A5 (a) and (b) show the results of electrochemical impedance spectroscopy in the form of Bode plots of the thermally oxidized and anodized samples, respectively with and without illumination. The impedance values decreased orders of magnitude under the illumination for all the samples when compared to the impedance of the dark (not illuminated) condition. The impedance data can be fitted into a Randel's type equivalent circuit consisting of one resistor connected in series with a parallel RC circuit (the capacitance replaced with a constant phase element) as shown in figure S6. The fitted parameters are summarized in Table A2. The anodized iron oxide sample showed the highest impedance value among all the samples tested in both the dark and illuminated conditions. The impedance (Z(ω)) results showed a single time constant and can be described by the relation[15]:

$$Z(\omega) = R_s + \frac{R_{ct}}{1+R_{ct}Y_O(j\omega)^{\alpha}} \qquad [1]$$

Where, R_s = electrolyte resistance, R_{ct} = charge transfer resistance, Y_o represents interfacial capacitance and has a unit of capacitance when $\alpha = 1$, surface heterogeneity or continuously distributed time constants for charge-transfer reaction are represented by $\alpha < 1$. The impedance values of the FeNdB oxide samples were having similar kind of magnitude reported for α-Fe_2O_3 by other researchers.[16]

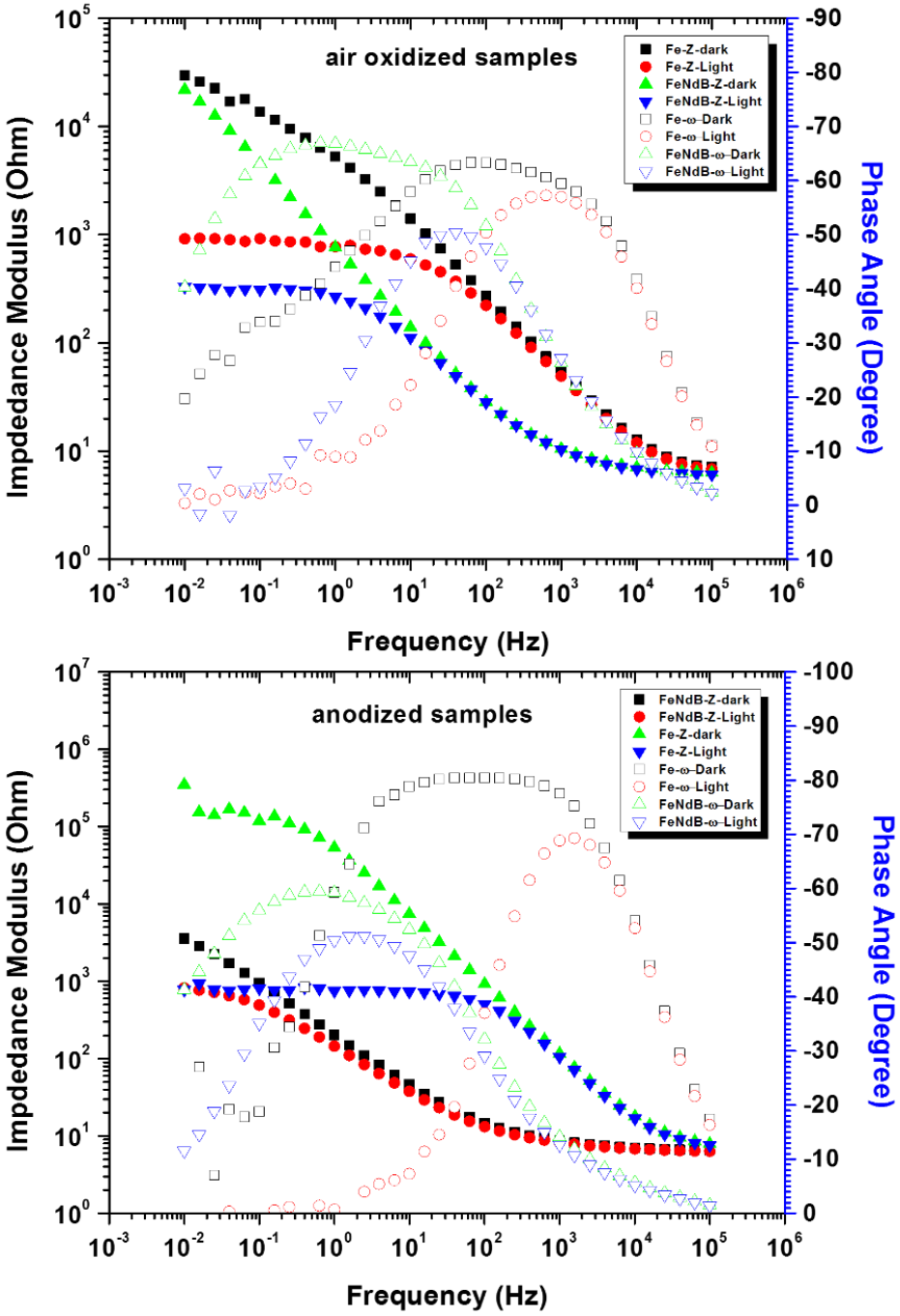

Figure A5. (a) Electrochemical impedance spectroscopy results (Bode plots) of thermally oxidized iron and FeNdB samples in 1 M KOH solution with and without illumination. The samples were biased by an external potential of 0.5 $V_{Ag/AgCl}$. (b) Electrochemical impedance spectroscopy results (Bode plots) of anodized iron and FeNdB samples in 1 M KOH solution with and without illumination. The samples were biased by an external potential of 0.5 $V_{Ag/AgCl}$.

The oxide of FeNdB in both thermally oxidized and anodized conditions showed higher magnitude of capacitance (Y_o) than iron oxide samples. The capacitance value increased upon

illumination for all the samples. On the other hand, the charge transfer resistance decreased when illuminated which could be attributed to photogenerated charge carriers. Klahr et al[17] correlated the interfacial capacitance of surface states of the hematite photoelectrodes to the DOS by the relation:

$$\text{Capacitance } (F/cm^2) = q^2 * DOS \qquad (2)$$

Where q= elementary charge (Coulomb), DOS = density of states having units as $cm^{-2}eV^{-1}$. The higher capacitance values noted for the FeNdB oxide samples could be readily correlated with the large area of the valence band structure observed during the XPS analyses as seen in Figure A2. If the valence structure is considered to represent the electron density of states (DOS) near the Fermi level, apparently the FeNdB oxide showed higher DOS than the iron oxide. It was observed that the value of α decreased marginally upon illumination as compared to the non-illuminated condition. This could be attributed to the increased heterogeneity of the surface due to oxygen bubble formation during the illumination of the electrodes.

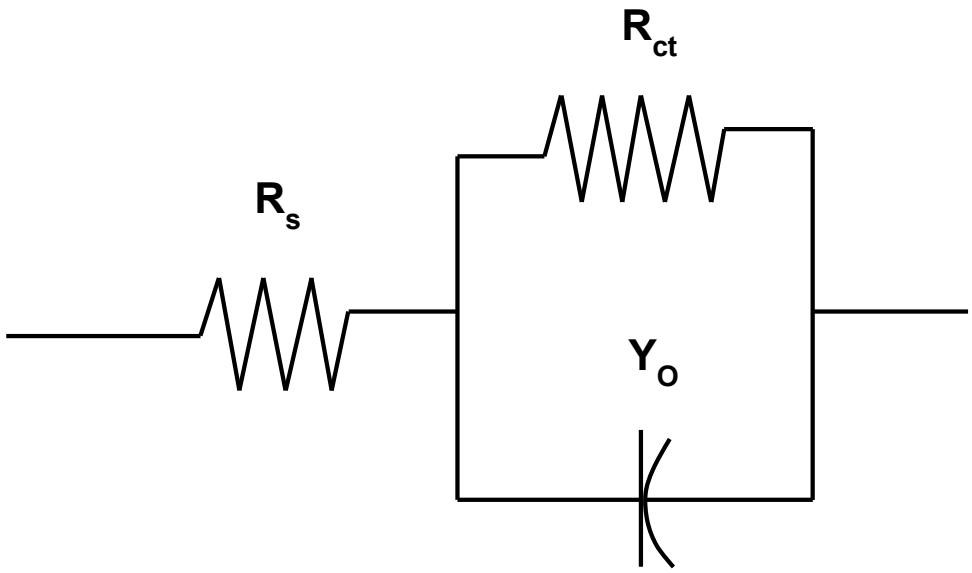

Figure A6. Equivalent circuit for the EIS data in Table A2.

Table A2. Model parameters for electrochemical impedance spectroscopic results of the oxide layers of pure iron and FeNdB alloy under an applied potential of 0.5 $V_{Ag/AgCl}$ in 1 M KOH

Sample	Condition	R_{ct} (Ωcm^2)	R_s, (Ωcm^2)	Y_0, $(\Omega cm^2)^{-1}s^{\alpha}$	α
Thermal iron oxide	Dark	2.3×10^4	5.26	3.40×10^{-5}	0.741
	Illuminated	858.8	5.78	3.74×10^{-5}	0.727
Oxidized FeNdB	Dark	5.1×10^4	6.70	3.10×10^{-4}	0.752
	Illuminated	330	6.2	4.23×10^{-4}	0.71
Anodized iron oxide	Dark	1.56×10^5	7.58	3.35×10^{-6}	0.895
	Illuminated	770.6	7.06	4.49×10^{-6}	0.874
Anodized FeNdB	Dark	1.03×10^4	6.96	1.40×10^{-3}	0.671
	Illuminated	1.01×10^3	6.7	1.97×10^{-3}	0.644

References

1. Grosvenor, A. P.; Kobe, B. A.; Biesinger, M. C.; McIntyre, N. S., Investigation of multiplet splitting of Fe 2p XPS spectra and bonding in iron compounds. *Surface and Interface Analysis* **2004,** *36* (12), 1564-1574.

2. Suzuki, C.; Kawai, J.; Takahashi, M.; Vlaicu, A.-M.; Adachi, H.; Mukoyama, T., The electronic structure of rare-earth oxides in the creation of the core hole. *Chemical Physics* **2000,** *253* (1), 27-40.

3. Herrera-Erazo, A. E.; Habazaki, H.; Shimizu, K.; Skeldon, P.; Thompson, G. E., Anodic film growth on Al–Nd alloys. *Corrosion Science* **2000,** *42* (10), 1823-1830.

4. McIntyre, N. S.; Zetaruk, D. G., X-ray photoelectron spectroscopic studies of iron oxides. *Analytical Chemistry* **1977,** *49* (11), 1521-1529.

5. Yuan, M.; Zhang, J.; Yan, S.; Luo, G.; Xu, Q.; Wang, X.; Li, C., Effect of Nd2O3 addition on the surface phase of TiO2 and photocatalytic activity studied by UV Raman spectroscopy. *Journal of Alloys and Compounds* **2011,** *509* (21), 6227-6235.

6. Raghu, R. R.; Raja, K. S.; Panday, A.; Misra, M., Low-cost photoelectrocatalyst based on a nanoporous oxide layer of low-carbon steel. *Journal of Physics D: Applied Physics* **2010,** *43* (44), 445301.

7. Liu, Z.; Pesic, B.; Raja, K. S.; Rangaraju, R. R.; Misra, M., Hydrogen generation under sunlight by self ordered TiO2 nanotube arrays. *International Journal of Hydrogen Energy* **2009,** *34* (8), 3250-3257.

8. Magnan, H.; Stanescu, D.; Rioult, M.; Fonda, E.; Barbier, A., Enhanced photoanode properties of epitaxial Ti doped α-Fe2O3 (0001) thin films. *Applied Physics Letters* **2012,** *101* (13), -.

9. Rohrer, G. S., *Structure and Bonding in Crystalline Materials*. Cambridge University Press: 2001.

10. Guidelli, R.; Compton Richard, G.; Feliu Juan, M.; Gileadi, E.; Lipkowski, J.; Schmickler, W.; Trasatti, S., Defining the transfer coefficient in electrochemistry: An assessment (IUPAC Technical Report). In *Pure and Applied Chemistry*, 2014; Vol. 86, p 245.

11. Liao, P.; Toroker, M. C.; Carter, E. A., Electron Transport in Pure and Doped Hematite. *Nano Letters* **2011,** *11* (4), 1775-1781.

12. Vincent, T.; Gross, M.; Dotan, H.; Rothschild, A., Thermally oxidized iron oxide nanoarchitectures for hydrogen production by solar-induced water splitting. *International Journal of Hydrogen Energy* **2012,** *37* (9), 8102-8109.

13. Frites, M.; Shaban, Y. A.; Khan, S. U. M., Iron oxide (n-Fe2O3) nanowire films and carbon modified (CM)-n-Fe2O3 thin films for hydrogen production by photosplitting of water. *International Journal of Hydrogen Energy* **2010,** *35* (10), 4944-4948.

14. Chang, C.-Y.; Wang, C.-H.; Tseng, C.-J.; Cheng, K.-W.; Hourng, L.-W.; Tsai, B.-T., Self-oriented iron oxide nanorod array thin film for photoelectrochemical hydrogen production. *International Journal of Hydrogen Energy* **2012,** *37* (18), 13616-13622.

15. Orazem, M. E.; Tribollet, B., *Electrochemical Impedance Spectroscopy*. Wiley: 2011.

16. Klahr, B. M.; Hamann, T. W., Current and Voltage Limiting Processes in Thin Film Hematite Electrodes. *The Journal of Physical Chemistry C* **2011,** *115* (16), 8393-8399.

17. Klahr, B.; Gimenez, S.; Fabregat-Santiago, F.; Hamann, T.; Bisquert, J., Water Oxidation at Hematite Photoelectrodes: The Role of Surface States. *Journal of the American Chemical Society* **2012,** *134* (9), 4294-4302.

Appendix B. Supplementary Information for Chapter 3

Pore size distribution of anodic bismuth oxide

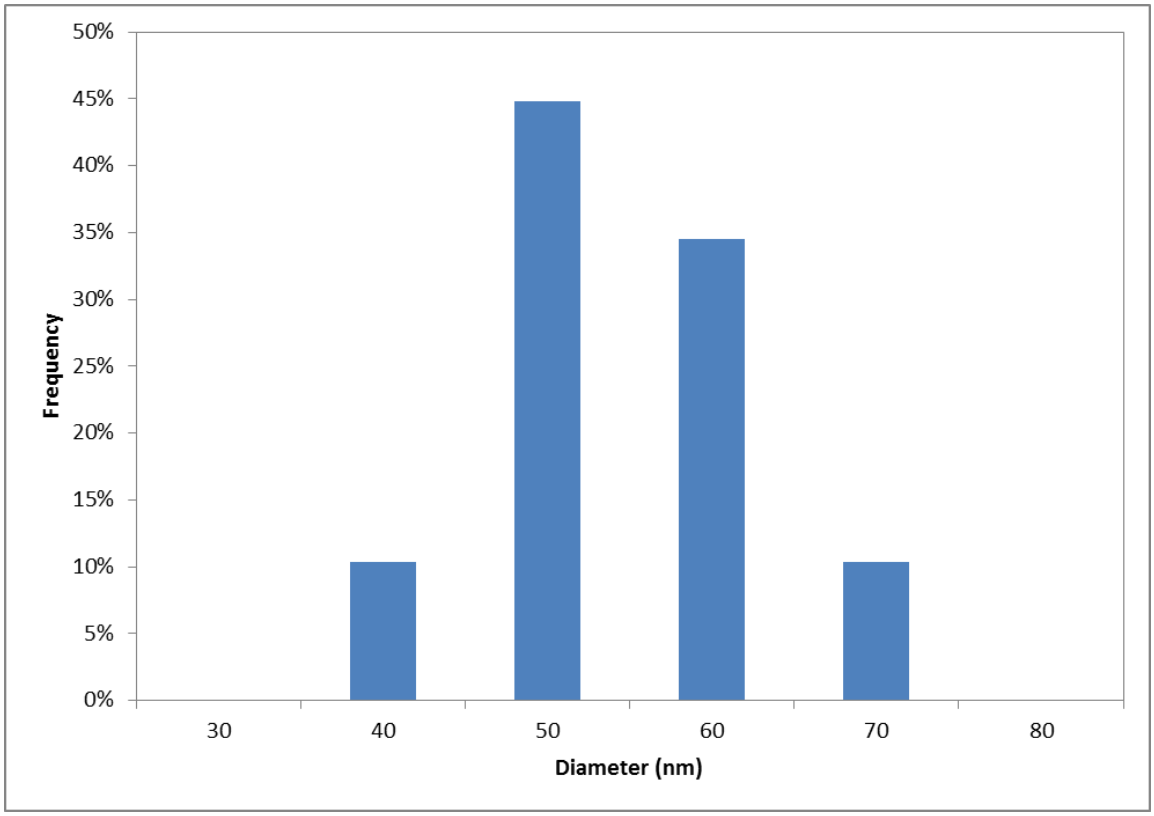

Figure B1. Pore size distribution of anodic bismuth oxide prepared by anodization at 60 V for 30 min. similar frequencies of distribution were observed for other anodization conditions as well.

Table B1 Estimated surface area of the anodic Bi_2O_3 samples per 1 cm^2 projected area based on geometric relation

Anodization potential, V	**Surface area of the sample, cm^2 /cm^2 of projected area**
3	11.37
5	15.72
10	27.77
20	26.46
40	27.78
60	27.45

Cross-sectional SEM

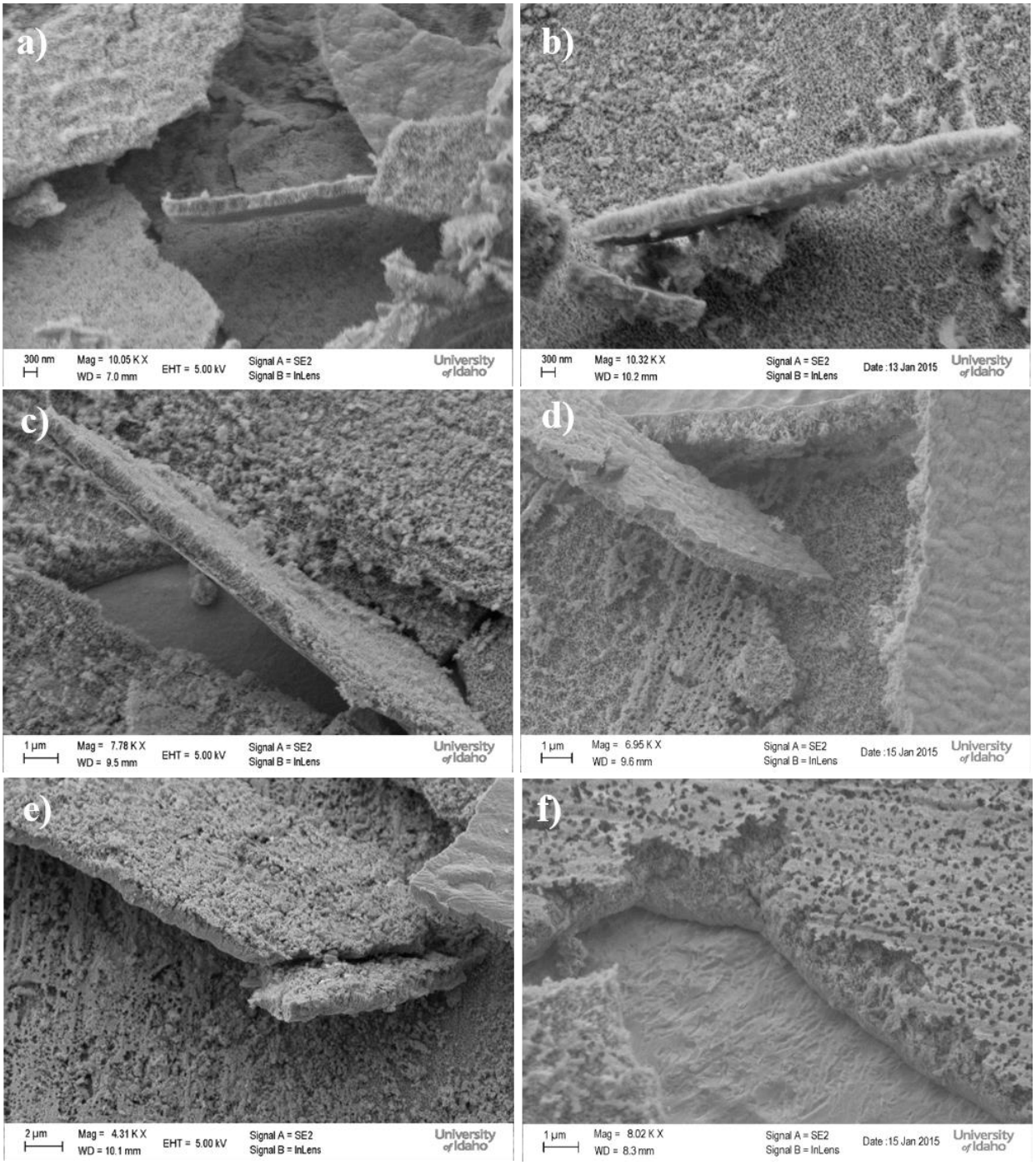

Figure B2. Cross-sectional FESEM images of the bismuth oxide nanoporous oxide layer prepared at various anodization potentials, a) 3 V, b) 5 V, c) 10 V, d) 20 V, e) 40 V and f) 60 V for 30mins

Stability test carried out for 1h

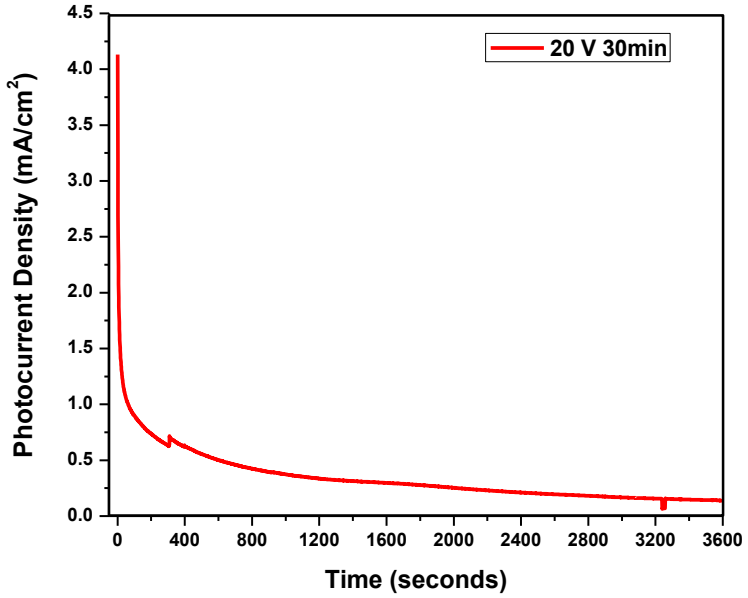

Figure B3. Result of a long term potentiostatic photoelectrochemical test carried out on the nanoporous Bi_2O_3 sample anodized at 20 V 30 min. in 1 M KOH at 0.5 $V_{Ag/AgCl}$.

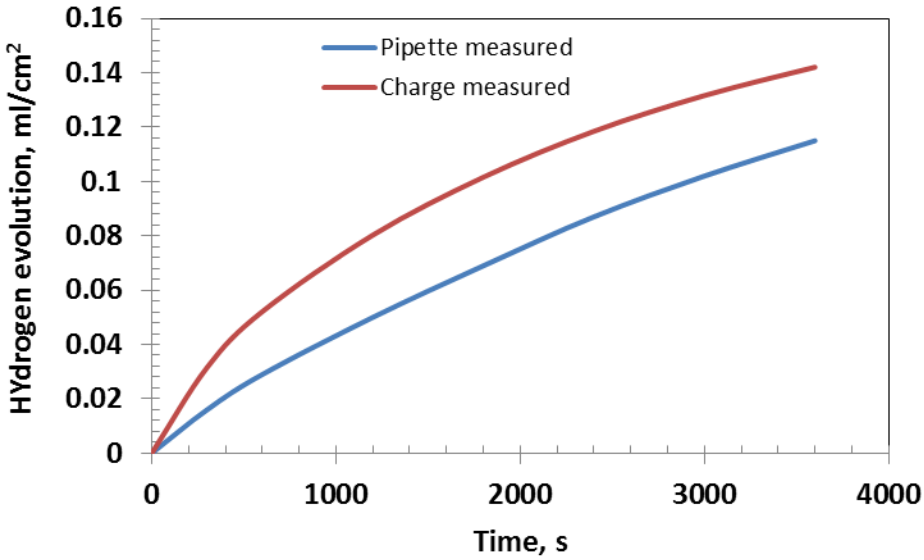

Figure B4. Hydrogen evolution measurement during potentiostatic (0.5 $V_{Ag/AgCl}$) polarization of the nanoporous anodic bismuth oxide sample (anodized at 20 V, 30 min.) in 1 M KOH. The top curve is constructed based on the charge accumulation due to photocurrent. The bottom curve is the actual hydrogen volume measured by water displacement. The difference in the values is attributed to the dissolved hydrogen in the KOH and other experimental limitations.

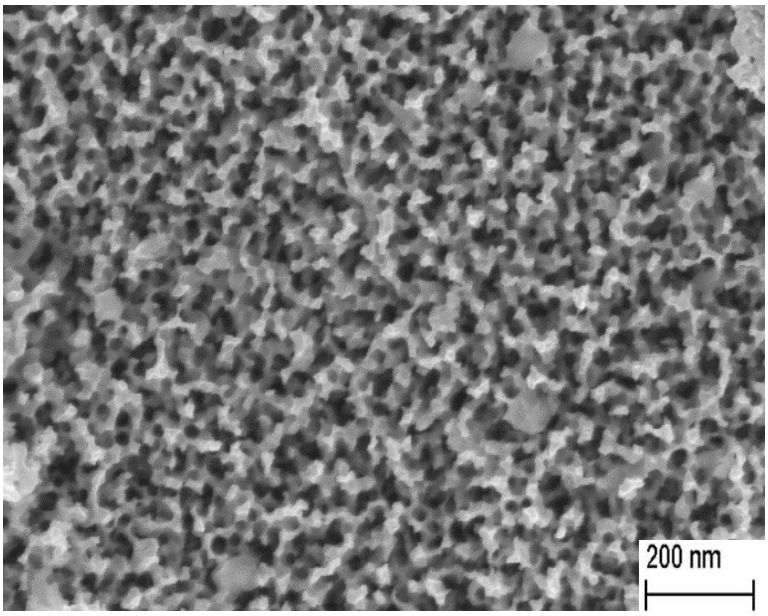

Figure B5. SEM image of the surface morphology of the nanoporous bismuth oxide sample (anodized at 20 V, 30 min.) after potentiostatic photoelectrochemical test at 0.5 $V_{Ag/AgCl}$ for 1 h. The nanoporous morphology was not significantly altered after 1 h exposure to simulated sunlight and applied potential.

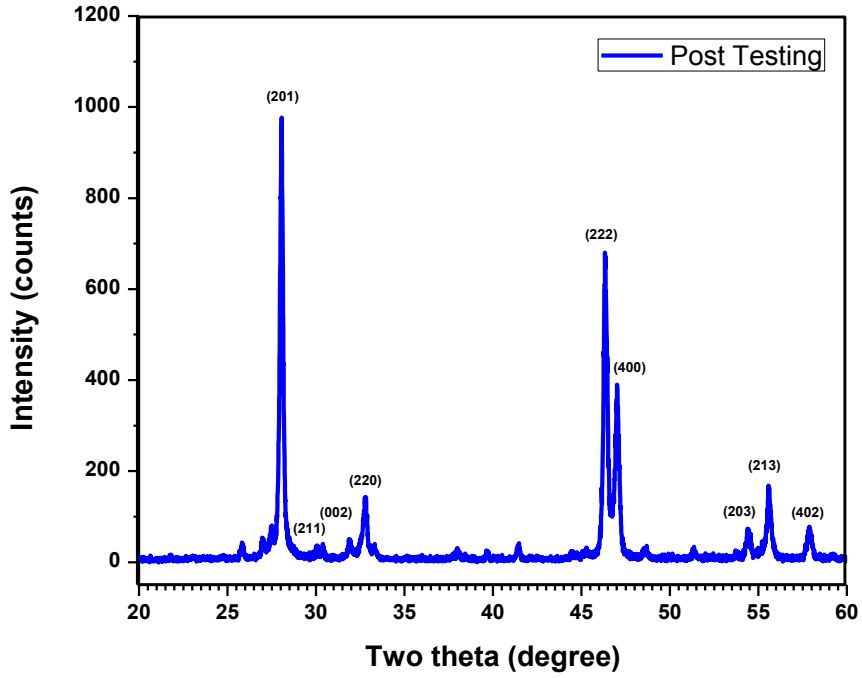

Figure B6. XRD of the nanoporous bismuth oxide sample (anodized at 20 V, 30 min.) after potentiostatic photoelectrochemical test at 0.5 $V_{Ag/AgCl}$ for 1 h.

Electrochemical Impedance Characterization (Nyquist Plots)

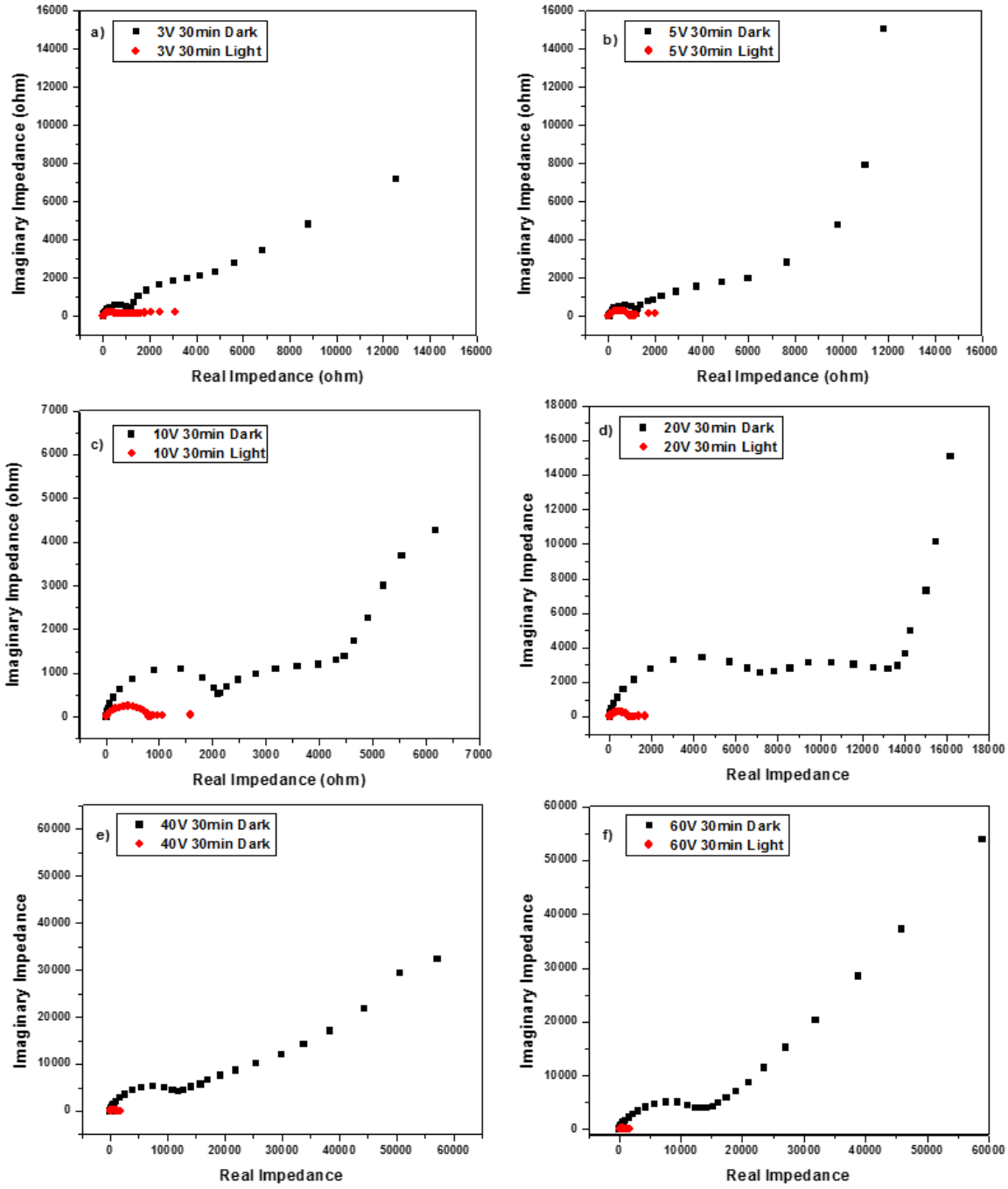

Figure B7. Electrochemical impedance spectroscopy (Nyquist plots) of the anodic nanoporous Bi_2O_3 samples anodized at a) 3 V, b) 5 V, c) 10 V, d) 20 V, e) 40 V and f) 60 V for 30mins with and without illumination.

Electrochemical Impedance Characterization (Bode Plots)

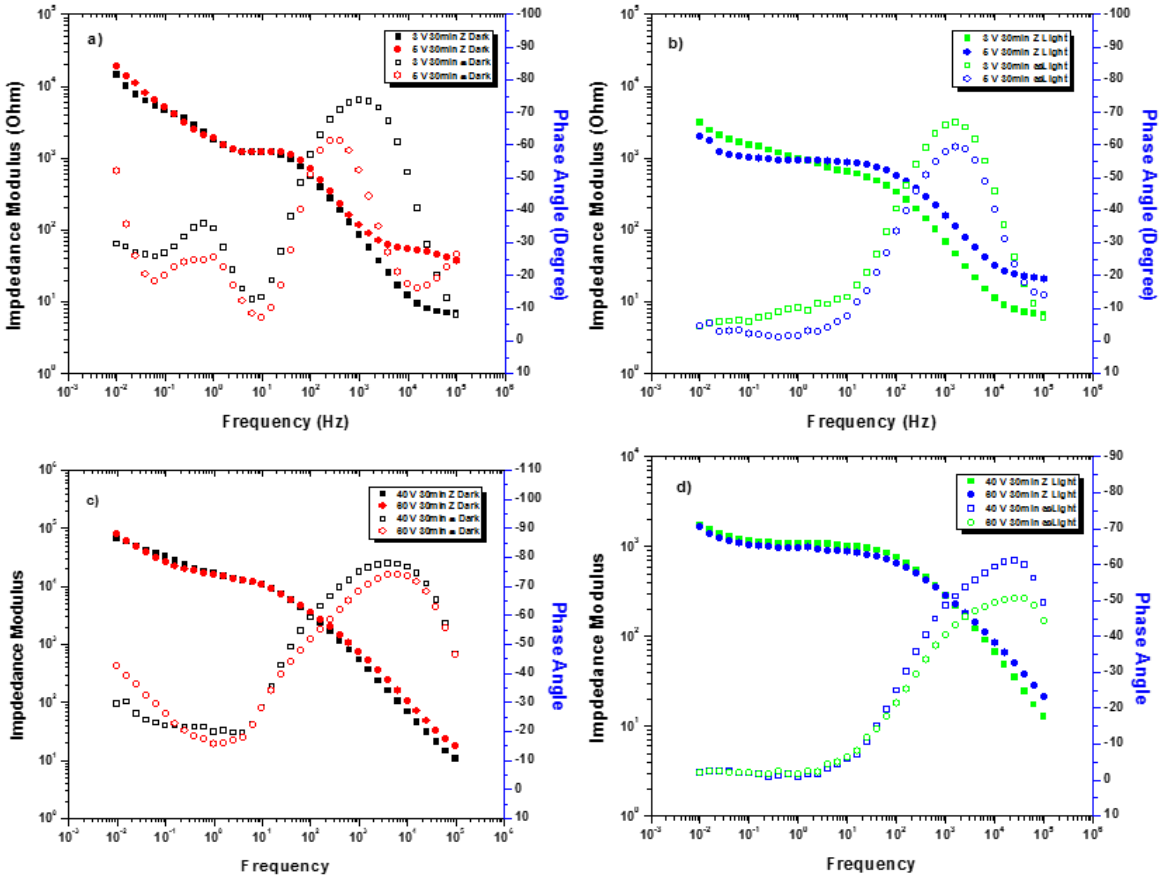

Figure B8. Electrochemical impedance spectroscopy (Bode plots) of the anodic nanoporous Bi_2O_3 samples anodized at a) 3 V & 5 V without illumination., b) 3 V & 5 V with illumination, c) 40 V & 60 V without illumination and d) c) 40 V & 60 V with illumination

Mott-Schottky analysis

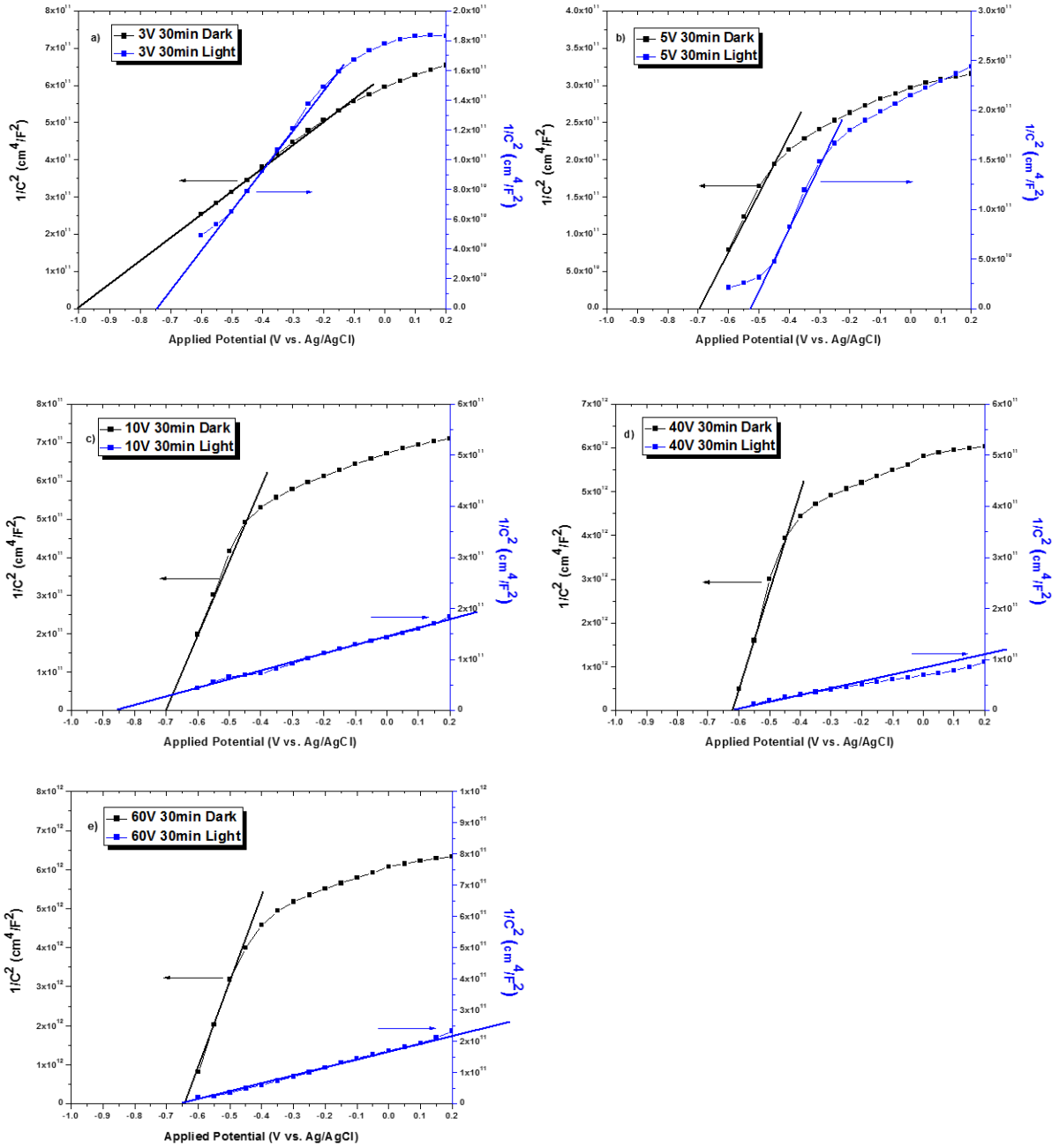

Figure B9. Mott-Schottky analysis of the anodic nanoporous Bi_2O_3 samples anodized at a) 3 V, b) 5 V, c) 10 V, d) 40 V and e) 60 V for 30mins with and without illumination.

Appendix C. Supplementary Information for Chapter 4

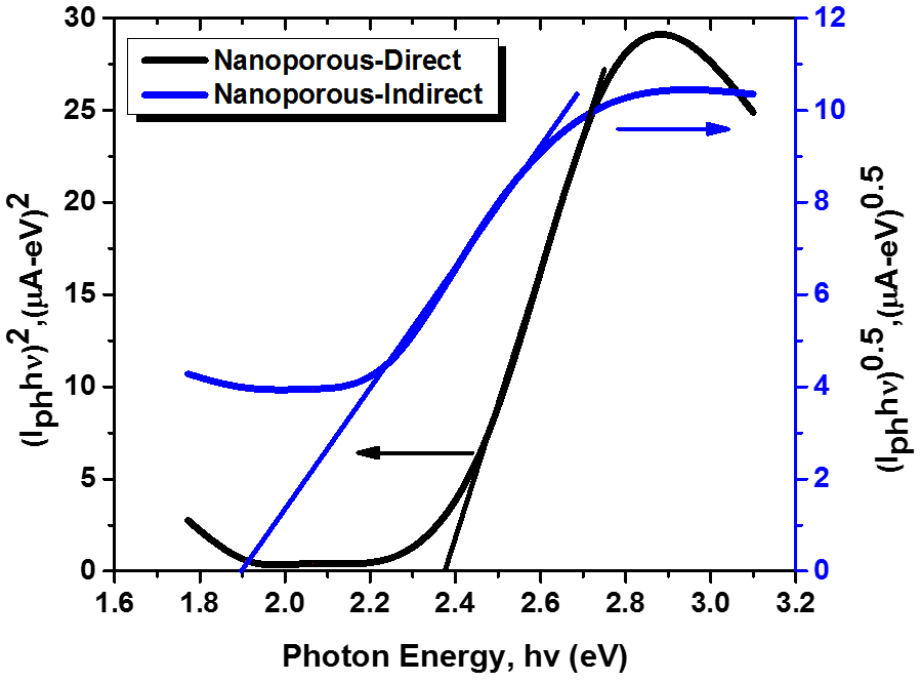

Figure C1. Tauc plots of nanoporous anodic Bi_2O_3 based on the photo current measurements in 1 M KOH at a bias potential of 1.5 V_{RHE}.

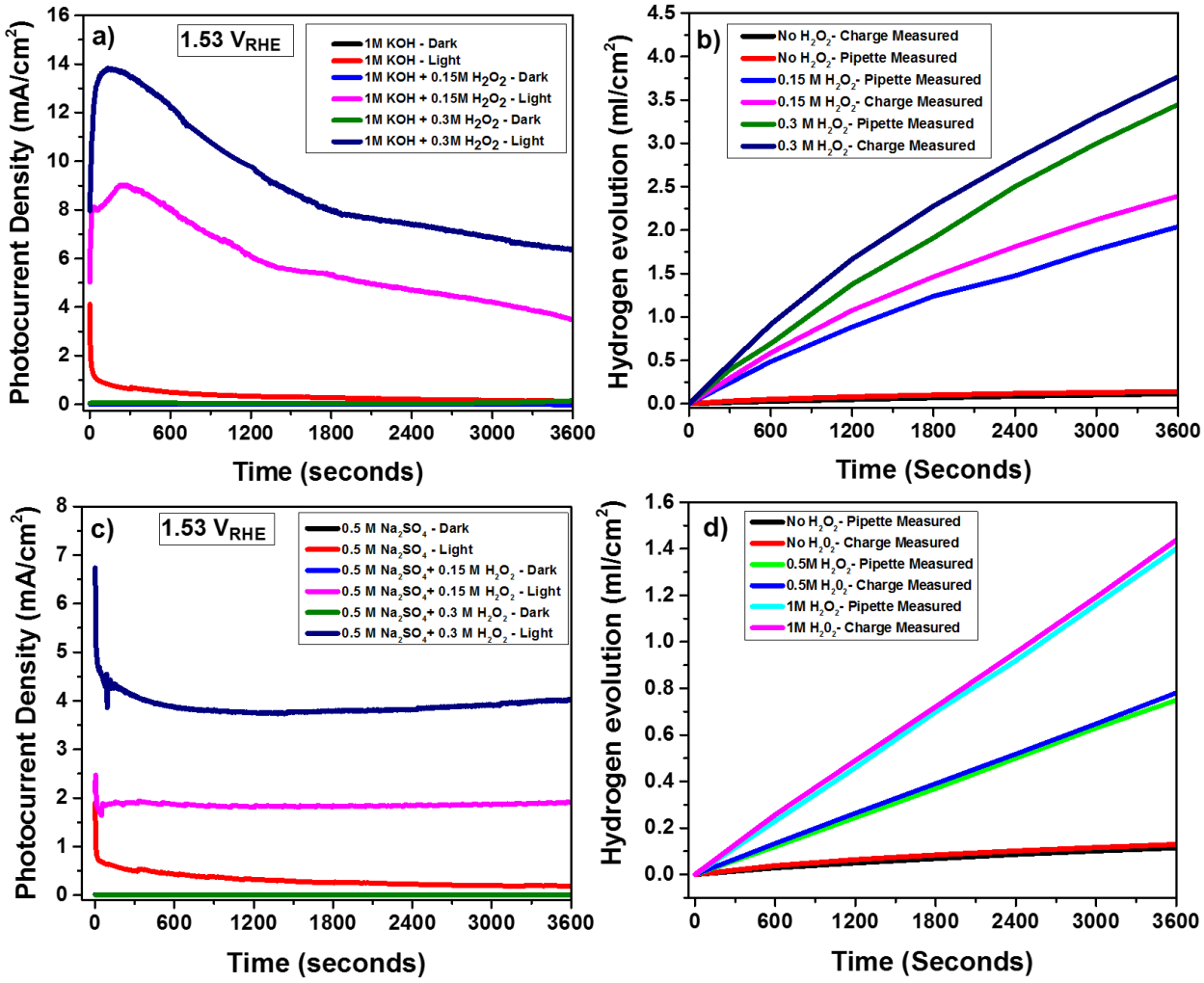

Figure C2. (a) Potentiostatic current transients with the addition of H_2O_2 as hole-scavenger for the nanoporous Bi_2O_3 at 1.5 V_{RHE} in 1 M KOH solution; (b) Cumulative hydrogen evolution as a function of time measured by water displacement using a pipette in comparison with the charge accumulation with and without H_2O_2. (c) Potentiostatic current transients with the addition of H_2O_2 as hole-scavenger for the nanoporous Bi_2O_3 at 1.5 V_{RHE} in 0.5 M Na_2SO_4 solution; (d) Cumulative hydrogen evolution as a function of time measured by water displacement using a pipette in comparison with the charge accumulation with and without H_2O_2 .

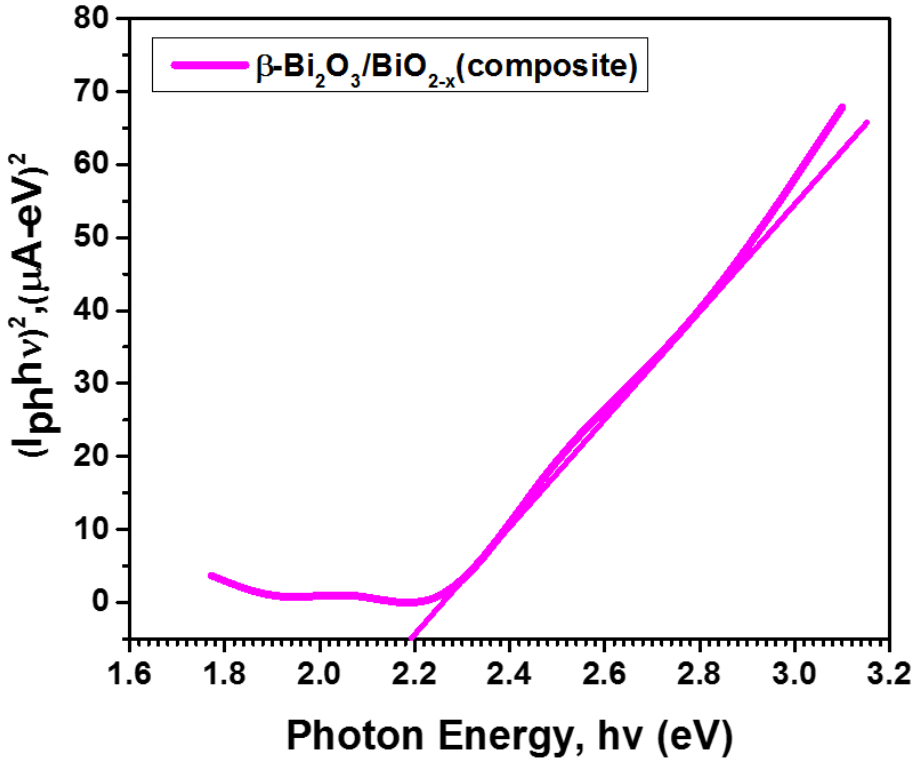

Figure C3. Tauc plot constructed using the β-Bi_2O_3/BiO_{2-x} composite sample.

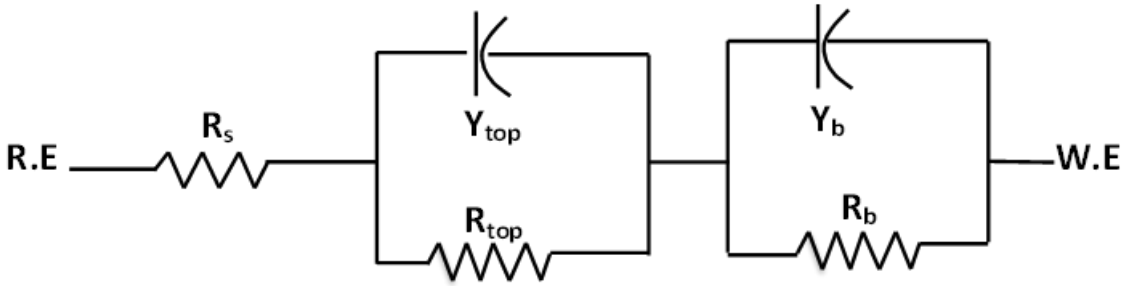

Figure C4. Equivalent circuit diagram of the ‘‘2 RC-in-series’ model used for fitting the experimental values and derived the values of circuit parameters listed in Tables S1-S2.

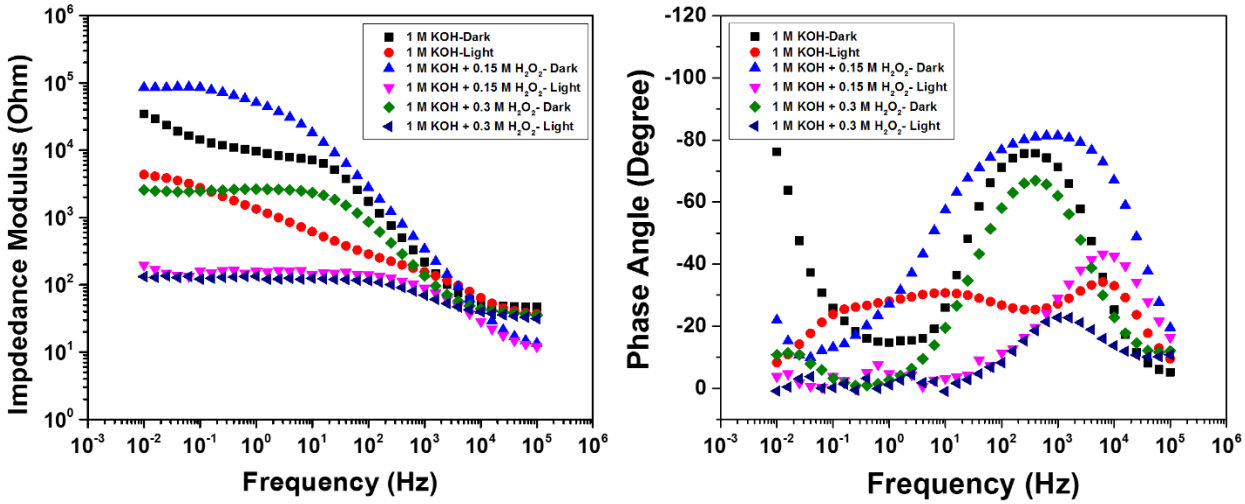

Figure C5. Summary of the values of equivalent circuit components fitted using the '2RC-in series model' with the EIS data of nanoporous bismuth oxide in 1 M KOH with and without addition of hole scavengers.

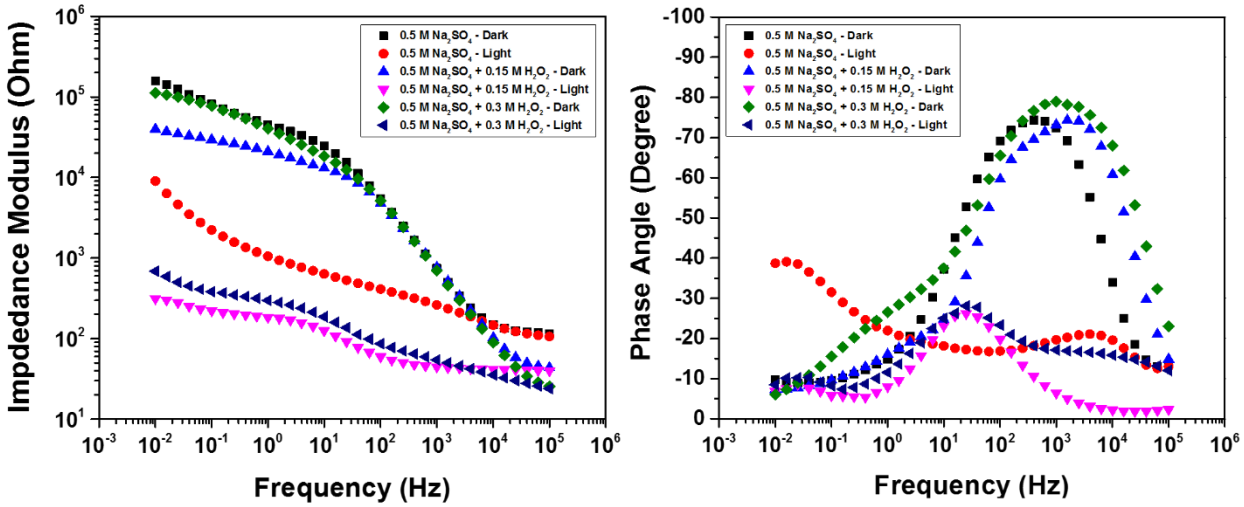

Figure C6. Summary of the values of equivalent circuit components fitted using the '2CPE-Warburg model' with the EIS data of nanoporous bismuth oxide in 0.5 M Na_2SO_4 with and without addition of 0.15 M and 0.3 M of hydrogen peroxide.

Table C1. Summary of the values of equivalent circuit components fitted using the '2RC-in series model' with the EIS data of nanoporous bismuth oxide in 1M KOH with and without addition of hole scavengers.

1M KOH	R_u Ohm	Y_{Top} $S.s^{\alpha}$	α	$R_{barrier}$ Ohm	$Y_{barrier}$ $S.s^{a2}$	a_2	R_{top} Ohm
NO H_2O_2 Dark	45.67	1.39×10^{-6}	0.934	15.23×10^{9}	231.3×10^{-6}	0.776	8.85×10^{3}
NO H_2O_2 Light	28.05	282.4×10^{-6}	0.444	71.65	1.715×10^{-6}	0.937	5.9×10^{3}
0.15 M H_2O_2 Dark	11.97	8.36×10^{-6}	0.867	32.87×10^{3}	1.1×10^{-6}	0.929	54.7×10^{3}
0.15 M H_2O_2 Light	9.325	13.45×10^{-6}	0.726	33.64	466×10^{-3}	1.00	144.8
0.3 M H_2O_2 Dark	35.83	3.8×10^{-6}	0.873	3.77×10^{6}	23.48×10^{-6}	1.00	2.52×10^{3}
0.3 M H_2O_2 Light	0.2	$2.1x\ 10^{-3}$	0.30	82.62	27.13×10^{-4}	0.743	2.67×10^{3}

Table C2. Summary of the values of equivalent circuit components fitted using the 'Rc in series model' with the EIS data of nanoporous bismuth oxide in 0.5 M Na_2SO_4 with and without addition of hole scavengers.

Na_2SO4	R_u Ohm	Y_{Top} $S.s^{\alpha}$	α	$R_{barrier}$ Ohm	$Y_{barrier}$ $S.s^{a2}$	a_2	R_{top} Ohm
NO H_2O_2 Dark	107.2	17.8×10^{-6}	0.721	35.06×10^{3}	602.2×10^{-9}	0.903	94.5×10^{3}
NO H_2O_2 Light	73.28	678.8×10^{-6}	0.538	547.1	91×10^{-6}	0.433	1.59×10^{3}
0.15 M H_2O_2 Dark	36.87	591.6×10^{-6}	0.902	22.53×10^{3}	23.92×10^{-6}	0.711	12.8×10^{3}
0.15 M H_2O_2 Light	41.04	$406.1x\ 10^{-6}$	0.690	104	44.9×10^{-3}	0.921	166.6
0.3 M H_2O_2 Dark	20.4	8.23×10^{-6}	0.763	17.4×10^{3}	563.3×10^{-9}	0.929	80.6×10^{3}
0.3 M H_2O_2 Light	3.877	250×10^{-6}	0.882	608.6	3.877×10^{-6}	0.689	119.8

Table C3. Flat band potentials and charge carrier densities as a function of frequency based on the Mott-Schottky analyses of nanoporous Bi_2O_3 in 1 M KOH without hole scavengers.

Electrolyte	Illumination	Flat band potential (V_{RHE})	Charge carrier density, (cm^{-3})
3000 Hz	Dark	0.29	1.27×10^{18}
	Illuminated	0.40	1.58×10^{18}
1000 Hz	Dark	0.29	1.09×10^{18}
	Illuminated	0.40	8.79×10^{18}
300 Hz	Dark	0.33	1.42×10^{18}
	Illuminated	0.40	3.64×10^{19}
100 Hz	Dark	0.40	3.18×10^{18}
	Illuminated	0.40	1.62×10^{20}

Table C4. Flat band potentials and charge carrier densities as a function of frequency based on the Mott-Schottky analyses of nanoporous Bi_2O_3 in 1 M KOH with the addition of 0.15 M H_2O_2.

Frequency	Illumination	Flat band potential, (V_{RHE})	Charge carrier density, cm^{-3}
3000 Hz	Dark	0.25	3.45×10^{17}
	Illuminated	0.24	2.47×10^{18}
1000 Hz	Dark	0.38	1.93×10^{17}
	Illuminated	0.28	1.15×10^{19}
300 Hz	Dark	0.38	1.37×10^{7}
	Illuminated	0.23	1.34×10^{20}
100 Hz	Dark	0.40	2.14×10^{17}
	Illuminated	0.37	7.30×10^{20}

Table C5. Flat band potentials and charge carrier densities based on the Mott-Schottky analyses of nanoporous Bi_2O_3 in different solutions at 1000 Hz.

Electrolyte	Illumination	Flat band potential ($V_{Ag/AgCl}$)	Flat band potential (V_{RHE})	Charge carrier density (cm^{-3})
1M KOH	Dark	-0.71	0.29	1.09×10^{18}
	Illuminated	-0.60	0.40	8.79×10^{18}
1 M KOH + 0.15 M H_2O_2	Dark	-0.62	0.38	1.93×10^{17}
	Illuminated	-0.72	0.28	1.15×10^{19}
1 M KOH + 0.3 M H_2O_2	Dark	-0.64	0.36	5.51×10^{18}
	Illuminated	-0.68	0.32	1.03×10^{20}
0.5 M Na_2SO_4	Dark	-0.57	-0.02	9.27×10^{16}
	Illuminated	-0.50	0.04	2.50×10^{19}
0.5 M Na_2SO_4 + 0.15 M H_2O_2	Dark	-0.29	0.25	4.13×10^{16}
	Illuminated	-0.48	0.06	2.83×10^{19}
0.5 M Na_2SO_4 + 0.3 M H_2O_2	Dark	-0.40	0.14	8.55×10^{16}
	Illuminated	-0.45	0.09	1.85×10^{19}

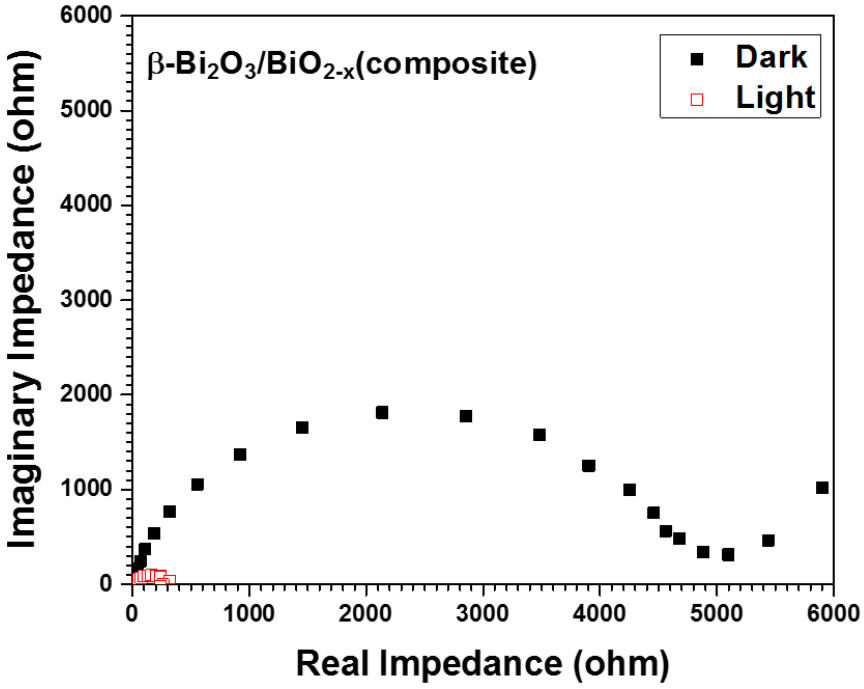

Figure C7. Nyquist plots of β-Bi_2O_3 tested in 1 M KOH + 0.3 M H_2O_2 with illumination (labeled as light) and without illumination (labeled as dark).

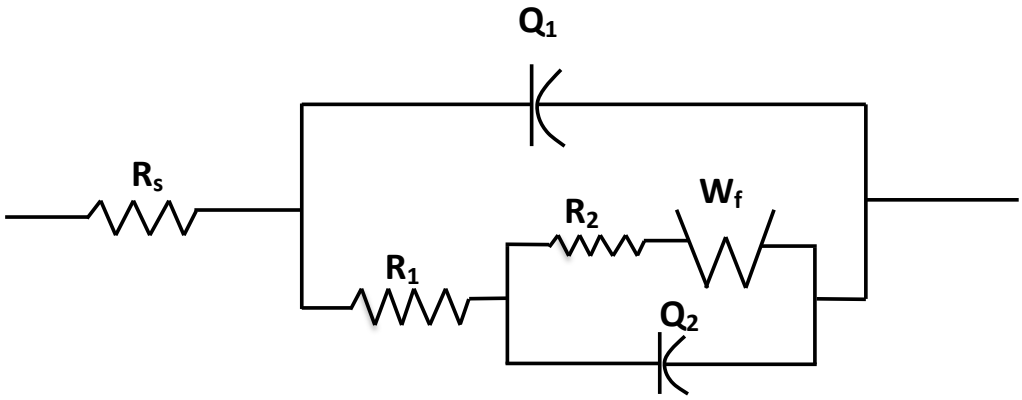

Figure C8. Equivalent circuit for fitting the electrochemical impedance spectroscopic data.

Table C6. Summary of the values of equivalent circuit components fitted using the model in Figure S7 with the EIS data (Figure S5 and S6) of nanoporous bismuth oxide in 1 M KOH and 1 M KOH + 0.3 M H_2O_2 with and without illumination.

Electrolyte	condition	R_s, Ohm	R_1, Ohm	R_2, ohm	Q_1, $S.s^n$	n	Q_2, $S.s^m$	m
1 M KOH + 0.3 M H_2O_2	Dark	13.65	4140	42.4 $x10^3$	1.78 x 10^{-6}	0.88	8.53$x10^{-4}$	0.24
	Light	13.68	217.8	1410	8.19 $x10^{-6}$	0.78	24.5 x 10^{-3}	1.0
1 M KOH	Dark	18.6	1660	50.4 x 10^3	1.2 x 10^{-6}	0.91	1.74 x 10^{-4}	0.68
	Light	12.6	304	755	8.6 x 10^{-6}	0.7	15.9 x 10^{-3}	0.98